178
2-15-74

W-1576

GULF GENERAL ATOMIC

Gulf-GA-A12725
UC-77

HTGR BASE PROGRAM
QUARTERLY PROGRESS REPORT
FOR THE PERIOD ENDING
AUGUST 31, 1973

Prepared under
Contract AT(04-3)-167
Project Agreement No. 17
for the
San Francisco Operations Office
U.S. Atomic Energy Commission

Date Published - September 28, 1973

MASTER

GULF GENERAL ATOMIC COMPANY
P.O. BOX 81608, SAN DIEGO, CALIFORNIA 92138

Printed in the United States of America
Available from
National Technical Information Service
U.S. Department of Commerce
5285 Port Royal Road
Springfield, Virginia 22151
Price: Printed Copy $7.60; Microfiche $0.95

DISCLAIMER

GULF GENERAL ATOMIC

Gulf-GA-A12725
UC-77

HTGR BASE PROGRAM
QUARTERLY PROGRESS REPORT
FOR THE PERIOD ENDING
AUGUST 31, 1973

Prepared under
Contract AT(04-3)-167
Project Agreement No. 17
for the
San Francisco Operations Office
U.S. Atomic Energy Commission

Gulf General Atomic Project 317

Date Published - September 28, 1973

GULF GENERAL ATOMIC COMPANY
P.O. BOX 81608, SAN DIEGO, CALIFORNIA 92138

QUARTERLY REPORT SERIES

GA-4072-December, 1962, through February, 1963
GA-4350-March, 1963, through May, 1963
GA-4569-June, 1963, through August, 1963
GA-4937-September, 1963, through November, 1963
GA-5104-December, 1963, through February, 1964
GA-5366-March, 1964, through May, 1964
GA-5618-June, 1964, through August, 1964
GA-5866-September, 1964, through November, 1964
GA-6113-December, 1964, through February, 1965
GA-6418-March, 1965, through May, 1965
GA-6671-June, 1965, through August, 1965
GA-6869-September, 1965, through November, 1965
GA-7010-December, 1965, through February, 1966
GA-7181-March, 1966, through May, 1966
GA-7396-June, 1966, through August, 1966
GA-7553-September, 1966, through November, 1966
GA-7801-December, 1966, through February, 1967
GA-7981-March, 1967, through May, 1967
GA-8200-June, 1967, through August, 1967
GA-8356-September, 1967, through November, 1967
GA-8530-December, 1967, through February, 1968
GA-8662-March, 1968, through May, 1968
GA-8860-June, 1968, through August, 1968
GA-9090-September, 1968, through November, 1968
GA-9227-December, 1968, through February, 1969
GA-9372-March, 1969, through May, 1969
GA-9660-June, 1969, through August, 1969
GA-9815-September, 1969, through November, 1969
GA-9944-December, 1969, through February, 1970
GA-10088-March, 1970, through May, 1970
GA-10288-June, 1970, through August, 1970
GA-10399-September, 1970, through November, 1970
GA-10501-December, 1970, through February, 1971
GA-10661-March, 1971, through May, 1971
Gulf-GA-A10784-June, 1971, through August, 1971
Gulf-GA-A10930-September, 1971, through November, 1971
Gulf-GA-A10999-December, 1971, through February, 1972
Gulf-GA-A12150-March, 1972, through May, 1972
Gulf-GA-A12222-June, 1972, through August, 1972
Gulf-GA-A12422-September, 1972, through November, 1972
Gulf-GA-A12515-December, 1972, through February, 1973
Gulf-GA-A12575-December, 1972, through February, 1973
Gulf-GA-A12599-March, 1973, through May, 1973

ABSTRACT

This publication continues the quarterly report series on the HTGR Base Program. The Program covers items of the base technology of the High-Temperature Gas-cooled Reactor (HTGR) system. The development of the HTGR system will, in part, meet the greater national objective of more effective and efficient utilization of our national resources. The work reported here includes studies of basic fission-product distribution mechanisms, recycle fuel studies (including designing and testing of recycle test elements) and exploration of head-end reprocessing methods (as part of a national recycle plan and of a recycle fuel plan), and physics and fuel management studies. Materials studies include irradiation and analysis of fuel particles in capsules to evaluate fuel systems, and basic studies of control materials and of carbon and graphite. Experimental procedures and results are discussed and, where appropriate, the data are presented in tables, graphs, and photographs. More detailed descriptions of experimental work are presented in topical reports, and these are listed at the end of the report for those concerned with the field.

INTRODUCTION

This report covers the work performed by Gulf General Atomic under U.S. Atomic Energy Commission Contract AT(04-3)-167, Project Agreement No. 17. This Project Agreement calls for support of basic technology associated with gas-cooled, nuclear power reactor systems. The program is based on the concept of the High-temperature Gas-cooled Reactor (HTGR) developed by Gulf General Atomic.

Large HTGR systems will be placed in operation starting in the late 1970's following the operation of the 330-MW(e) prototype in 1973. Characteristics of these advanced systems include:

1. A single-phase gas coolant allowing generation of high-temperature, high-pressure steam with consequent high-efficiency energy conversion and low thermal discharge.

2. A prestressed concrete reactor vessel (PCRV) offering advantages in field construction, primary system integrity, and stressed member inspectability.

3. Graphite core material assuring high-temperature structural strength, large temperature safety margins, and good neutron economy.

4. Thorium fuel cycle leading to U-233 fuel which allows good utilization of nuclear resources and minimum demands on separative work.

CONTENTS

FIGURES

TABLES

TASK IV
FISSION PRODUCT MECHANISMS

VAPOR PRESSURE STUDIES

The vapor pressure of cesium sorbed on H-327 graphite is being studied utilizing the Knudsen cell method. The objective of this work is to extend the vapor pressure data to low concentrations (below 10 ppm), comparable to presently predicted end-of-life concentrations of cesium in fuel element graphite at the graphite-helium interface. The low concentration data are important for use in refining predicted releases of cesium nuclides in HTGR systems.

As reported in the previous Quarterly Progress Report (Gulf-GA-A12599), isotherms obtained using the mass spectrometric Knudsen cell technique have shown a downward pressure break at a concentration of about 5 ppm (5×10^{-3} mg Cs/g graphite). Demonstration that this is a real equilibrium vapor pressure break could lead to a significant reduction in the predicted release of cesium nuclides in HTGR systems. Accordingly, a systematic investigation was undertaken to characterize the pressure break. Two experimental approaches have been utilized:

1. Experiments utilizing a two-compartment Knudsen cell in the mass spectrometer.

2. An independent experiment utilizing a Knudsen cell tracer technique.

The results of this investigation are described below. In summary, the results indicate that the pressure break is due to a kinetic effect and not a thermodynamic effect (i.e., not a break in the equilibrium vapor pressure).

Vapor Pressure Studies Using the Two-Compartment Knudsen Cell Technique

Three cesium isotherm experiments using the two-compartment Knudsen cell (described in previous Quarterly Progress Report Gulf-GA-A12599) have been performed. In these tests, one of the compartments is loaded with a cesium-graphite powder mixture, whereas the other compartment initially contains only graphite powder. The two cells are connected by an orifice; thus, during an experiment, two separate cesium signals are distinguishable. One signal is from the cesium-graphite (source) side, which during a run is in the process of unloading cesium, and the other signal is from the graphite (sink) side, which is in the process of loading.

Data from one experiment are shown in Fig. 4-1. The vapor pressure data for the source cell show normal behavior, that is, low pressures during heatup, a Langmuir region (where the pressure is proportional to the concentration), and a rapid drop in pressure as the cesium concentration reached approximately 0.007 mg Cs/g graphite.

The vapor pressure data for the sink cell are quite novel and enlightening. The early portion of the loading of the sink sample occurred at pressures even higher than the Langmuir extension of the unloading data. Later, there is good agreement with the Langmuir extension. As the experiment progressed, the loading rate approached zero as demonstrated by the multitude of points near 10^{-8} atm and 0.0038 mg Cs/g graphite. This was followed by an unloading period where the pressure data were divergent from the loading data in such a way as to parallel the pressure drop of the source sample. At the same cesium concentration, the pressures for the sink cell were markedly higher during loading than during unloading, and this deviation appeared to be widening during the unloading period. This divergence demonstrates the lack of achieving equilibrium in the sink cell during this period.

Two other double-cell experiments yielded data that generally corroborate the data of Fig. 4-1. One experiment was identical except that it was terminated very near the peak loading point of the sink

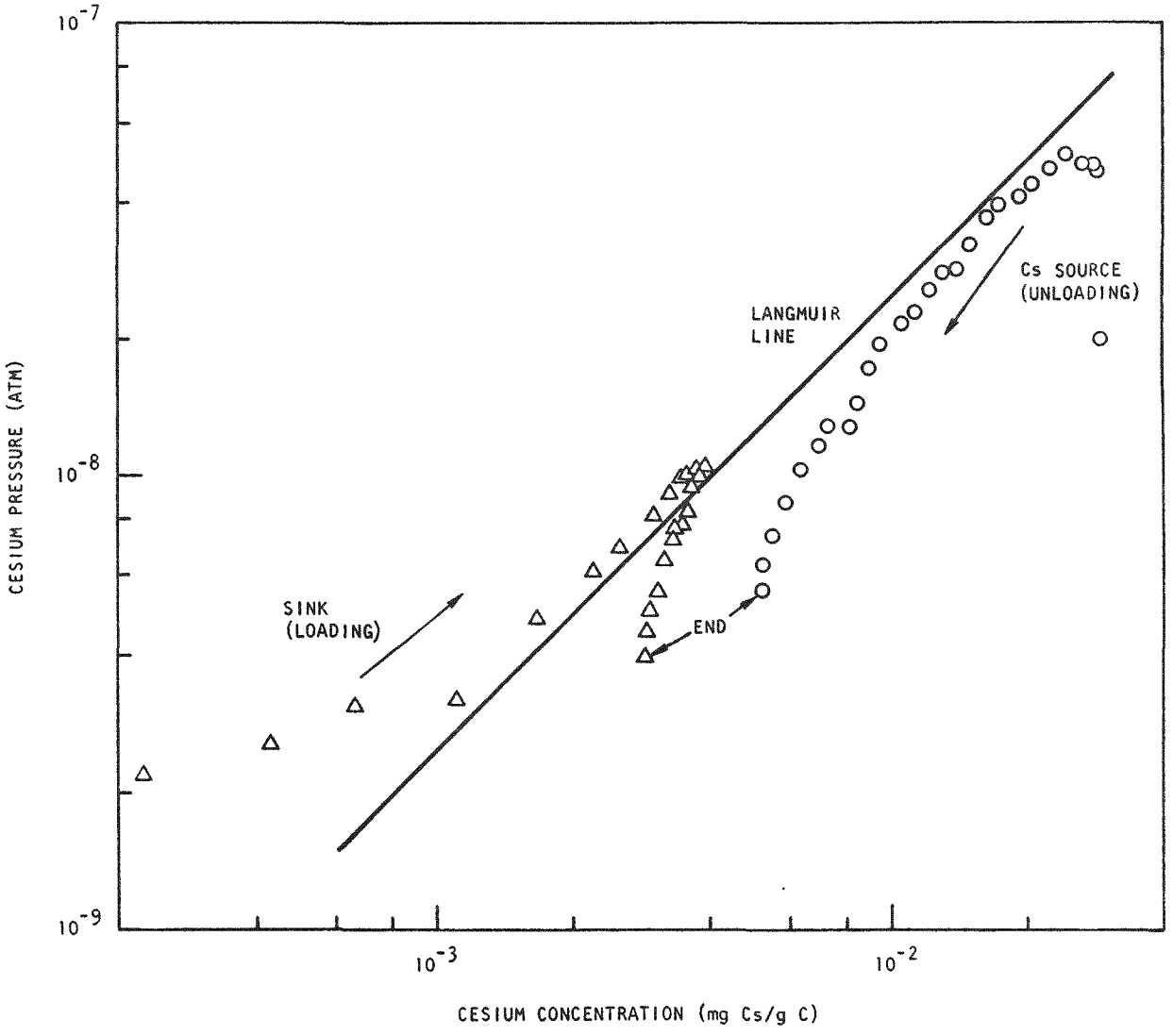

Fig. 4-1. Results of double-cell experiment to study the vapor pressure of cesium sorbed on H-327 graphite powders at 1450°K

sample. The other experiment was performed with a larger ratio of carbon in the sink cell to that in the source cell to make the turnaround occur at lower concentration. This is indeed what occurred. However, the turnaround point was not nearly as sharp, suggesting either more limiting kinetics as the concentration decreases or increased pressure uncertainties at these low values. The turnaround occurred in agreement with the extension of the Langmuir line of Fig. 4-1.

These results show that lack of equilibration is a problem in Knudsen cell studies of the vapor pressure of cesium at low concentration on graphite. It is concluded, therefore, that the pressure break observed in earlier studies is due to a kinetic effect and is not a real equilibrium pressure effect. To what degree the kinetic effect will influence the transport of cesium in the reactor needs to be evaluated.

The double-cell experiments have also yielded important information on the equilibrium vapor pressure. As shown in Fig. 4-1, both the loading and unloading curves for the sink cell converge at 1.03×10^{-8} atm and 0.00375 g Cs/g graphite. The net flux of cesium from the sink cell at this point condition was approximately zero (i.e., the flux through the small orifice interconnecting the source and sink cells supplied as much cesium as escaped through the orifice used to sample the sink cell pressure). This condition applied for approximately 2 hr of the 7.5-hr experiment. During this entire 2-hr period, the pressure changed by no more than 5%, which is within the experimental uncertainty. The fact that the loading and unloading vapor pressure data converge in a sharp manner also implies the establishment of equilibrium during this 2-hr period.

The fact that the convergence of the loading and unloading portions of the sink cell data is sharp (see Fig. 4-1) suggests that the kinetic factor is not one of solid-state diffusion into the graphite crystals. If diffusion is not a problem, the difficulty could reside in evaporation coefficients. It could be that much of the graphite surface fails to participate in effective evaporation and condensation because of the effective cesium sorption sites being appreciably distant from each other.

In addition to the three experiments described above, another double-cell experiment was performed at a smaller ratio of carbon in the sink cell to that in the source cell in order to force the juncture of the loading and unloading data to higher pressures. This experiment yielded unreasonable data and is being rerun.

Vapor Pressure Studies Using the Knudsen Cell Tracer Technique

An experiment was performed utilizing a Knudsen cell tracer technique to study the vapor pressure of cesium sorbed at low concentration on H-327 graphite. This experiment served as an independent check on the break in the cesium vapor pressure curve observed in studies utilizing the mass spectrometric Knudsen cell method.

A diagram of the apparatus, which is a modification of apparatus used in earlier strontium vaporization studies (see Quarterly Progress Report Gulf-GA-A12515), is shown in Fig. 4-2. The Knudsen cell, which is made of molybdenum, is loaded with a cesium-graphite mixture. The cesium is tagged with Cs-137. The cell is suspended in a quartz furnace tube which is evacuated by means of mechanical and oil duffusion pumps to less than 2×10^{-7} torr, a necessary requirement for Knudsen cell vaporization studies.

The vapor effusing from the orifice is collected on a water-cooled cold finger previously electroplated with copper. Cesium is removed from the cold finger by immersion in nitric acid, which also removes the copper plating thereby assuring quantitative cesium removal. The acid solution is counted to determine the cesium content. The Knudsen cell is suspended by a molybdenum wire and is provided with an orifice on the bottom, facilitating use of a cold finger inserted from the bottom. The suspension technique allows the cell to be withdrawn into a separate vacuum chamber through a large bore stopcock, while the cold finger is removed for assay. The dimensions of the cell were about 1.6 cm in diameter by 1.7 cm long. The cell was made and loaded so that no graphite powder could fall through the orifice during an experiment. The graphite powder used and the method of impregnating the graphite with cesium were the same as used in the mass spectrometric studies.

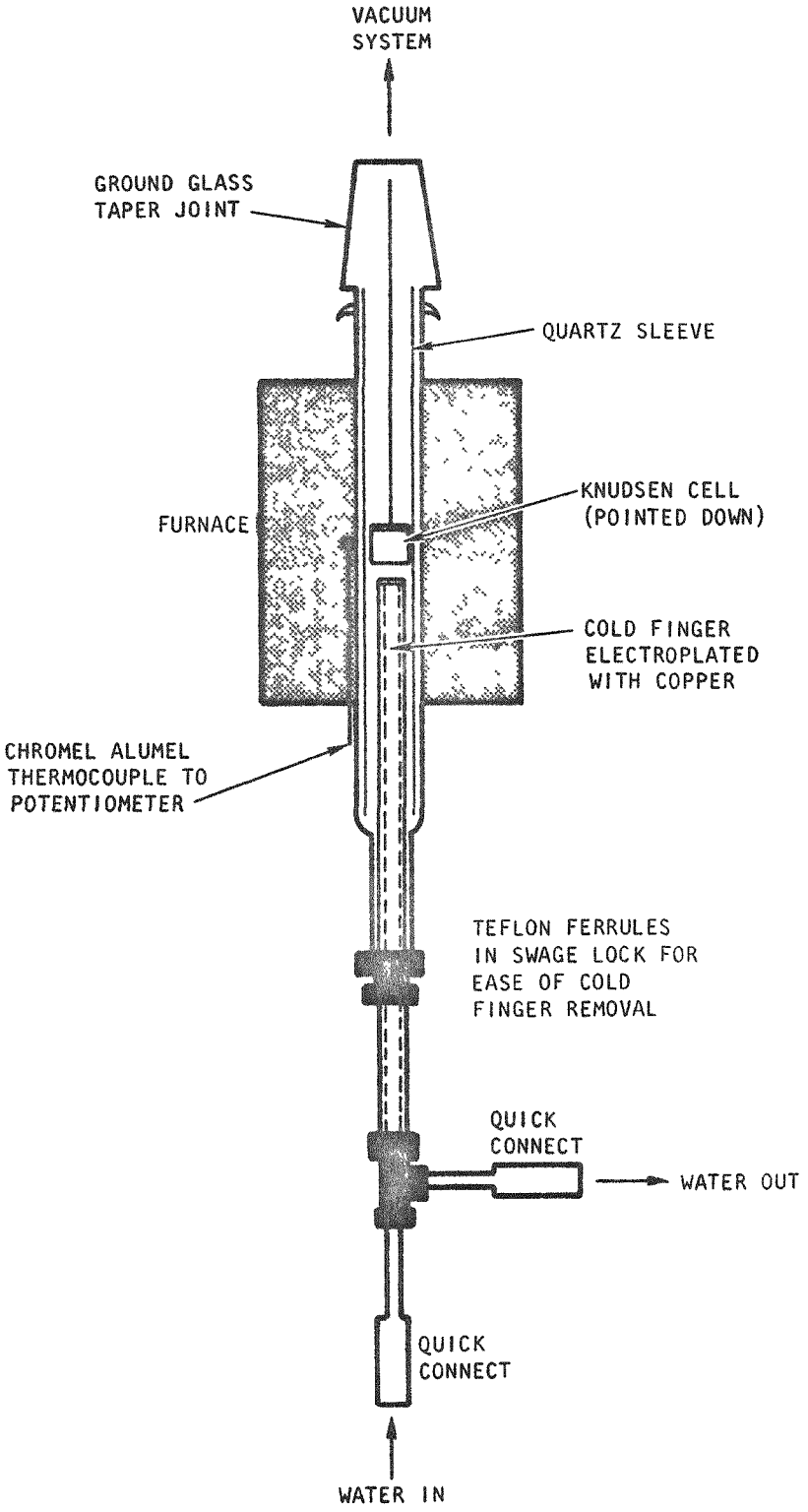

Fig. 4-2. Apparatus for measuring vapor pressures by the Knudsen cell tracer technique

The vapor pressure data are calculated from a form of the Langmuir equation:

$$P_{Cs} = \frac{G'(17.14)}{KAt(760)} (T/M)^{1/2} ,$$

where P_{Cs} = vapor pressure cesium, atm
G' = quantity cesium effused, g
K = Clausing factor (0.3996)*
A = orifice area, cm^2
t = time, sec
T = temperature, °K
M = molecular weight, g/mole

One experiment has been conducted. At the end of the experiment, the cesium content of the Knudsen cell was determined by gamma counting. The cesium loading was found to be 8.8×10^{-3} mg Cs/g C; this value is in reasonable agreement with the calculated value of 11.1×10^{-3} calculated from the amount vaporized. This close agreement in the measured and calculated final loadings indicates that the assumptions used in the Langmuir equation are reasonably correct.

The experimental data are given in Fig. 4-3, which is a plot of vapor pressure versus loading for the temperature of 1300°K (1027°C). Mass spectrometric data for the same temperature are included for comparison. The two sets of data are in reasonable agreement, and both show downward pressure breaks at loadings around 10^{-2} mg Cs/g C.

The conclusion of this study is that the pressure break is not just a characteristic of the mass spectrometric vapor pressure data. It should not

---

*The Clausing factor is the ratio of the number of gaseous atoms that escape through the orifice to the number that enter the orifice. The factor is related to the dimensions of the orifice.

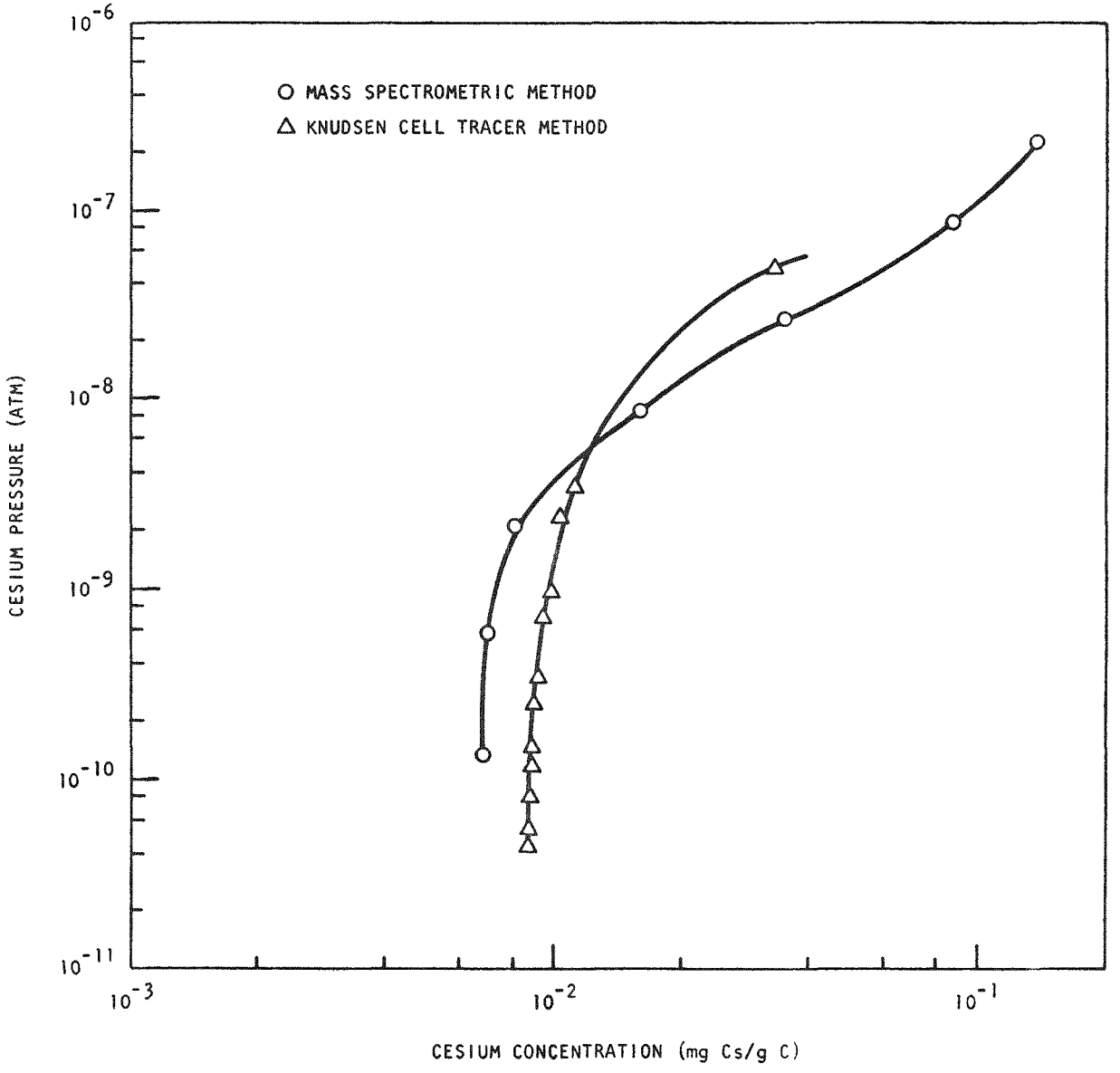

Fig. 4-3. Comparison of cesium vapor pressure data at 1027°C (on H-327 graphite powder) obtained by the mass spectrometric and Knudsen cell tracer methods

be overlooked that the reasonable agreement between the two sets of data (see Fig. 4-3) serves to substantiate the reliability of vapor pressure data determined by the mass spectrometric method.

In view of the above described findings of the experiments utilizing the double compartment Knudsen cell, indicating that the pressure break is caused by kinetic effects, no further work using the Knudsen cell tracer technique is planned.

FISSION PRODUCT PLATEOUT AND LIFTOFF STUDIES

A deposition loop, assembled at GGA, is being used to study the plateout characteristics of cesium, strontium, and iodine under conditions similar to HTGR conditions. Helium at 350 psia circulates in the loop with Reynolds numbers of around 15,000 and temperatures varying from 150° to 320°C. The type of steel used for the loop tubing is representative of steel used in the steam generators of HTGRs. Surface temperatures in the loop vary from 200° to 400°C. The source of fission products in the loop is obtained by heating graphite crucibles within the loop that are loaded with the fission products sorbed on graphite matrix material.

The objectives of the loop work are to obtain plateout distribution data and to obtain liftoff data by subjecting sections of the loop to conditions of higher shear ratios than obtained in the loop. The plateout data are used to test and refine the PAD code. The liftoff data are used for safety analyses associated with HTGR depressurization accidents.

Experimental work on deposition loop experiment No. 4 was completed during the quarter. Cesium tagged with Cs-137 was deposited at loop surface temperatures of 300° to 400°C. As reported in the previous Quarterly Progress Report (Gulf-GA-A12599), the specific activities (cpm/cm) for the two parallel legs of the loop differed by as much as a factor of three with leg No. 1 showing the lowest count rate. Recounting

of selected samples has confirmed this difference. This difference in plateout could reflect differences in flow rates caused by unequal flow resistances in the two legs, but this possibility is not substantiated by the results in Fig. 4-4(see below).

Liftoff tests for loop experiment No. 4 gave very low cesium liftoff fractions. Less than 0.35% of the deposited activity was removed by shear ratios as high as 11. The results are summarized in Fig. 4-4. Mean values of these data are plotted in Fig. 4-5 for comparison with the GAIL IV liftoff data. The loop liftoff data are considerably below the GAIL data. Agreement of liftoff fraction data between an earlier experiment (experiment No. 1, reported in Gulf-GA-A12422) and experiment No. 4 is good.

For conservatism, the shear ratios (the wall shear stress during liftoff divided by the shear stress during normal operation) were calculated by assuming the highest credible loop velocities in both legs (obtained from a flow resistance measured experimentally). If the actual velocity in leg No. 1 was lower than the assumed velocity, then the actual shear ratio for this leg would have been higher than the reported one by a factor of 6.8 (ratio of the velocities to the -1.75 power). Inspection of Fig. 4-4 shows no apparent difference between the two sets of data. Thus, the liftoff data do not support the contention that the loop velocities for the two legs were different.

The PAD code is being applied to observed plateout data for the Dragon and Peach Bottom reactors. This work is yielding encouraging results. Using large extrapolations of data of cesium vapor pressures on steels, a relatively crude PAD model of the Dragon reactor predicted the specific cesium activity in the primary heat exchangers to within ±50% and in the cold return leg to within a factor of about five. Cesium activity in Peach Bottom after Core 1 was predicted to within ±10% for the hot ducts and to within a factor of three for the cold return ducts.

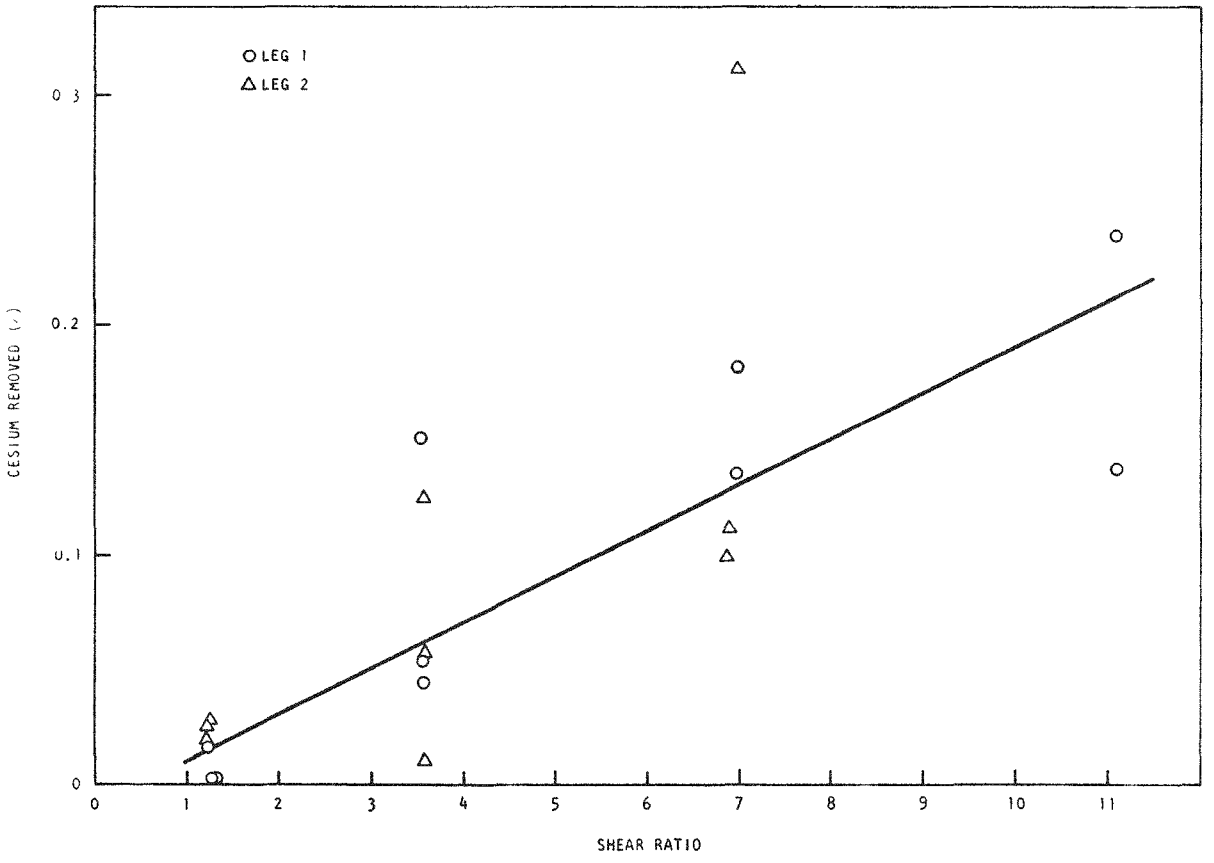

Fig. 4-4. Results of cesium liftoff tests for deposition loop experiment No. 4

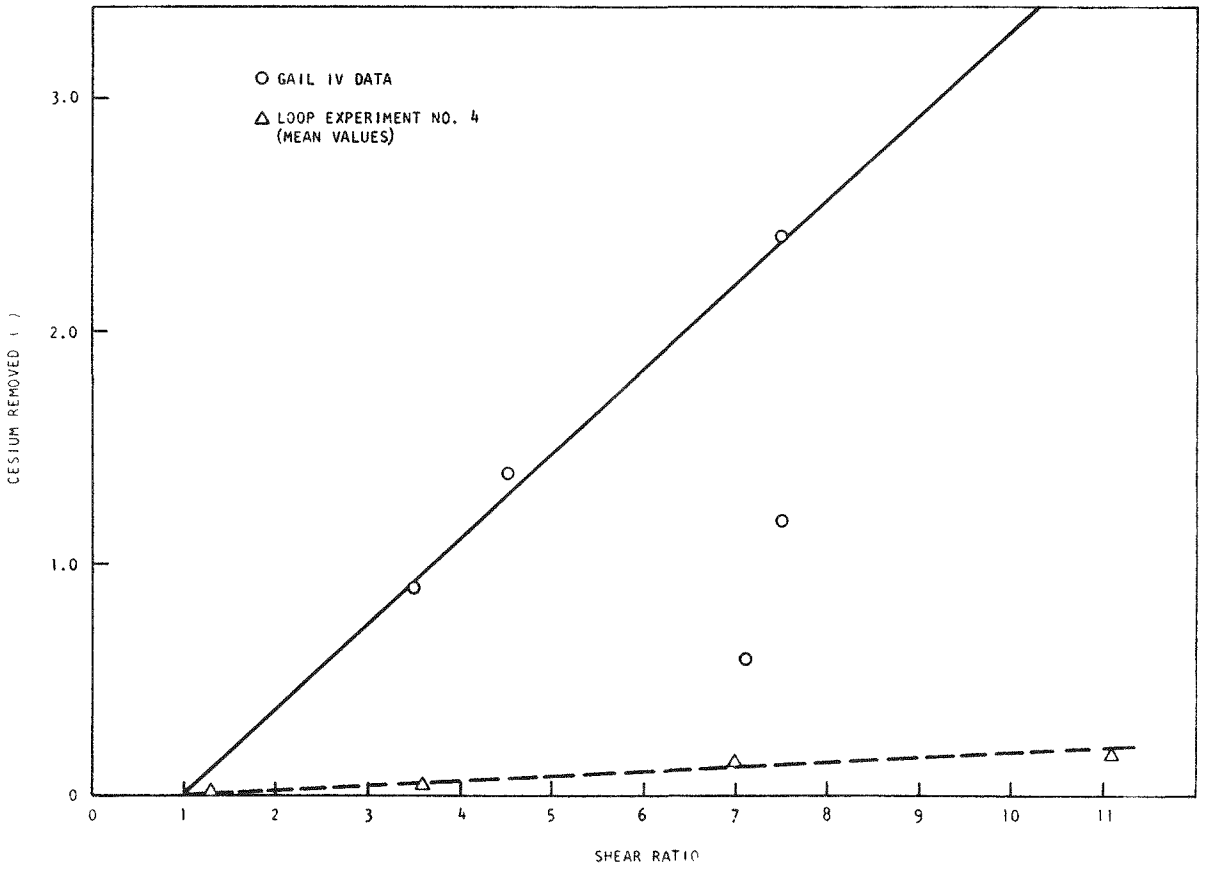

Fig. 4-5. Comparison of cesium liftoff results for GAIL IV and deposition loop experiment No. 4

FIPER CODE WORK

The FIPER code is used for calculating the release of metallic fission products into the primary coolant circuit of HTGR systems. Two forms of the FIPER code are utilized. One form is the FIPER Q code, which is the basic, rigorous version; the other form is the FIPER S code, which has a relatively short computing time obtained by incorporating various approximations into the code.

FIPER Code Development

The FIPER S computer program is a diffusion transport model embedded in a core survey code that samples a large number of fuel blocks throughout the HTGR core. At each spatial position the time history of fission product release is calculated. End-of-life releases for all the blocks are summed to obtain the total release, categorized by core reload segment and year.

Due to the large number of detailed calculations, it has been necessary to resort to some approximations in order to obtain reasonable running times. In contrast to FIPER Q, which uses a more or less exact finite difference solution to a nonlinear partial differential equation, FIPER S uses an approximate, closed-form solution to a simplified linear differential equation. The approximations that were used to make this possible in the original version of FIPER S are, briefly:

1. Diffusion in the fuel region is instantaneous.
2. Loss of mass from the fuel and graphite is neglected.
3. Thermal diffusion is neglected.
4. Radioactive decay is neglected.
5. Mixed species interaction is neglected.
6. Approximate boundary conditions.
    a. Known concentration at fuel hole.
    b. Insulated at coolant hole.

Many of the above assumptions are known to lead to significant errors under certain conditions. One might well ask why it is better to apply such an approximate model to a large number of spatial positions rather than apply a more exact model (i.e., FIPER Q) to fewer positions and then extrapolate the results to the full core. The answer is that release is highly nonlinear with temperature, and the temperatures vary in an irregular way with both spatial position and time. Under these circumstances, extrapolation of FIPER Q analyses is inexact. Critical locations cannot be found without a core survey, and, even if the critical locations were known, extrapolation to full core release could not be done without using a fine spatial grid in the analysis.

Recent concern over the adequacy of the approximations used in the original FIPER S model has led to a reevaluation of the assumptions and the model. It has been determined that a reasonably rapid exact analytical solution is still possible with an improved model that uses very few of the above restrictive assumptions. In particular, a new model has been proposed that includes:

1. Conservation of mass.
2. Thermal diffusion.
3. Radioactive decay.
4. Mixed species interaction on the coolant boundary.
5. A mass flux boundary condition at the coolant hole.

The principles of the new model are similar to those of the original model, but the equations, being considerably more complicated, require a slightly different solution technique. A brief description of the new model follows.

The region of solution is divided into two subregions, the fuel and the graphite. As shown below, the fuel region is assumed to be axisymmetric with cylindrical geometry, and the graphite region is represented by a uniform slab geometry. The birth of fission products in the fuel

particles is a known function of the integrated power. The release of these into the fuel rod matrix is assumed to be given by an empirical model that is related to particle failures and diffusion through the coating. Fission products that so escape from the particles are assumed to diffuse instantaneously through the fuel rod matrix material. The average concentration in the fuel rod is then related to the particle release and the integrated mass flux J_o out of the rod.

The assumption of instantaneous diffusion in the fuel rod region effectively removes the time variable from the differential equation in that region and permits calculation of a quasi-steady concentration shape in the fuel rod. In contrast to the original FIPER S, where this shape was flat, the new model results in an exponential shape due to the competition between the thermal gradient and the concentration driving forces. This shape, along with the average concentration found by the above mass balance, gives the fuel rod surface concentration C_s (see Fig. 4-6).

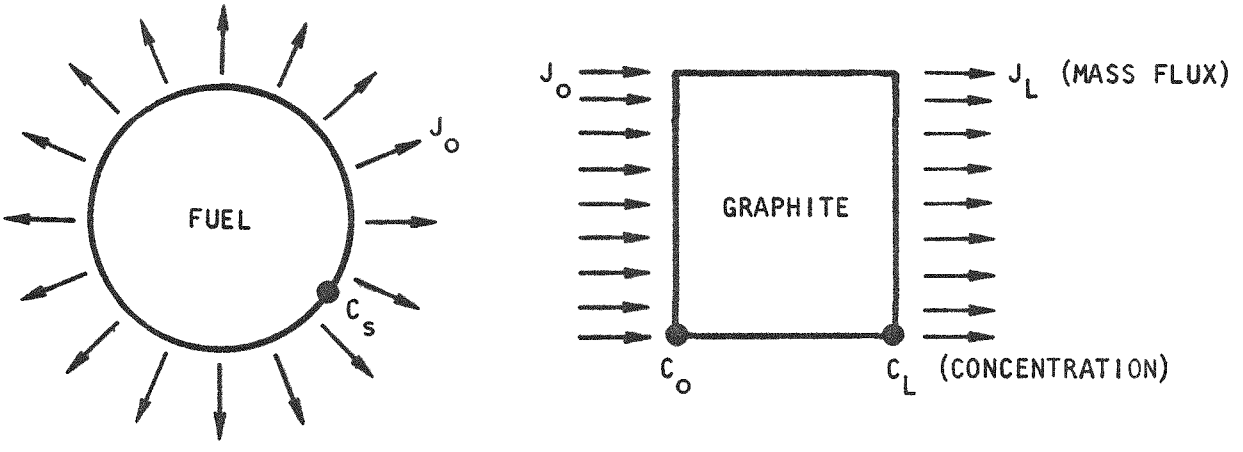

Fig. 4-6. Flux and concentration relationships

This surface concentration C_s is then related to the inner graphite concentration C_o through sorptivity and vapor pressure relations. The boundary concentration C_o obtained in this manner is then used as a known

boundary condition for the solution of the diffusion equation in the graphite region. Thus, solutions in the two regions are decoupled.

The partial differential equation for diffusion in the graphite region, including the effects of thermal diffusion and radioactive decay, has been derived and reduced to the form:

$$\frac{\partial C}{\partial \rho} = \frac{\partial^2 C}{\partial \xi^2} + \beta \frac{\partial C}{\partial \xi} - \gamma C \quad , \tag{4-1}$$

where $\rho = \frac{1}{L^2} \int_o^t D(\tau)\, d\tau$ (effective time)

$\xi = \frac{X}{L}$ (nondimensional X)

$\beta = \frac{QL}{BRT^2} \frac{\partial T}{\partial X}$ (thermal diffusion parameter)

$\gamma = \frac{\lambda L^2}{\overline{D}}$ (radioactive decay parameter)

It is noted that the last two terms of Eq. (4-1), the thermal diffusion and the radioactive decay terms, were not present in the original FIPER S model. The general solution of Eq. (4-1) is

$$C(\rho,\xi) = \exp(-\beta\xi/2) \left(A_o\, e^{\theta\xi} + B_o\, e^{-\theta\xi} \right)$$

$$+ \exp(-\beta\xi/2)\, \exp(-\theta^2\rho) \sum_{i=1}^{\infty} (A_i \cos \omega_i\, \xi + B_i \sin \omega_i\, \xi), \tag{4-2}$$

where $\theta = \sqrt{\frac{\beta^2}{4} + \gamma}$.

The boundary conditions applicable to our problem are (1) known concentration C_o on the left boundary, and (2) known mass flux J_L emerging from the right boundary. The algebra of the particular solution that incorporates these boundary conditions is lengthy and complicated. The particular solution has the general form

$$C(\rho,\xi) = C_o F_1(\rho,\xi,\beta,\gamma) + J_L F_2(\rho,\xi,\beta,\gamma) \quad . \tag{4-3}$$

It is noted that this solution is strictly applicable only to the case of constant boundary conditions. In actuality, the boundary conditions C_o and J_L both vary with time.

To solve the problem with time-varying boundary conditions, the principle of superposition known as Duhamel's theorem is employed. It it further noted that the spatial distribution of concentration $C(\xi)$ in the slab is of no concern. The objective is only to calculate the outer boundary concentration C_L and the mass flux J_L. Thus, evaluating Eq. (4-3) at $\xi = 1$ and then applying Duhamel's theorem, the solution is

$$C_L(\rho) = \int_o^\rho F_1(\rho-\lambda,\beta,\gamma)\frac{d}{d\lambda} C_o(\lambda)\, d\lambda + \int_o^\rho F_2(\rho-\lambda,\beta,\gamma)\frac{d}{d\lambda} J_L(\lambda)\, d\lambda \; . \tag{4-4}$$

The evaluation of the integrals in Eq. (4-4) involves repeated evaluations of the solution functions F_1 and F_2. Since these are complicated expressions involving infinite series [c.f. Eq. (4-2)], a great deal of computer time might be spent in finding these solutions. The approach taken in the proposed new model is to first evaluate the solution functions for a predetermined set of points, these points being the intersections in a three-dimensional grid of the three independent variables.

$$F_1(I,J,K) = F_1(\rho_i,\beta_j,\gamma_k) \quad \left\{\begin{matrix} 1\le i\le 50 \\ 1\le j\le 10 \\ 1\le k\le 10 \end{matrix}\right\} \tag{4-5}$$

Having established the tabulated matrix of solution functions at the beginning of a run (or by an external program), future evaluations of the solution can be accomplished by a triple linear interpolation. This process is much faster than performing the complete evaluation each time.

It is noted that the evaluation of Eq. (4-4) requires that we know the mass flux into the coolant, J_L, as a function of time. In fact, the entire past history of J_L is known at any time, but the next projected future value, which is required in the incremental evaluation of Eq. (4-4), is not known. However, the mass flux J_L can be calculated once C_L is known. The technique used to solve this problem is to make a trial guess at a projected J_L, calculate C_L, and then iterate until the projected J_L and the calculated C_L are consistent.

The differential equation solution and the triple linear interpolation scheme have been programmed. Problems encountered in the solution were (1) poor convergence of the series expansions for small values of ρ, (2) the calculation of limiting solutions for certain critical combinations of ρ and γ where the normal expressions became singular, and (3) the unexpected appearance of an imaginary eigenvalue ω that occurred only for $\beta < -2$. These problems have all been reconciled, and the subroutines for solving the differential equation are now complete.

FIPER Code Applications

One source option used in the FIPER code for calculating the release of fission product metals from coated particles is based on a release constant model, in which the release rate of a fission product metal is taken to be proportional to RN, where R is the release constant based on

observed release data and N is the concentration of metal in the fuel particle. Another option is to assign fractional release values, which change with burnup. These source options are overly simple and conservative and need to be replaced by more accurate source calculations. Accordingly, work is in progress to evaluate diffusion coefficients and other parameters for use in calculating the release of fission product metals from coated particles.

FIPER Q code analyses of cesium release data obtained from annealing experiments of BISO coated fuel particles have been carried out. The code determinations of diffusion coefficient values for cesium in pyrolytic carbon and kernel material are found to be very close to hand-calculated values, showing that the FIPER code is not required to analyze the data. Simple hand calculations suffice.

The apparent diffusion coefficient value for cesium in UO_2 kernel material (irradiated to 3% FIMA burnup in the P13M capsule) is found to be around 2×10^{-13} cm^2/sec at 1650°C. This is slightly higher than the diffusion coefficient value (6×10^{-14} cm^2/sec) for the self-diffusion of the uranium ion in UO_2 crystals at the same temperature but lower than the value for krypton diffusion in UO_2.

The cesium release data generally show an initial, rapid release of 0.1 to 0.3 fraction of the cesium. This is a higher release than can be attributed to recoil. This behavior needs an explanation.

TRITIUM STUDIES

A joint effort by Los Alamos Scientific Laboratory (LASL) and Gulf General Atomic (GGA) to determine the retention of tritium in irradiated HTGR core materials has been initiated. In this effort, samples are selected and characterized by GGA and the tritium analyses are performed by LASL.

The principal sources of tritium in HTGR systems are ternary fission and neutron activation of (1) He-3 present in the helium coolant, (2) Li-6 and Li-7 present as impurities in the core and reflector materials, and (3) B-10 in the control rods and reflector materials. The main concern with tritium is its possible release to the environment via diffusion through the steam generator tube walls into the secondary coolant.

Six H-327 graphite samples and five coated particle samples (of four irradiated particles each) have been sent to LASL. The graphite samples consisted of one sample of unirradiated graphite (for a lithium determination) and five samples of irradiated graphite.

The particle samples consisted of three samples of TRISO coated particles and two samples of BISO coated particles. Irradiation temperatures for the particles ranged from 715° to 1575°C and burnups from 6 to 75% FIMA. Each sample was gamma counted, and the counting data were used to calculate the tritium content of the particles assuming 100% retention. All the particles were radiographed to determine coating integrity and to ensure that all the particles sent had intact coatings.

REACTION OF STEAM WITH GRAPHITE

Studies are in progress to determine the quantitative effect of helium pressure on the rate of reaction of H-327 graphite with steam over the range of 800° to 1000°C using pressures of 15 to 750 psia. The purpose of this study is to gather data on the steam-graphite reaction rate as a function of helium pressure for comparison with theoretical predictions utilized in computer calculations of steam in-leakage situations. A description of the apparatus is given in Quarterly Progress Report Gulf-GA-A12515.

Preliminary results (given in Gulf-GA-A12515) have indicated that the reaction rate as a function of helium pressure is in reasonable agreement with the predicted inverse square root of pressure dependence. Additional

studies have generally verified the earlier results, but have also pointed out the unexpected importance of carbon transport, as evidenced by carbon deposits on the wall of the metal reaction vessel. Carbon transport, which occurs by the reaction

$$C + H_2O = CO + H_2 \quad ,$$

is known to be catalyzed by reduced metal surfaces maintained at elevated temperatures.

Results obtained when carbon transport was occurring yielded contradictory results:

1. Unexpectedly low reaction rate values when gas chromatography was used to monitor the reaction rate, due to removal of reaction products within the reaction vessel (reverse of the above reaction).

2. Unexpectedly high values when weight loss measurements were used to monitor the reaction, due to regeneration of steam within the reaction vessel, causing an increase in the steady-state steam concentration.

In an effort to eliminate the carbon transport problem, extend the range of pressures studied, and improve the reproducibility of earlier preliminary data, several improvements were incorporated into the apparatus.

To eliminate the carbon transport problem, a quartz liner was placed inside the inner chamber tube of the reaction vessel. This step eliminated contact between the metal tube and carbon monoxide in the hot zone of the furnace. Recent qualitative results indicate that carbon transport has been eliminated via the addition of the liner.

A new water saturator capable of safely maintaining 750 psi was installed. The previous saturator was limited to 400 psi. An initial problem of water surge when using the new saturator, with resultant

rapid and undesired oxidation of the graphite sample, has been eliminated via the addition of a surge trap downstream of the saturator.

The helium flow rate was increased in direct proportion to an increase in the helium pressure within the vessel. This step was taken to assure adequate steam concentration in the helium as it passed the graphite sample. It is conceivable that at the higher temperatures and pressures studied, steam depletion of the helium gas could occur while in the vicinity of the sample if flow rates were not increased accordingly.

TASK V

RECYCLE FUEL STUDIES

HTGR FUEL RECYCLE PLANT STUDY

Recycle Plant Shielding

A study was carried out to evaluate shielding requirements for the recycle plant. Shielding for the refabrication plant will be controlled primarily by thallium-208, a daughter product of U-232; the latter is formed, in the reactor, by both natural Th-232 and Th-230. Typically, bred U-233 from thorium containing 0, 10, or 100 ppm Th-230 will contain approximately 370, 470, and 1400 ppm U-232, respectively. This study was part of an overall effort to determine the effect of anticipated possible variations in Th-230 in thorium; an evaluation was made between 10 ppm (since all thorium contains some Th-230) and 100 ppm Th-230 (a level which should include a large fraction of the available thorium sources).

Source strengths are given below for the refabrication and reprocessing plant sources:

Source Strengths for Refabrication Plant Analyses (600 ppm U-232)

Case	U-232 (mg/cm^3)	Source Strength (MeV/cm^3-sec)
RFP-I*	0.138	1.07×10^7 (1)**
RFP-II	0.215	1.67×10^7 (2)
RFP-III	0.674	5.22×10^7 (2)
RFP-IV	0.0686	5.32×10^6 (2)
RFP-IV	0.0455	3.53×10^6 (1)

*Refabrication plant Case I.

**Number in parentheses is the number of such sources present.

Source Strengths for Reprocessing Plant Analysis

Energy Range (MeV)	W/cm^3	MeV/cm^3-sec*	Assumed E (MeV)
0.0-0.45	1.4×10^8	1.77×10^9	0.30
0.45-0.9	1.4×10^9	1.77×10^{10}	0.675
0.9-1.425	9.5×10^6	1.20×10^8	1.16
1.425-1.8	3.0×10^6	3.78×10^7	1.61
1.8-2.2	1.9×10^7	2.42×10^8	2.0
2.2-2.65	2.2×10^5	2.77×10^6	2.43
>2.65	5.2×10^3	6.57×10^4	2.7

*Power density of 0.8 of the beginning-of-life power density (8.55 W/cm^3) is assumed. Also each fuel block contains 89,000 cm^3 and the solution volume is 2.41×10^6 cm^3.

A hand estimate of the maximum dose at the inside surface of the shield (assuming no self-shielding) showed all four of the refabrication plant sources to be of nearly equal strength. Therefore, each of these cases was mocked up and inputted to the PATH computer code. The reprocessing plant was also treated with this code. Results are summarized for the shielding required to give a maximum dose rate of 0.25 mrad/hr on the far side of the shield. The specified criterion was a dose rate of 0.5 mrad/hr with a 100% safety factor.

Concrete shielding requirements (inches) for a 0.25 mrad/hr dose at the far side of the shield are as follows:

Case	600 ppm U-232	1900 ppm U-232
RFP-I*	41	46
RFP-II	41	46
RFP-III	40	44
RFP-IV	39	44
RPP**	58	58

*Refabrication plant Case I.
**Reprocessing plant.

In the case of the reprocessing plant, the dose contribution from U-232 contamination can be estimated from the 2.7-MeV source contribution by multiplying that contribution by the ratio of the U-232 source strength to the 2.7-MeV source strength. For the 1900 ppm U-232 case, the contribution was slightly greater than 1% of the total dose rate at 48 in. of concrete. The percentage increases with concrete thickness.

Finally, the self-shielding of the source was estimated from hand estimates of the dose rate with no self-shielding and the PATH results with self-shielding.

A cursory investigation of the shielding required for fabricating recycled U-235 was made. Employing conservative approaches of (1) 1000 ppm U-233 contamination in the reprocessed U-235 (with its associated U-232), (2) aging time of 100 days, (3) material quantities compatible with a commercial-size plant (approximately 30 kg U/day), and (4) exposure levels to production personnel of less than 1 mrad/hr, the results indicated that shielded facilities (approximately 1 ft of concrete) would be needed even if the feed thorium contained only 10 ppm Th-230.

Reprocessing Product Impurities

Six documents on thoria surface chemistry work, carried out by the University of Utah during the 10-year period 2/58 to 1/68, were reviewed to determine if any investigations were made for the effect of impurities on the sol-gel process. Only a minimal amount of information could be found. The effect of four impurities (phosphate, sulfate, iron, and fluoride) was evaluated at concentrations greater than 3000 ppm. The results suggested that each of the impurities reduced the ease with which steam-denitrated thoria could be formed into a sol, with increased impurity levels exaggerating the effect. Sintering tests carried out on gels which contained the phosphate and sulfate impurities, at temperatures less than those required for full densification, implied further ill effects from these additions.

Carbon-14

Conclusions from the work done to date pertaining to the nitrogen content of fuel element components can be summarized as follows:

1. Using the reference fuel element description and N_2 determinations obtained on reject Fort St. Vrain carbide particles, an average nitrogen content of 76 ppm is obtained instead of the 100 ppm assumed in Design Criteria DC-18-9. The approximate carbon-14 production would be 0.177 g/fuel element rather than 0.245.

2. Using the reference fuel element description and the N_2 determination results obtained by analysis of sol-gel oxide fertile particles, the average fuel element has a nitrogen content of ∿40 ppm and a carbon-14 production of 0.11 g/fuel element.

3. If the nitrogen content of the fuel element is reduced to zero, the carbon-14 production due to the natural abundance of carbon-13 is 0.012 g/fuel element.

Review of ICPP System Design Descriptions

Preliminary drafts of five System Design Descriptions were prepared by ICPP personnel for the HTGR Fuel Reprocessing Demonstration to be carried out at Idaho under the National HTGR Fuel Recycle Development Program. The System Design Descriptions pertained to "Production Denitration, Packaging, Storing and Shipping, and the Head End." The documents were reviewed and comments were forwarded to ICPP for inclusion in revision of the documents. A study was performed to investigate the possibility of fabricating the kernels at ICPP to avoid double processing. To avoid problems of shipping liquid $^{233}UO_2(NO_3)_2$ to ORNL, ICPP tentatively

plans to denitrate the nitrate solutions, by a fluid-bed approach, and ship UO_3 particles to ORNL. An alternate technique of preparing HTGR fuel kernels for shipment to ORNL was evaluated to avoid the extra operation of UO_3 preparation (at ICPP) and redissolution at ORNL. It was concluded that if new remotely operated shielded facilities must be constructed for UO_3 particle preparation at ICPP, the alternate approach of fabrication of mixed oxide kernels at ICPP (in lieu of the UO_3 particles) would be more favorable. This conclusion does not take into consideration the practical aspects of personnel and technology know-how which are available at ORNL and not at ICPP.

HEAD-END REPROCESSING

Summary

Crushing data on full-size fuel elements indicate greater size reductions result from feeding fuel elements to the primary crusher in a vertical orientation as opposed to a horizontal manner.

A vacuum pneumatic transport system has been purchased for testing in the cold pilot plant.

A new feeder (pneumatic) for the 20-cm-diameter primary burner has been constructed. This design has many advantages over the previous system and is expected to minimize particle breakage in the feed system.

An air classification system and two double-roll particle crushers have been ordered.

A new hopper/auger feed system for the fluidized-bed burners is being bench tested.

Test runs on the 10-cm-diameter primary burner indicate that, as expected, the cooling gas heat transfer coefficient is controlling the heat transfer rate from the burner. Equipment changes have been made to this burner to reduce elutriated fines from settling out in overhead lines and to provide for more accurate sampling of elutriated fines.

Burner product is now continuously removed from the 10-cm-diameter primary burner with the aid of a rotary valve instead of an auger. This device should allow increased metering accuracy and reduce the amount of particle breakage. Also, the auger feed system has been modified on this burner to minimize particle breakage and to reduce operating problems.

Modifications to the 20-cm-diameter burner are under way.

A newly designed bed removal system has been successfully tested on the 10-cm-diameter secondary burner.

Size distributions for solids that will be encountered in the leaching operations were established using two different techniques.

Gas holdup (expanded bed volume) data were established for the air-sparged leacher.

Required air-sparge rates for the leachers were investigated, and correlations for two-phase spouted beds were utilized to establish upper limits on required sparge rates. Experimental data indicate that sparge air is not required to obtain efficient dissolution of secondary burner ash resulting from processing crushed ThC_2 particles.

Crushing

Primary and Secondary Crushers

Several full-size standard (Fort St. Vrain type) fuel elements have been sequentially reduced in the primary and secondary jaw crushers. The resulting crushed product (H-327 graphite) was analyzed in terms of size and shape in order to determine (1) the optimum machine settlings and (2) the differences between horizontal and vertical positioning of the fuel element in the primary crusher.

The term "size" means the diametral dimension through which the crushed particle will just fit, i.e., ring size, b, of Fig. 5-1.

The term "shape" was defined by the shape factor, S, represented in Fig. 5-1.

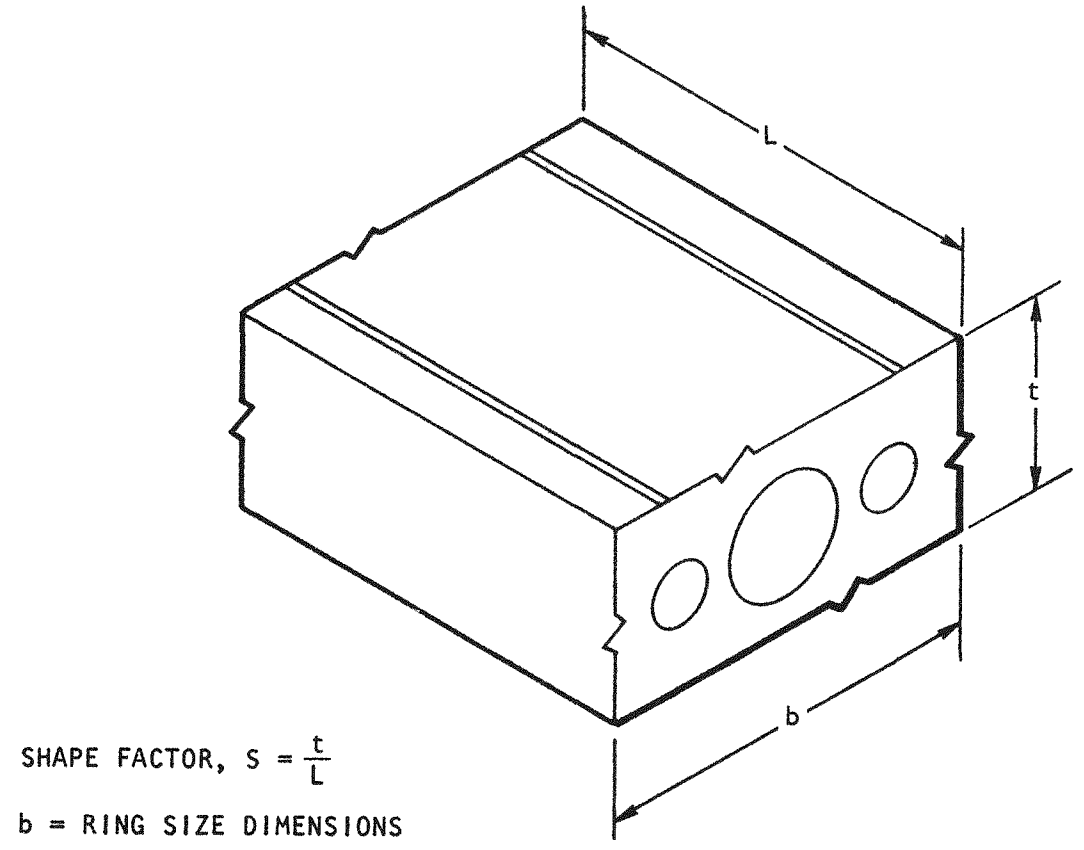

Fig. 5-1. Definition of shape factor

The distinguishing differences between horizontal and vertical (major axis of fuel element normal to the ground) orientations are related by Table 5-1. These data are typical of several full-size fuel elements which were crushed in both the horizontal and vertical positions.

Vertical crushing was performed in two modes. First the fuel element was placed vertically in an unobstructed feed opening (18-in. gap x 32-in. width). Although this fuel element was not restrained to this orientation by mechanisms other than the sides of the crushing cavity, it did remain - for the most part - in this position. This mode is henceforth referred to as vertical (not captured).

Second, the feed opening of the primary crusher was fitted with two guides that reduced the width of the crushing cavity to 18 in. The effect of the guides was to restrict the fuel element to a vertical position throughout the crushing action. This mode is henceforth referred to as vertical (captured).

TABLE 5-1
SIZE-SHAPE DATA FROM PRIMARY CRUSHER PRODUCT[a]

Orientation	Calculated Parameters		
	$D_{50\%}$[b] (in.)	$S_{50\%}$[c]	R[d]
Horizontal	6.5	0.20	0.34
Vertical			
Captured	5.3	0.29	0.48
Not captured	5.2	0.33	0.36

[a] Closed side setting (CSS) = 4 in.

[b] $D_{50\%}$ = geometric mean size.

[c] $S_{50\%}$ = geometric mean shape.

[d] $R = \frac{\text{Weight of crushed product passing 1-in. screen}}{\text{Total weight of fuel element}}$.

Table 5-1 shows that the vertical (not captured) crushing position yielded a higher reduction ratio as reflected by the change in the geometric mean size ($D_{50\%}$) from 6.5 in. (horizontal) to 5.2 in. (vertical). A vertical (not captured) crushing position also provides a more cubical product, which is indicated by a change in the geometric mean shape ($S_{50\%}$) from 0.20 to 0.33. Figures 5-2 and 5-3 relate the respective cumulative size distributions from which $D_{50\%}$ and $S_{50\%}$ were obtained.

The differences in the crushed primary product from the vertical (captured) and the vertical (not captured) tests show a comparative advantage to be realized from the vertical (captured) arrangement. The advantage is threefold: (1) the value of R (Table 5-1) is the highest of all three physical arrangements, (2) the vertical (captured) arrangement admits to a physically narrower machine than would otherwise be required, and (3) a vertical fuel element orientation is well suited to existing fuel element handling equipment.

The sequential size-reduction characteristics of the primary and secondary crushers are shown in Figs. 5-4 and 5-5. These figures describe typical size and shape distributions of full-size Fort St. Vrain fuel elements after each stage of crushing [vertical (captured)] for two different discharge settlings [i.e., closed side setting (CSS) = 3 and 4] of the primary crusher and a single CSS value (0.125 in) for the secondary crusher.

Tertiary Crusher

A tertiary roll crusher has been ordered and continued testing with the same product described by Figs. 5-4 and 5-5 is planned.

Pending the outcome of (1) graphite crushing tests and (2) particle breakage tests in the tertiary crusher, a decision will be reached on the advisability of constructing the cascade-stack structure (see earlier Quarterly Progress Report Gulf-GA-A12150, Fig. 5.4, page 25).

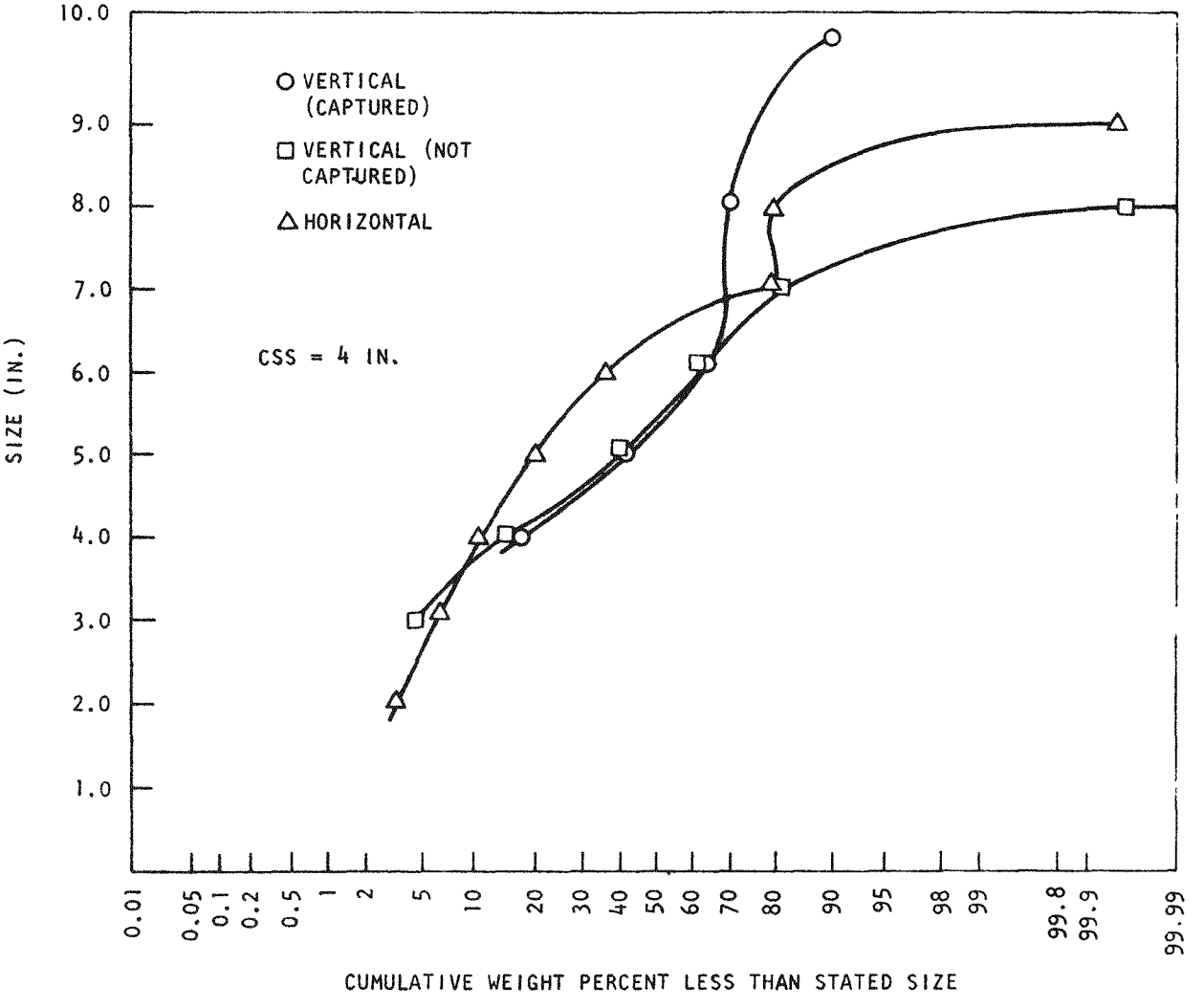

Fig. 5-2. Cumulative weight percent versus size

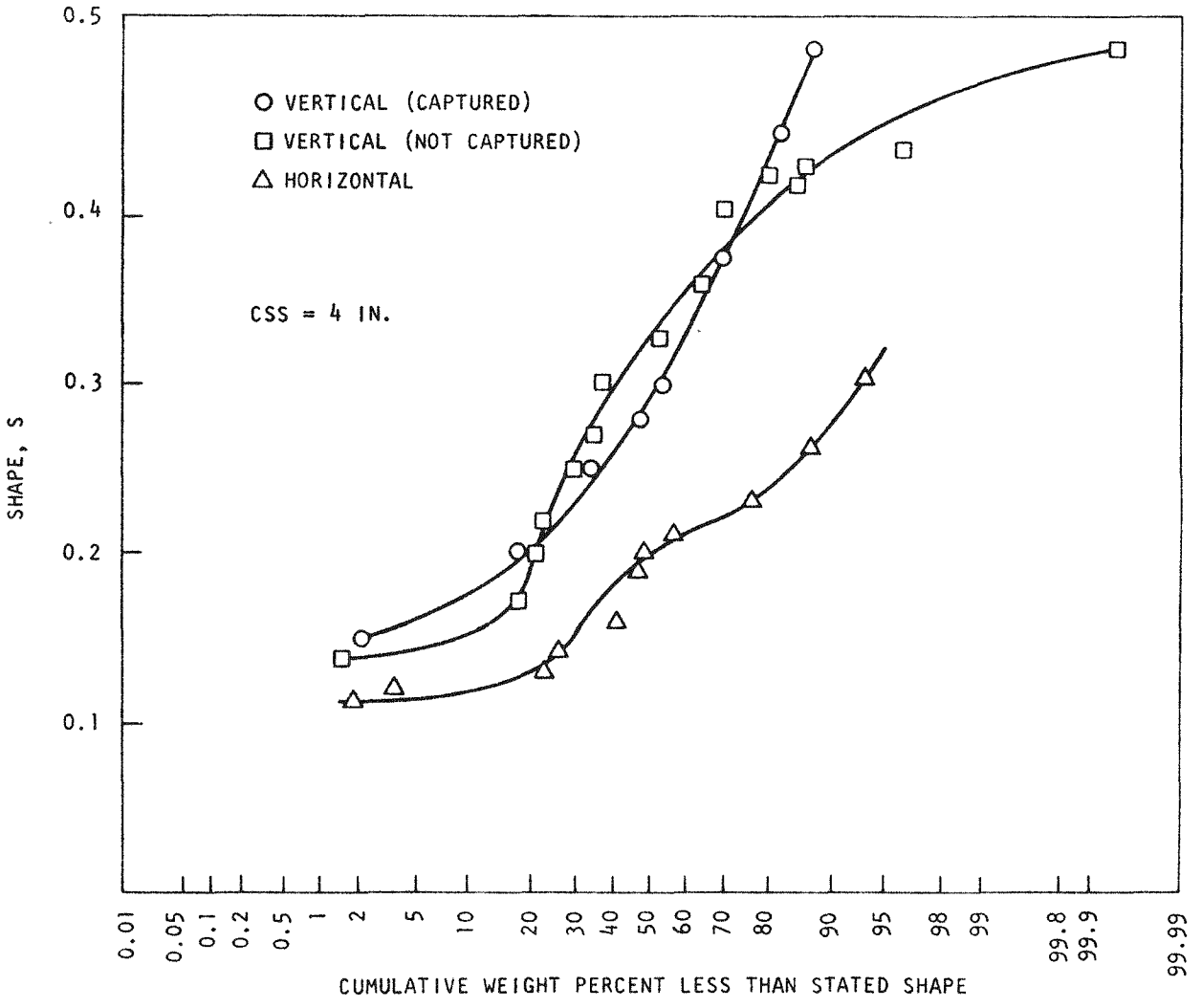

Fig. 5-3. Cumulative weight percent versus shape

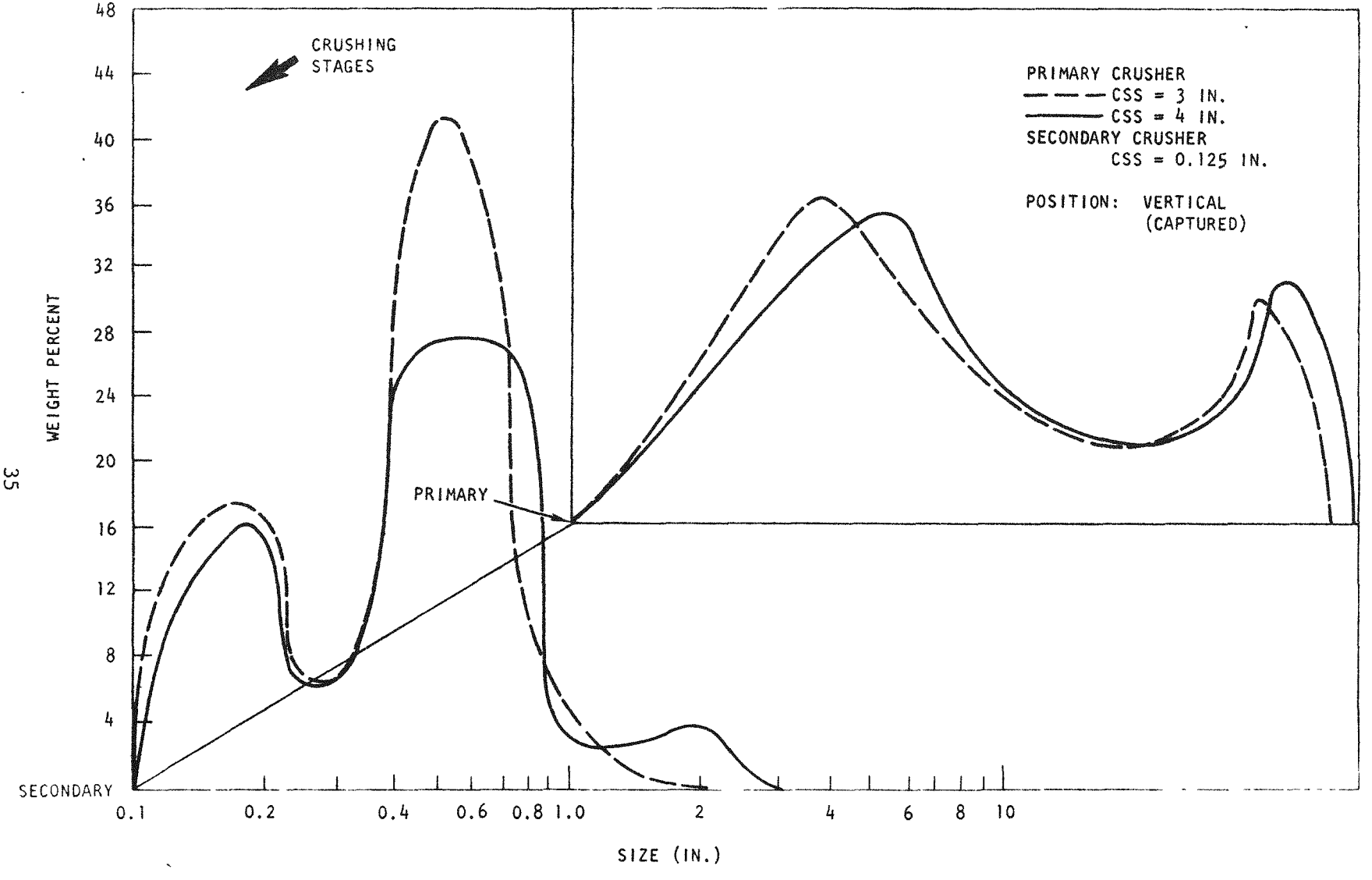

Fig. 5-4. Size distribution for successive crushing stages

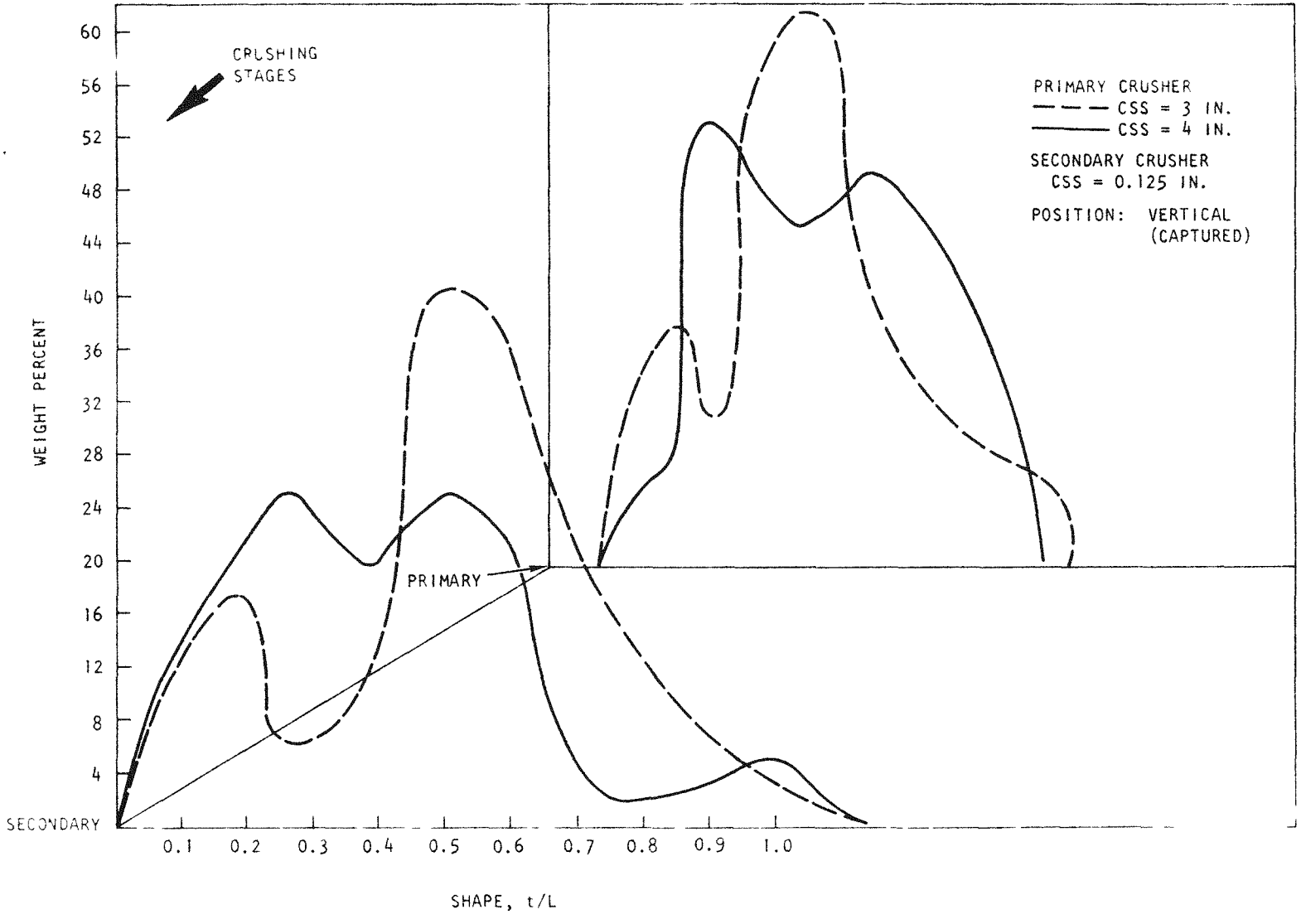

Fig. 5-5. Shape distribution for successive crushing stages

Solids Handling

Pneumatic Transport Systems

Quotations from three equipment manufacturers were received for a pneumatic conveyance system composed of three subsystems for handling the following streams:

1. Crusher product to the primary burners.
2. Primary burner product to the air classifier.
3. Secondary burner product to the leachers.

A vacuum transport system was selected for testing in the Cold Pilot Plant Development Program. This system will operate on a vacuum principle utilizing a positive displacement blower for each subsystem. Also, the system includes stainless steel pneumatic conveyance lines, bag (cloth) filters, product hoppers, and secondary filters (cloth).

Following equipment installation, extensive tests will be performed aimed at gathering design data.

Pneumatic Feeder for Primary Burner

A pneumatic feeder has been built which is adaptable to the present primary (20-cm-diameter) burner. The feeder assembly incorporates (1) a funnel-flow type hopper, (2) a drop-through rotary feeder, and (3) a blow-through feeder.

The system will operate in a continous mode over a range of solids flow rates and will provide the following advantages over the previous system:

1. Minimize particle breakage.

2. Stabilize flow rates.

3. Eliminate problems associated with mechanical constraints on the fluid bed due to thermal expansions.

4. Allow for several "fines recycle" options.

5. Provide capability of operating as a hybrid pneumatic system, i.e., vacuum delivery to the feeder hopper from the crushers and positive pressure discharge from the feeder to the burner.

Conceptual Description. In batch-wise fashion, the feed hopper illustrated in Fig. 5-6 will receive crushed graphite and particles from an existing feed hopper. The intermittent batching sequence will be controlled by level indicators in the hoppers such that the system can operate continuously; i.e., the feed hopper is never to be completely empty. By maintaining a set level, the hopper can be filled by a vacuum-pneumatic transport system while feeding the pressure-pneumatic feeder system below.

Feed material leaves the hopper under gravity flow conditions and is received by a drop-through rotary feeder (see Fig. 5-6). The clearance between the rotors and housing will be sufficient to eliminate the possibility of jamming particles and/or graphite within this space.

The drop-through rotary feeder will provide a constant discharge rate relative to that which the offset feed hopper would otherwise provide the blow-through feeder (see Fig. 5-6). It is intended that the two feeders be volumetrically coupled so as to provide a two-capacity constant period process. Matching the respective "pocket volumes" of the drop-through and blow-through rotary feeders, where the latter is greater than the former, will permit greater clearance tolerances, significantly reducing particle breakage and the possibility of jamming, and will provide a constant feed rate to the pneumatic system.

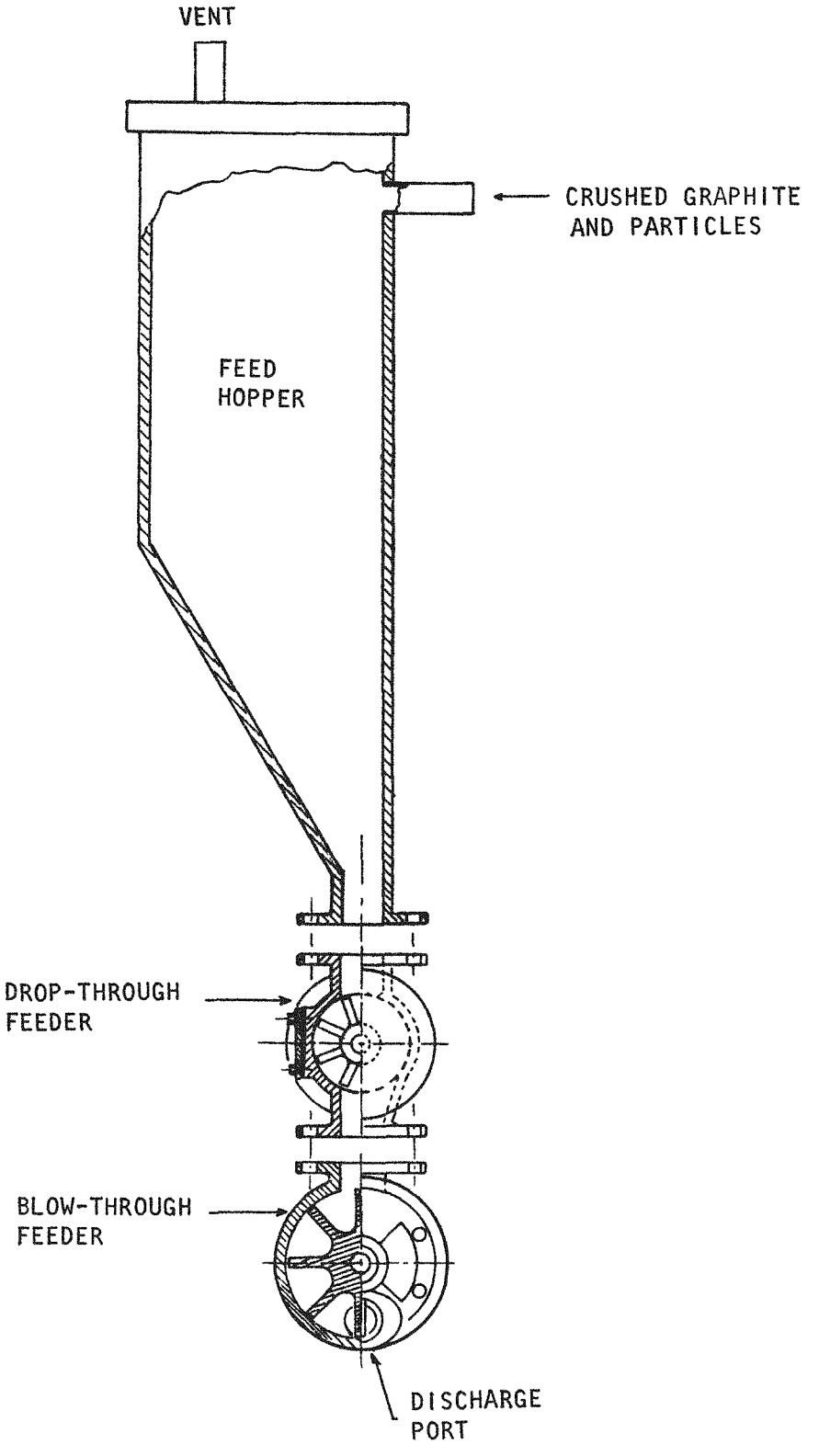

Fig. 5-6. Fluid bed pneumatic feeder assembly

The feed material upon discharging from the blow-through feeder enters an "acceleration pipe," i.e., a length of pipe used to accelerate the particles to the velocity required for stable flow. The acceleration pipe discharges into a "transition pipe," which is shown in Fig. 5-7. The transition pipe is to be oriented in the near horizontal position (dotted lines) when the fluid-bed burner is in its cold position. Upon attaining equilibrium, the burner will have expanded through a distance D_t. The dimension R will be dictated by calculation methods related to pneumatic transport.

The relative rotational motion of each end of the transition pipe will be taken up by the rotary seal illustrated in Fig. 5-8. The transition pipe will be fitted with two such rotary seals, one connecting to the acceleration pipe and the other to a length of pipe called a "fluid-bed connector." The rotary seal will consist of a sealed ball bearing and bearing housing flange connector. The respective acceleration pipe and fluid-bed connector are to be pressed into and/or welded to the far side of the inner raceway. The bearing will be pressed into a bearing housing, which will also serve as a transition pipe flange connector. The fluid-bed connector will be fitted with a thermal barrier(s) to reduce axial thermal expansion and thereby permit the transition pipe to rotate freely.

Performance characteristics of the pneumatic feeder will be reported in a future Quarterly Progress Report.

Air Classification and Particle Crushing

An air classification system and two particle crushers have been ordered. It is intended that (1) the primary burner product be classified into a fissile and fertile particle stream, where the residual graphite is expected to follow the fissile particles, and (2) the fertile stream be subsequently split into large and small fractions for parallel crushing. Although not a direct goal, a separation between fissile particles and residual graphite will be effected (see Fig. 5-9).

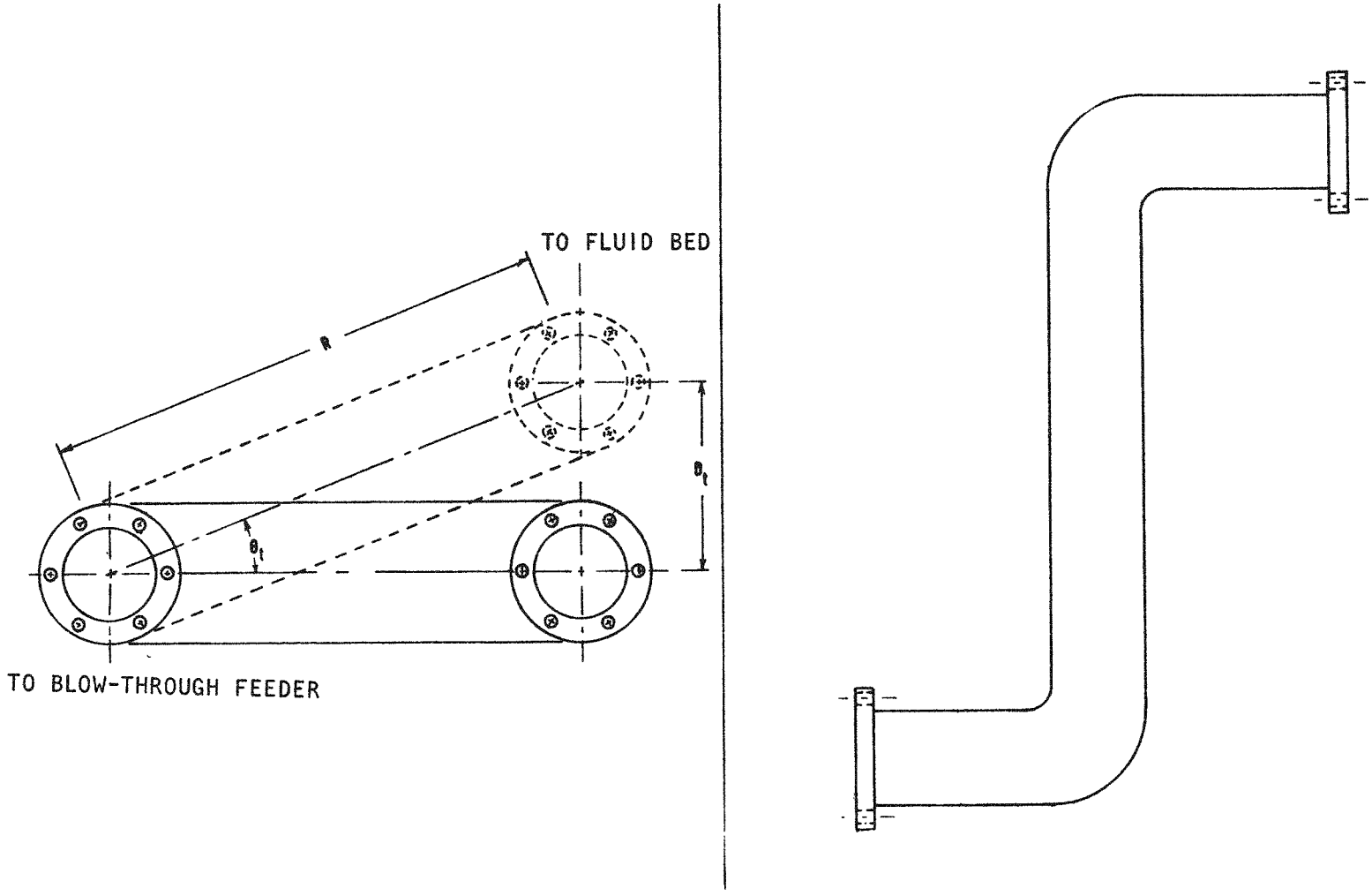

Fig. 5-7. Transition pipe

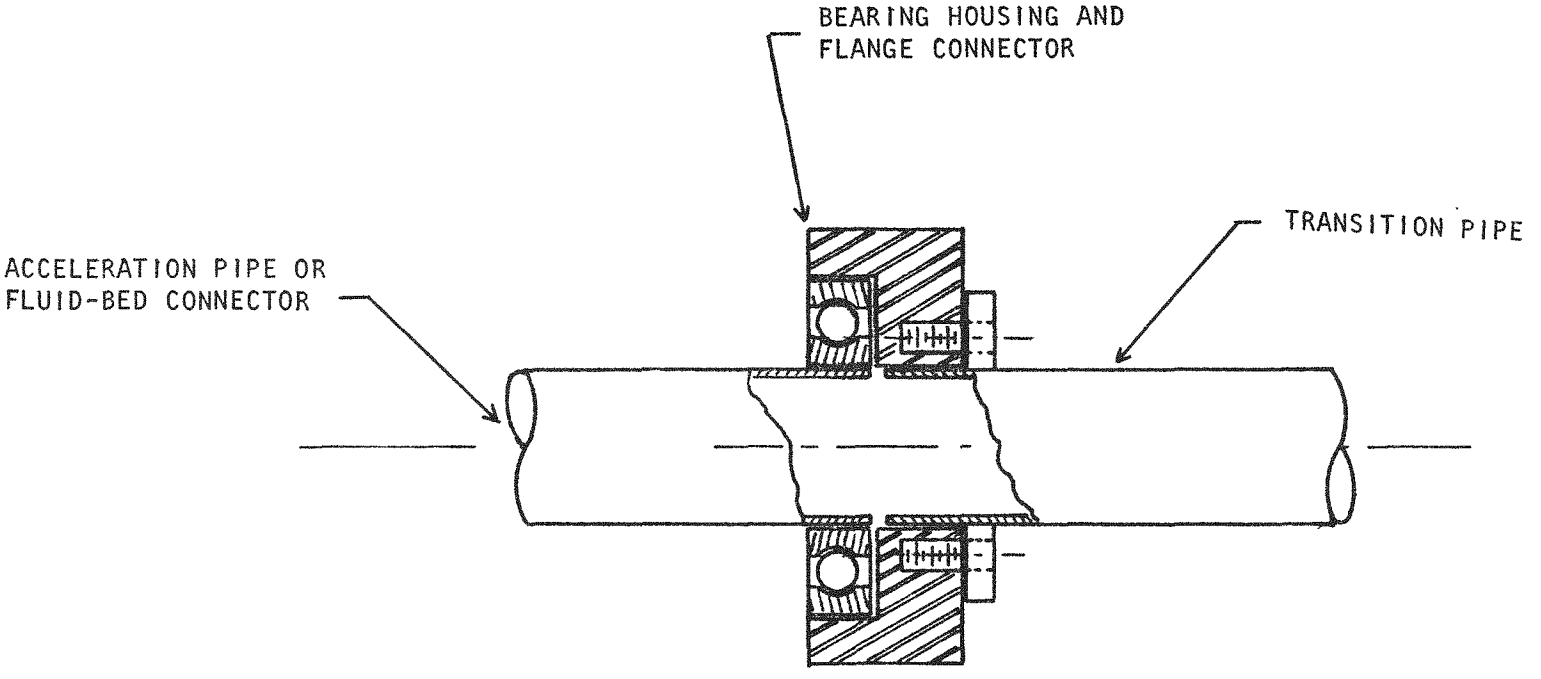

Fig. 5-8. Rotary seal (typical of both ends of transition pipe)

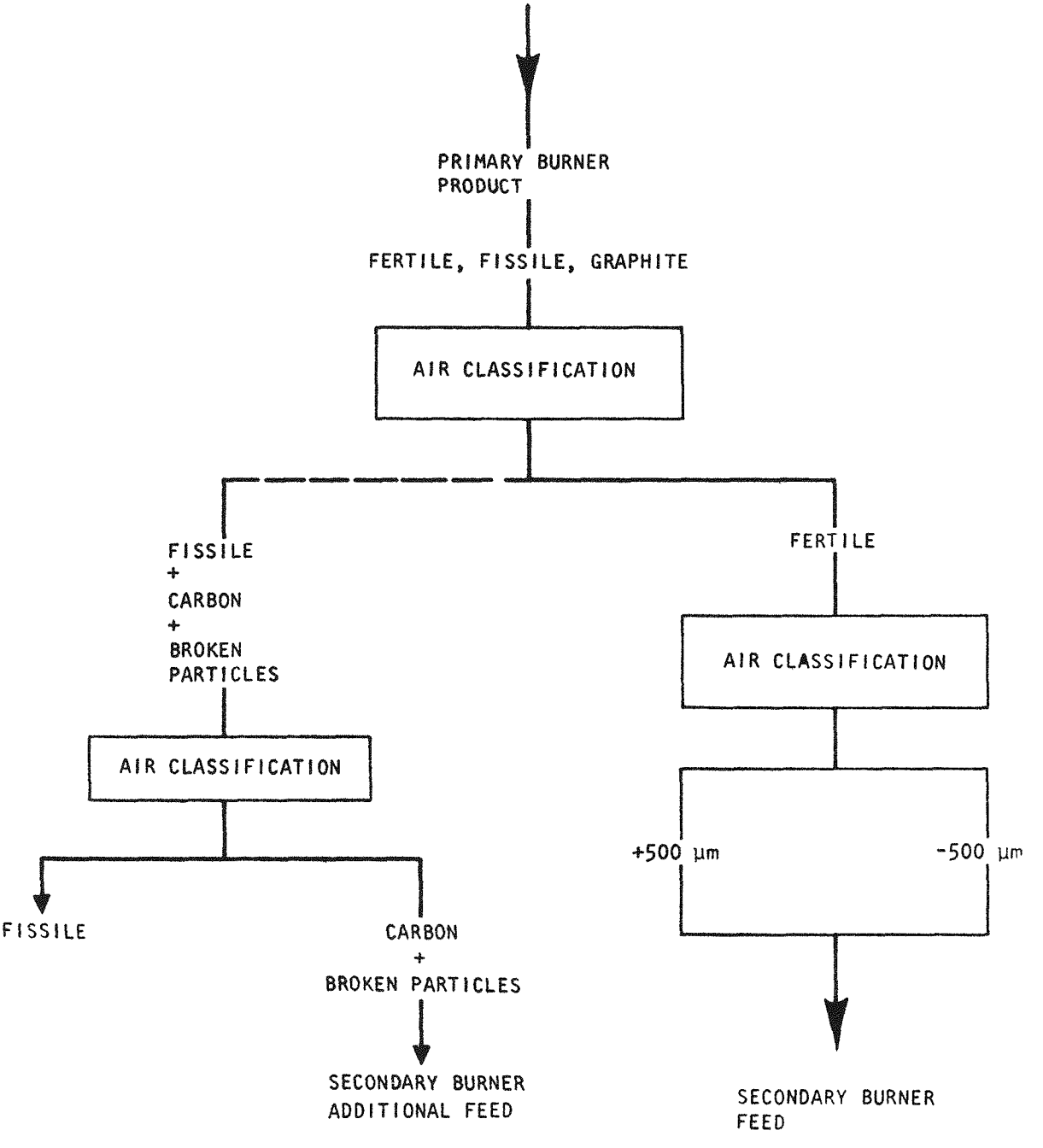

Fig. 5-9. Particle classification and crushing

Data to be gathered on these separations are:

1. Effeciency versus gas flow rate.
2. Reproducibility of results.
3. Recycle effectiveness.
4. Maximum solids feed rate.

The classifier will be operated using pneumatically transported feed and product removal in order to determine ease of interface with that mode of transport.

Present particle crushing work indicates that double-roll crushers generate a crushed product with good fluidization characteristics (i.e., not pulverized) but less than 100% particle breakage.

In order to increase the present "once-through" efficiency, two multiple crushing schemes have been proposed. The first involves splitting the fertile particle stream into large and small fractions, each stream being processed by a roll crusher of suitable gap. This would yield a more efficient "once-through" crushing scheme without pulverizing.

The second scheme is to pass all the material through two crushers arranged in series, the first having a larger gap than the second. The intent of this scheme is to eliminate the need for air classification beyond the fissile-fertile separation, but it has the definite disadvantage of overcrushing the large fertile particles - a point which needs to be established.

Efficiencies versus size range crushed will be determined for both concepts.

Hopper/Auger Feed System for Fluidized-Bed Burners

A new auger system has been constructed which differs conceptually from the previous system. This system is being bench tested and has a

potential use on both the primary and secondary burners. The new hopper/auger arrangement utilizes a transition pipe and rotating seals (much like that described for the pneumatic feeder), with the exception that the transition pipe has more generous radii. The rotating seals (see Fig. 5-8) are each fitted with straight lengths of pipe which are connected to the hopper and fluid bed, respectively. The pipe assembly has been fitted with a flexible auger which is, in fact, a spring form driven at the hopper end.

The intent of the design is to eliminate the thermal expansion problems attending the coupling of a rigid auger to a primary fluid-bed burner.

Primary Fluidized-Bed Burner Development

Work is under way on the burners to develop more reliable equipment, thus enabling the demonstration of longer term operability. This work has required modification of some burner equipment components, which has reduced the accumulation of data. Equipment development is being given increased emphasis; the burners are being modified to more closely resemble the type of equipment which would be used in a commercial plant. This program is being done in close cooperation with ICPP personnel to ensure that the GGA development program is responsive to the ICPP hot demonstration program.

10-cm-Diameter Burner Development

Two runs (F4B-M21 and F4B-M22) were made to further investigate the use of "mixed" recycle fines and fresh feed. Using mixed fresh feed and recycle fines for burner feed minimizes cyclical variations in off-gas concentrations and bed temperatures; stable operating conditions appear to offer better process control. Table 5-2 summarizes these two runs. The feed and fines were mixed by maintaining a continuous flow of fresh feed (-4760. μm ring size graphite mixed with fertile particles in a ratio

TABLE 5-2
PRIMARY BURNER OPERATING CONDITIONS

	Run F4B-M18	Run F4B-M19	Run F4B-M20	Run F4B-M21	Run F4B-M22
Burn rate,[a] g/cm^2-min	0.39	0.47	0.64	0.30	0.49
Superficial velocity, cm/sec	64	78	85	64	80
Bed size per unit area, g/cm^2	52	53	59	67	74
Bed temperature, °C	1015	995	975	1020	1010
Oxygen concentration, % in	87	88	91	88	90
Fines elutriation rate, g/g burned	1.04	2.15	2.13	3.42	1.27
Off-gas concentrations, %					
O_2	0	0	0	0.7	12.0
CO	4.5	8.0	8.2	1.2	5.0
CO_2	83	80	82	83	72
Final bed properties					
d_{sv}, µm	600	580	655	606	--
Carbon, %	6.3	10.9	23.2	0.5	3.9
Broken particles,[b] %	3.2	0.8	1.5	1.0	5.3

[a] The proposed target for commercial operation is 0.6 g/cm^2-min.

[b] Percent of nonburnable material less than 420 µm.

of 4:1) into the recycle bottom hopper together with the fines, which are continuously fed to the hopper by a cyclone separator and off-gas filter chamber. As was observed during two previous runs (F4B-M19 and F4B-M20), the off-gas CO concentration was lower and relatively constant when operating in this manner; the CO concentration remained in a range between 0.8 and 1.6%. Temperature profiles and off-gas concentrations remained stable during the last 4 hr of these runs. Run F4B-M22 terminated when the bed burned out of carbon; the conditions in Table 5-2 prevailed just before the bed was extinguished. The run was made with twice the cooling rate of the previous run. However, the bottom feeder was not capable of delivering twice the rate of feed and fines, thus depleting the bed of carbon.

After Run F4B-M22 was terminated, the burner was shut down for modifications. The burner and auxiliaries were evaluated to determine what modifications should be made before continuing with experimental runs. Data obtained on burner operations are being compared with the fluidized-bed design equations in the literature to determine which areas need further investigation.

From information on cooling gas flow rates and the burner temperature profiles, overall heat transfer coefficients were calculated. The experimentally determined values were 80 kcal/m^2-°C-hr for the bottom section and 67 kcal/m^2-°C-hr for the top section of the cooling clamshell (see Fig. 5-13 in Section on "Auger Feed System"). These values are about the same as the calculated value of h, the cooling gas film coefficient, indicating that the cooling gas film coefficient controls the heat transfer. The bed and disengagement section offer no apparent significant resistance. Heat transfer will be given further attention because the burn rate is limited by the ability to remove the heat of combustion. Also, at some point the burn will be limited by limitations in the ability of the feeder mechanism to feed the fresh feed and recycled fines.

Fines Elutriation and Sampling. The dependence of fines elutriation on run conditions is also being studied. The data on fines elutriation have been inconsistent. This problem may have been due to saltation of fines in the off-gas piping. When this piping was removed, it was observed that half of the area was blocked with fines which had settled out. This section of piping was replaced with a smaller section which, based on literature predictions, should not have saltation problems. This section of piping was provided with pressure taps to allow comparison of the pneumatic transport design equations with operating data. Saltation could have caused problems with elutriation rate measurements due to bulk flow of the solids (waves of settled-out material moving like sand dunes).

Another possible source of error in measuring elutriation rates was the measuring technique. The rate was measured by closing a valve for a period of time and then dumping the collected material into a container. Due to timing inaccuracies and loss of collected material, this procedure resulted in errors. A rotary sampling device has been installed (see Fig. 5-10). With this sampler the fines down comer is rotated from the normal position over the recycle hopper to a position over a sample container. Product is collected for some arbitrary time and then returned to its normal position. Sample collection times should be known more accurately than with the previous system and material containment will be absolute. Modification of the fines sampler and the off-gas lines should allow accurate determination of the fines elutriation rates.

Rotary Valve Product Removal Mechanism. One area of concern has been particle breakage. Data from the 10-cm burner have shown that the fluidized bed breaks few particles (<1%); however, the product removal auger was breaking excessive (approximately 15%) amounts of particles. The product removal auger has been replaced by a 1-in. rotary valve. This valve broke 0.3% of the particles in bench tests and delivered a throughput of 10.5 g/min at 1 rpm (at a 40 g C/min burn rate, the product rate is ~10 g/min). A thin metal bellows with a sliding metal insert is mounted between the rotary valve and the burner to account for thermal expansion of the burner. The product takeoff is a weir overflow leg with the rotary valve acting as a product removal metering device. Figure 5-11 is a sketch of the rotary valve. Figure 5-12 is a photograph of the valve as assembled on the

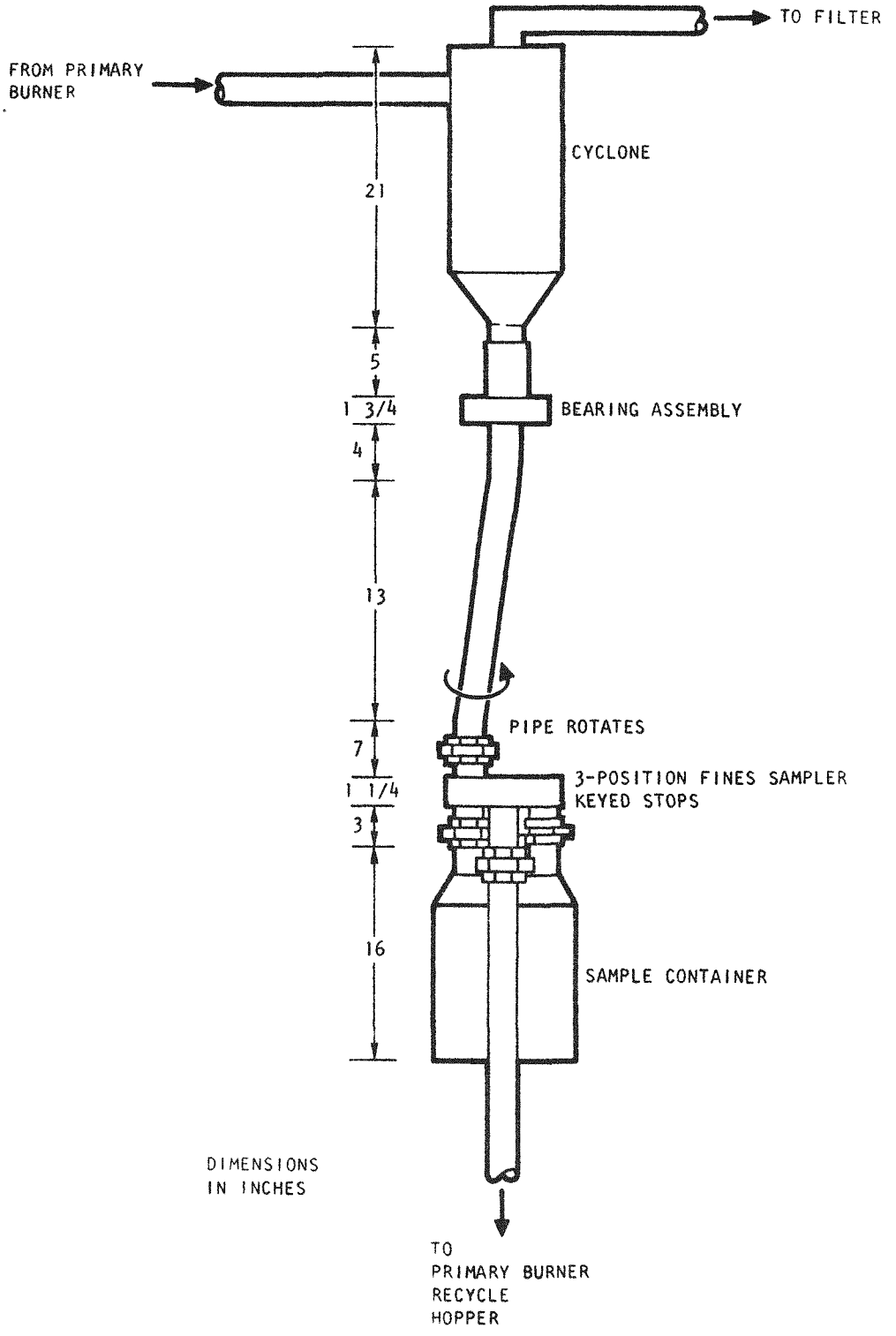

Fig. 5-10. Fines sampler for 10-cm primary burner

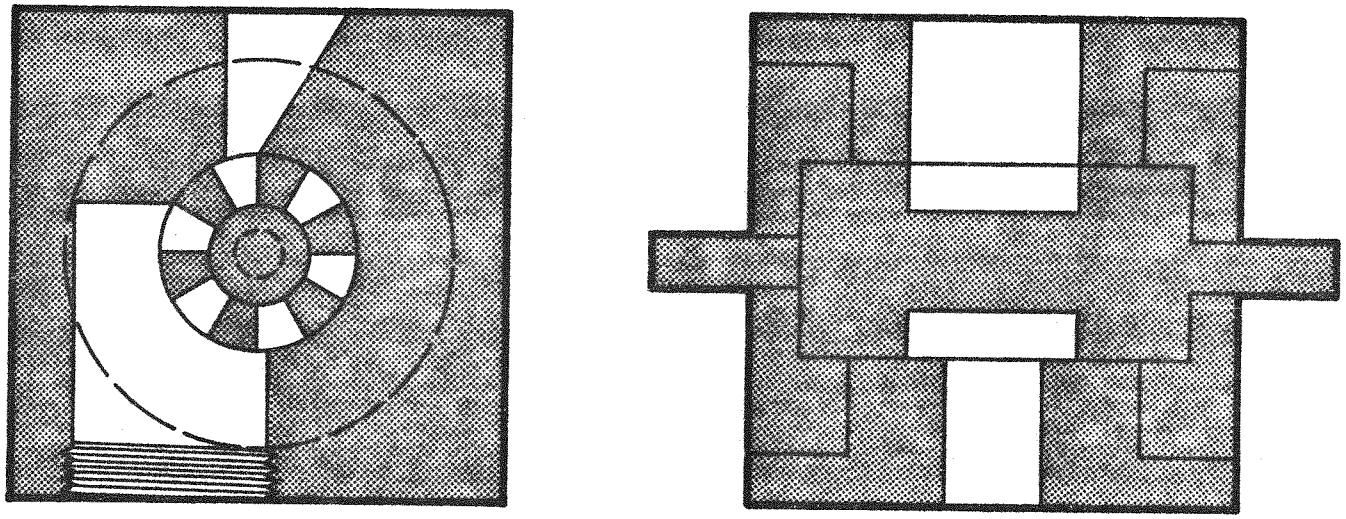

Fig. 5-11. Rotary valve, assembled

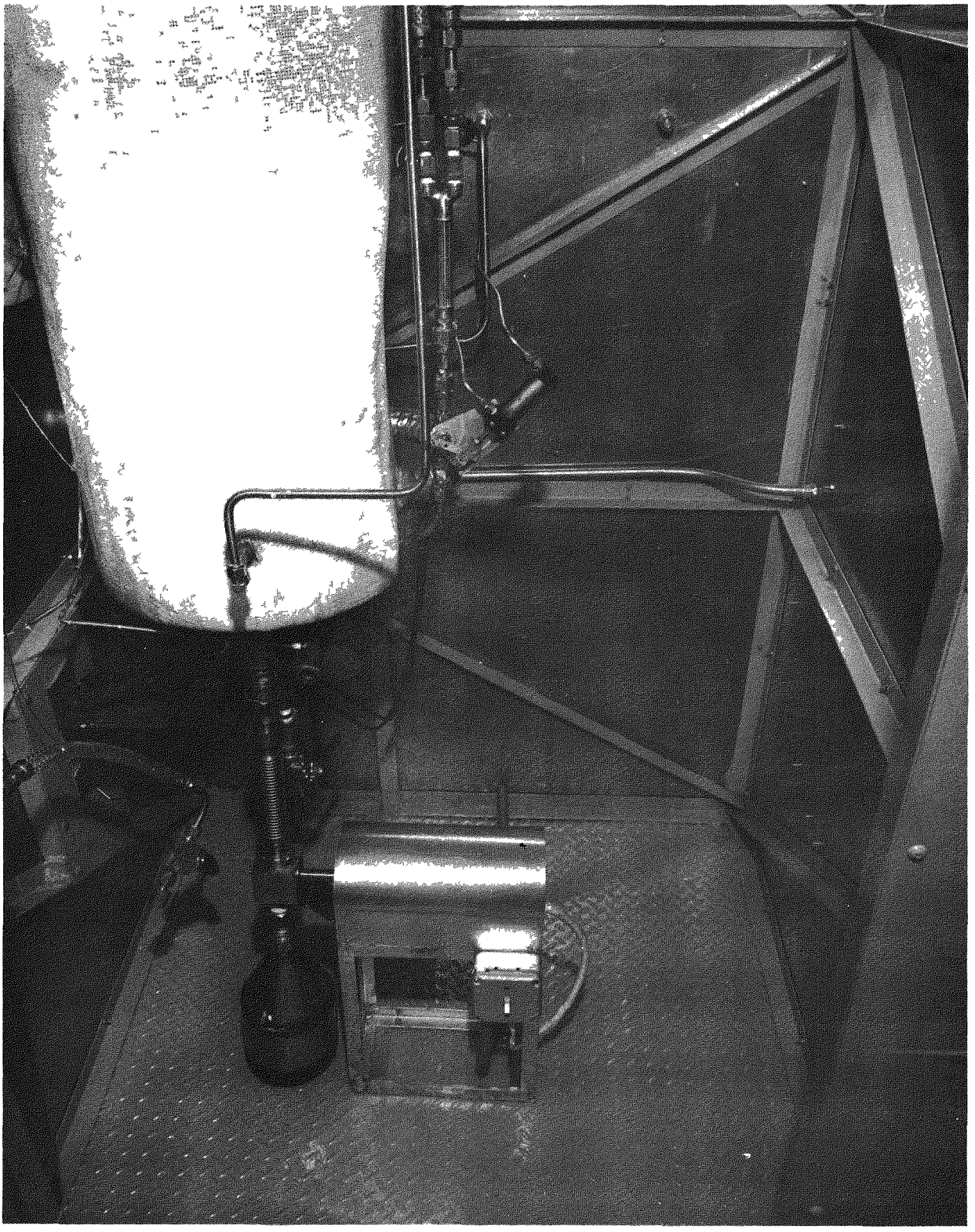

73HT768

Fig. 5-12. Product removal mechanism for 10-cm burner

burner. The product removal rate is controlled by the bed ΔP, the same as when an auger was used to remove the product. This valve is similar to (but smaller than) commercially available rotary valves and lends itself to use as an airlock for pneumatic transport. This modification resembles the type of equipment that might be used on a commercial burner and hopefully will result in a product with an acceptably low fraction of broken particles.

Auger Feed System. The bed addition auger - used to add the initial bed during startup of cold pilot plant runs (the commercial unit will have a whole bed ignition system) - was also modified to reduce particle breakage. The auger, a 2.54-cm-diameter, 15-cm-long ships auger, is the same as the one which was previously used for bed addition and product removal. Tests on the old system indicated 8 to 16% particle breakage. The old system supported the auger with a bushing at one end, allowing the auger to cantilever. Particles were crushed at the discharge end where the auger rested on the auger housing. The new auger is simply supported using bearings at either end of the auger. With this system the particle breakage is <1%. Modification of the bed addition auger and product removal system should substantially reduce particle breakage and demonstrate that the fluidized-bed system is capable of achieving low particle breakage.

The burner feeder configuration is presently being modified (see Fig. 5-13). The top feed hopper has been moved to a position directly above the bottom (recycle) hopper. The top feed auger is a 3.8-cm-diameter, 15-cm-long ships auger. This auger is intended to act only as a metering device. One area that has caused recurring problems is the bottom feed auger. This auger, which was a 3.8-cm-diameter, 98-cm-long ships auger, has caused problems due to binding and erratic flow characteristics. An attempt was made to analyze the problem areas and a new system, including a new core auger designed on the basis of an earlier study of auger systems, will be installed and hopefully will be more reliable. The old auger was contained by a housing that had a flexible metal bellows in line to adjust

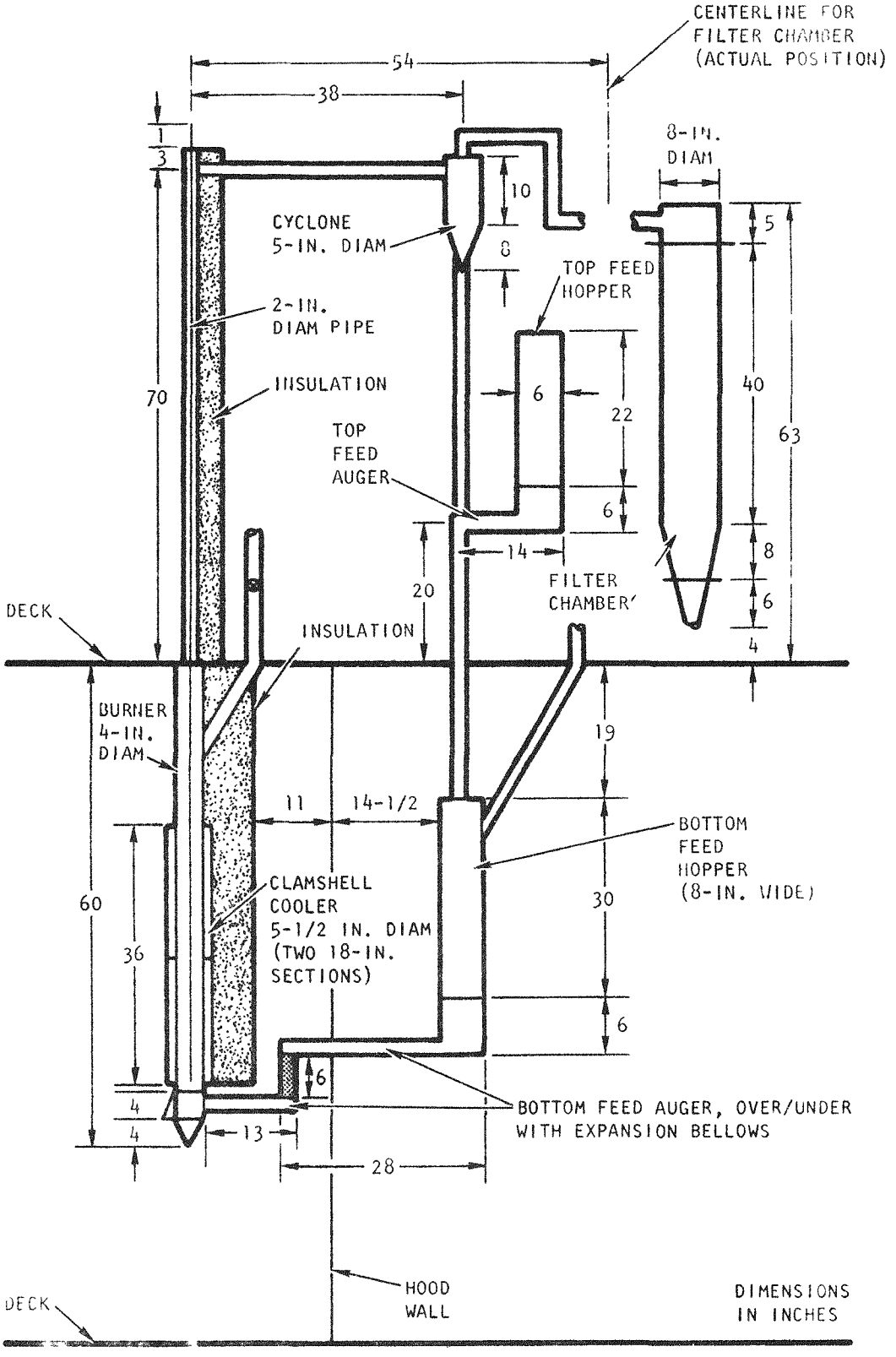

Fig. 5-13. 10-cm primary burner

for alignment changes when the burner expands (see Fig. 5-14). Problems arose from several sources: (1) the bellows was too stiff, straining the burner (stainless steel at ∿1000°C) and causing alignment problems when the burner deformed; (2) the auger (98-cm long) was cantilevered, being supported by a bushing at one end and rubbing on the housing wall near the burner; and (3) the method of level control used for the bottom hopper stratified the material in the hopper causing erratic auger output. The ships auger is being replaced with a core auger designed on the basis of the earlier auger studies: 3.2-cm-diameter housing, 2.2-cm-diameter auger, 1.3-cm core diameter, and 21° helix angle. The longest section of the auger will be simply supported with a bearing on each end; this should eliminate binding caused by the auger dragging on the auger housing and bellows. A short 33-cm-long auger with a bearing support on one end will feed directly into the burner; hopefully this section is short enough that cantilevering of the auger will not cause binding. The relative motion between the burner and bottom hopper caused by thermal expansion will be taken up by a thin metal bellows, spring rate 31 lb/in., between the two augers. The top auger housing will be rigid. The alignment between the top and bottom augers will be maintained by constraining the bottom of the burner to pure vertical motion using a Peaucellier cell (see Section on "Secondary Fluidized-Bed Burner"). Since the augers do not rotate inside the bellows, misalignment of the auger housing will not cause binding at this point, which was a possibility with the old system (see Fig. 5-14). Auger binding and erratic feed problems will hopefully be solved by these modifications.

The modifications presently being made are equipment improvement related items. As more reliable equipment is developed, more design data can be obtained. Fluid-bed literature makes it clear that fines entrainment and transport disengagement information is very dependent on the specific system and that the correlations are of limited usefulness; thus, obtaining reliable data on fines elutriation as a function of operating conditions is very important.

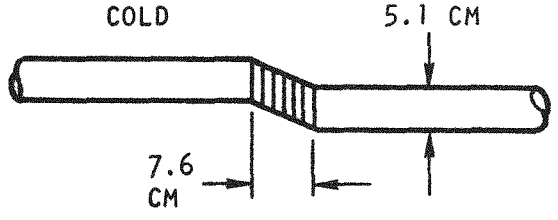

Fig. 5-14. Auger housing alignment

20-cm-Diameter Burner Development

The off-gas heat exchanger has been removed and the off-gas piping is being reassembled. The 20-cm burner will be modified to use a pneumatic feeder and to use an alternate product removal control method which is as yet unspecified. In this manner alternate feeders and metering devices can be used on the two burners, creating development experience with two complementary systems. The most promising system will be utilized on the commercial-scale burner.

A limited number of previous experimental runs were made evaluating a perforated plate gas distributor on the 10-cm primary burner as an alternate to the present cone-shaped gas distributor. The results were unacceptable due to the formation of agglomerates which plugged the plate. It is felt that these agglomerates formed when the $CO-O_2$ flame came into direct contact with the particles. Present plans are to delay further evaluation of distributor plates until an adequate startup technique is developed at ICPP. This evaluation will be made on the 20-cm burner. It is felt that use of a distributor plate on a small burner (10-cm) is unnecessary; with a small burner, even distribution should not be a major problem, especially when compared with the distribution problems in large commercial burners (70-cm and larger diameters) where wall effects predominate.

Secondary Fluidized-Bed Burner Development

Bed Removal System

Work on the 10-cm-diameter secondary burner (Fig. 5-15) has concentrated on fabrication of a high-temperature bed removal system. The system is designed to allow quick discharge of an entire burner batch.

As shown in Fig. 5-16, the bed removal system consists of a 1-in. exhaust valve and a mating valve seat (welded into the burner wall) from

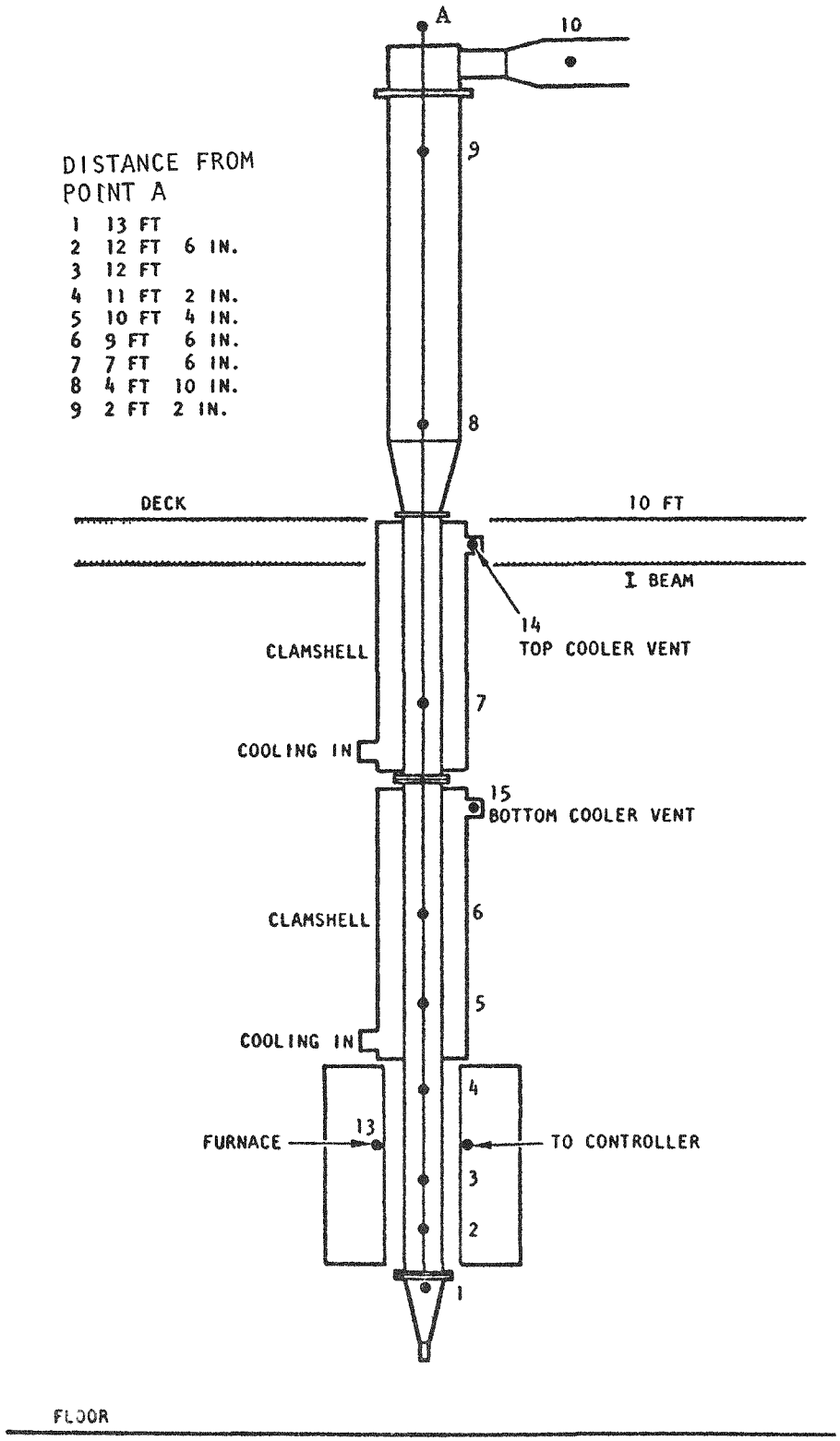

Fig. 5-15. 10-cm secondary burner layout

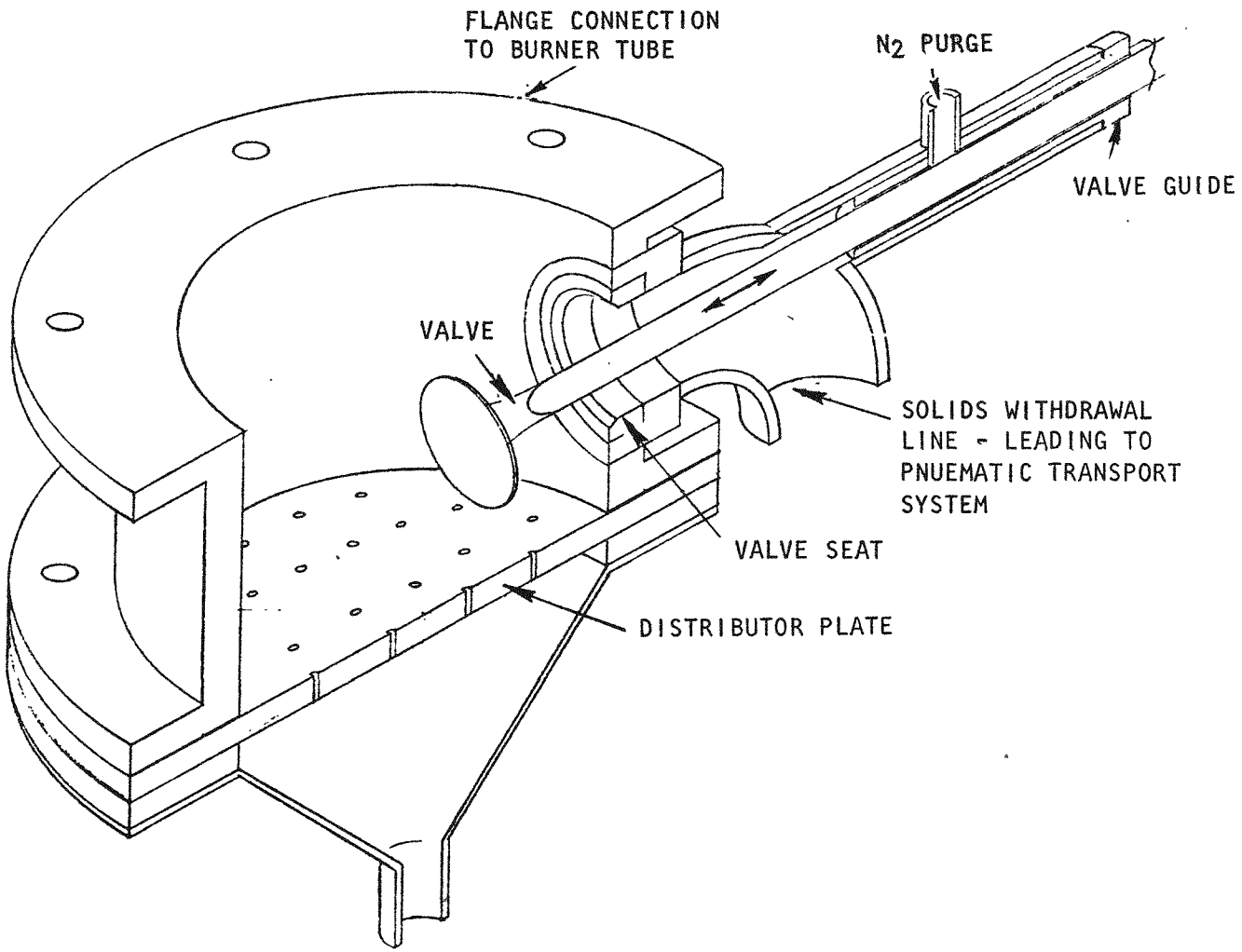

Fig. 5-16. High-temperature bed removal system for 10-cm secondary fluid-bed burner

an air-cooled, spark ignition engine. The valve is opened and closed by a double-acting pneumatic cylinder. The valve stem is supported by a standard valve guide equipped with a nitrogen purged seal.

Preliminary operating tests have been completed on the system. In these tests, 5 kg of -60 mesh Al_2O_3 were fluidized with N_2 and then dumped into a product receiver for weighing. Table 5-3 contains the discharge rates for three tests, as well as the alumina bed temperature during the tests. Secondary burner runs involving combustion of crushed TRISO fertile particles will start soon and will be reported in the next Quarterly Progress Report.

TABLE 5-3
RESULTS OF 10-CM SECONDARY BURNER
HIGH-TEMPERATURE BED REMOVAL SYSTEM TEST

Test No.	Alumina Removed (%)		Alumina Temperature (°C)
	After 5 Min	After 15 Min	
1	98	100	25
2	96	100	600
3	96	100	800

Burner Alignment

Burner alignment mechanisms (Peaucellier cells) have been fabricated and installed. These mechanisms restrict the burner tube to vertical movement only, thus preventing lateral movement and subsequent tube "kinking." Two such mechanisms were installed perpendicular to one another on the burner distributor plate flange. They are braced by the resistance furnace support pedestal.

Induction Heating

Induction heating is being investigated as an alternate to the present resistance-type heaters. Advantages of induction heating over resistance heating include:

1. More available area for air jacket cooling.
2. More rapid startup due to increased heating rate.
3. Higher reliability of in-cell equipment.

Recommendations for the type of heater to be used for secondary burners located in a hot cell will be made in the near future.

Materials of Construction

Several high-temperature metals are being evaluated for burner tube material. The presently used austenitic stainless steel is undesirable because of high creep rates and low oxidation resistance at typical burner temperatures (>900°C). The suitability of one candidate metal, Hastelloy X, for use on an induction-heated secondary burner is being determined.

Leaching

Size Distributions of Solids Encountered in the Leaching System When Reprocessing TRISO Carbide Fertile Particles

The particle size of solids encountered in the leaching system is of importance to the design and operation of:

1. The system (pneumatic, etc.) for transporting secondary burner product to leacher feed hoppers.

2. Leacher feed hoppers.

3. Leacher (loading, dissolution rates, emptying).

4. Solids-liquid separation following leaching.

5. Drying insolubles from leacher.

6. The system for transporting and loading insolubles into suitable storage containers.

Size distributions of solids fed to the leacher, leacher insolubles, and ThO_2 fed to the leacher were determined as discussed below.

Solids Fed to Leacher. Secondary burner ash (72 kg from burner runs F4-RHB-M3-14, -15, -20, -21, -22, and -23) was mixed to form a uniform composite to be used in leaching tests. This material resulted from burning crushed TRISO ThC_2 particles. The particles were crushed in laboratory-size double-roll crushers. The rolls of the crusher are 1 in. wide and 3 in. in diameter, and rotate at about 10 rpm. The gap between the rolls is 0.015 in. (381 μm).

The size distribution of this burner ash was determined using standard screening techniques (Table 5-4). As can be seen, over 24 wt % of the burner ash is smaller than the smallest available screen (44 μm). This necessitated determining the size distribution of the smaller than 44-μm material by an alternate method. The Coulter counter (Ref. 5-1) technique was selected to supplement the screen analysis. Three samples of the burner ash and three samples of the -44 μm screen fraction were submitted for Coulter counter analysis. Results of these analysis are included in Tables 5-5 and 5-6 and Fig. 5-17. Data from the screen analysis (Table 5-4) are also plotted in Fig. 5-17 and illustrate the extent of disagreement that exists between the two size distribution determination methods. It is not certain at this time which method is in error; however, the screen analysis is suspect.

Leacher Insolubles. The size distribution of insoluble silicon carbide (SiC) hulls (resulting from leaching the above burner ash in leaching runs 43 through 52) was also determined using the screen technique and the Coulter counter method. The screen analysis for insolubles resulting from

TABLE 5-4
SCREEN ANALYSIS OF 72-KG COMPOSITE
OF SECONDARY BURNER ASH
(BURNED-BACK CRUSHED TRISO ThC_2 PARTICLES)

Screen Size (μm)	Material Retained on Screen (wt %)
500	0
420	0.119
250	0.899
210	1.166
149	7.244
105	9.774
74	11.374
53	37.358
44	8.035
-44	24.031
Total	100.000

TABLE 5-5
SIZE DISTRIBUTION BASED ON COULTER COUNTER RESULTS
SECONDARY BURNER ASH, 72 KG (COMPOSITE)

Diameter (μm)	Cumulative wt %			Differential wt %		
	Sample 1 △(a)	Sample 2 ○(a)	Sample 3 □(a)	Sample 1	Sample 2	Sample 3
1.26						
1.59						
2.00	100	100	100	1.1	1.4	0.7
2.52	98.9	98.6	99.3	1.1	1.4	0.7
3.17	97.9	97.3	98.6	1.1	1.4	1.0
4.00	96.8	95.9	97.6	1.6	1.4	1.4
5.04	95.2	94.5	96.2	1.6	2.1	1.4
6.35	93.7	92.4	94.8	2.6	2.1	2.1
8.00	91.0	90.4	92.8	3.2	2.7	2.4
10.08	87.8	86.9	90.4	4.8	3.4	3.1
12.27	83.1	83.5	87.3	5.8	4.8	4.1
16.00	77.2	78.7	83.2	6.3	5.5	5.5
20.20	70.9	73.2	77.7	6.3	6.2	6.2
25.40	64.6	67.0	71.5	5.3	6.9	6.2
32.00	59.3	60.1	65.3	4.8	6.9	6.2
40.30	54.5	53.3	59.1	3.7	6.9	5.5
50.80	50.8	46.4	53.6	4.2	5.5	4.8
64.00	46.6	40.9	48.8	4.2	4.1	4.8
80.60	42.3	36.8	44.0	5.3	5.5	6.2
101.60	37.0	31.3	37.8	7.4	6.9	6.9
128.00	29.6	24.4	30.9	8.5	8.2	8.9
161.00	21.2	16.2	22.0	9.5	8.2	9.6
203.00	11.6	7.9	12.4	5.3	6.9	8.9
256.00	6.3	1.0	3.4	3.2	1.0	2.7
322.00	3.2		0.7	2.1		0.7
406.00	1.1			1.1		
Totals				100.1	99.4	100.0

(a) Symbol used in Fig. 5-17.

TABLE 5-6
SIZE DISTRIBUTION BASED ON COULTER COUNTER RESULTS
-44 μm SCREEN FRACTION OF SECONDARY BURNER PRODUCT, 72 KG (COMPOSITE)

	Cumulative wt %			Differential wt %		
Diameter (μm)	Sample 1 ◇(a)	Sample 2 ▽(a)	Sample 3 ●(a)	Sample 1	Sample 2	Sample 3
1.26	100	100		1.0	1.4	
1.59	99.0	98.6	100	1.2	1.4	1.0
2.00	97.9	97.2	99.0	1.2	1.8	1.0
2.52	96.7	95.4	98.1	1.7	2.1	1.5
3.17	95.0	93.3	96.6	2.1	2.5	2.4
4.00	92.8	90.8	94.1	2.6	3.2	2.9
5.04	90.2	87.6	91.2	3.6	4.1	3.4
6.35	86.6	83.4	87.8	4.5	5.1	4.9
8.00	82.1	78.3	82.9	6.2	6.5	6.3
10.08	75.9	71.9	76.6	8.6	8.8	9.3
12.27	67.3	63.1	67.3	11.5	11.5	11.7
16.00	55.8	51.6	55.6	14.3	13.8	15.1
20.20	41.5	37.8	40.5	16.2	14.7	16.1
25.40	25.3	23.0	24.4	14.8	13.4	14.1
32.00	10.5	10.0	10.2	8.6	8.3	8.8
40.30	1.9	1.4	1.5	1.9	1.4	1.5
50.80						
64.00						
80.60						
101.60						
128.00						
161.00						
203.00						
256.00						
322.00						
406.00						
Totals				100.0	100.0	100.0

(a) Symbol used in Fig. 5-17.

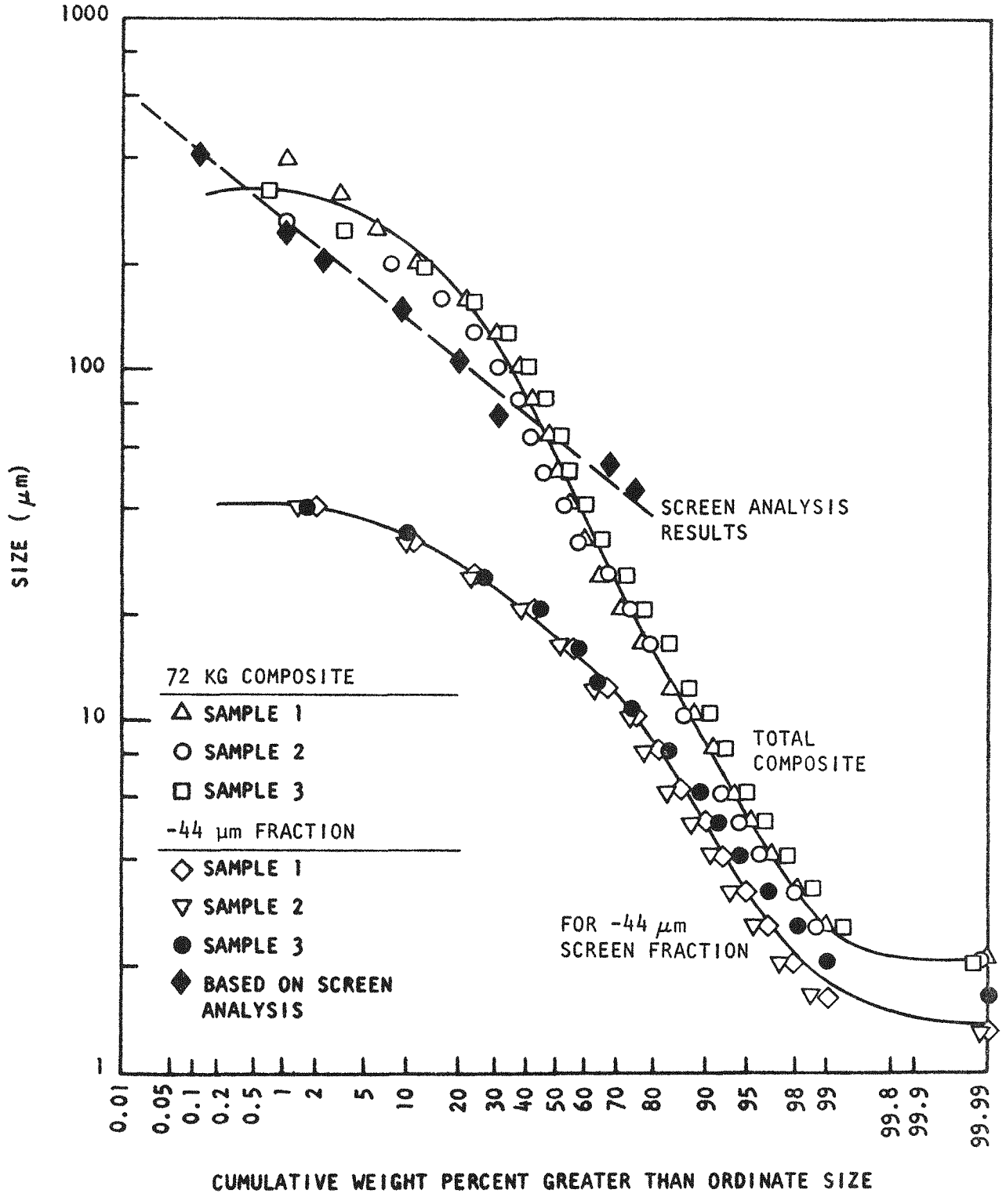

Fig. 5-17. Cumulative weight percent size distribution for 72-kg burner ash composite based on Coulter counter results

leach run 49 is given in Table 5-7. The Coulter counter analysis for the insolubles and the -44 μm screen fraction of the insolubles is included in Table 5-8 and Fig. 5-18. The screen analysis data (Table 5-7) are also included in Fig. 5-18 and indicate good agreement with Coulter counter results.

The insolubles resulting from leaching runs 43 through 52 were mixed together to form a composite. A screen analysis for this composite of insolubles is given in Table 5-9. Three samples of the insolubles and three samples of the -44 μm screen fraction of the insolubles were submitted for Coulter counter analysis. Results of these analyses are given in Table 5-10 and Fig. 5-19. Screen analysis data (Table 5-9) are also plotted in Fig. 5-19 and indicate good agreement with the Coulter counter results.

A comparison of Tables 5-7 through 5-10 and Figs. 5-18 and 5-19 indicates that a reasonable agreement exists between screen analysis and Coulter counter results for insolubles. Also, results are in good agreement between different samples of insolubles, i.e., run 49 insolubles as compared with the composite of run 43 through 52 insolubles. It is therefore assumed that the discrepancy between screen analysis and Coulter counter results for the burner ash is due to the presence of ThO_2 as opposed to SiC. Future studies will attempt to delineate this discrepancy.

Calculated Size Distribution of ThO_2 Fed to Leacher. The size distribution of ThO_2 in the burner ash fed to the leachers is a primary variable affecting the rate of dissolution. An attempt was therefore made to establish this information. A sample of each size fraction of the burner ash (Table 5-4) was submitted for chemical analysis. The resulting chemical analyses are given in Table 5-11. The size distribution of ThO_2 in the burner ash was then calculated as indicated in Table 5-11.

An alternate method of establishing the size distribution of ThO_2 in the solids fed to the leacher was also carried out. The screen analysis (Table 5-4) for the burner ash was used to establish the amount of ThO_2 plus SiC in each size fraction. In addition, a chemical analysis of the

TABLE 5-7
SCREEN ANALYSIS OF INSOLUBLES
REMAINING AFTER LEACH RUN 49
(LEACH RUN 49 USED BURNER ASH OF TABLE 5-4 AS FEED)

Screen Size (μm)	Material Retained on Screen (wt %)
500	0
420	0.596
250	4.523
210	6.134
149	25.260
105	22.147
74	16.274
53	8.257
44	4.361
-44	12.448
Total	100.000

TABLE 5-8
SIZE DISTRIBUTION BASED ON COULTER COUNTER RESULTS
RUN 49

Diameter (μm)	Run 49 Insolubles		-44μm Screen Fraction of Run 49 Insolubles	
	Cumulative wt % Sample 1 △(a)	Differential wt % Sample 1	Cumulative wt % Sample 1 ○(a)	Differential wt % Sample 1
1.26				
1.59				
2.00				
2.52				
3.17			100.0	0.5
4.00			99.5	0.5
5.04			98.0	1.0
6.35			97.9	1.8
8.00	100.0	0.7	96.1	3.6
10.08	99.3	0.7	92.4	6.0
12.27	98.5	0.7	86.5	8.6
16.00	97.8	0.7	77.9	12.2
20.20	97.0	1.5	65.6	17.4
25.40	95.5	2.2	48.2	21.1
32.00	93.3	3.7	27.1	18.8
40.30	89.6	5.2	8.3	7.8
50.80	84.3	6.0	0.5	0.5
64.00	78.4	6.0		
80.60	72.4	10.4		
101.60	61.9	13.4		
128.00	48.5	14.9		
161.00	33.6	19.4		
203.00	14.2	10.4		
256.00	3.7	3.0		
322.00	0.7	0.7		
406.00				
Total		99.6		99.8

(a) Symbol used in Fig. 5-18.

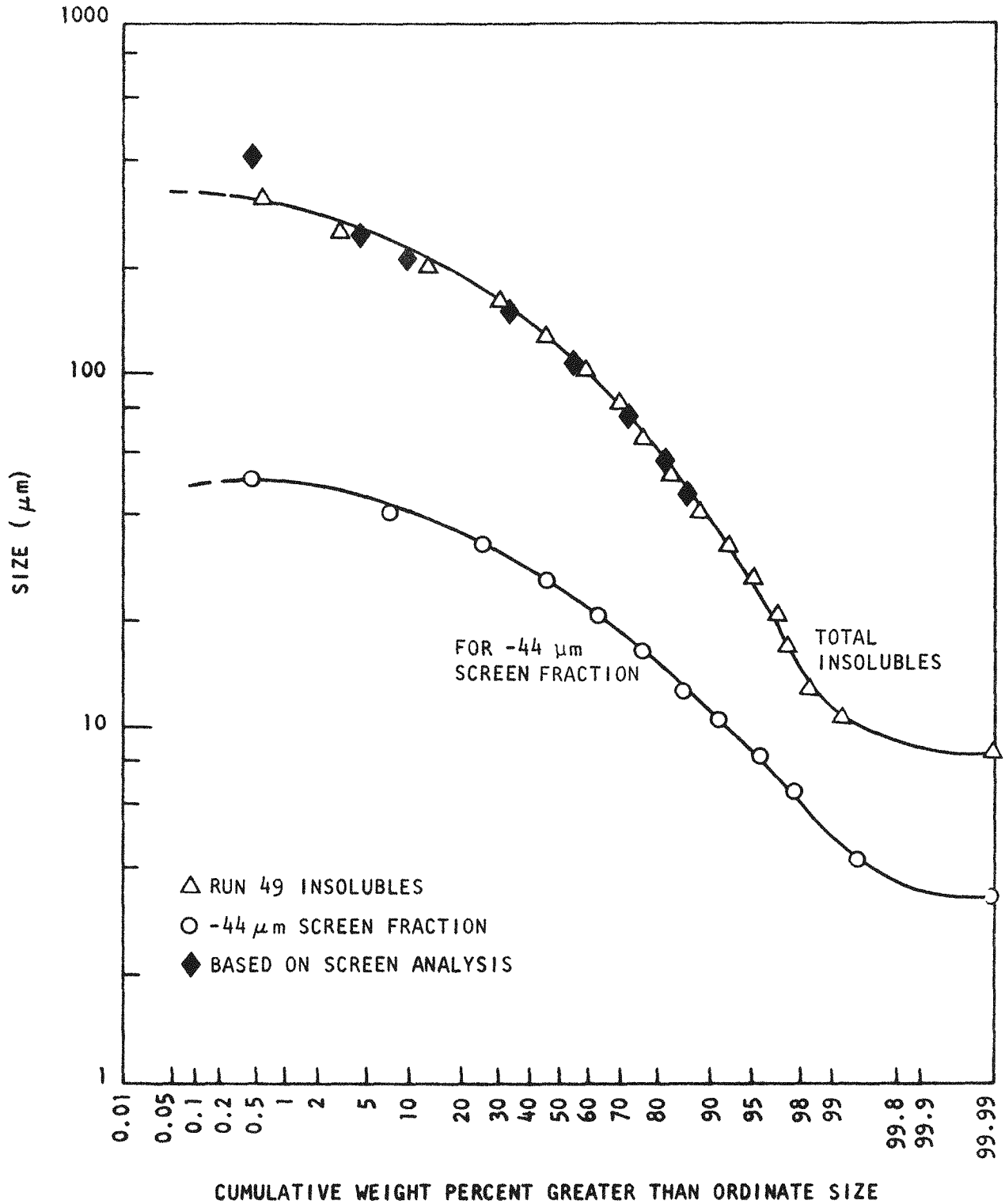

Fig. 5-18. Cumulative weight percent size distribution for insolubles re-remaining after leach run 49 based on Coulter counter results

TABLE 5-9
SCREEN ANALYSIS FOR COMPOSITE OF
INSOLUBLES REMAINING AFTER LEACH RUNS 42 THROUGH 53
(LEACH RUNS 43 THROUGH 52 USED BURNER ASH OF TABLE 5-4 AS FEED)

Screen Size (μm)	Material Retained on Screen (wt %)
500	0
420	0.062
250	2.176
210	4.969
149	28.239
105	20.239
74	25.621
53	8.781
44	2.419
-44	7.494
Total	100.000

TABLE 5-10
SIZE DISTRIBUTION BASED ON COULTER COUNTER RESULTS
RUNS 43 THROUGH 52

	Insolubles from Leach Runs 43-52 (Composite)						-44 µm Screen Fraction of Insolubles from Runs 43-52 (Composite)					
	Cumulative wt %			Differential wt %			Cumulative wt %			Differential wt %		
Diameter (µm)	Sample 1 △[a]	Sample 2 ○[a]	Sample 3 □[a]	Sample 1	Sample 2	Sample 3	Sample 1 ◇[a]	Sample 2 ▽[a]	Sample 3 ●[a]	Sample 1	Sample 2	Sample 3
1.26												
1.59												
2.00							100.0	100.0		0.3	0.3	
2.52							99.7	99.7	100.0	0.5	0.5	0.5
3.17							99.2	99.2	99.5	0.5	0.5	0.5
4.00							98.7	98.7	99.0	1.0	1.0	0.5
5.04							97.7	97.7	98.5	1.5	1.5	1.3
6.35							96.2	96.2	97.2	2.8	2.6	2.1
8.00	100.0			0.5			93.4	93.6	95.1	4.1	4.1	3.6
10.08	99.5			0.5			89.3	89.5	91.5	6.6	6.1	6.2
12.27	99.0			0.5			82.7	83.4	85.3	9.6	9.2	9.3
16.00	98.5	100.0	100.0	1.0	0.9	1.0	73.1	74.2	76.1	13.2	12.3	12.3
20.20	97.6	99.1	99.0	1.5	0.9	1.0	59.9	61.9	63.8	17.8	17.9	17.5
25.40	96.1	98.2	98.1	1.9	1.8	1.9	42.1	44.0	46.3	20.3	21.0	21.6
32.00	94.2	96.5	96.1	2.4	2.6	2.9	21.8	23.0	24.7	16.8	17.4	18.5
40.30	91.7	93.9	93.2	3.4	4.4	3.9	5.1	5.6	6.2	5.1	5.6	6.2
50.80	88.3	89.5	89.3	4.9	5.3	4.9						
64.00	83.5	84.2	84.5	6.8	7.0	6.8						
80.60	76.7	77.2	77.7	9.7	10.5	9.7						
101.60	67.0	66.7	68.0	13.6	12.3	14.6						
128.00	53.4	54.4	53.4	17.5	14.0	18.4						
161.00	35.9	40.4	35.0	18.4	15.8	17.5						
203.00	17.5	24.6	17.5	13.6	14.0	11.7						
256.00	3.9	10.5	5.8	2.9	5.3	3.9						
322.00	1.0	5.3	1.9	1.0	3.5	1.9						
406.00		1.8			1.8							
Total				100.1	100.1	100.1				100.1	100.0	100.1

(a) Symbol used in Fig. 5-19.

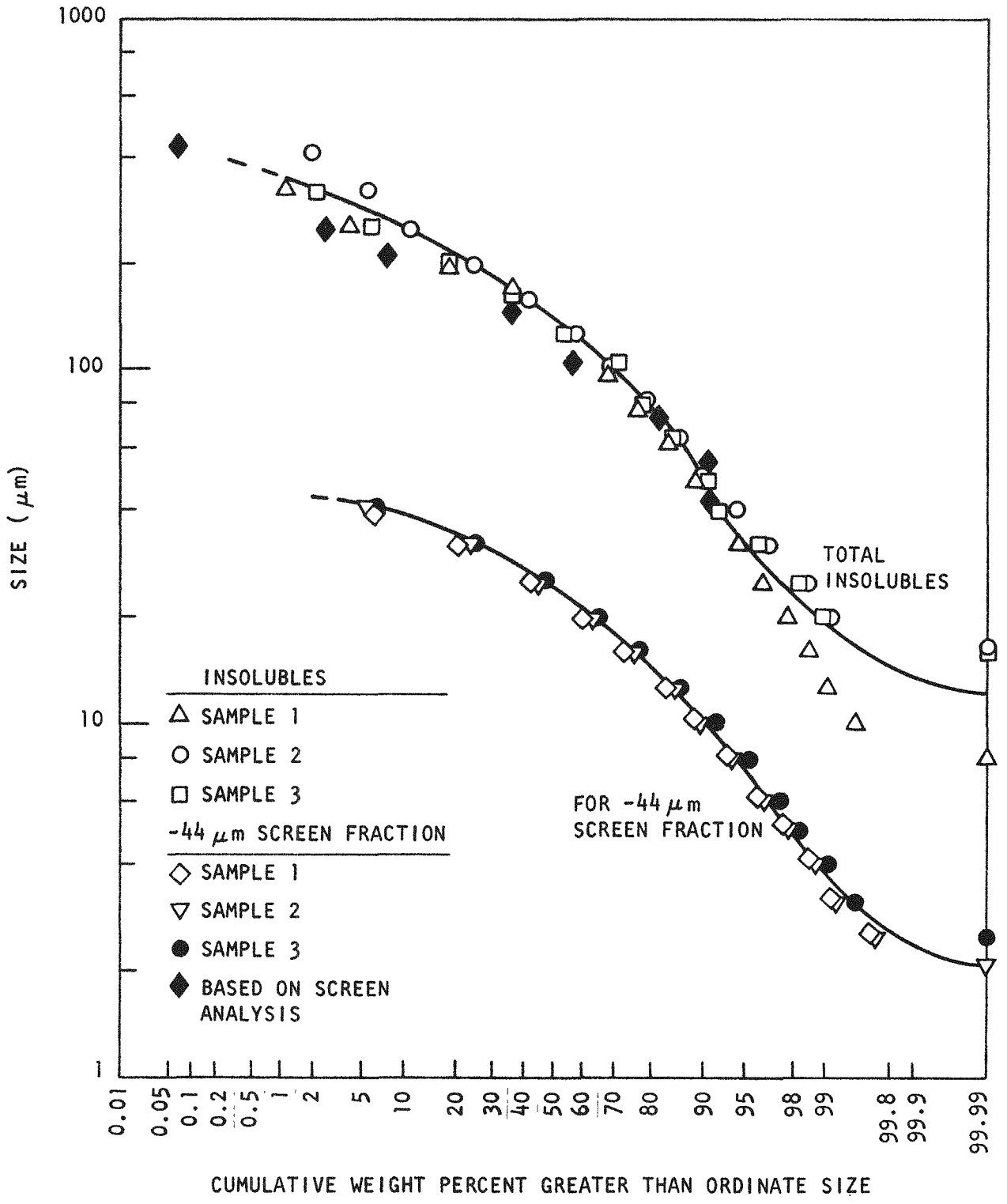

Fig. 5-19. Cumulative weight percent size distribution for insolubles remaining after leach runs 43 through 52 based on Coulter counter results

TABLE 5-11
SIZE DISTRIBUTION OF ThO_2 IN LEACHER FEED
BASED ON CHEMICAL ANALYSIS OF SCREEN FRACTIONS

Size Fraction (μm)	Size Distribution of Feed from Screen Analysis (wt %)	Chemical Analysis of Size Fraction (wt % ThO_2)	Amount of ThO_2 in Each Size Fraction (g ThO_2/100 g feed)	ThO_2 in Each Size Fraction (wt %)
0-44	24.031	94.321	22.666	27.133
44-53	8.035	92.102	7.400	8.858
53-74	37.358	86.367	32.265	38.631
74-105	11.374	72.917	8.294	9.928
105-149	9.774	91.203	8.914	10.671
149-210	7.244	51.433	3.726	4.460
210-250	1.166	21.825	0.254	0.304
250-420	0.899	1.138[a]	0.012	0.014
420-500	0.119	5.690[a]	0.007	0.001
Total	100.000		83.538	100.000

[a] Percent estimated from microscopic observation of fraction.

burner ash was conducted and indicated a 71.3 wt % Th content. Thus, a corresponding 18.87 wt % SiC in the burner ash was established. Based on this information and the screen analysis (Table 5-9) for the insolubles remaining after leach runs 42 through 53, it was possible to establish the amount of SiC in each size fraction of the insolubles. This information is included in Table 5-11. By assuming that the size distribution of SiC in the feed does not change during leaching, it is possible to determine the amount of ThO_2 in the burner ash for each size fraction by the difference between the quantity of burner ash and insoluble SiC. This allows the size distribution of ThO_2 to be calculated as illustrated in Table 5-12.

This procedure was repeated based on the Coulter counter analyses of Figs. 5-17 and 5-19. The results are included in Table 5-13.

A graphical comparison of the three calculated ThO_2 size distributions of Tables 5-11 through 5-13 is given in Fig. 5-20. This comparison indicates that the ThO_2 size distribution calculated by differences between screen analyses (Table 5-12) agrees closely with the results based on screen analysis and subsequent chemical analysis of the different size fractions (Table 5-11). Thus, the more expensive and time-consuming procedure of chemically analyzing each size fraction will not be utilized in further testing.

The Coulter counter results (Table 5-13) differ appreciably from those based on the screen analysis (Tables 5-11 and 5-12). This is due to the difference between the screen analysis and Coulter counter analysis of the burner ash. As can be seen from Fig. 5-20, the screen analysis results indicate that about 27 wt % of the ThO_2 in the leacher feed is smaller than 44 μm; however, the Coulter counter results indicate that well over 50 wt % of the ThO_2 in the leacher feed is smaller than 44 μm. As mentioned previously, it is not clear at this time which technique yields the most accurate results. Additional testing will be conducted in the future.

TABLE 5-12
CALCUALTED SIZE DISTRIBUTION OF ThO_2 IN LEACHER FEED
BASED ON SCREEN ANALYSIS OF FEED AND INSOLUBLES

Size Fraction (μm)	Size Distribution of Feed (ThO_2 + SiC) (wt %)[a]	Amount of SiC in Insolubles, (g SiC/100 g feed)[b]	Amount of ThO_2 (By Difference) (g ThO_2/100 g feed)	Calculated ThO_2 Distribution (wt %)
0-44	24.031	1.414	22.617	27.877
44-53	8.035	0.456	7.579	9.342
53-74	37.358	1.645	35.713	44.020
74-105	11.374	4.841	6.533	8.053
105-149	9.774	3.819	5.955	7.340
149-210	7.244	5.329	1.915	2.360
210-250	1.166	0.938	0.228	0.281
250-420	0.899	0.416	0.483	0.595
420-500	0.119	0.012	0.107	0.132
Total	100.000	18.870	81.130	100.000

[a] Based on screen analysis of feed from Table 5-4.

[b] Based on screen analysis of insolubles from Table 5-7 and chemical analysis of feed - average 71.3% Th.

TABLE 5-13
CALCULATED SIZE DISTRIBUTION OF ThO_2 IN LEACHER FEED
BASED ON COULTER COUNTER ANALYSIS

Size Fraction (μm)	Size Distribution of Feed (ThO_2 + SiC) (wt %)[a]	Amount of SiC in Insolubles, (g SiC/100 g feed)[b]	Amount of ThO_2 (By Difference) (g ThO_2/100 g feed)	Calculated ThO_2 Distribution (wt %)
0-44	45.0	1.70	43.30	53.4
44-53	5.0	0.37	4.63	5.7
53-74	8.0	1.51	6.49	8.0
74-105	9.0	3.02	5.98	7.4
105-149	10.0	3.96	6.04	7.4
149-210	11.0	4.53	6.47	8.0
210-250	5.0	1.89	3.11	3.8
250-420	7.0	1.89	5.11	6.3
420-500	0.0	0.0	0.0	0.0
Total	100.0	18.87	81.13	100.0

[a] Based on Coulter Counter analysis of feed (from Fig. 5-17).

[b] Based on Coulter Counter analysis of insolubles (from Fig. 5-19).

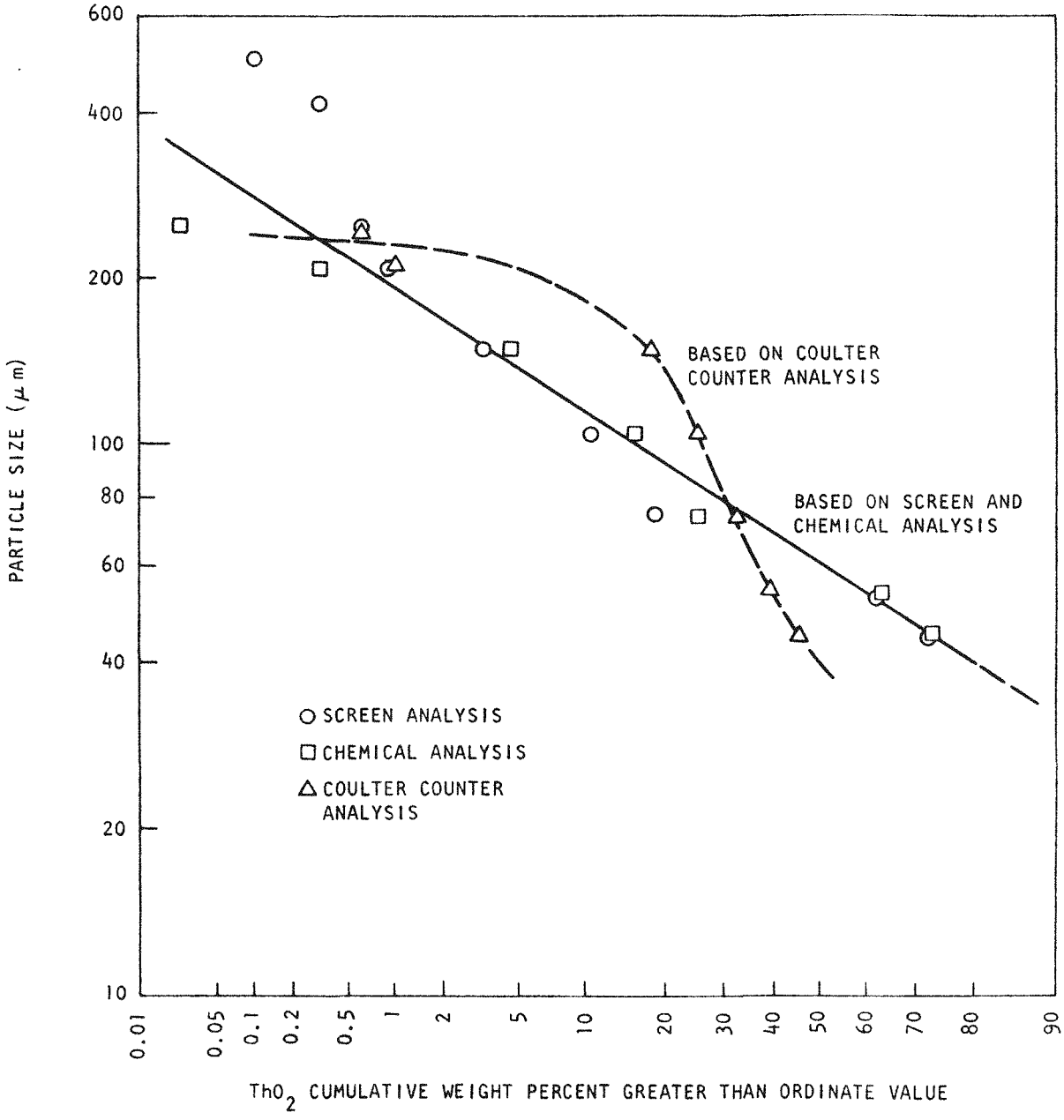

Fig. 5-20. Calculated size distribution of ThO_2 in leacher feed

Determination of Gas Holdup in Air-Sparged Leachers

As sparge air is introduced into the leacher, it is dispersed through the slurry (burner ash and acid) volume. This creates an expanded "bed" volume that must be considered in sizing equipment and placing control instrumentation. It is therefore important to establish the amount of expansion, or gas holdup, for the leachers.

If h_N is the non-sparged liquid height and h_S is the sparged (expanded or aerated) bed height in the leacher, then the gas holdup volume is

$$V_g = S(h_S - h_N) \quad , \tag{1}$$

where S is the leacher cross-sectional area.

It follows that the fractional gas holdup is

$$\varepsilon = \frac{(h_S - h_N)}{h_S} \quad . \tag{2}$$

As pointed out by Braulick et al. (Ref. 5-2), ε can vary with height depending upon how the bubbles are formed, contacted, and coalesced. However, the usual approach in design is to use total heights in the vessel. Under these conditions, ε corresponds to an overall fractional gas holdup. This is the meaning of ε utilized in this presentation.

Gas holdup can be broken up into two different hydrodynamic regions: (1) a static region and (2) a dynamic region. The static region corresponds to conditions where:

1. Superficial gas velocities are below about 0.2 ft/sec (6.1 cm/sec).
2. Bubble formation is particulate and almost ordered.
3. Agitation is minimal.

The dynamic region corresponds to conditions where:

1. Superficial gas velocities are above about 0.2 ft/sec (6.1 cm/sec).
2. Bubble formation appears random and bubble definition is poor.
3. Contacting action is turbulent and erratic.

Leaching tests conducted on secondary burner ash (TRISO carbide fertile material) have indicated that sparge rates of 10 to 20 liters (STP) air/min provide acceptable dissolution rates (see previous Quarterly Progress Reports, Gulf-GA-A12515 and Gulf-GA-A12599 for details) in the 13-cm-diameter and 20-cm-diameter leachers. Thus, superficial air velocities that fall into the static region are encountered at the beginning (heatup phase) of a leaching run. Therefore, some gas holdup data were gathered at ambient temperatures to provide a reference point.

Static Region. The results of air-sparge tests with Thorex [13M HNO_3/0.05M HF/0.1M $Al(NO_3)_3$] at about 30°C are given for the 13-cm-diameter and 20-cm-diameter leachers in Figs. 5-21 and 5-22, respectively. (The procedure utilized to measure gas holdup is outlined later in the section under "Experimental Method.") The data indicate that the fractional gas holdup in the static region is not a function of the height of material in the leacher, but is a linear function of the superficial gas velocity as follows:

$$\text{13-cm-diameter leacher:} \quad \varepsilon = U_{OG} \tag{3}$$

$$\text{20-cm-diameter leacher:} \quad \varepsilon = 2U_{OG} \quad , \tag{4}$$

where the superficial gas velocity $U_{OG} \leq 0.08$ ft/sec (2.4 cm/sec) and is based on the empty cross-sectional area of the leachers.

The data of Figs. 5-21 and 5-22 also indicate that the presence of about 0.22 kg burner ash/kg Thorex does not affect the fractional gas holdup.

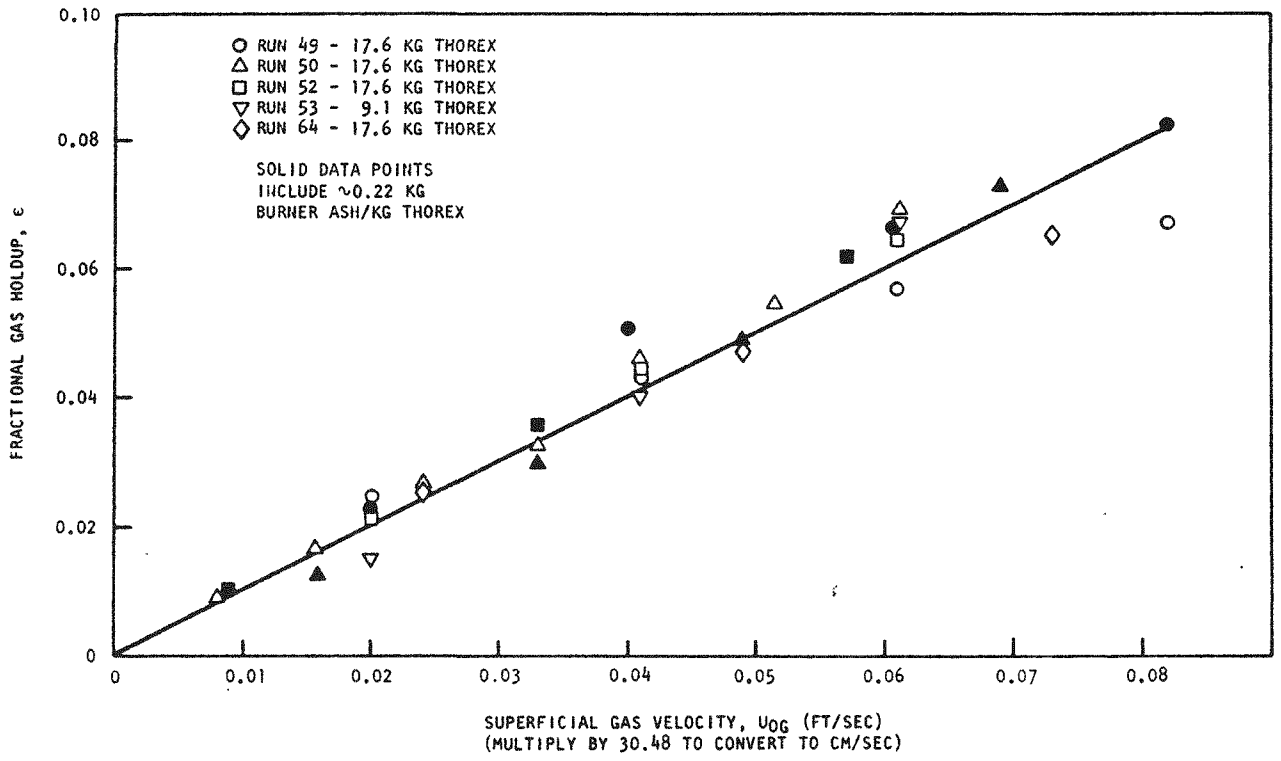

Fig. 5-21. Fractional gas holdup as a function of superficial gas velocity, 13-cm leacher, T = 30°C

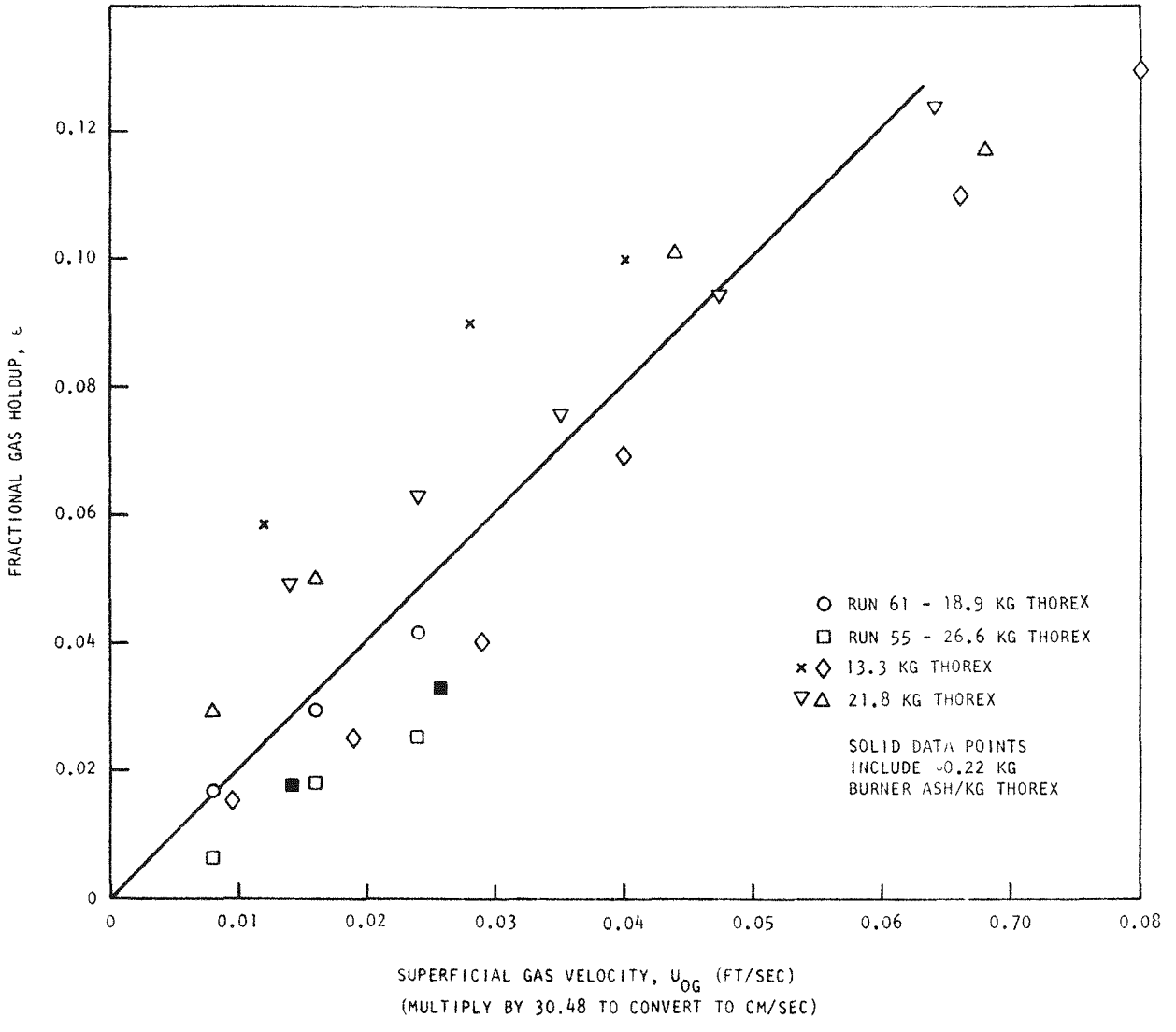

Fig. 5-22. Fractional gas holdup as a function of superficial gas velocity, 20-cm leacher, T = 30°C

Dynamic Region. Data obtained utilizing boiling Thorex (T ≃ 118°C) are given in Figs. 5-23 and 5-24. These data indicate a relationship between gas holdup and "external" superficial gas velocity. As can be seen, the range of "external" superficial gas velocity is less than 0.07 ft/sec (2.1 cm/sec). This gas velocity is a result of only the sparge air being introduced into the boiling Thorex. Obviously the "actual" superficial gas velocity (from sparge air and from vaporization of Thorex) is larger than these values and this operation is in the dynamic region.

The fractional gas holdup values shown in Figs. 5-23 and 5-24 have been corrected for change in volume due to heating.

$$\Delta V \text{ (liters)} = (\text{kg Thorex}) \times \left(\frac{1}{\substack{\text{SG Thorex} \\ \text{(at 118°C)}}} - \frac{1}{\substack{\text{SG Thorex} \\ \text{(at 30°C)}}} \right) \qquad (5)$$

$$= (\text{kg Thorex}) \times (0.1173)$$

With this information (and the fact that the 13-cm-diameter leacher holds about 0.131 liters/cm of height and the 20-cm-diameter leacher holds about 0.323 liters/cm of height), the increase in height due to changing specific gravity was calculated. This height increase was added to the solution height at ambient temperature to establish the nonsparged liquid height for use with Eq. (2). Thus, the gas holdup shown (Figs. 5-23 and 5-24) at an "external" superficial gas velocity equal to zero is due to vapor produced only by boiling Thorex.

Unlike the gas holdup in the static region, the gas holdup for boiling Thorex is not only a function of the leacher diameter, but is also a function of the height of liquid in the leacher. This is due in part to the fact that increased height of material in the leacher provides increased heat transfer area for boiling Thorex. The gas holdup is also related to energy input into the boiling Thorex. The heaters on the 13-cm-diameter

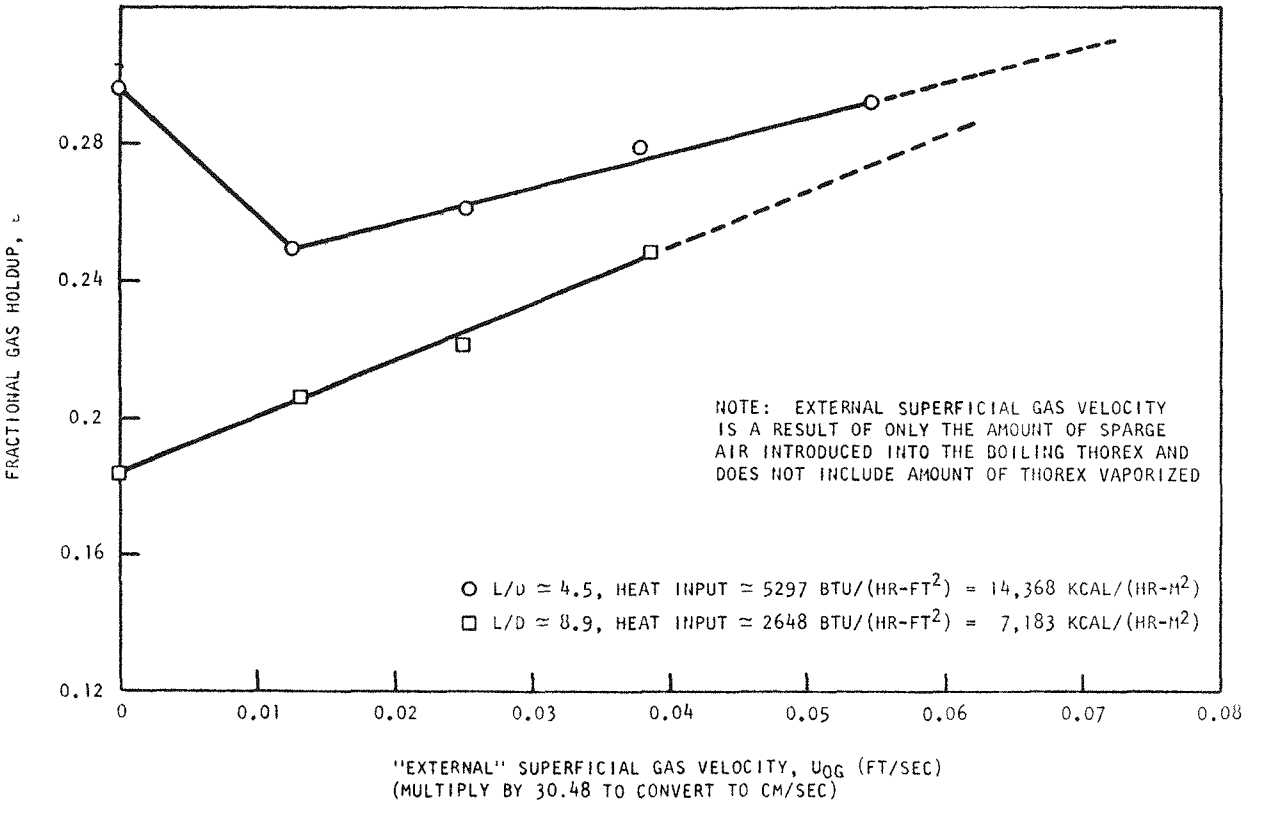

Fig. 5-23. Fractional gas holdup as a function of "external" superficial gas velocity, 13-cm leacher, Thorex at boiling point (~118°C)

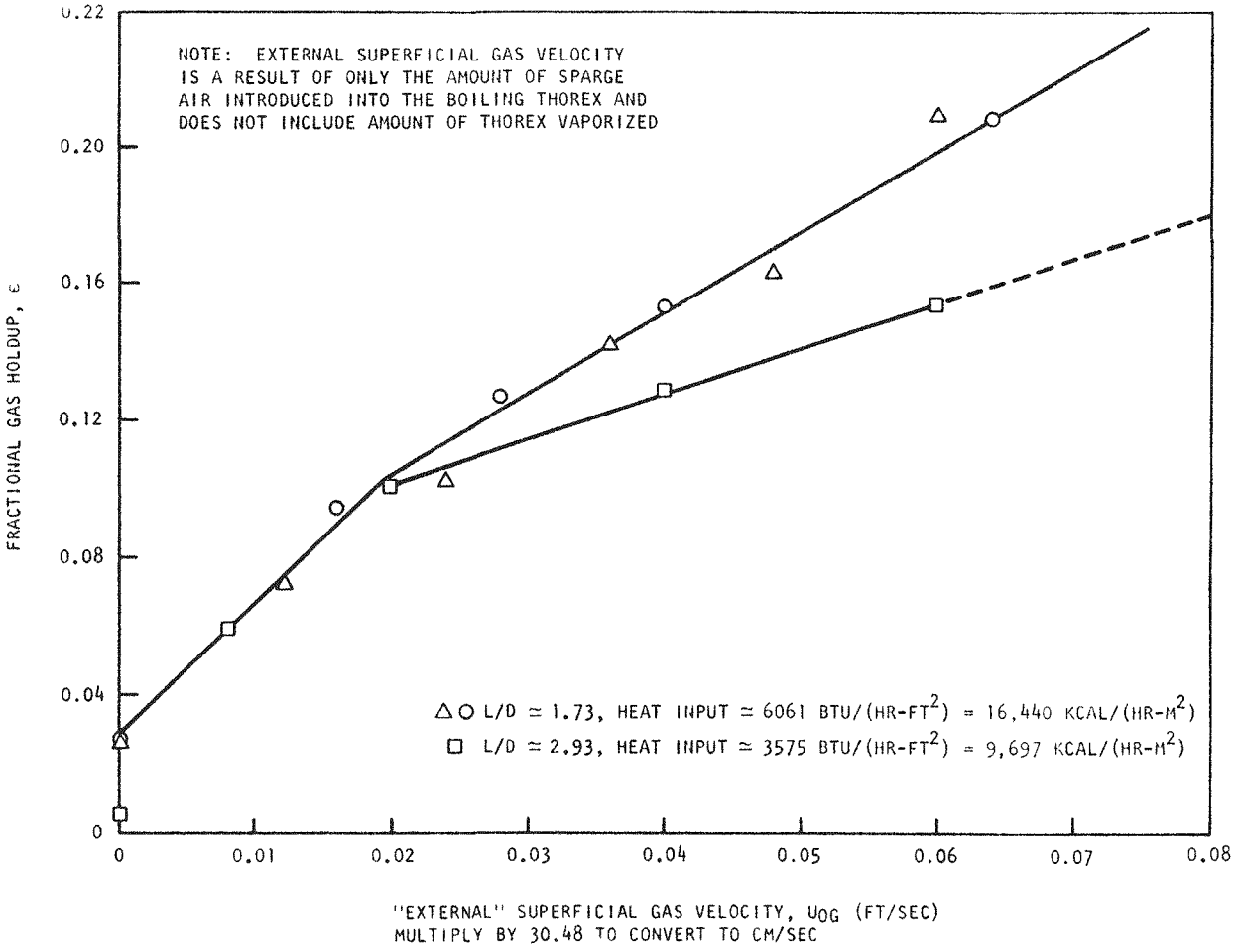

Fig. 5-24. Fractional gas holdup as a function of "external" superficial gas velocity, 20-cm leacher, Thorex at boiling point (∿118°C)

and 20-cm-diameter leachers have a rating of 3268 kcal/hr and 3679 kcal/hr, respectively. These values have been used (assuming no heat loss) to calculate the heat input values shown in Figs. 5-23 and 5-24.

The correlation of the "external" superficial gas velocity with gas holdup presented here has only limited utility. Gas holdup is very much a function of leacher geometry and the method of heat input to the leacher. Thus, the correlation is only valid for the leacher design tested and under the range of variables investigated.

Examination of Fig. 5-23 reveals what at first seems to be a bad data point. Namely, the gas holdup for L/D = 4.5 at zero "external" sparge rate is greater than at any of the sparge rates investigated. However, this phenomenon does not occur for the L/D = 8.9 case. The formation of very small bubbles (and thus high gas holdup) on the leacher walls in the area of the heaters is thought to be the primary cause.

For the case of the small L/D, the solution surface is very close to the point where the bubbles are formed. Thus, as the bubbles rise they do not have time to coalesce and form larger bubbles before they reach the top of the liquid level. When the sparge air was introduced into the boiling Thorex, it provided sites for vaporization of Thorex and formation of larger bubbles. The gas holdup at zero "external" superficial gas velocity was therefore higher than at increased sparge rates.

For an extension of this reasoning, it might be concluded that all bubbles would increase in size with both elevation and sparge rate because of increased coalescence rate. Actually, the size of bubbles in gas-liquid contactors has been found to be almost independent of elevation and sparge rate (Ref. 5-3). The reason bubble size is not a function of elevation is that small bubbles increase in size by coalescence until a size is reached that is unstable in the existing turbulent field. The intensity of the turbulence will depend only on sparge rate so that the turbulence can be the same at all elevations. The fact that bubble size

is not a function of sparge rate can similarly be explained by a balance between bubble breakup and coalescence. For example, the higher sparge rates should result in higher gas holdups and thus higher coalescence rates. However, higher sparge rates also mean higher turbulence, which will result in a higher rate of bubble breakup.

To establish a general correlation for gas holdup in the leachers, it is obviously necessary to determine some measure of "actual" superficial gas velocity under boiling conditions. Thus, overhead condenser reflux rates were measured for different sparge rates. These data are included in Figs. 5-25 and 5-26 for the 13-cm-diameter and 20-cm-diameter leachers, respectively. They provide several interesting observations (not necessarily related to gas holdup):

1. The 13-cm-diameter leacher "floods" (blows excessive liquid overhead) when the sparge rate is $\geq$8 SCFH (3.8 liters/min) while boiling 17.6 kg Thorex.

2. The 20-cm-diameter leacher cools off when the sparge rate is $\geq$20 SCFH (9.4 liters/min) when containing 21.7 kg Thorex.

It was possible to estimate the "actual" superficial gas velocities (resulting from sparge air plus vaporized Thorex) in the leachers by utilizing the reflux rate at zero sparge rate (from Figs. 5-25 and 5-26) and the following assumptions:

1. The specific gravity of reflux is 1.29.

2. The average molecular weight of reflux is 33.

3. The reflux is 38 mole percent HNO_3 and 62 mole percent H_2O (HNO_3-H_2O azeotrope).

4. The ideal gas law can be applied.

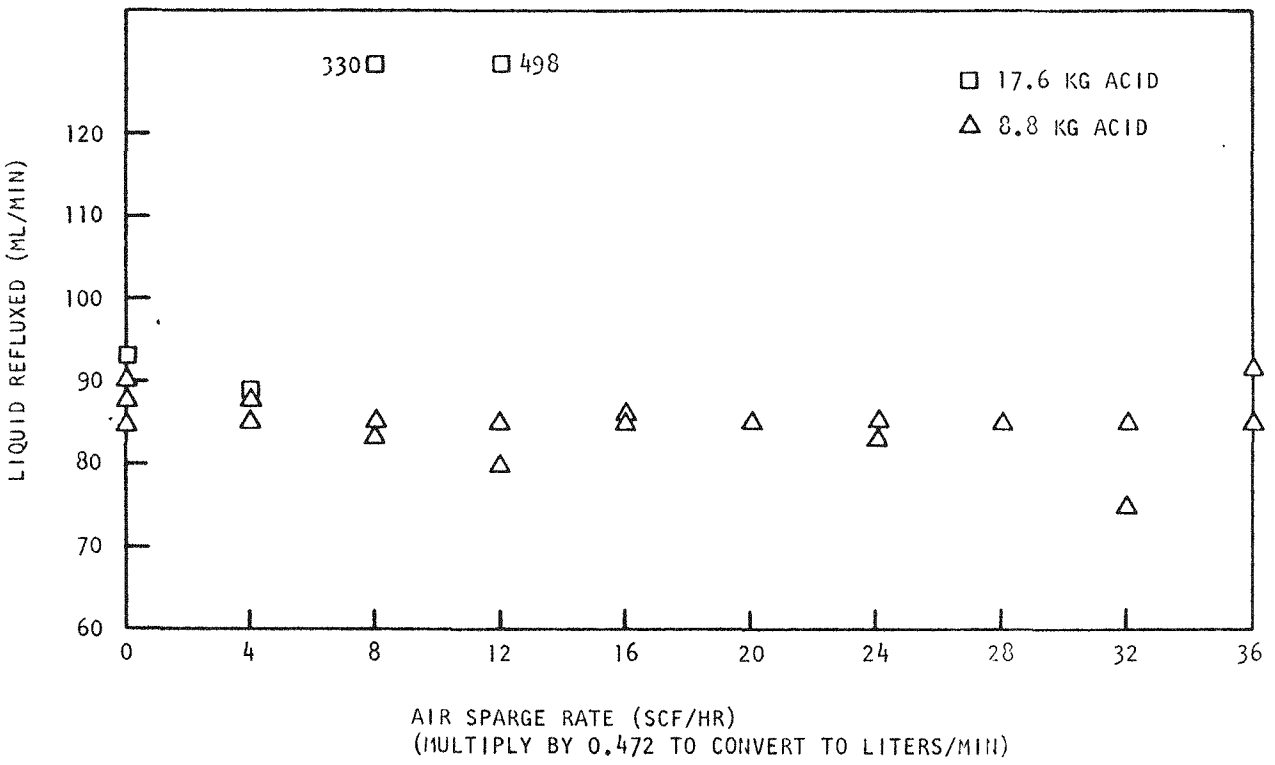

Fig. 5-25. Reflux, 13-cm leacher

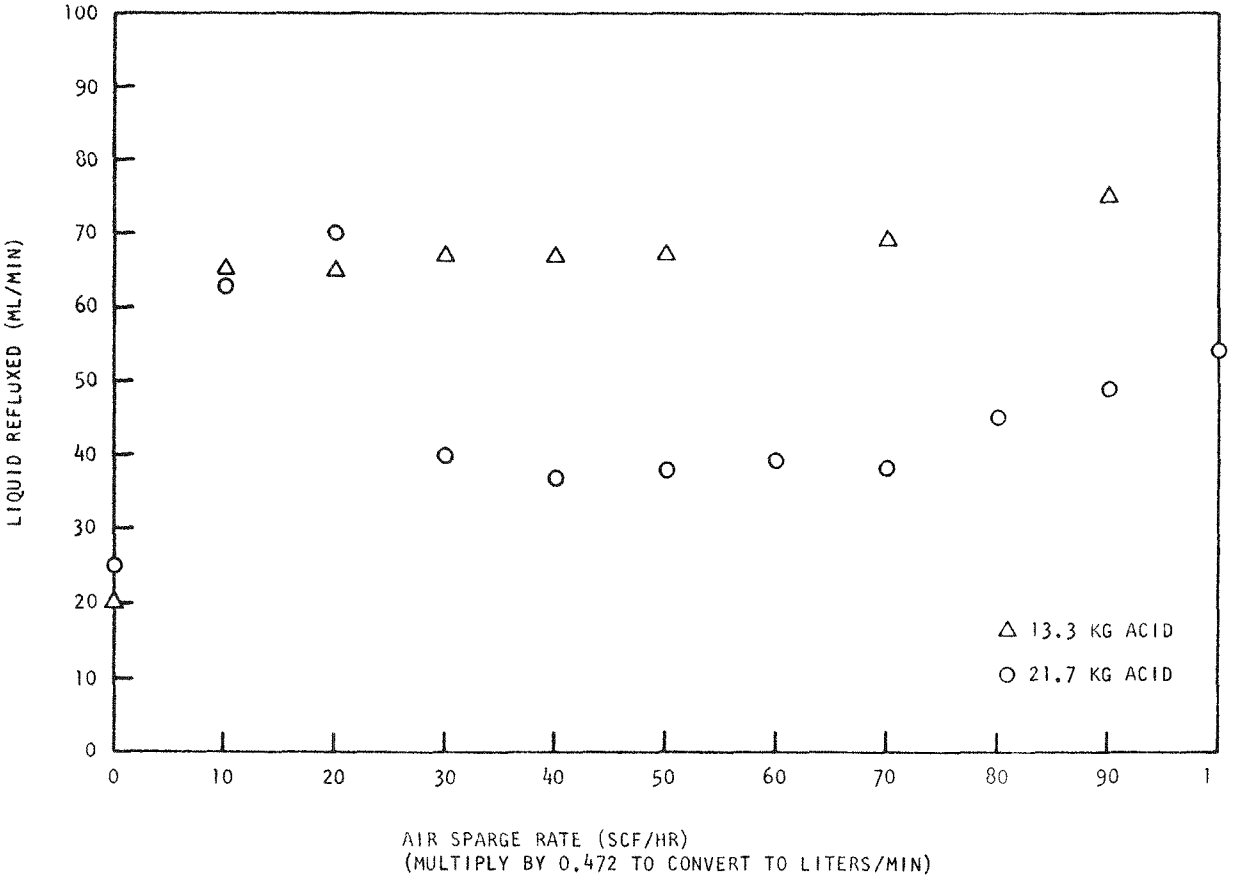

Fig. 5-26. Reflux, 20-cm leacher

The estimated "actual" superficial gas velocity at the boiling point and zero sparge rate was 0.479 ft/sec (14.6 cm/sec) for the 13-cm-diameter leacher and 0.141 ft/sec (4.3 cm/sec) for the 20-cm-diameter leacher. By adding these superficial gas velocities to the "external" gas velocities (result of only sparge air) of Figs. 5-23 and 5-24, it is possible to estimate "actual" superficial gas velocities in the leachers. Replotting the relationship of Figs. 5-25 and 5-26 on this basis results in a correlation (Fig. 5-27) for fractional gas holdup as a function of "actual" superficial gas velocity for the 13-dm-diameter and 20-cm-diameter leachers. Additional data (Ref. 5-4) for the air-water system are also included in Fig. 5-27 and can be seen to be in reasonable agreement with the air-Thorex system.

It is felt that the data of Figs. 5-21 through 5-27 [along with existing data for air-water (Refs. 5-2 through 5-4)] should provide sufficient information on gas holdup in the Thorex system to allow design of commercial-size air-sparged leachers. However, it should be cautioned that these results do not consider foaming, which might occur with irradiated fuels. A separate study should be initiated to establish the foaming tendency of irradiated fuels and its contribution to gas holdup.

Experimental Method Used to Determine Fractional Gas Holdup. An adjustable dip leg utilizing a nitrogen purge system (Fig. 5-28) was used to locate the level (height) of material in the leachers at different sparge rates. This technique suffers from the fact that gas holdup does change with height at the upper solution level. The indication of level is somewhat dependent upon the ability to correctly predict the specific gravity of material in the top of the leacher (and therefore establishing a relation between pressure drop in inches of water and actual height in inches). However, this technique is believed adequate and the better alternate to (1) constructing a separate glass system and using visual determinations, (2) constructing a separate fixed height system and using an overflow technique, or (3) purchasing special instrumentation to be used only for gas holdup determinations.

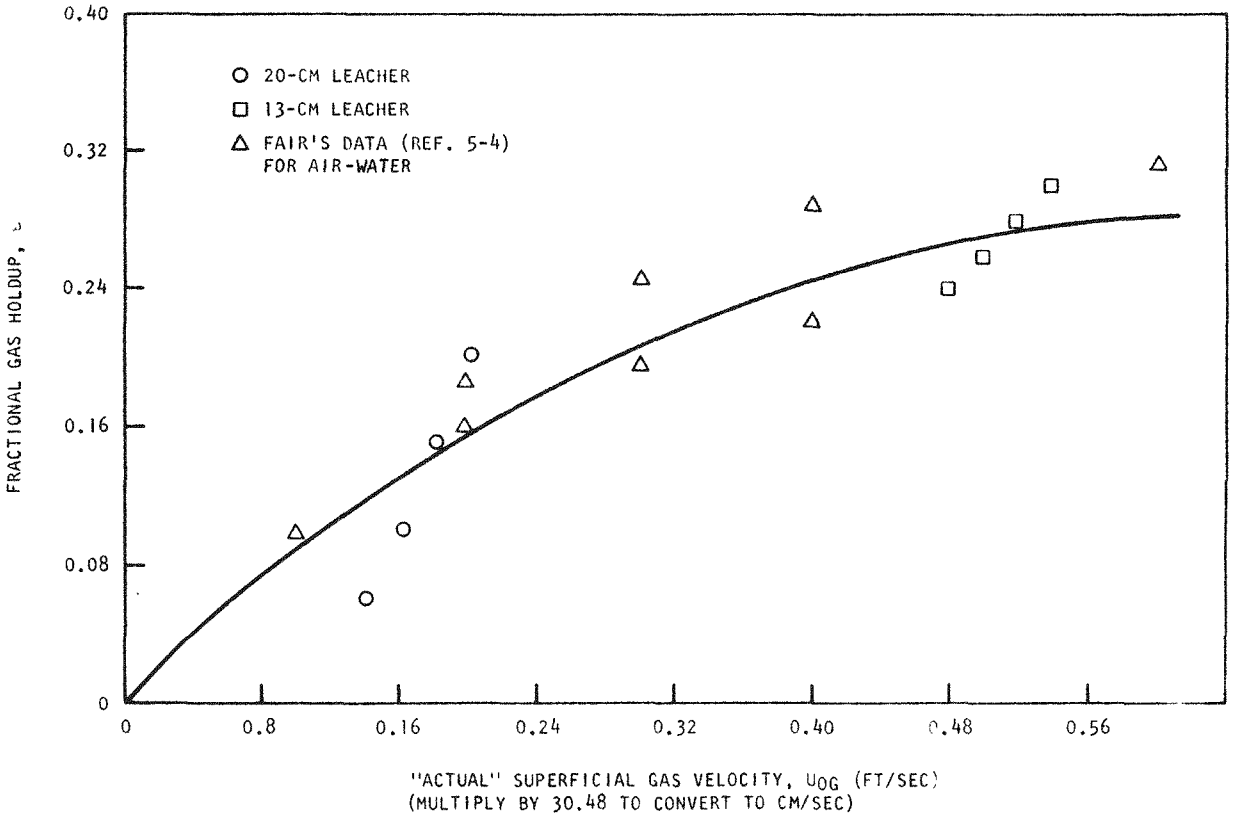

Fig. 5-27. Fractional gas holdup for Thorex as a function of superficial gas velocity

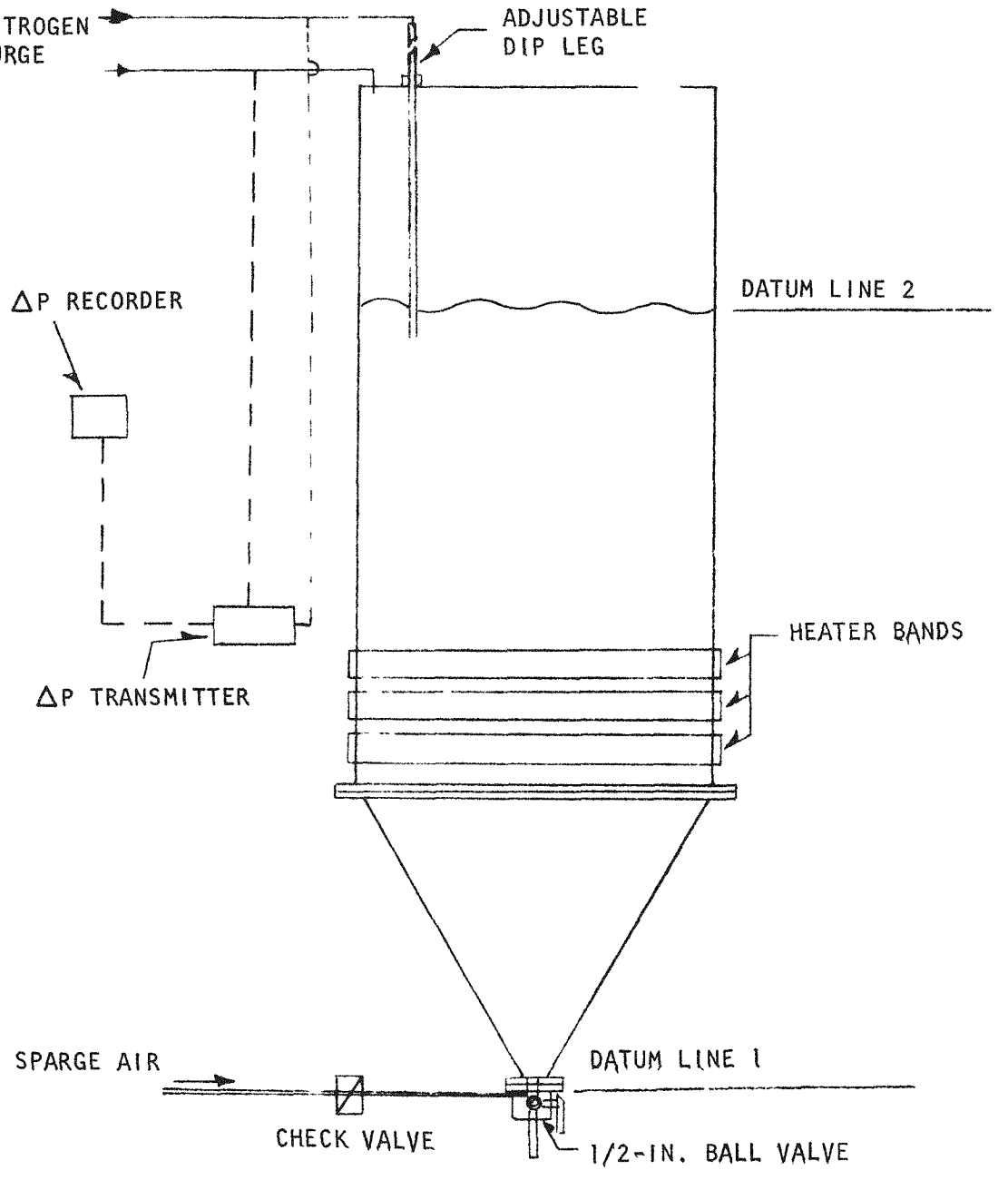

Fig. 5-28. Equipment to determine height of material in leacher at different sparge rates

Air Sparge Rates in the Leachers

Background Information. Air has been widely used for many years in the nuclear industry to agitate the contents of storage tanks and processing vessels (Ref. 5-5). Although low mixing efficiencies are obtained using sparge air, this technique will undoubtably be employed in the future because it requires no moving parts and very little maintenance. However, in spite of the widely accepted use of air spargers, there is very limited quantitative data on the subject in the literature. The data that do exist are of questionable value. For example, from Long's text on nuclear fuel reprocessing (Ref. 5-5):

> "Sparger design involves little science. A pipe almost reaching the bottom of the vessel is capped, and holes are drilled in the cap. A gas rate sufficient to provide 1.3 ft^3 of gas per minute per square foot of tank cross section is recommended."

Recommended for what materials? What system? To accomplish what? It turns out this recommendation is based on an experiment carried out by Kaufman in 1930 (Ref. 5-6) and refers specifically to a tank containing liquid to a 9-ft depth. Kaufman (Ref. 5-6) also states that to obtain the "same degree of agitation" for a 3-ft-deep solution, twice this quantity of air is required. Unfortunately no quantitative measure of "degree of agitation" is offered and the reader is left to assume the appearance of the liquid surface might have been used. Obviously, caution must be used in utilizing existing data.

Leaching is basically a diffusion process, and the leaching rate (and thus efficiency) is a function of the rate of diffusion through the solution layers adjacent to the solid surface. Thus, if sufficient agitation is utilized, the boundary layer can be reduced and ideally the dissolution rate will become primarily a function of exposed solid surface area. It is therefore necessary to determine the sparge air rate necessary to provide "sufficient agitation" for efficient dissolution.

Two separate and different arguments are presented to show that the required leaching sparge rate is a function of the mass of solids contained in the leacher.

Energy Transferred from Air Bubbling Through Leacher. The agitation of solids in the three-phase system (air-acid-burner ash) is accomplished by momentum transfer from the air to the burner ash via the acid medium. Therefore, a look at energy transferred from air bubbling through a leacher should be a good starting point. The work of Lamont (Ref. 5-7) provides the basis of the following argument.

Theoretically, the rise of a volume of air from the bottom to the top of a leacher is equal to the fall of the same volume of slurry from the leacher top to the bottom. Thus, the energy transferred from the air can be equated to the energy converted in the fall from potential to mechanical form.

$$W = M \times H \quad , \tag{7}$$

where $M = 62.4\ sV$ = lb of slurry of volume V

H = height from leacher bottom, ft

s = specific gravity of slurry

If the perfect gas law is assumed and no vapor pressure effects are included, it follows from Eq. (7) that

$$\frac{dW}{dH} = \frac{144\ P_2 V_2 s}{2.31\ P_2 + s\ (L - H)} \quad , \tag{8}$$

where L refers to the total depth in the leacher (depth where air is released into leacher). Subscript 2 refers to the top of the leacher.

This relationship shows the energy transfer per foot of depth at any depth. If this differential energy transfer rate is equated with the degree of agitation, then Eq. (8) can be used for guidance in scaleup between leachers, as follows:

1. For equal agitation at the leacher tops (H = L), the depth of solution in the leacher is not a factor, and the required sparge rates for different leachers would be equal.

$$V_A = V_B \quad , \tag{9}$$

where A and B refer to leachers A and B.

2. For equal agitation at the bottom of the leacher (H = 0), the depth of solution is a factor, and

$$\frac{V_A}{34 + sL_a} = \frac{V_B}{34 + sL_B} \quad , \tag{10}$$

indicating a deep tank requires more sparge air than a shallower tank.

If the primary function of the sparge air is to suspend solids, then the bottom conditions are the most important. Thus, the relationship given in Eq. (10) should form a basis for scaleup of required sparge rate for the leachers.

Energy Balance Around Leacher. Based on a similar presentation by Madonna and Lama (Ref. 5-8), an energy balance around the leacher using the datum lines given in Fig. 5-28 would be as follows (symbols defined under Nomenclature at end of section):

$$\frac{g}{g_c} H_1 + \frac{u_1^2}{2g_c} + \frac{P_1}{\rho_1} + E_1 + (Q - W) = \frac{g}{g_c} H_2 + \frac{u_2^2}{2g_c} + \frac{P_2}{\rho_2} + E_2 \quad . \qquad (11)$$

Since there is no work given to or taken from (or no heat lost or gained by) the system between point 1 and point 2, and the internal energy of the system is constant,

$$W = Q + E = 0 \, . \qquad (12)$$

It can also be assumed that:

1. There is no density change between points 1 and 2.

$$\rho_1 = \rho_2 = \rho_f$$

2. The average velocity at point 2 is negligible compared with the average velocity at point 1.

On the basis of these conditions and assumptions, Eq. (11) reduces to

$$\frac{u_1^2}{2g_c} = \frac{g}{g_c} H_2 + \frac{\Delta P}{\rho_f} \quad . \qquad (13)$$

Or, since $H_2 = L$, Eq. (13) can be arranged as follows:

$$u_1 = \sqrt{2gL + \frac{2g_c \, \Delta P}{\rho_f}} \quad . \qquad (14)$$

But, $\Delta P = L(1 - \gamma)(\rho_s - \rho_f)$, or the weight of bed per unit area (Ref. 5-9). Thus Eq. (14) takes the form:

$$u_1 = \sqrt{2gL + 2g_c\, L(1 - \gamma)\, \frac{(\rho_s - \rho_f)}{\rho_f}} \quad . \tag{15}$$

In terms of superficial velocity through the leacher,

$$u_c = u_1 \left(\frac{D_c}{D_1}\right)^2 \sqrt{2g_c L + 2g_c L(1 - \gamma)\, \frac{(\rho_s - \rho_f)}{\rho_f}} \quad . \tag{16}$$

Note that this relationship is not rigorous for the case of a three-phase system. However, it is felt indicative of the fact that the sparge rate is not only a function of leacher dimensions, and liquid and solid properties, but also a function of the amount of solids contained in the leacher.

The fluidization studies of Mathur and Gishler (Ref. 5-10) resulted in an empirical equation developed from experimental data that is very similar in form to Eq. (16), namely,

$$u_c = \left(\frac{D_p}{D_c}\right)\left(\frac{D_1}{D_c}\right)^{1/3} \sqrt{2gL\, \frac{(\rho_s - \rho_f)}{\rho_f}} \quad . \tag{17}$$

Also, Ghosh (Ref. 5-11) presented a theoretical analysis of spouted beds resulting in the following equation:

$$u_c = \sqrt{\left(\frac{2kn}{3}\right)}\left(\frac{D_p}{D_1}\right)\left(\frac{D_1}{D_c}\right)^2 \sqrt{2gL\, \frac{(\rho_s - \rho_f)}{\rho_f}} \tag{18}$$

Therefore, experimental testing was carried out in an attempt to establish an analogy between the operation of a two-phase spouted bed and the leachers.

Determination of "Spouting" Velocities for Air-Sparged Leachers. A series of tests was conducted to try and establish a "spouting" velocity utilizing the fluidization equations (17) and (18) and experimental data on the leachers. All tests were conducted with 4.4 kg Thorex*/kg burner ash. This ratio was selected to correspond to a final solution concentration of about 1M thorium. The burner ash resulted from combustion of crushed TRISO ThC_2 particles in the 10-cm-diameter secondary burner. The size distribution for the burner ash is shown in Fig. 5-17. (This same burner ash was utilized as feed for leaching runs 49 through 57.) In Eqs. (17) and (18), u_c corresponds to what is defined as the minimum spouting velocity. Unlike the minimum fluidization velocity, the minimum spouting velocity, as seen from Eq. (17) or (18), decreases with decreasing bed height and with increasing column diameter; in addition, the size of the air inlet has an effect.

The existence of a spouting bed is suggested by the characteristic pressure drop versus air flow curve shown in Fig. 5-29. The following discussion of this characteristic curve is taken almost verbatim from Leva (Ref. 5-13).

For low air velocities, the system may behave as a fixed bed. This is indicated by the linearity of branch ab of Fig. 5-29. If the air velocity is increased beyond point b, the solids at the base of the cone are lifted and a short internal channel, or spout, is formed. Since the solids concentration in the short spout is lower than in the near vicinity surrounding the short spout, a decrease in pressure drop must accompany an air mass-velocity increase beyond point b. With further increases in air velocity, the height of the spout increases and the pressure drop decreases further to a point c. Due to substantial displacement of solids from the central channel, an appreciable rise in bed level may have occurred. Thus, a further increase in sparge rate, say to point d, will result in little or no increase in pressure drop. Up to this point the

---

*13M HNO_3/0.05M HF/0.1M $Al(NO_3)_3$.

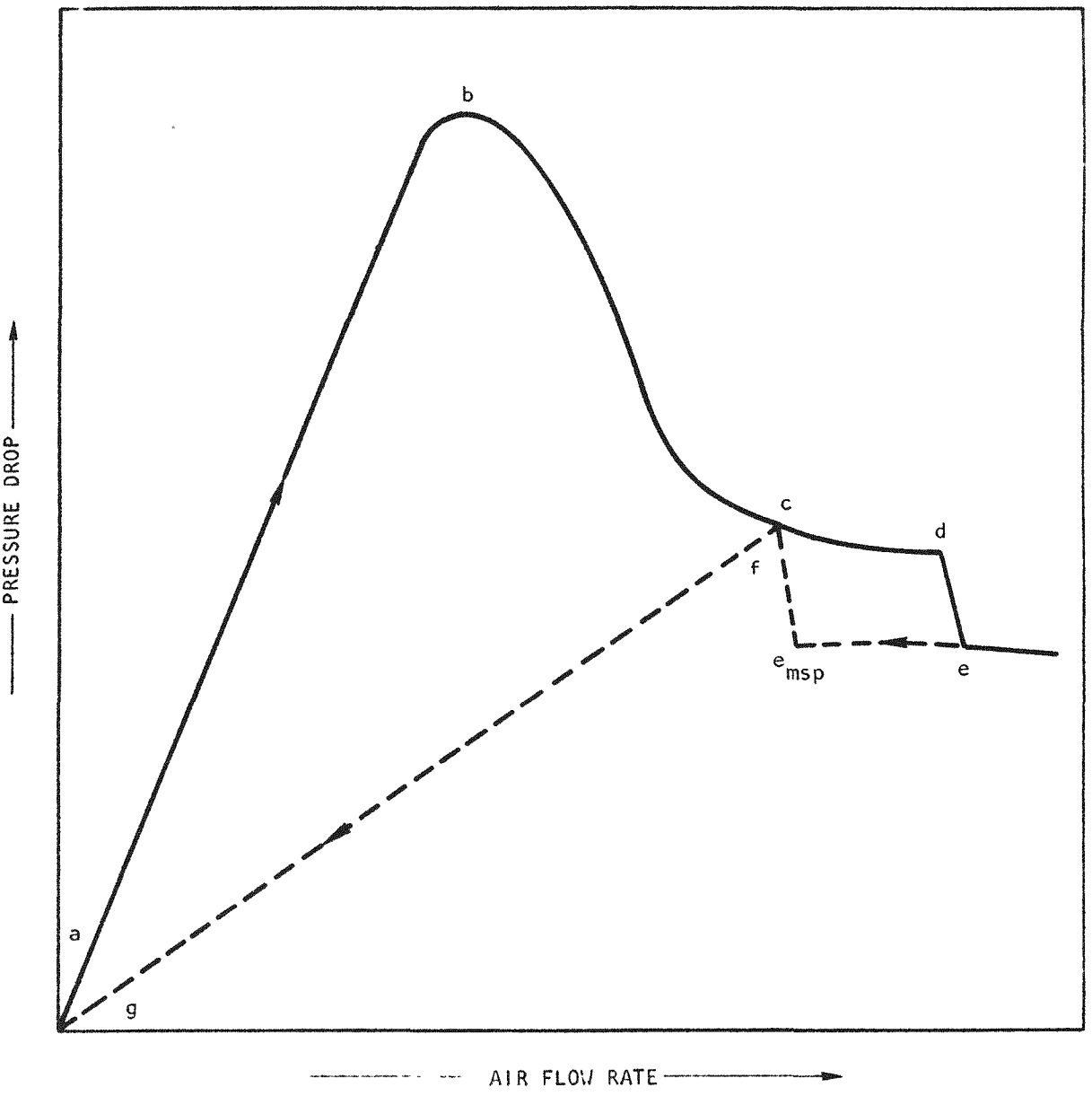

Fig. 5-29. Pressure drop versus air flow rate

spout is still confined to the inside of the bed; i.e., the spout has not penetrated through the upper-bed boundary. A further increase in sparge rate, to point e, causes the spout to break through the bed. The solids concentration in the spout decreases abruptly and a further pressure drop reduction is noted. At point e, the bed is spouting in a steady state. Beyond point e the pressure drop remains almost independent of sparge rate.

If the sparge rate is reduced, the bed will remain in a spouting condition until point e_{msp} is reached. This corresponds to the point of minimum spouting velocity u_c calculated by Eq. (17) or (18).

If the sparge rate is reduced further, the spout will collapse. Thus, at point f the spout has virtually entirely collapsed. The linear pressure drop relationship of segment fg is characteristic of a fixed bed. The hysteresis loop d-e-e_{msp}-f is due to the fact that certain energy is required to overcome the normal compaction of the bed.

For additional information on spouted beds, the presentation of Mathur (Ref. 5-14) is recommended.

Air-Thorex-Burner Ash System. Based on the above information for the gas-solid system as a background, tests were performed to try and establish whether or not spouting occurs in the leachers. Pressure drop measurements were obtained for the air-Thorex-burner ash system using the equipment depicted in Fig. 5-30.

Due to the highly reactive nature of the burner ash in boiling Thorex, and the difficulties of measuring pressure drop resulting from a spout formation in boiling Thorex, it was decided that the initial experimentation should be performed with Thorex at ambient temperature (~30°C). It was reasoned that if a sparge rate (denoted by formation of a spout) could be found at a temperature of about 30°C, this same sparge rate would provide sufficient agitation at the boiling point.

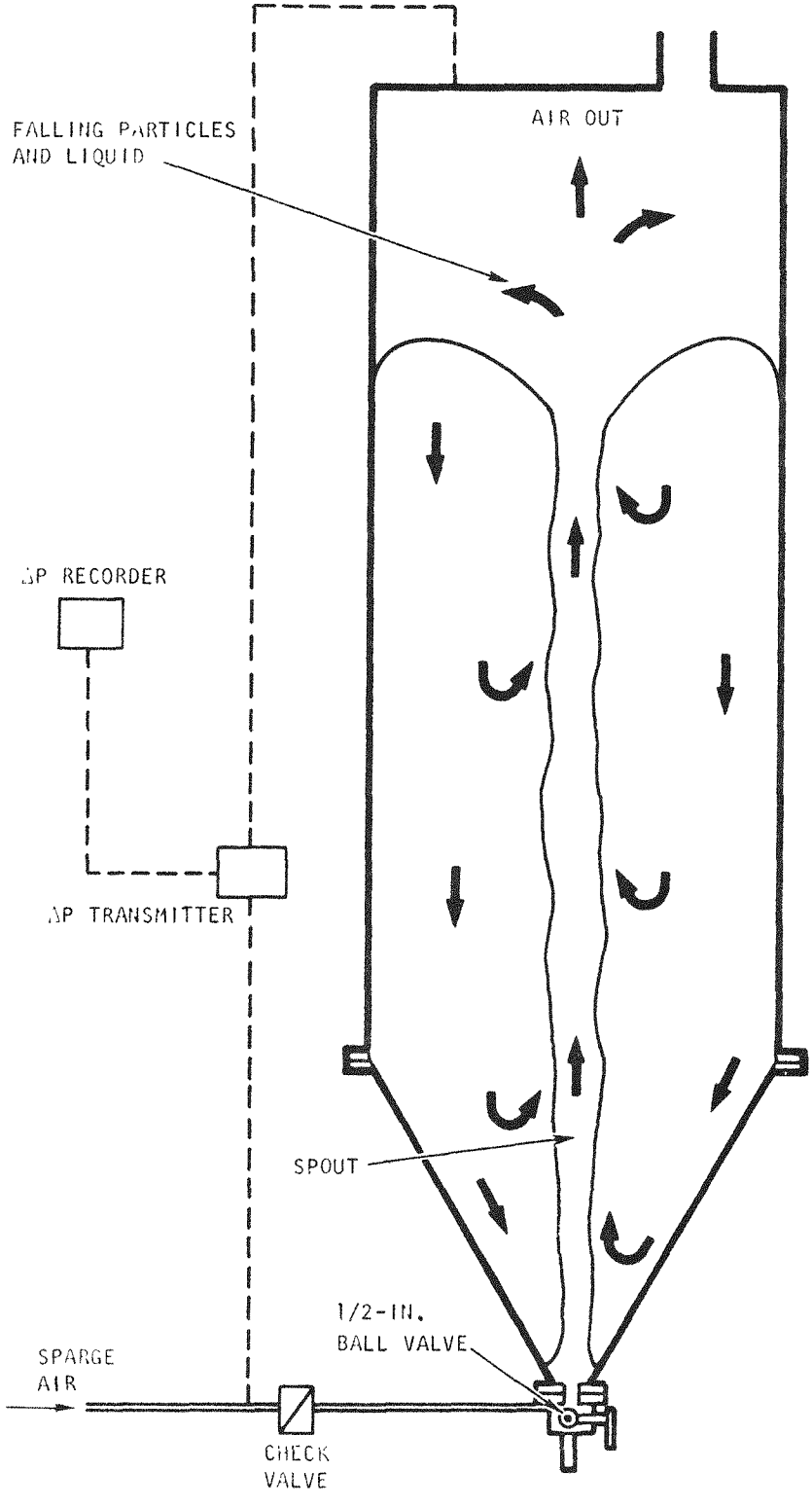

Fig. 5-30. Equipment for obtaining pressure drop measurements for the air-Thorex-burner ash system

Pressure drop versus sparge rate data of ~~Figs. 5-31 and 5-32~~ were obtained for the 13-cm-diameter leacher (Figs. 5-31 and 5-32) and for the 20-cm-diameter leacher (Figs. 5-33 and 5-34). These data were obtained immediately following addition of burner ash to the leachers and preceding the time the heaters were turned on.

Examination of Figs. 5-31 through 5-34 does not reveal any hysteresis loop as shown in Fig. 5-29. Possibly for the three-phase system this effect is very small. In any case, the other characteristics of Fig. 5-29 are present. It is, therefore, not certain whether the fairly large reduction in pressure drop indicates the formation of a spout or simply the point at which the solids are well mixed. (An indication of either of these points should be of value.)

The use of Eq. (18) depends on experimental evaluation of the group $\sqrt{2kn/3}$, while Eq. (17) depends on experimental evaluation of the exponent of (D_l/D_c). Equation (18) has been arbitrarily chosen to evaluate the data of Figs. 5-31 through 5-34.

Based on the data from Fig. 5-31, it is suggested that a "spout" is formed at a sparge rate of about 14 SCFH (u_c = 0.0294 ft/sec).

By assuming

D_p = 66 μm (50 wt % point from Fig. 5-17)
D_c = 5 in. (12.7 cm)
D_l = 0.5 in. (1.27 cm)
ρ_s = 9 g/cm^3
ρ_f = 1.3 g/cm^3

$$L = (\text{kg burner ash charged to leacher})\left(\frac{4.4 \text{ kg Thorex}}{\text{kg burner ash}}\right) \text{ times}$$

$$\left(\frac{1 \text{ liter}}{1.38 \text{ kg Thorex}}\right)\left(\frac{1 \text{ in.}}{(0.333 \text{ liter})^*}\right)\left(\frac{1 \text{ ft}}{12 \text{ in}}\right)$$

*0.82 for 20-cm-leacher

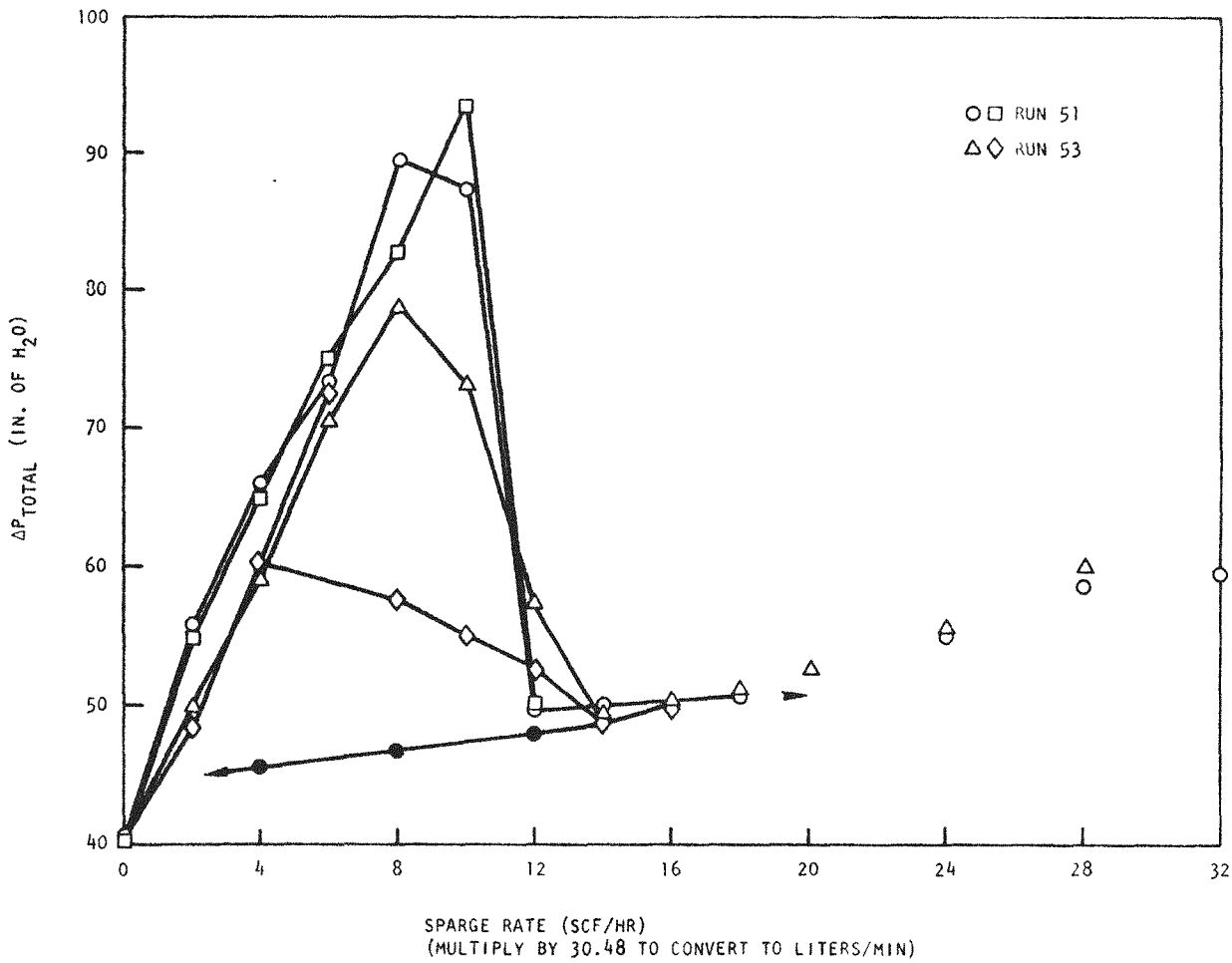

Fig. 5-31. Pressure drop versus sparge rate, 13-cm leacher, 2 kg burner ash, T = 30°C

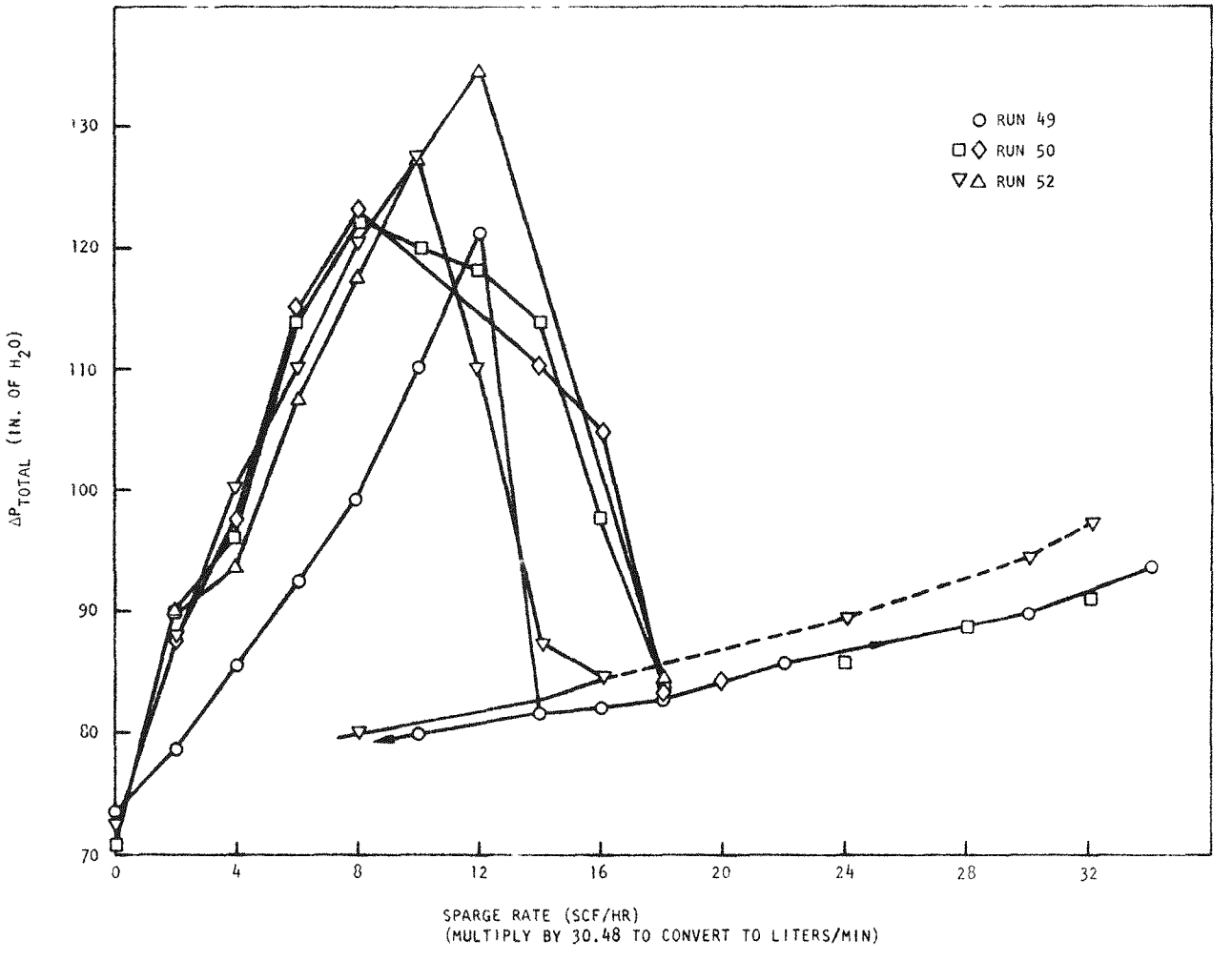

Fig. 5-32. Pressure drop versus sparge rate, 13-cm leacher, 4 kg burner ash, T = 30°C

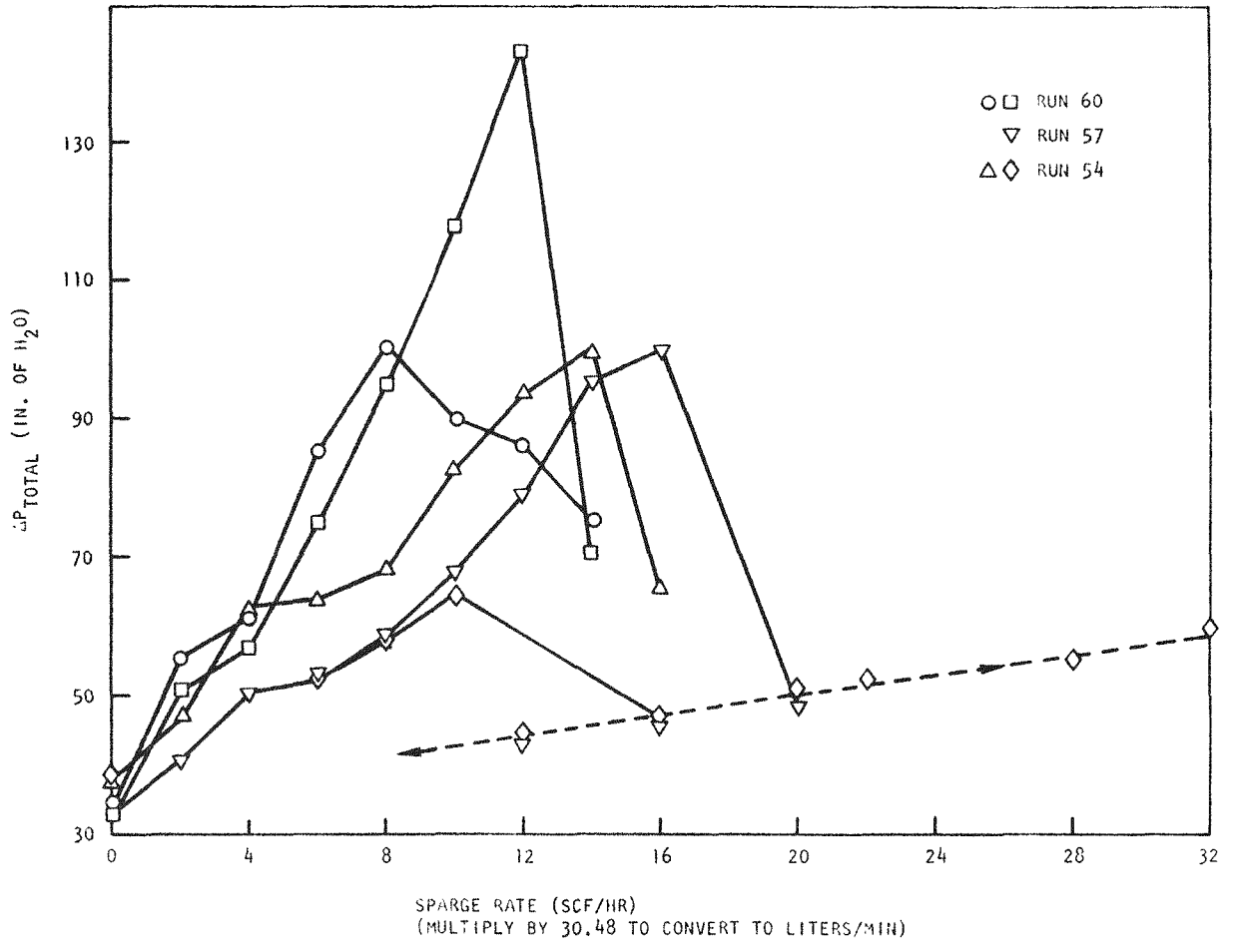

Fig. 5-33. Pressure drop versus sparge rate, 20-cm leacher, 4 kg burner ash, T = 30°C

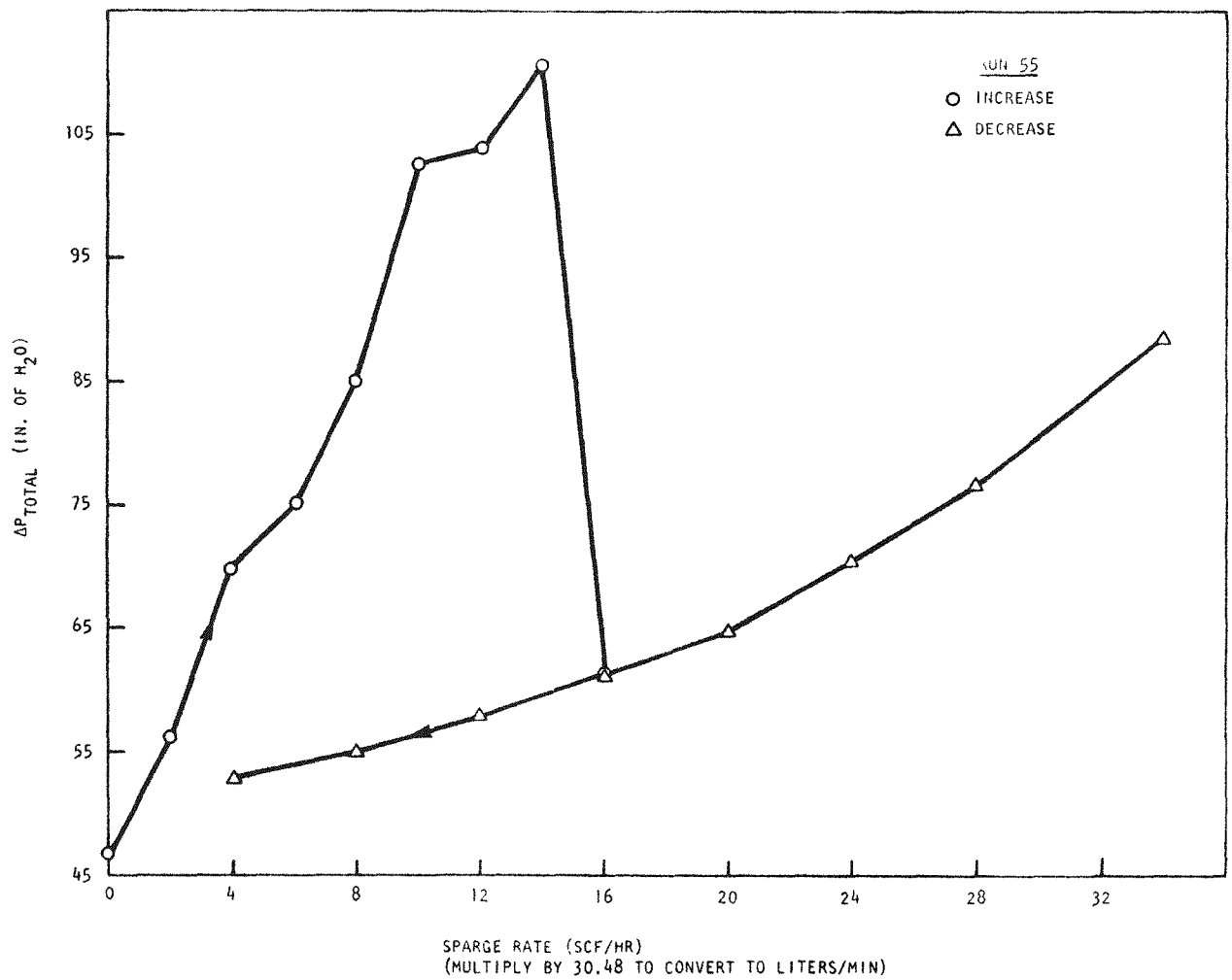

Fig. 5-34. Pressure drop versus sparge rate, 20-cm leacher, 6 kg burner ash, T = 30°C

and using Eq. (18), it can be found that

$$\sqrt{\frac{2kn}{3}} = 38.17 \quad . \tag{19}$$

Using this derived constant and Eq. (18), it was calculated that the minimum "spouting" velocity or sparge rate corresponding to the conditions of Figs. 5-32 through 5-34 would be as shown in Table 5-14.

TABLE 5-14
MINIMUM SPOUTING VELOCITY OR SPARGE RATE
CALCULATED FROM EQ. (18) USING EQ. (19)

	u_c (ft/sec)	Sparge Rate (SCFH)
Case depicted in Fig. 5-32	0.0415	19.8
Case depicted in Fig. 5-33	0.0103	13.0
Case depicted in Fig. 5-34	0.0126	15.8

Examination of Figs. 5-32 through 5-34 indicates that these calculated values correspond very closely to observed values.

It therefore appears that Eqs. (18) and (19) adequately describe the observed data. Using Eq. (19) and the assumptions included above, Eq. (18) takes the form:

$$u_c = 38.173\ (31.3117 \times 10^{-4}) \left(\frac{0.5}{D_c}\right)^2 (19.47)\sqrt{L} \quad . \tag{20}$$

Or,

$$u_c = \frac{0.5818\sqrt{L}}{D_c^2} \quad . \tag{21}$$

But,

$$u_c = \text{sparge rate in SCFH} \times \frac{4}{3600\pi \left(\frac{D_c}{12}\right)^2} \tag{22}$$

$$= \text{sparge rate in SCFH} \times \frac{(0.050929)}{D_c^2} \, . \tag{23}$$

Therefore, equating Eqs. (21) and (23),

$$\text{sparge rate in SCFH} = 11.426\sqrt{L} \quad . \tag{24}$$

But,

$$L \simeq \frac{\text{kg burner ash} \times 4.4}{1.38 \times 0.0129\ D_c^2 \times 12} = \frac{20.6 \times \text{kg burner ash}}{D_c^2} \quad . \tag{25}$$

Therefore,

$$\text{minimum sparge rate in SCFH} \simeq \frac{51.86\ \sqrt{\text{kg burner ash}}}{D_c} \, . \tag{26}$$

Results calculated from Eq. (26) are plotted in Fig. 5-35. It is felt that these results are valid for the system under study (assumption stated above), and these predicted sparge rates for the leachers could be used to establish an upper realistic sparge rate for commercial-size leachers.

Experimental Leaching Runs

Secondary burner ash from crushed TRISO ThC_2 particles was processed through the leaching system in leaching runs 49 through 57, 60, 61, and

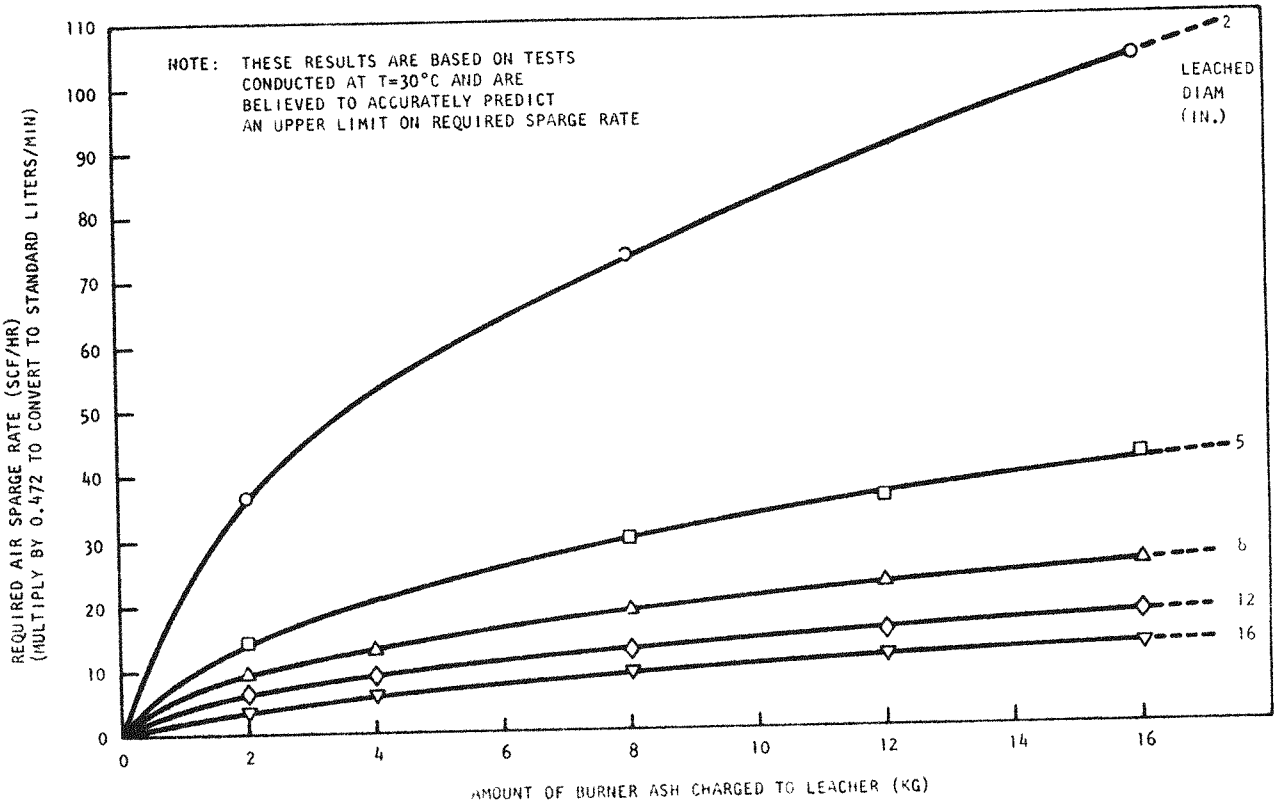

Fig. 5-35. Sparge rate as calculated from Eq. 26

63 through 66. Results of this work are given here. Additional leaching runs 58, 59, and 62 were carried out using BISO sol-gel ThO_2 from ORNL. The results of these runs will be reported in the next Quarterly Progress Report.

The primary objective of these runs was to determine the effect of sparge air rate on leaching efficiency. Based on these tests, it was established that sparge air is not required for efficient dissolution of burned-back crushed TRISO ThC_2 particles (see Figs. 5-36 and 5-37).

This and other results are discussed in more detail in the section under "Conclusions and Recommendations."

Summary of Leach Runs. Nine test runs were conducted on the 13-cm-diameter leacher, and six test runs were conducted on the 20-cm-diameter leacher. All tests were made utilizing secondary burner product, resulting from burning crushed TRISO ThC_2 particles. The burner product from six burner runs (F4-RHB-M3-14, -15, -20, -21, -22, and -23) was mixed to form a 72-kg composite. The burner ash charged to the leacher contained 0 wt % burnable carbon. The size distribution of the burner ash is given in Fig. 5-17. All test runs were conducted with approximately 3.2 liters of Thorex [13M HNO_3/0.05M HF/0.1M $Al(NO_3)_3$] per kg of burner ash. Operating data for the 13-cm-diameter and 20-cm-diameter leachers are given in Tables 5-15 and 5-16, respectively.

The steam-jet ejector system was not used for transfer of liquids because of inadequate steam supply system (see previous Quarterly Progress Report Gulf-GA-A12599). All liquid transfers were accomplished with a peristaltic pump.

The liquid-solid separation of leacher product was accomplished with a batch-basket centrifuge. Centrifuge operating data for all runs are as follows:

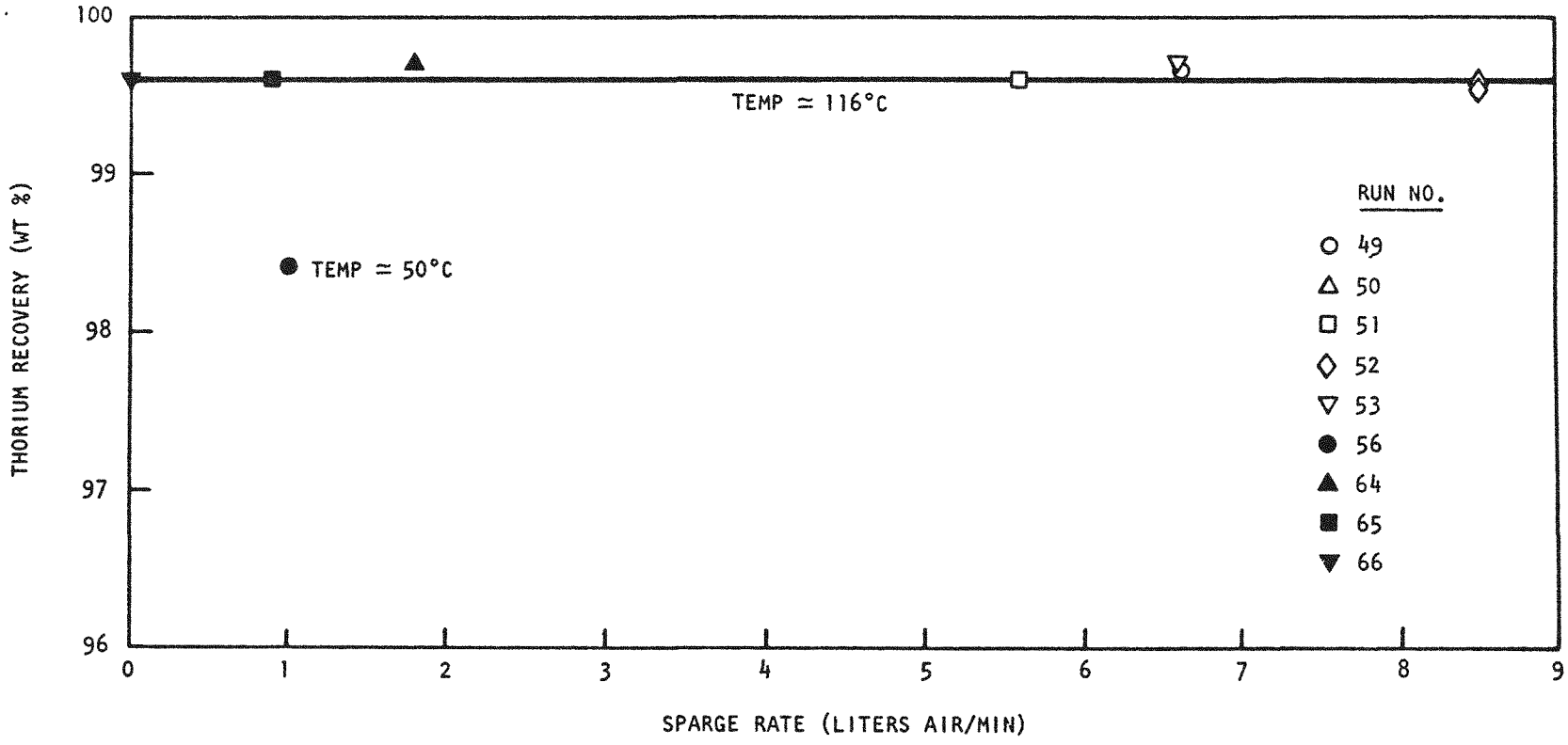

Fig. 5-36. Thorium recovery versus sparge rate for 13-cm-diameter leacher

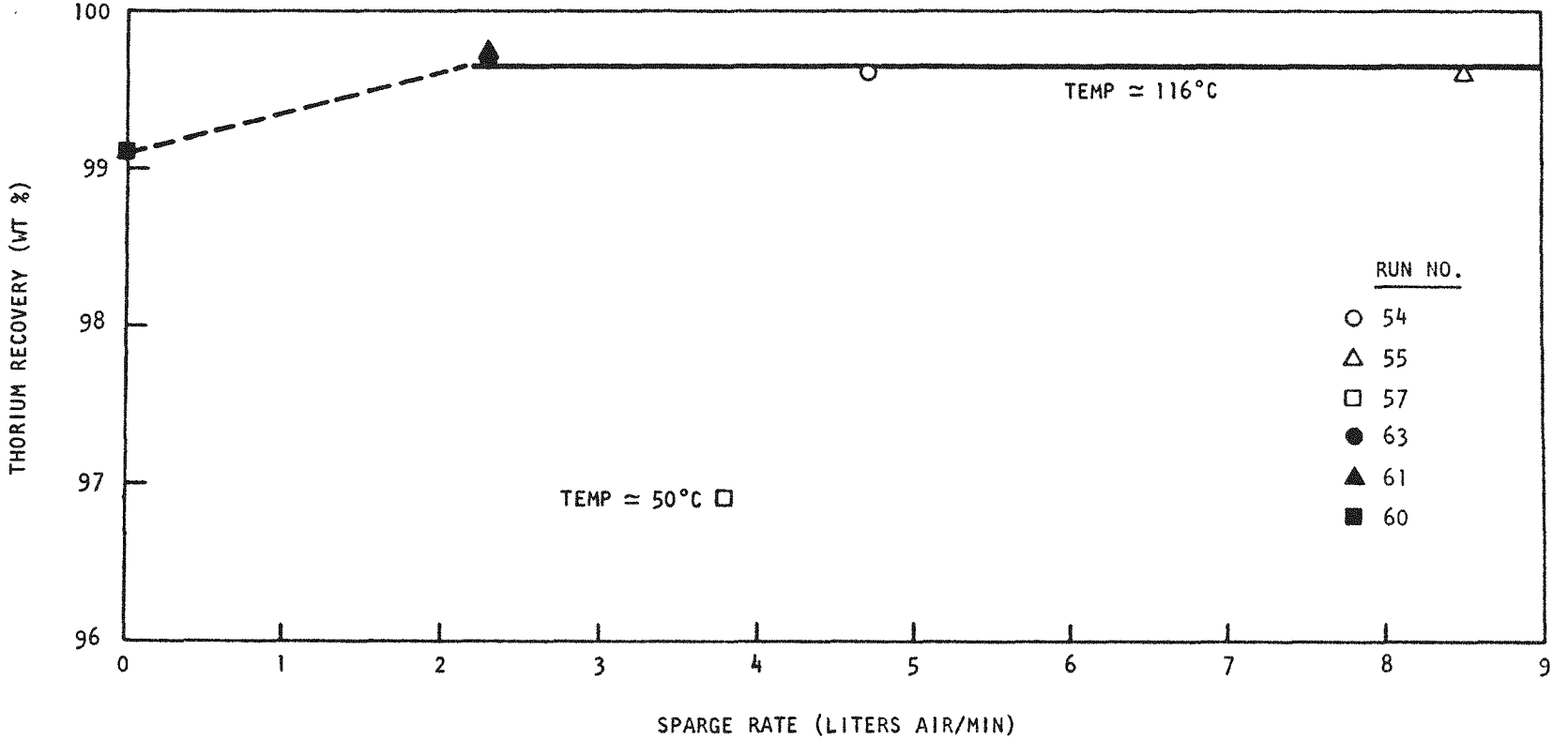

Fig. 5-37. Thorium recovery versus sparge rate for 20-cm-diameter leacher

TABLE 5-15
13-CM LEACHER OPERATING DATA

	Leach Run No.								
	49	50	51	52	53	56	64	65	66
Burner ash charged, kg	4	4	2	4	2	4	4	4	4
Thorex charged, liters	12.75	13.08	6.40	12.72	6.22	12.59	12.73	12.40	12.75
Air sparge rate, liters/min	6.6	8.5	5.6	8.5	6.6	0.9	1.8	0.9	0
Leaching time, hours	1	1	1	1	1.25	2.50	1	1	1
Average leaching temp, °C	116	116	115	116	119	50	116	116	116
Insolubles after leach (dry wt), g	700	727	429	810	408	871	675	682	867
Mother liquor, liters[(a)]	14.0	13.0	6.93	13.25	6.92	13.83	14.0	13.6	15.49

[(a)] Includes some wash water.

TABLE 5-16
20-CM LEACHER OPERATING DATA

	Leach Run No.					
	54	55	57	60	61	63
Burner ash charged, kg	4	6	4	4	4	4
Thorex charged, liters	11.59	18.38	12.75	11.91	12.75	11.38
Air sparge rate, liters/min	4.7	8.5	3.8	0	2.3	2.3
Leaching time, hours	1	1	4	1.75	1.1	1
Average leaching temp, °C	118	118	50	119	118	118
Insolubles after leach (dry wt), g	697	1159	840	945	561	692
Mother liquor, liters[a]	13.41	24.18	14.67	14.64	14.21	14.50

[a] Includes some wash water.

1. 30-cm-diameter perforate basket.
2. Polypropylene filter bag (5 to 6 μm openings).
3. 682 purging force at basket sheet (2000 rpm).
4. After washing filter cake, spin dry for about 5 min.

The weight of insolubles included in Tables 5-15 and 5-16 was calculated based on the following relationship:

$$\begin{aligned}\text{Weight of dry insolubles} &= [(\text{weight of damp insolubles + bag}) \\ &\quad - (\text{estimated weight of damp bag})] \\ &\quad \text{times (estimated fraction of damp} \\ &\quad \text{insolubles that are dry insolubles)} \\ &= [(\text{weight of damp insolubles + bag}) \\ &\quad - (120\ \text{g})] \times 0.9.\end{aligned}$$

Since the same centrifuge operating conditions and filter bag were used for all runs, this relationship is believed accurate. The quantity and specific gravity of liquids in all storage tanks and leaching vessels were continuously and automatically monitored and recorded. Tank calibration relations are included in Table 5-17. Analyses of samples submitted to the Analytical Chemistry Department are given in Table 5-18 (13-cm leacher) and Table 5-19 (20-cm leacher). These data were utilized in material balance calculations (see Tables 5-20 and 5-21 for 13-cm-diameter and 20-cm diameter leachers, respectively).

Conclusions and Recommendations

1. Greater than 99 wt % thorium recovery is obtained without sparge air and only 1-hr dissolution time. These results are valid for the burner ash under study for both the 13-cm-diameter and 20-cm-diameter leachers (see Figs. 5-35 and 5-36, respectively). It is felt that the action of the boiler solution provides sufficient agitation to leacher contents for efficient dissolution of this type burner ash.

TABLE 5-17
WEIGHT FACTOR AND SPECIFIC GRAVITY
CALIBRATIONS FOR VESSELS

Vessel	Weight Factor[(a)] kg	Specific Gravity
Thorex	0.56084X - 0.2503	0.2x 10.406
20-cm leacher	0.48822X + 3.20925	0.2x 5.22
13-cm leacher	0.29283X + 1.80287	0.2x 5.174
Mother liquor tank	0.73555X + 0.55201	0.2x 10.15

[(a)] These calibrations were obtained with water using "least-squares" regression techniques, where

X is percent reading on weight factor leg (red pen on recorder)

x is percent reading on specific gravity leg (green pen on recorder)

TABLE 5-18
13-CM LEACHER SAMPLE ANALYSIS RESULTS[a]

	Leach Run No.								
	49	50	51	52	53	56	64	65	66
Burner ash, wt % Th	71.3	71.3	71.3	71.3	71.3	71.3	71.3	71.3	71.3
Insolubles, wt % Th	1.36	1.55	1.36	1.62	1.16	6.01	1.24	1.70	1.44
Mother liquor,[b] g Th/liter	207	220	204	217	207	209	203	211	188

[a] Based on gravimetric determination by oxalate precipitation.

[b] Includes some wash water.

TABLE 5-19
20-CM LEACHER SAMPLE ANALYSIS RESULTS[a]

	Leach Run No.					
	54	55	57	60	61	63
Burner ash, wt % Th	71.3	71.3	71.3	71.3	71.3	71.3
Insolubles, wt % Th	0.016	0.016	0.12	0.25	1.4	1.2
Mother liquor,[b] g Th/liter	213	178	193	182	202	197

[a] Based on gravimetric determination by oxalate precipitation.

[b] Includes some wash water.

TABLE 5-20
13-CM LEACHER, THORIUM MATERIAL BALANCE RESULTS

	Leach Run No.								
	49	50	51	52	53	56	64	65	66
Thorium input, g									
Burner ash	2852	2852	1426	2852	1426	2852	2852	2852	2852
Thorium output, g									
Mother liquor[(a)]	2898	2853	1412	2875	1435	2889	2841	2867	2907
Insolubles	10	11	6	13	5	4.7	8	11	12
Total output	2908	2871	1417	2888	1440	2936	2849	2878	2919
Material balance closure,[(b)] wt %	102	100.4	99.4	101	101	103	99.9	100.9	102.4
Thorium recovery,[(c)] wt %	99.66	99.37	99.6	99.54	99.67	98.39	99.7	99.6	99.6

[(a)] Includes some wash water.

[(b)] Output/input.

[(c)] Based on outlet quantities.

TABLE 5-21
20-CM LEACHER, THORIUM MATERIAL BALANCE RESULTS

	Leach Run No.					
	54	55	57	60	61	63
Thorium input, g						
Burner ash	2852	4278	2852	2852	2852	2852
Thorium output, g						
Mother liquor[a]	2858	4296	2833	2783	2867	2852
Insolubles	11	16	91	23	8	8
Total output	2869	4313	2923	2806	2875	2860
Material balance closure,[b] wt %	100.6	100.8	102.5	98.4	100.82	100.30
Thorium recovery,[c] wt%	99.6	99.6	96.9	99.18	99.7	99.7

[a] Includes some wash water.

[b] Output/input.

[c] Based on outlet quantities.

There is a small difference between thorium recovery at 0 and 2.25 liters sparge air/min for the 20-cm leacher. This could be due to experimental error, or because the heaters are further removed from the base of the cone on the 20-cm leacher than on the 13-cm leacher. Thus, proper location of the heaters to take maximum advantage of agitation resulting from solution boiling should completely eliminate the need for sparge air (at least for the type feed material studied here).

2. Thorium recoveries of greater than 96 wt % were obtained in less than 4 hr without using external heat (the band heaters were not turned on). Temperatures of about 50°C were obtained from the heat of reaction (see Figs. 5-36 and 5-37). Therefore, it might be possible to take advantage of lower temperature dissolution (materials of construction, fission product release, eliminate reflux condenser, etc.). This should be given further consideration, especially with the design of equipment for the Hot Demonstration. The resulting burner ash from reprocessing the Fort St. Vrain fuel elements should be very similar to the type tested here. Also, irradiated fuels are expected to be more readily dissolved than unirradiated fuels.

3. Thorium material balance closures for these runs were 100 ± 3%.

4. The reproducibility of experimentally determined thorium recoveries based on duplicate experiments is very good (<0.1% variation).

5. The "dilution" tubes (see Fig. 5-38) utilized in previous runs (see previous Quarterly Progress Report Gulf-GA-A12599) to dilute the solids concentration of the slurry fed to the centrifuge were removed for these runs. As a result (it is concluded), no further difficulties were experienced while removing or sparging leacher contents during this series of runs. Thus, it is not planned to utilize the dilution tubes in any future leaching

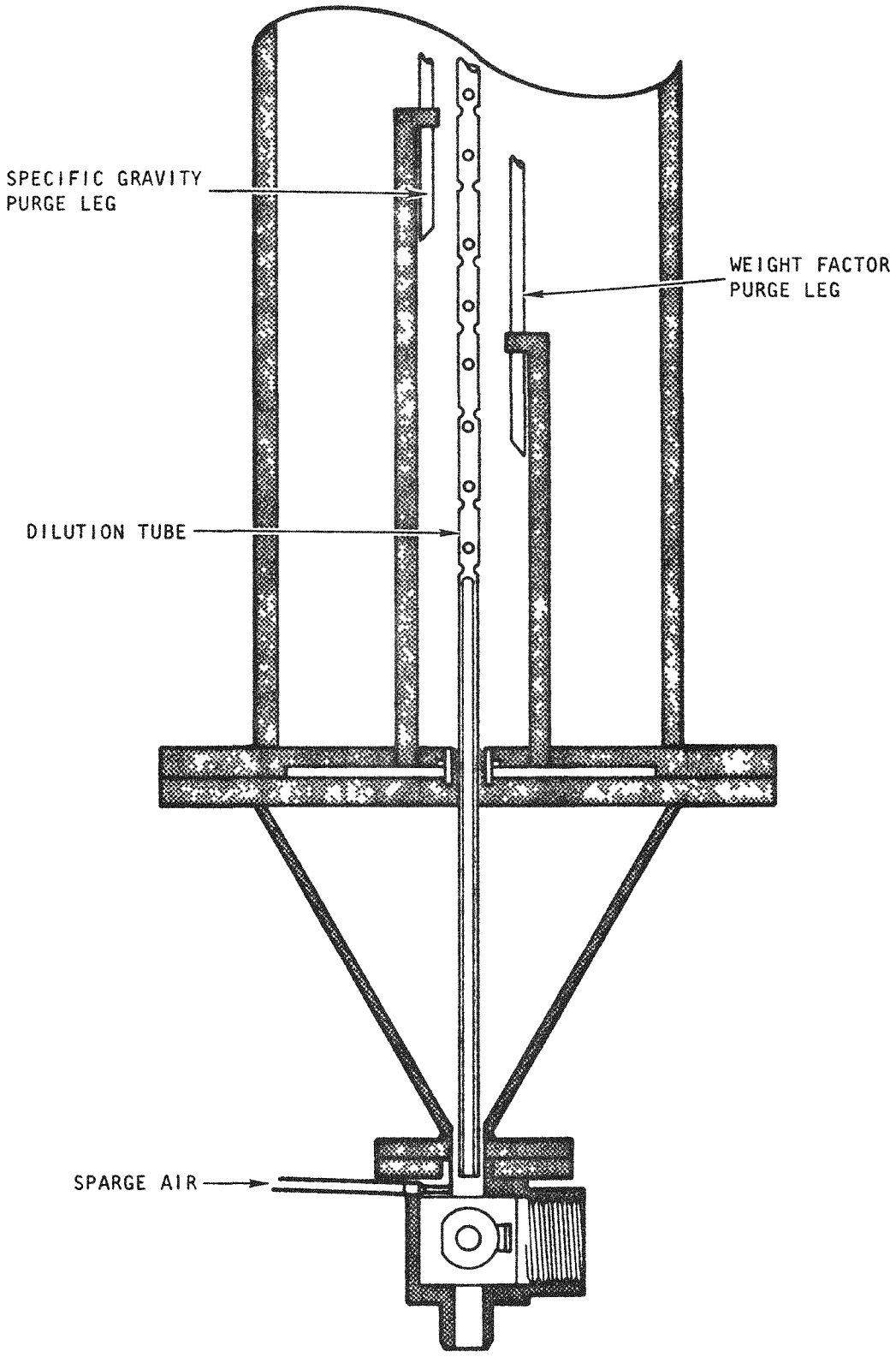

Fig. 5-38. Location of leacher dilution tube and spider

tests. An appropriate design for a different type dilution device will be made if problems with slurry removal from the leachers are encountered in the future.

6. A comparison between the mother liquor tank calibration relations of Table 5-17 and measured quantities is presented in Table 5-22. By assuming an error of 0.5 in. reading the recorder values required for the relationship included in Table 5-17, the following order of magnitude errors will result:

Vessel	Kilograms of Material	Specific Gravity
Thorex	0.28	0.01
20-cm leacher	0.24	0.019
13-cm leacher	0.15	0.019
Mother liquor	0.37	0.01

Based on this information and the data of Table 5-22, it is suggested:

a. The mother liquor tank should be recalibrated.

b. A buildup of thorium nitrate (or insolubles) is taking place in the specific gravity leg.

7. Internal "spiders" were installed in the leachers prior to this series of runs (see Fig. 5-38) to help hold the purge legs securely in place during leacher sparging and boiling operations. It was suspected (see previous Quarterly Progress Report Gulf-GA-A12599) that physical movement of the purge legs was resulting in variations in level and specific gravity readings between leaching runs. A comparison between the Thorex tank and the leachers using the calibration relations from Table 5-17 is given in Tables 5-23 and 5-24 for this series of runs. Examination of Tables 5-23 and 5-24 suggests:

TABLE 5-22
COMPARISON BETWEEN STORAGE TANKS USING CALIBRATION RELATIONS FROM TABLE 5-17

	Leach Run No.														
	49	50	51	52	53	54	55	56	57	60	61	63	64	65	66
Mother liquor tank															
Leachate transferred to mother liquor tank, kg	--	21.74	10.76	22.03	11.95	21.66	37.33	22.18	24.02	23.72	23.21	23.57	22.99	22.54	23.43
Specific gravity	1.576	1.612	1.602	1.600		1.578	1.517	1.604	1.561	1.551	1.537	1.537	1.545	1.561	1.527
Measured quantities															
Using 2-liter graduate and weighting, kg	22.13	20.83	11.03	21.32	11.05	21.46	36.68	--	22.97	22.73	22.11	22.68	22.06	21.64	24.02
Specific gravity using hydrometer	1.581	1.606	1.592	1.61	1.596	1.60	1.517	1.600	1.566	1.552	1.556	1.564	1.572	1.591	1.550
Error between mother liquor tank reading and measured quantity															
Quantity, kg	--	0.91	-0.27	0.71	0.90	0.20	0.65	--	1.05	0.99	1.1	0.89	0.93	0.9	0.59
Specific gravity	-0.005	0.006	0.010	-0.010	--	0.022	0	0.004	-0.005	-0.001	-0.019	-0.027	-0.027	-0.03	-0.023

TABLE 5-23
COMPARISON BETWEEN STORAGE TANKS USING CALIBRATION RELATIONS FROM TABLE 5-17, 13-CM LEACHER

	Leach Run No.								
	49	50	51	52	53	56	64	65	66
Thorex tank									
Thorex transferred to leacher, kg	17.95	17.97	9.48	17.78	9.14	18.00	17.59	17.67	17.60
Specific gravity	1.380	1.374	1.384	1.384	1.378	1.380	1.382	1.382	1.380
Leacher									
Thorex transferred from storage tank, kg	17.59	17.21	8.83	17.56	8.60	17.38	16.44	17.03	17.49
Specific gravity	1.380	1.384	1.384	1.368	1.361	--	1.391	1.418	1.410
Difference between leacher readings and Thorex tank readings									
Quantity, kg	0.36	0.76	0.65	0.22	0.54	0.62	1.15	0.64	0.11
Specific gravity	0.0	-0.01	0.0	0.016	0.017	--	-0.009	-0.036	-0.038

TABLE 5-24
COMPARISON BETWEEN STORAGE TANKS USING CALIBRATION RELATIONS FROM TABLE 5-17, 20-CM LEACHER

	Leach Run No.					
	54	55	57	60	61	63
Thorex tank						
Thorex transferred to leacher, kg	18.06	26.64	18.86	18.84	17.58	17.22
Specific gravity	1.378	1.384	1.380	1.384	1.384	1.382
Leacher						
Thorex transferred from storage tank, kg	16.00	25.37	16.88	16.39	15.51	15.76
Specific gravity	1.379	1.395	1.372	1.425	1.414	1.418
Difference between leacher readings and Thorex tank readings						
Quantity, kg	2.06	1.27	1.98	2.45	2.07	1.46
Specific gravity	-0.001	-0.011	0.008	-0.041	-0.03	-0.036

a. The leachers should be recalibrated, particularly the 20-cm leacher.

b. There are increased errors in the specific gravity predictions as the number of leaching runs increases.

It is not clear whether the errors in specific gravities are a result of (1) continued shifting of purge legs, (2) buildup of thorium nitrate (or insolubles) in the purge legs, or (3) faulty differential pressure transmitters, recorders, or purge system. Further testing will be done.

NOMENCLATURE

D_p - Particle diameter, in.
D_c - Column or leacher diameter, in.
D_1 - Air inlet diameter to bottom of leacher, in.
E - Internal energy, ft-lb/lb
g_c - Gravitational constant, ft/hr^2
H - Height from leacher bottom, ft
K - Dimensionless proportionality constant
L - Length of depth of bed, ft
M - Weight of slurry of volume V, lb
P - Pressure, lb/ft^2
ΔP - Pressure drop, lb/ft^2
P - Vapor pressure, $lb/in.^2$
Q - Heat, ft-lb/lb
s - Specific gravity
u - Velocity, ft/sec
V - Air volume rate, ft^3/min
W - Rate of energy tranfer, ft-lb/min
w - Work, ft-lb/lb

GREEK SYMBOLS

μ - Viscosity of fluid, lb/ft-hr

ρ - Density, lb/ft^3

γ - Void fraction, dimensionless

ε - Fractional gas holdup, defined by Eq. (2)

SUBSCRIPTS

1 - Position at bottom (air inlet orifice) of leacher

2 - Position at top of leacher solution

f - Fluid

g - Gas

s - Solids

c - Based on column diameter

REFERENCES

5-1. Lauer, O., Grain Size Measurements on Commercial Powders, A Guide for Experts, Alpine American Corp., Natick, Massachusetts (1966).

5-2. Braulick, W. J., J. R. Fair, and B. J. Lerner, "Mass Transfer in a Sparged Contactor: Part I. Physical Mechanisms and Controlling Parameters," A.I.Ch.E. J. 11, 73 (1965).

5-3. Towell, G. D., C. P. Strand, and G. H. Ackerman, "Mixing and Mass Transfer in Large Diameter Bubble Columns," A.I.Ch.E. - I. Chem. Eng. Symp. Series No. 10, London (1965), p. 97.

5-4. Fair, J. R., "Designing Gas-Sparged Reactors," Chem. Eng. 74, 67 (1967).

5-5. Long, J. T. (Ed.), Engineering for Nuclear Fuel Reprocessing, Gordon and Breach Science Publishers (1967), p. 330.

5-6. Kaufman, H. L., Chem. Met. Eng. 37, 178 (1930).

5-7. Lamont, A. G. W., "Air Agitation and Pachuca Tanks," Can. J. Chem. Eng. 36, 153 (1958).

5-8. Madonna, L. A., and R. F. Lama, "The Derivation of an Equation for Predicting Minimum Spouting Velocity," A.I.Ch.E. J. 4, 497 (1958).

5-9. Frantz, J. F., "Design for Fluidization, Part 1," Chem. Eng. 69, 169 (1962).

5-10. Mathur, K. B., and P. E. Gishler, "A Technique for Contacting Gases with Coarse Solid Particles," A.I.Ch.E. J. 1, 157 (1955).

5-11. Ghosh, B., "A Study on the Spouted Bed, Part I - A Theoretical Analysis," Indian Chem. Eng. 7, 16 (1965).

5-12. Zenz, F. A., and D. F. Othmer, Fluidization and Fluid-Particle Systems, Reinhold, New York (1960), Chapter 15.

5-13. Leva, M., Fluidization, Chemical Engineering Series, McGraw-Hill, p. 170.

5-14. Mathur, K. B., "Spouted Beds," in Fluidization, J. F. Davidson and D. Harrison (Eds.), Academic Press, New York (1971), Chapter 17, p. 711.

TASK VIII
PHYSICS AND FUEL MANAGEMENT

ENDF/B PARTICIPATION

A report (Ref. 8-1) documenting the GAND2 and GFE2 cross-section processing codes was issued and the codes were sent to the Argonne Code Center.

A preliminary draft of the ANS-19.1 standard for nuclear data sets was critically reviewed and comments were forwarded to the AEC.

Work on updated documentation for the GANDY3 unresolved resonance cross-section computation code was initiated preparatory to transmittal of the code to the Argonne Code Center.

ANALYSIS OF HTGR AND HTLTR CRITICAL EXPERIMENTS

Recent HTLTR Calculations

Summary

Calculations using current HTGR methods and cross sections were completed for all five HTLTR lattices. The agreement with experiment is slightly improved over previous calculations but no large changes were found. With the exception of Lattice 3, the agreement with experiment is quite good. The large discrepancy for Lattice 3 remains unexplained. The basic results are summarized in Table 8-1.

TABLE 8-1

BASIC HTLTR RESULTS

Lattice	1	2	3	4	5
BNWL experiment					
k_∞(300°K)	1.111	1.0582	1.064	1.085	1.0287
Δk(1273°K)	0.079	0.0345	0.004	0.056	0.0250
GGA calculation					
k_∞(300°K)	1.1022	1.0471	1.1068	1.0809	1.0404
Δk(1273°K)	0.0622	0.0338	0.0181	0.0527	0.0267

Some additional discussion and amplification of these results are presented in this report. A more complete discussion will be contained in a topical report, now in preparation, covering both the HTGR and HTLTR critical experiment programs.

Discussion

Up-to-date calculations for all five HTLTR lattices were completed. The procedure used was to generate standard nine-group diffusion cross sections with MICROX (Ref. 8-2). The atom densities and cell dimensions used were those for the lattice fuel blocks without end caps. Nine-group bucklings from previous calculations were used to obtain systems that were approximately critical at all temperatures. These nine-group cross sections were used in GAZE (Ref. 8-3) to search for a critical system at 300°K and 1273°K. This allowed the bucklings used in MICROX to be checked and corrected, if necessary, to get critical systems for a second MICROX calculation. The atom densities used in the GAZE calculation were for the lattice fuel blocks without end caps. This buckling iteration procedure between MICROX and GAZE is necessary because the k_∞ value calculated by MICROX is fairly sensitive to changes in the buckling values used. The sensitivity is on the order of 50 $\Delta k/k$ per cm^{-2}. The error in k_∞ will generally be about 10% of the difference between the value of k calculated by MICROX and 1.00.

Both experiment and calculation should explicitly account for the fact that the lattice fuel blocks have end caps on the fuel channels. Battelle Northwest Laboratories (BNWL), however, reported experimental results that were corrected to subtract the effect of the end caps. The results reported here, then, should be consistent with BNWL's results.

Table 8-1 gives room-temperature infinite multiplication values [k_∞(300°K)] and temperature defects to 1273°K [Δk(1273°K)]. Agreement between experiment and calculation is generally quite good with the exception of Lattice 3.

Note that there is no particular pattern to our agreement with experiment. For Lattices 1, 2, and 4 our calculated 300°K k_∞ values are slightly lower (less than 1%) than the experimental values, as are calculated temperature defects. For Lattice 5 the calculated values are slightly higher than experiment (about 1%). For Lattice 3 the calculated values for both k_∞(300°K) and Δk(1273°K) are very much higher than experiment. There is no discernable pattern to the results of the U-233 lattices (2, 3, and 5) that would correlate with the lattice loadings summarized in Table 8-2.

Table 8-3 is a more complete summary of the data for all five lattices. Experimental and calculated results from BNWL are shown as well as our data. Included are the previously reported GGA results as well as the most recent results. The overall agreement with experiment is generally somewhat improved and, with the exception of Lattice 3, is quite good. The large discrepancy for Lattice 3 remains unexplained.

The differences between the present results and the previous data are due to the following changes in calculational procedure:

1. Calculations were performed at exactly the same temperature as was used for the experiment. This was made possible by the addition of temperature interpolation in the MICROX code.

TABLE 8-2

HTLTR LATTICE LOADINGS

Lattice	Fissile Particle Description			Fissile Loading		Thorium Loading		
	Fissile Nuclide	Kernel Material	Average Kernel Diameter (mm)	Carbon / Fissile Atom Ratio	Fissile Density (kg/ℓ)	Carbon / Thorium Atom Ratio	Thorium Density (kg/ℓ)	Median Particle[a] Diameter (mm)
HTGR #1	^{235}U (93.5%)	UC_2	0.330	5910	0.00468	193	0.141	0.065
HTGR #2	^{233}U (97.5%)	ThO_2/UO_2 (3/1)	0.280	10292	0.00264	189	0.143	0.044
HTGR #3	^{233}U (97.5%)	ThO_2/UO_2 (3/1)	0.322	13756	0.00199	278	0.0981	0.143
HTGR #4	^{239}Pu (73% + 23% ^{240}Pu, 3% ^{241}Pu, 1% ^{242}Pu)	PuO_2	0.209	9847	0.00285	250	0.109	0.065
MSBR (ORNL)	^{233}U (97.5%)	ThO_2/UO_2 (3/1)	0.032	9469	0.00304	146	0.196	0.092

[a] ThO_2 in powder form (uncoated).

TABLE 8-3

HTLTR LATTICE RESULTS SUMMARY

Lattice	k_∞ 300°K	k_∞ 1273°K	Δk_∞
Lattice 1			
C/Th = 193, C/U^{235} = 5910			
BNWL Experiment (Ref. 8-6)	1.111	1.032	-0.079
Previous GGA Calculation	1.0881	1.0306	-0.0575
New GGA Calculation	1.1022	1.0400	-0.0622
Lattice 2			
C/Th = 189, C/U^{233} = 10292			
BNWL Experiment (Ref. 8-5)	1.0582	1.0237	-0.0345
BNWL Calculation (Ref. 8-5)	1.0500	1.0034	-0.0466
Previous GGA Calculation	1.0421	1.0093	-0.0328
New GGA Calculation	1.0471	1.0133	-0.0338
Lattice 3			
C/Th = 278, C/U^{233} = 13756			
BNWL Experiment (Ref. 8-7)	1.064	1.060	-0.004
BNWL Calculation (Ref. 8-7)	1.101	1.0686	-0.0324
Previous GGA Calculation	1.0951	1.0772	-0.0179
New GGA Calculation	1.1068	1.0887	-0.0181
Lattice 4			
C/Th = 250, C/Pu_f = 9847			
BNWL Experiment (Ref. 8-8)	1.085	1.029	-0.056
BNWL Calculation (Ref. 8-8)	1.092	1.039	-0.053
Previous GGA Calculation	1.0809	1.0357	-0.0452
New GGA Calculation	1.0809	1.0282	-0.0527
Lattice 5			
C/Th = 146, C/U^{233} = 9469			
BNWL Experiment (Ref. 8-9)	1.0287	1.0037	-0.0250
BNWL Calculation (Ref. 8-9)	1.0474	1.0051	-0.0423
Previous GGA Calculation	1.0341	1.0080	-0.0261
New GGA Calculation	1.0404	1.0137	-0.0267

2. Resonance data at 315°K were used for the 300°K lattice calculations to account for molecular bonding effects in ThO_2, UO_2, and PuO_2.

3. Improvements in the MICROX code allowed two grain types (fissile and fertile) to be explicitly represented.

4. The atom densities used previously for Lattice 2 were calculated using data obtained from Ref. 8-4. These data are incorrect. Using correct data from Ref. 8-5, new Lattice 2 atom densities were determined for the present set of calculations.

5. The impurities in the HTLTR graphite are modeled using boron-10 in the lattice calculations. The amount of B-10 in some previous GGA calculations was previously overestimated by a factor of six because of the neglect of the presence of nitrogen in the graphite when calculating the B-10 necessary to represent impurities. This error has been corrected in the present set of calculations.

6. The calculational technique used in the past was to generate cross sections with MICROX for the actual lattice material, that is, for fuel blocks with end caps. These were then used in GAZE with atom densities for a lattice without end caps. This technique is wrong. The present results were calculated using without end cap atom densities in both MICROX and GAZE calculations.

Individual Lattice Results

Results for each of the five lattices are reported in Tables 8-4 through 8-13 and Figs. 8-1 through 8-5. All the data necessary to repeat the calculation are shown, as are BNWL's experimental and calculated results. Also shown are some of the reactor physics parameters of interest. These were calculated using the following formulae and a 2.38-eV thermal cutoff energy.

TABLE 8-4

LATTICE 1 DATA

Uranium-235 and thorium

C/Th = 193, C/U-235 = 5910

Fuel rod diameter 1.1938 cm, VF in cell 0.3084
Grain 1, UC_2, 330μ diameter, VF in rods 0.001706
Grain 2, ThO_2, 65μ diameter, VF in rods 0.05197
Dancoff correction 0.4595 at $\Sigma_m = 0.385$ cm^{-1}

Nuclide	UC_2	ThO_2	Fuel Rod	Moderator	Cell Average
B-10	8.286-10	--	7.9791-10	1.3767-9	1.1980-9
Carbon	4.8814-2	--	4.7005-2	8.1114-2	7.0577-2
Nitrogen	--	--	2.8229-5[a]	1.41-5[a]	1.8454-5[a]
Oxygen	--	4.5692-2	2.3720-3	--	7.3160-4
Thorium	--	2.2821-2	1.1860-3	--	3.6580-4
U-234	1.3903-4	--	2.3717-7	--	7.315-8
U-235	2.2698-2	--	3.8720-5	--	1.1942-5
U-236	7.2993-5	--	1.2452-7	--	3.841-8
U-238	1.4970-3	--	2.5537-6	--	7.876-7

[a] At 300°K. For other temperatures $N_\eta(T) = N_n(300)\ \frac{300}{T°K}$.

TABLE 8-5

LATTICE 1 RESULTS

Temperature (°K)		300	423	573	823	973	1273	1500
GGA Calculation	k_∞	1.1022	1.0901	1.0764	1.0601	1.0525	1.0400	1.0321
	Δk_∞	0	−0.0121	−0.0258	−0.0421	−0.0497	−0.0622	−0.0701
BNWL Experiment[a]	k_∞	1.111[b]	1.096	1.081	1.052	1.037	1.032	--
	Δk_∞	0	-0.015	-0.030	-0.059	-0.074	-0.079	--
Calculated Physics Parameters	ηf_2	1.438	1.438	1.438	1.438	1.439	1.440	1.441
	p	0.710	0.702	0.694	0.685	0.681	0.677	0.676
	τ	343	340	337	331	328	321	316
	L^2	187	205	226	248	260	285	304
	ηf_1	0.315	0.305	0.293	0.280	0.274	0.264	0.259
	B^2	2.16-4	1.82-4	1.49-4	1.15-4	9.95-5	7.75-5	6.79-5
	ϕ_1/ϕ_2	2.00	1.87	1.77	1.61	1.53	1.39	1.29

[a] Ref. 8-6.
[b] Interpolated between 293°K and 423°K.

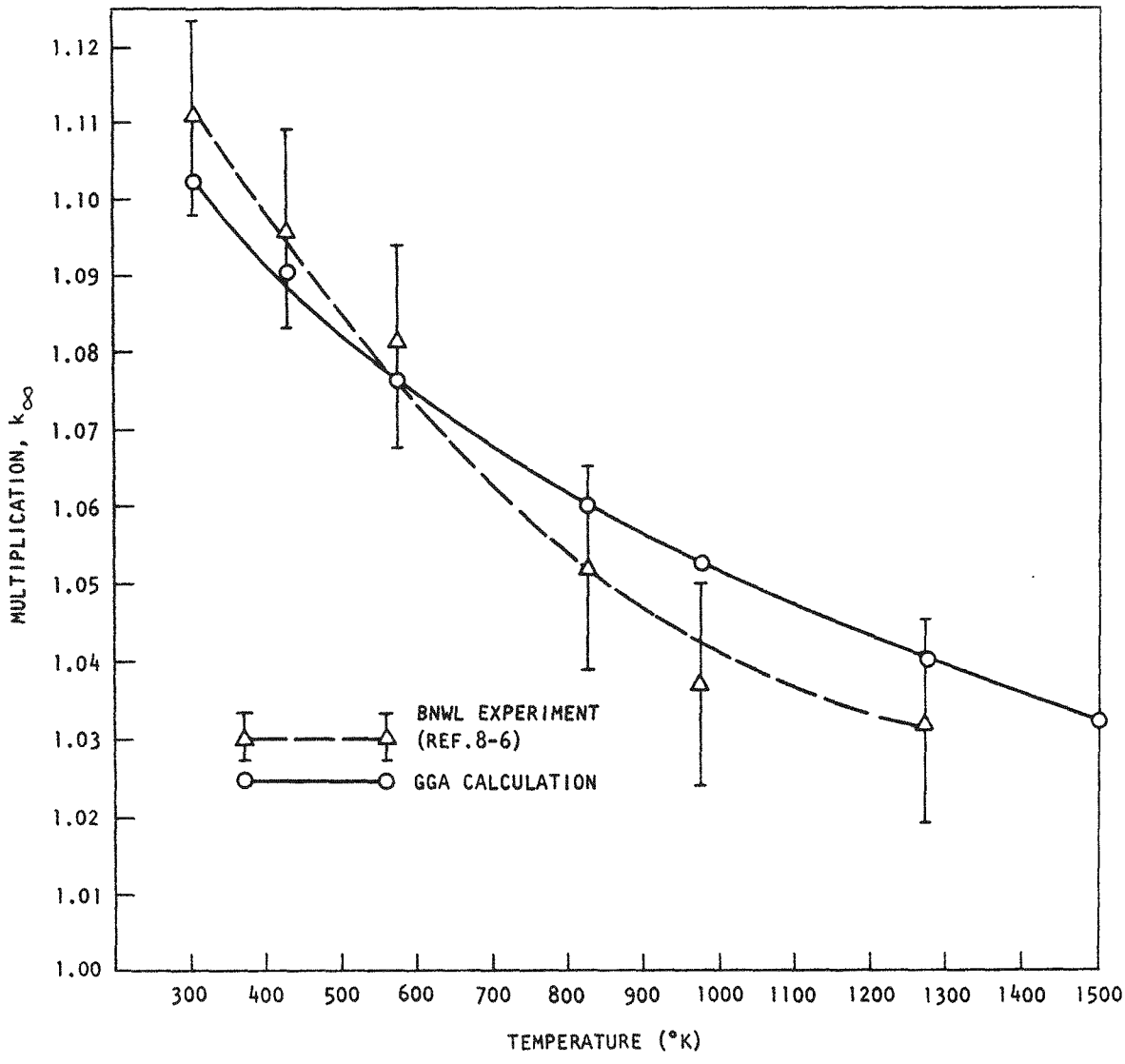

Fig. 8-1. k_{eff} versus temperature, Lattice 1, $U^{235}C_2$-ThO2

TABLE 8-6

LATTICE 2 DATA

Uranium-233 and thorium

C/Th = 189, C/U-233 = 10292

Fuel rod diameter 1.1938 cm, VF in cell 0.3084
Grain 1, UO_2/ThO_2, 280μ diameter, VF in rod 0.004056
Grain 2, ThO_2, 44μ diameter, VF in rod 0.04975
Dancoff correction 0.4595 at Σ_m = 0.385 cm^{-1}

Nuclide	UO_2/ThO_2	ThO_2	Fuel Rod	Moderator	Cell Average
B-10	--	--	8.3057-10	1.3559-9	9.9258-10
Carbon	--	--	4.8929-2	7.9876-2	7.0332-2
Nitrogen[a]	--	--	2.624-5	1.424-5	1.7941-5
Oxygen	4.5574-2	4.5637-2	2.4560-3	--	7.5743-4
Thorium	1.7181-2	2.2818-2	1.2049-3	--	3.7159-4
U-233	5.4626-3	--	2.2158-5	--	6.8335-6
U-234	5.8178-5	--	2.360-7	--	7.278-8
U-235	5.3926-6	--	2.187-8	--	6.745-9
U-236	3.3214-7	--	1.35-9	--	4.163-10
U-238	7.8496-5	--	3.184-7	--	9.8195-8

(a) At 300°K. For other temperatures $N_n(T) = N_n(300) \frac{300}{T°K}$.

TABLE 8-7

LATTICE 2 RESULTS

Temperature (°K)		300	423	573	773	1023	1273	1500
GGA Calculation	k_∞	1.0471	1.0385	1.0285	1.0211	1.0158	1.0133	1.0125
	Δk_∞	0	−0.0086	−0.0186	−0.0260	−0.0313	−0.0338	−0.0346
BNWL Experiment[a]	k_∞	1.0582[b]	1.0471	1.0367	1.0297	1.0245	1.0237	--
	Δk_∞	0	−0.0111	−0.0215	−0.0285	−0.0337	−0.0345	--
BNWL Calculation[a]	k_∞	1.0500[b]	1.0370	1.0256	1.0156	1.0081	1.0034	--
	Δk_∞	0	−0.0130	-0.0244	−0.0344	−0.0419	−0.0466	--
Calculated Physics Parameters	$\eta f2$	1.322	1.327	1.331	1.340	1.353	1.366	1.379
	p	0.723	0.715	0.706	0.698	0.691	0.688	0.686
	τ	338	336	333	330	325	320	315
	L^2	227	254	283	309	337	363	385
	$\eta f1$	0.348	0.334	0.320	0.307	0.294	0.285	0.278
	B^2	8.33-5	7.14-5	4.83-5	3.28-5	2.40-5	2.10-5	2.05-5
	ϕ_1/ϕ_2	1.56	1.45	1.36	1.25	1.14	1.06	1.00

[a] From Ref. 8-5.

[b] Interpolated between 293°K and 423°K.

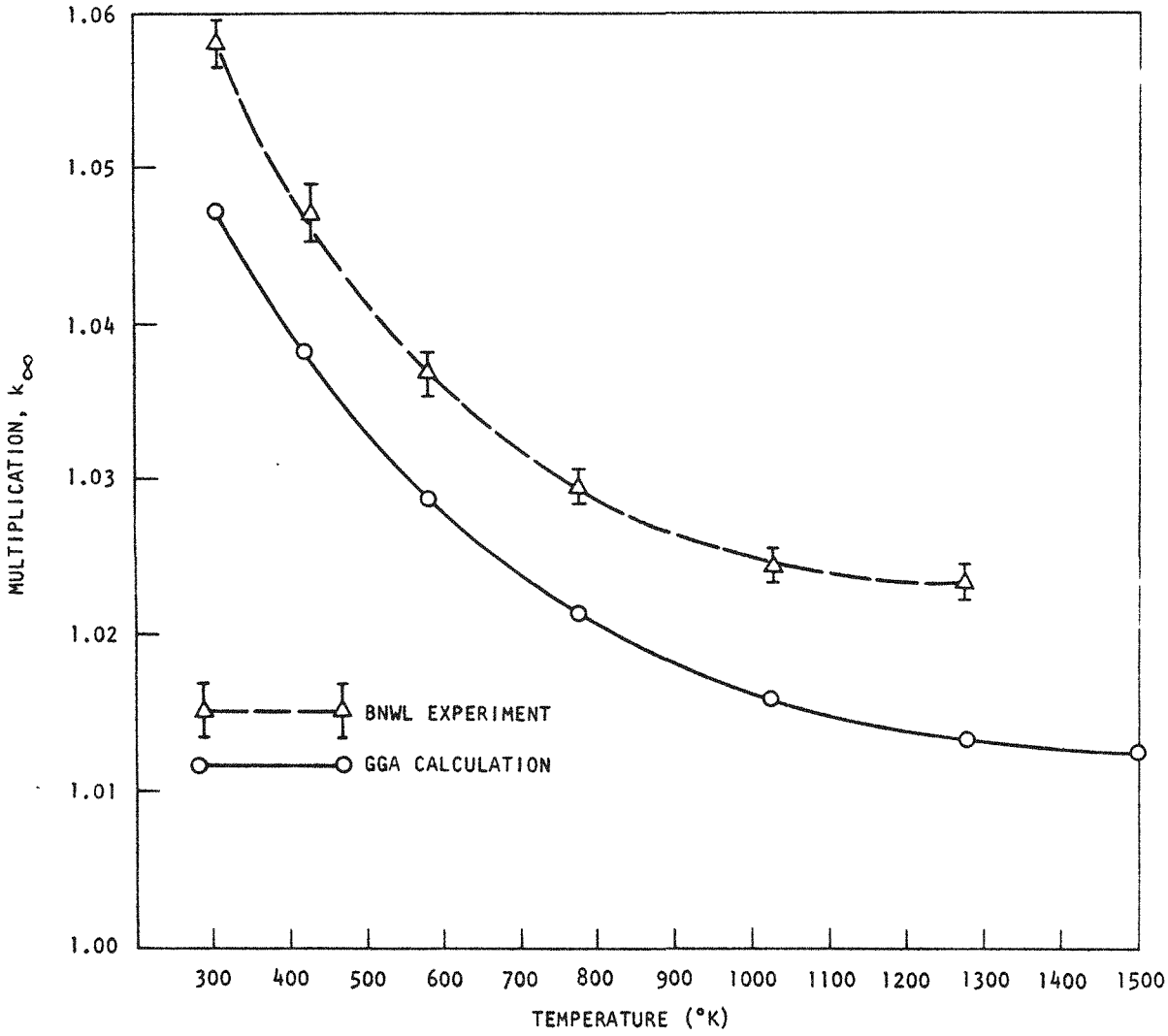

Fig. 8-2. k_{eff} versus temperature, Lattice 2, $U^{233}O_2$-ThO_2

TABLE 8-8

LATTICE 3 DATA

Uranium-233 and thorium

C/Th = 278, C/U-233 = 13756

Fuel rod diameter 1.1938 cm, VF in cell 0.3084
Grain 1, UO_2/ThO_2, 322μ diameter, VF in rod 0.003006
Grain 2, ThO_2, 65μ diameter, VF in rod 0.03619
Dancoff correction 0.4595 at $\Sigma_m = 0.385$ cm^{-1}

Nuclide	UO_2/ThO_2	ThO_2	Fuel Rod	Moderator	Cell Average
B-10	--	--	8.0288-10	1.3769-9	1.1999-9
Carbon	--	--	4.7298-2	8.1114-2	7.0684-2
Nitrogen[a]	--	--	2.7254-5	1.4093-5	1.8152-5
Oxygen	4.5634-2	4.5636-2	1.6857-3	--	5.1993-4
Thorium	1.7131-2	2.2818-2	8.2574-4	--	2.5469-4
U-233	5.5419-3	--	1.6660-5	--	5.1385-6
U-234	5.9053-5	--	1.7752-7	--	5.4753-8
U-235	5.4766-6	--	1.6463-8	--	5.0778-9
U-236	3.3749-7	--	1.0145-9	--	3.1291-10
U-238	7.9838-5	--	2.4001-7	--	7.4028-8

[a]At 300°K. For other temperatures $N_n(T) = N_n(300) \frac{300}{T°K}$.

TABLE 8-9

LATTICE 3 RESULTS

Temperature (°K)		300	423	573	828	973	1273	1500
GGA Calculation	k_∞	1.1068	1.1013	1.0944	1.0894	1.0883	1.0887	1.0903
	Δk_∞	0	−0.0055	−0.0124	−0.0174	−0.0185	−0.0181	−0.0165
BNWL Experiment[a]	k_∞	1.064	1.060	1.055	1.057	1.057	1.060	--
	Δk_∞	0	−0.004	−0.009	−0.007	−0.007	−0.004	--
BNWL Calculation[a]	k_∞	1.101	1.0904	1.0824	1.0746	1.0719	1.0686	--
	Δk_∞	0	−0.0106	−0.0186	−0.0264	−0.0291	−0.0324	--
Calculated Physics Parameters	$\eta f2$	1.335	1.340	1.346	1.358	1.366	1.383	1.395
	p	0.779	0.771	0.766	0.759	0.756	0.753	0.753
	τ	349	347	344	340	337	331	329
	L^2	293	332	374	422	444	489	521
	$\eta f1$	0.345	0.333	0.320	0.317	0.298	0.288	0.282
	B^2	1.76-4	1.60-4	1.41-4	1.29-4	1.25-4	1.21-4	1.22-4
	ϕ_1/ϕ_2	1.20	1.10	1.02	0.90	0.86	0.78	0.73

[a] From Ref. 8-7 (four-block cell).

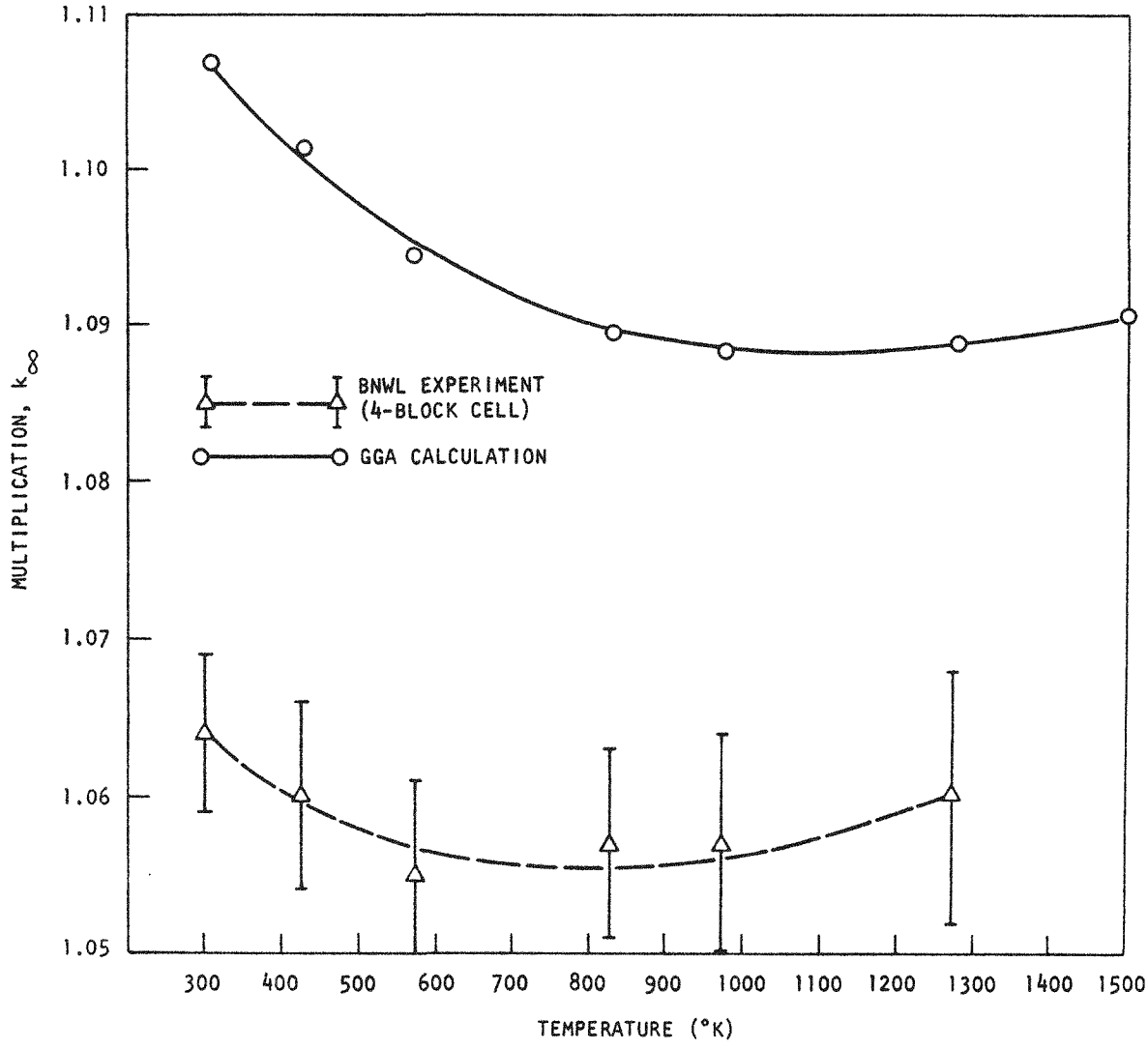

Fig. 8-3. k_{eff} versus temperature, Lattice 3, $U^{233}O_2$-ThO_2

TABLE 8-10

LATTICE 4 DATA

Plutonium and thorium

C/Th = 250, C/(Pu-239 + Pu-241) = 9847

Fuel rod diameter 1.1938 cm, VF in cell 0.3084
Grain 1, PuO_2, 209μ diameter, VF in rod 0.001233
Grain 2, ThO_2, 65μ diameter, VF in rod 0.04101
Dancoff correction 0.4595 at $\Sigma_m = 0.385\ cm^{-1}$

Nuclide	PuO_2	ThO_2	Fuel Rod	Moderator	Cell Average
B-10	--	--	8.108-10	1.374-9	1.200-9
Carbon	--	--	4.7767-2	8.0962-2	7.072-2
Nitrogen[a]	--	--	2.745-5	1.409-5	1.821-5
Oxygen	4.9588-2	4.4724-2	1.8953-3	--	5.846-4
Thorium	--	2.2362-2	9.1711-4	--	2.829-4
Pu-239	1.8075-2	--	2.2278-5	--	6.871-6
Pu-240	5.6531-3	--	6.9677-6	--	2.149-6
Pu-241	8.1822-4	--	1.0084-6	--	3.110-7
Pu-242	2.4704-4	--	3.0560-7	--	9.426-8

[a] At 300°K. For other temperatures $N_n(T) = N_n(300)\ \frac{300}{T°K}$.

TABLE 8-11

LATTICE 4 RESULTS

Temperature (°K)		300	573	773	1023	1273	1500
GGA Calculation	k_∞	1.0809	1.0664	1.0584	1.0457	1.0282	1.0076
	Δk_∞	0	−0.0145	−0.0225	−0.0352	−0.0527	−0.0733
BNWL Experiment[a]	k_∞	1.085	1.067	1.059	1.048	1.029	--
	Δk_∞	0	−0.018	−0.026	−0.037	−0.056	--
BNWL Calculation[a]	k_∞	1.092	1.076	1.068	1.056	1.039	--
	Δk_∞	0	−0.016	−0.024	−0.036	−0.053	--
Calculated Physics Parameters	$\eta f2$	1.338	1.347	1.352	1.349	1.335	1.313
	p	0.754	0.740	0.734	0.729	0.727	0.727
	τ	349	344	340	334	327	320
	L^2	127	132	126	121	119	119
	$\eta f1$	0.312	0.290	0.280	0.271	0.263	0.258
	B^2	1.83-4	1.47-4	1.33-4	1.07-4	6.77-5	1.72-5
	ϕ_1/ϕ_2	2.76	2.84	2.95	3.05	3.07	3.03

[a] From Ref. 8-8.

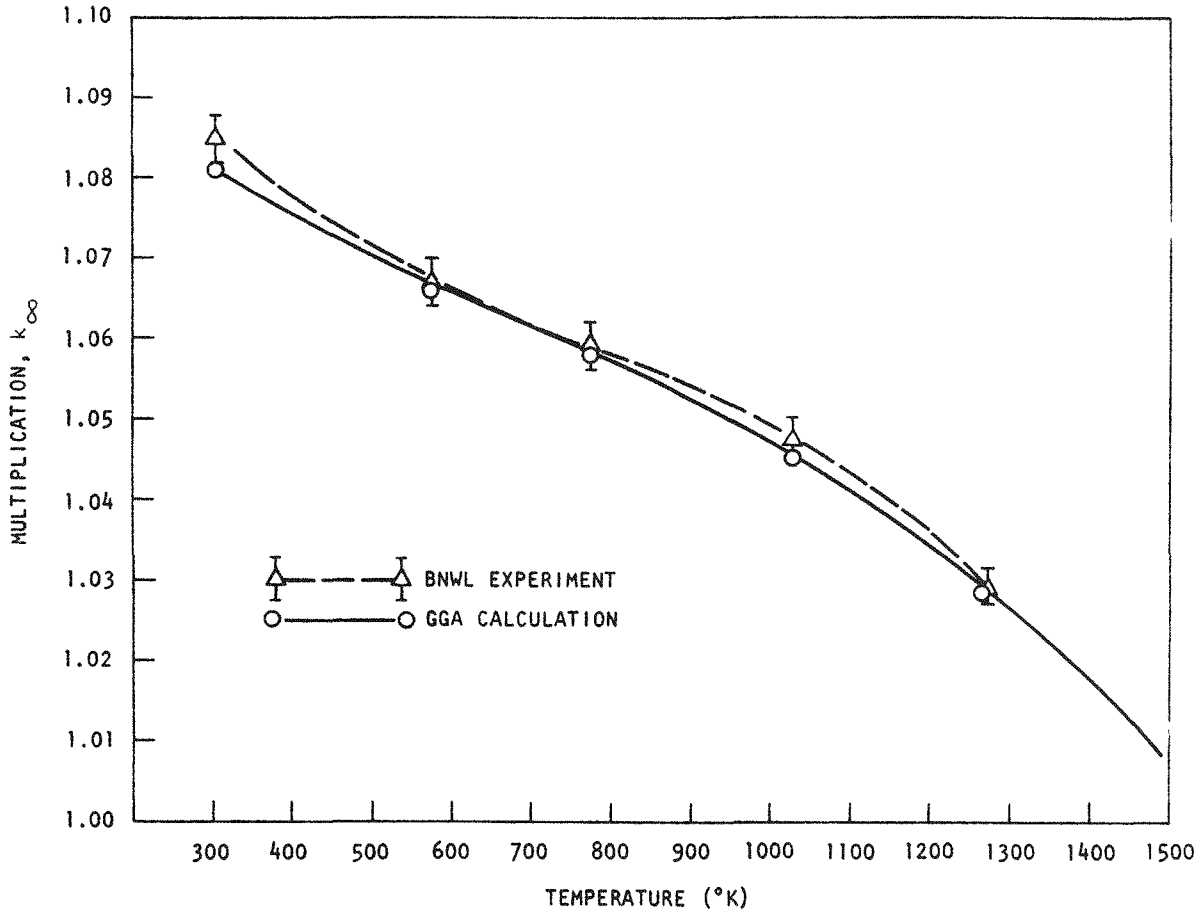

Fig. 8-4. k_{eff} versus temperature, Lattice 4, PuO_2-ThO_2

TABLE 8-12

LATTICE 5 DATA

Uranium-233 and thorium

C/Th = 146, C/U-233 = 9469

Fuel rod diameter 1.9964 cm, VF in cell 0.1380
Grain 1, UO_2/ThO_2, 302μ diameter, VF in rod 0.009894
Grain 2, ThO_2, 92μ diameter, VF in rod 0.1546
Dancoff correction 0.0907 at Σ_m = 0.385 cm^{-1}

Nuclide	UO_2/ThO_2	ThO_2	Fuel Rod	Moderator	Cell Average
B-10	--	--	6.576-10	1.359-9	1.262-9
Carbon	--	--	3.874-2	8.004-2	7.434-2
Nitrogen[a]	--	--	2.500-5	1.465-5	1.646-5
Oxygen	4.567-2	4.564-2	7.500-3	--	1.035-3
Thorium	1.693-2	2.282-2	3.696-3	--	5.100-4
U-233	5.750-3	--	5.689-5	--	7.851-6
U-234	6.178-5	--	6.080-7	--	8.390-8
U-235	5.429-6	--	5.320-8	--	7.342-9
U-236	4.130-7	--	4.000-9	--	5.520-10
U-238	8.338-5	--	8.080-7	--	1.115-7

[a] At 300°K. For other temperatures N_n (T) = N_n (300) $\frac{300}{T°K}$.

TABLE 8-13

LATTICE 5 RESULTS

Temperature (°K)		300	573	900	1273	1500
GGA Calculation	k_∞	1.0404	1.0255	1.0169	1.0137	1.0135
	Δk_∞	0	−0.0149	−0.0235	−0.0267	−0.0269
BNWL Experiment[a]	k_∞	1.0287[b]	1.0127	1.0065	1.0037	--
	Δk_∞	0	−0.0160	−0.0222	−0.0250	--
BNWL Calculation[a]	k_∞	1.0474[b]	1.0269	1.0136	1.0051	--
	Δk_∞	0	−0.0205	−0.0338	−0.0423	--
Calculated Physics Parameters	$\eta f2$	1.239	1.249	1.265	1.285	1.298
	p	0.756	0.741	0.729	0.722	0.720
	τ	300	296	291	284	279
	L^2	184	226	256	286	303
	$\eta f1$	0.436	0.401	0.374	0.353	0.343
	B^2	8.67-5	5.02-5	3.11-5	2.44-5	2.44-5
	ϕ_1/ϕ_2	1.64	1.44	1.27	1.13	1.08

[a] From Ref. 8-9.

[b] Interpolated between 293°K and 573°K.

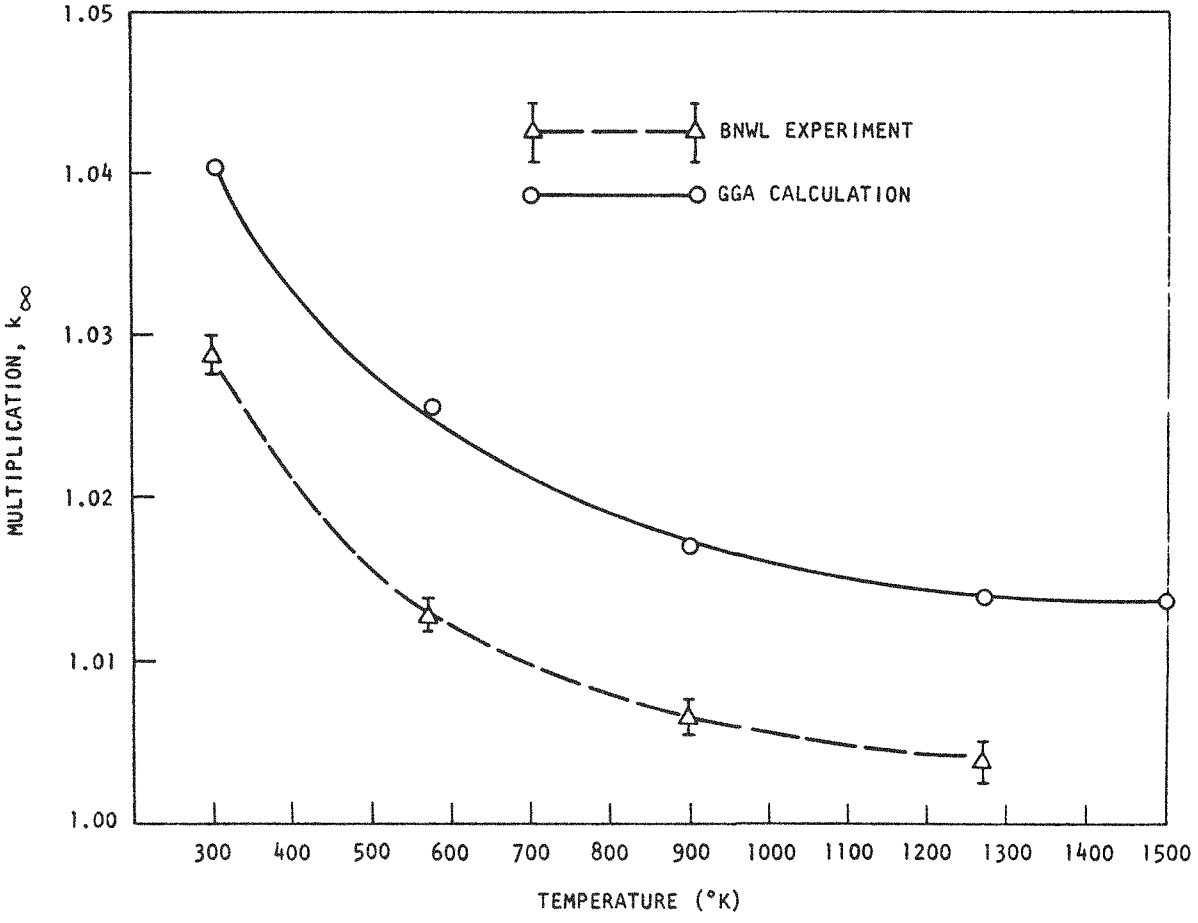

Fig. 8-5. k_{eff} versus temperature, Lattice 5, $U^{233}O_2$-ThO_2 (MSBR)

$$D = \frac{1}{3\,\Sigma^{tr}} \qquad \tau = \frac{D_1}{\Sigma_1^a + \Sigma_{12}}$$

$$L^2 = \frac{D_2}{\Sigma_2^a} \qquad p = \frac{\Sigma_{12}}{\Sigma_1^a + \Sigma_{12}}$$

$$\eta f = \frac{\nu\Sigma^f}{\Sigma^a}$$

Temperature coefficients were calculated for the five lattices and are shown in Table 8-14. The total coefficient, $\Delta k_\infty/\Delta T$, is shown as well as the Doppler coefficient, $(1/p)(\Delta p/\Delta T)$, and the thermal base coefficient, $(1/\eta f)(\Delta \eta f/\Delta T)$. The agreement between experiment and calculation is fairly good for Lattices 1, 2, 4, and 5. The large discrepancy for Lattice 3 still exists.

No further HTLTR calculations are presently planned except in the case of Lattice 3. When ENDF/B-III Adler-Adler temperature-dependent resonance data for U-233 become available, they will be used for another Lattice 3 calculation. The expectation, however, is that no significant change will occur in the results reported here.

Reanalysis of the C/U 5000 HTGR Critical Facility Core Assembly

In the spring of 1967, a core assembly with a C/U atom ratio of about 5000 was assembled in the modified HTGR Critical Facility. The reactivity worth of various sample materials was measured by substitution methods in the central location of that assembly, and the analysis showed the calculated k_{eff} for that assembly was too high by 0.01 Δk and that the calculated worths of the samples was generally 10% high (Ref. 8-10). A number of analytical variations were considered to resolve this difference with no success, so the core assembly was rebuilt in the spring of 1969 and the experimental measurements were then repeated. The experimental results

TABLE 8-14

HTLTR TEMPERATURE COEFFICIENTS ($\Delta k/\Delta T$) $\times 10^{-5}/°C$

		Lattice 1		Lattice 2		Lattice 3		Lattice 4		Lattice 5	
		Calc.	Exp.	Calc.	Exp.	Calc.	Exp.	Calc.	Exp.	Calc.	Exp.
Temperature Coefficient											
$\frac{\Delta k_\infty}{\Delta T}$	20° to 500°C	-8.23	-12.1	-5.56	-6.04	-3.48	-1.88	-4.82	-5.42	-4.35	-4.20
	500° to 750°C	-5.20	- 6.8	-2.12	-2.08	+0.80	+0.80	-5.08	-4.40	-1.52	-1.28
	750° to 1000°C	-4.20	- 2.0	-1.00	-0.32	+1.20	+1.20	-7.00	-7.60	-0.80	-0.64
Doppler Coefficient											
$\frac{1}{p}\frac{\Delta p}{\Delta T}$	20° to 500°C	-6.7		-7.3		-4.8		-5.6		-7.3	
	500° to 750°C	-3.9		-4.0		-2.7		-2.7		-5.0	
	750° to 1000°C	-2.0		-2.1		-1.3		-1.1		-2.6	
Thermal Base Coefficient											
$\frac{1}{nf}\frac{\Delta nf}{\Delta T}$	20° to 500°C	0		+2.9		+3.3		+2.2		+3.0	
	500° to 750°C	+0.5		+3.9		+4.1		-0.9		+3.9	
	750° to 1000°C	+0.2		+3.8		+4.1		-4.2		+4.2	

were identical to those previously measured. So that the difference could be more clearly understood, a modification to the assembly was made and the experiments repeated. The modification consisted of removing the C/U 5000 fuel elements immediately adjacent to the test sample and replacing them with the heterogeneous array of which the major part of the assembly had consisted; i.e., one C/U 859 fuel element and five all-graphite columns. The characteristic C/U atom ratio for the assembly was about 5465. The reactivity worth of the thermal absorbing samples, such as boron, U-235, and U-233, all increased by about 20% whereas the resonance absorbers, such as depleted uranium and thorium, essentially showed no change. The reactivity worth seemed quite sensitive to the core material immediately surrounding the sample or to the thermal spectrum at the location of the measurement.

A reanalysis was made in 1972, using the updated neutron spectrum code MICROX (Ref. 8-2) to calculate the effective broad group cross sections, and the calculated results were essentially the same as those obtained previously. The calculated worths were still too high by about 10%.

A reanalysis of this assembly was recently initiated using the present HTGR design methods. This analysis concentrated on more explicit details in the following analytical areas:

1. Effective cross sections in each of the specific core regions.

2. A refined description of the core region adjacent to the central exact C/U 5000 fuel.

3. Effect of impurities on calculated worths.

4. Effect of in-core perturbations caused by control rods, safety rods, and nuclear fuses on the calculated reactivity worths.

The results of this analysis also agree closely with those previously calculated. The calculated reactivity worth for the different sample materials is still about 10% higher than that measured. If the same impurity content is used as was used in the analyses for the other four critical assemblies, C/U 432 through C/U 2500, the calculated k_{eff} for the critical assembly agrees more closely with that measured, 0.004 Δk high. However, this does not necessarily represent the best estimate or the nominal impurity content, but rather what is thought to be an upper limit of the parasitic impurity.

It should be noted that although the C/U atom ratio is used to characterize the core assembly, none of the five core assemblies at the critical facility contained thorium, and consequently they do not correspond to the same thermal spectral index as used in the HTGR cores. For a C/Th atom ratio of 200, about 20% of the thermal absorptions are in the thorium and would affect the equivalent C/U atom ratio.

For the C/U 5000 core assembly, because of the lighter uranium loading, the neutrons diffuse further within the core. It has been assumed in all of the analyses for these cores that the presence of control rods or nuclear fuses within the assembly did not affect the reactivity measurements and, therefore, was ignored in the analysis. There is an indication in this reanalysis that this is not true for the 5000 assembly and that a two-dimensional analysis may be required.

A more complete report on the reanalysis of the C/U 5000 HTGR critical assembly is contained in a topical report, now in preparation, covering both the HTGR and HTLTR critical experiment programs. A short summary of the main results is given below.

Two different nuclear models were selected. The basic difference between the models is in the fuel cell description in the buffer region. In the first model, only the graphite columns are included in the outer

region of the radial cell surrounding the C/U 859 fuel element, whereas in the second model the outer region contains the graphite elements and the C/U 5000 fuel elements.

The analysis to determine the effective cross sections was made with two-region MICROX (Ref. 8-2) calculations for each of the core regions. The broad group structure was identical to that used in the HTGR design analysis and consisted of five fast groups and four thermal groups. The leakage for each core region was introduced into the spectrum calculation as group-dependent bucklings obtained from a previously calculated radial diffusion calculation.

Most of the results summarized in Table 8-15 seem quite reasonable and are consistent with the previous analysis. The calculated effective multiplication factor, k_{eff}, for the critical assembly is closer to the measured value, but this was because the parasitic impurity content was chosen to be consistent with the values used in the analysis for the earlier assemblies. The real boron equivalent content is unknown and since a better estimate of the impurities is not possible, it was thought that the same values as used in the other assemblies would be better. As a result, better agreement with the measured k_{eff} is obtained. This does not significantly affect the calculated values of the reactivity worths.

A different representation of the buffer region (model 1 versus model 2) has essentially no change on the calculated results for either k_{eff} or the sample reactivity worth.

It has been suggested that in-core perturbations caused by the presence of control rods or nuclear fuses might have an effect on the measured results. Since the core is lightly loaded, the migration length is quite large and perturbations can have an effect even at quite a distance from the test cell location. The previous analysis had considered the core to be homogeneous, and the measured k_{eff} was adjusted by experimental measurements to account

TABLE 8-15

CALCULATED REACTIVITY WORTHS AND k_{eff} FOR THE C/U 5000 CORE ASSEMBLY

Model Description	k_{eff}	Boron Worth($) 0.45 g Element	U-235 Worth($) 1718 Fuel Element	Thorium Worth($) 500 g Element
Measured	1.013	-0.341	0.216	-0.330
Original Analysis[a]	1.023	-0.378	0.247	-0.349
Original Analysis[a]	1.025	-0.367	0.232	-0.350
Reanalysis Model 1[b]	1.018	-0.361	0.236	-0.349
Model 2[b]	1.0176	-0.360	0.234	-0.349
Reanalysis with Control Rod Effects[c]	1.007	-0.371	0.243	

[a] 30 broad groups — original calculations using GGC and GAZE — impurities reduced from that used in analysis for other critical core assemblies.

[b] HTGR methods — 9 broad groups with MICROX impurities consistent with other core analysis.

[c] Approximate control rod corrections introduced in analysis.

for these effects. The measurements were made in an assembly that was just critical, k_{eff} = 1.0, but it was experimentally determined that for a completely homogeneous core with no safety or control rods or nuclear fuses, the k_{eff} would be about 1.013.

To evaluate what effect this might have on the sample reactivity worths, an anlaysis was made where poison was added in an annulus at a radial distance where the control rods were approximately located. The poison was worth about the same as the experimental corrections for the in-core perturbations. The results of this analysis are also given in Table 8-15. The calculated reactivity worths are definitely affected and it makes the difference between calculated and measured even greater. To account for these effects properly, it should not be done by adding poison only but by removing carbon and fuel as well, and the analysis should really be multidimensional (xy). Further analysis to investigate these effects appears to be required.

ANALYSIS OF NEUTRON NOISE EXPERIMENTS IN LARGE HTGRs

A package of computer codes for the frequency analysis of random and partially random signals was assembled. These codes were used to frequency-analyze simulated time records containing a narrow frequency-band signal superimposed upon white noise. Such a signal, for example, might be intentionally introduced into a reactor or might be due to the onset of a malfunction. If the power in the narrow band is of the order of 10% of the total power in the record, then no difficulty is encountered in the analysis. However, when the fractional power is reduced to 1%, detection of the band becomes difficult. Because of the finite number of points in a time record, averaging of the power spectral densities obtained from the frequency analysis of separate records has been found useful in the detection of narrow band signals. This indicates that a signal averager should be incorporated in the experimental equipment used for neutron noise analysis.

A few cases of cross correlation analysis were run using artifically generated noise records correlated by a transfer function. It was found

that, in order to obtain reasonable statistical accuracy, it is necessary to use a lower frequency resolution than the one used in comparable cases for autocorrelation analysis. This indicates that it is easier to obtain good estimates of auto-power spectra than of cross-power spectra.

A draft of the final report on the results obtained was completed (Ref. 8-11). The report emphasizes some of the problems encountered in the measurement of power spectra and contains some recommendations as to the amount of effort which would be required for an effective use of the technique.

TEST ELEMENT PROGRAM

Fuel Test Element FTE-3

Fuel test element FTE-3 was removed from Peach Bottom core position A03-03 on January 7, 1972 after completing 132 EFPD of irradiation. Disassembly of the test element has been completed. Detailed plans for the postirradiation examination and initial results of the postirradiation examination were reported in the previous Quarterly Progress Report (Gulf-GA-A12599).

The fuel combinations used in the outer beds of the test element are relevant to the initial and recycle cores of the large HTGR. These fuel rod particle blends include UO_2 TRISO/ThO_2 BISO, UC_2 TRISO/ThC_2 BISO, $(Th,U)C_2$ TRISO/ThC_2 BISO, and $(Th,U)C_2$ TRISO/ThC_2 TRISO. Two fuel holes in each of the three graphite bodies contained fuel rods of a particular particle combination. All fuel rods are nominally 0.490 in. in diameter and 1.94 in. long. The rods were fabricated by the hot-injection process using pitch binder and natural-flake graphite filler followed by a heat treatment at 1800°C. Both the fuel particles and fuel rods were made in production equipment using production processes and quality control techniques. The UC_2 kernels used were carried over from Phase 1 test element production, and the UO_2 and ThO_2 kernels were provided by Oak Ridge National Laboratory. The $(Th,U)C_2$ kernels, which have a nominal Th:U ratio of 2.71:1, were spheroidized for this phase of the test element program.

All fuel rods were removed from the three graphite bodies without difficulty and were in excellent condition. Photographs of representative fuel rods containing each type of particle combination, taken during the visual examination, are shown in Figs. 8-6 through 8-9.

Dimensional measurements were taken on ninety of the 336 fuel rod tests. These fuel rod dimensional change data are currently undergoing analysis and will be reported at a later date.

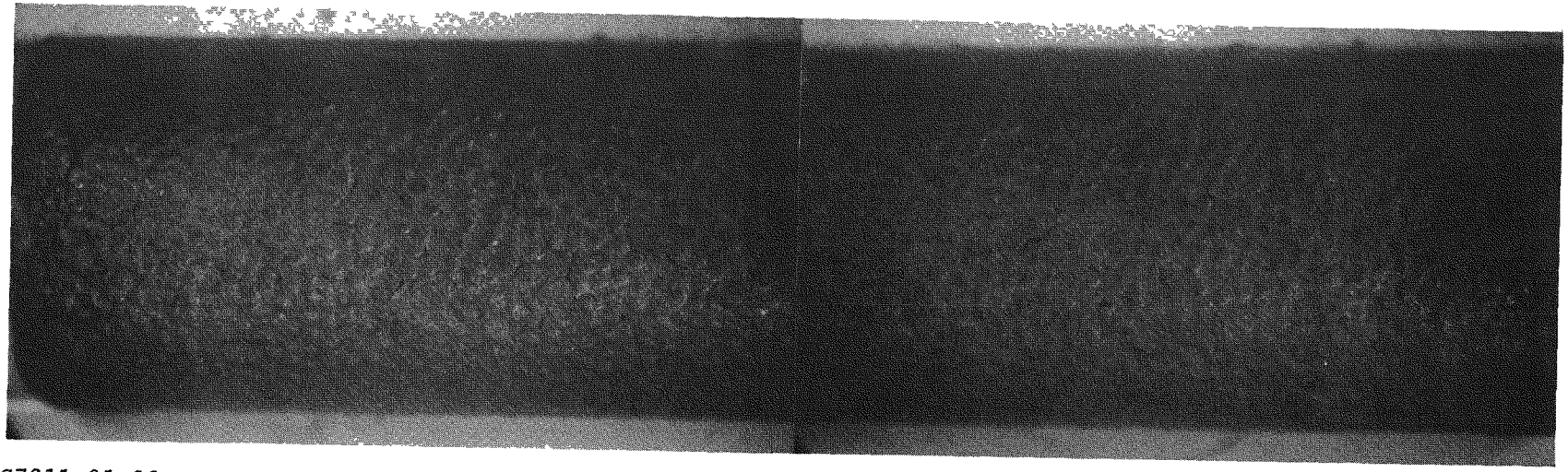

S7311-31,32

~4X

S7311-28 4X

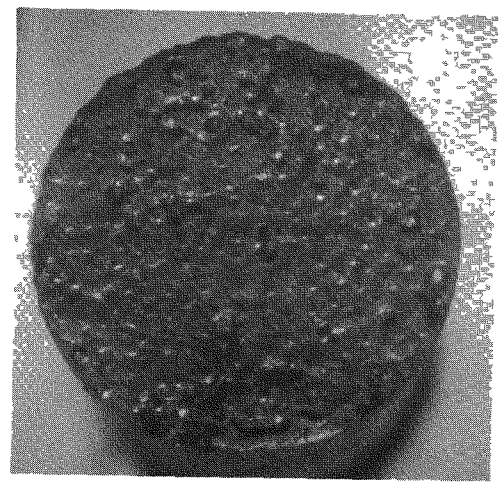

S7311-27 4X

Fig. 8-6. Fuel rod 1-1-9 after irradiation in FTE-3 to 0.6 x 10^{21} n/cm^2 at 1050°C. Rod 1-1-9 contained a blend of UO_2 TRISO fissile and ThO_2 BISO fertile particles.

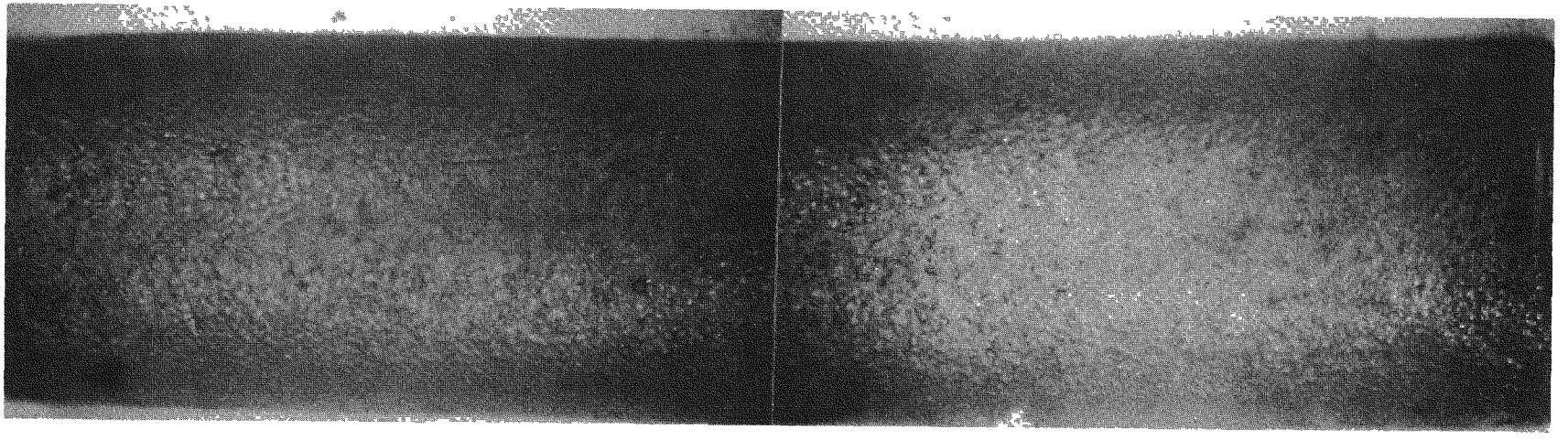

S7311-23,24 ~4X

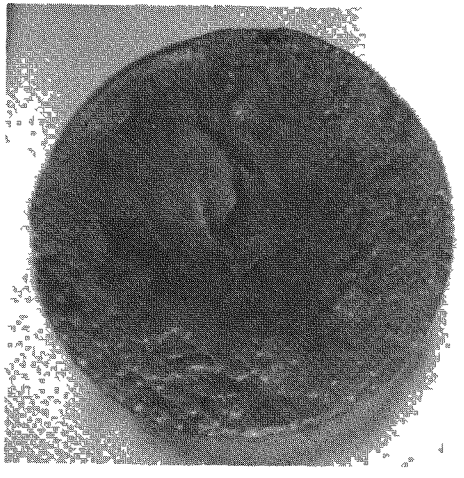

S7311-22 ~4X

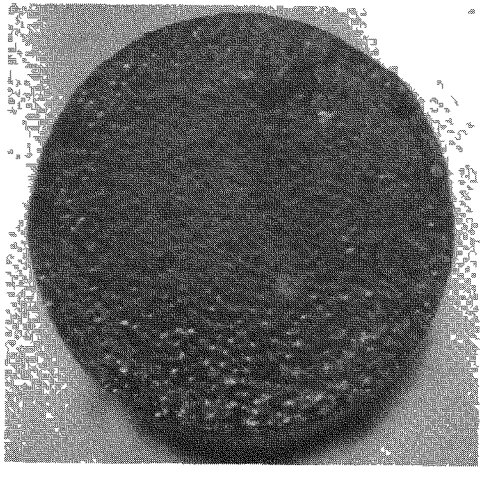

S7311-21 ~4X

Fig. 8-7. Fuel rod 2-8-7 after irradiation in FTE-3 to 0.6 x 10^{21} n/cm^2 at 1175°C. Fuel rod 2-8-7 contained a blend of UC_2 TRISO fissile and ThC_2 BISO fertile particles.

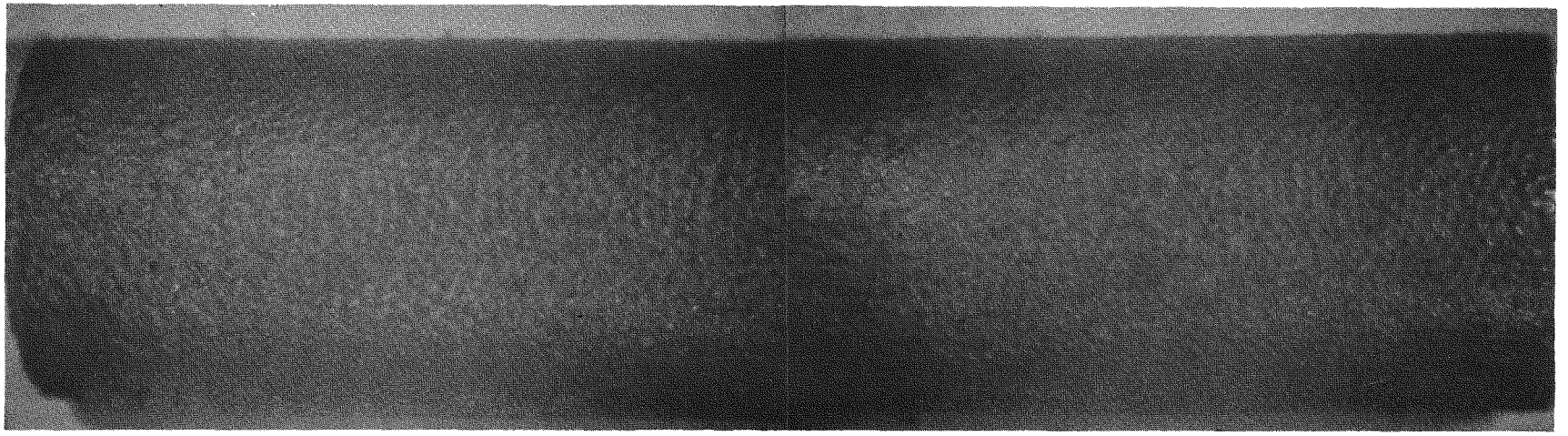

S7311-11,12 ∿4X

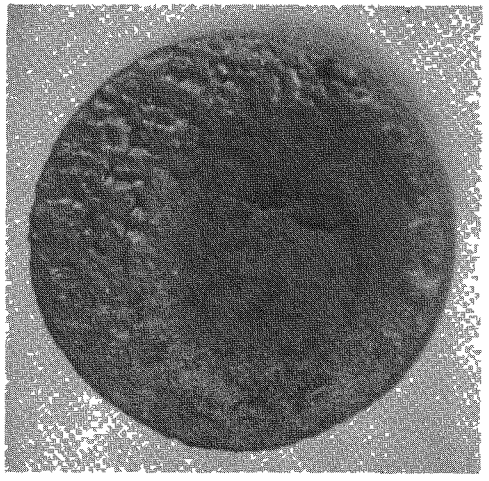

S7311-9 ∿4X

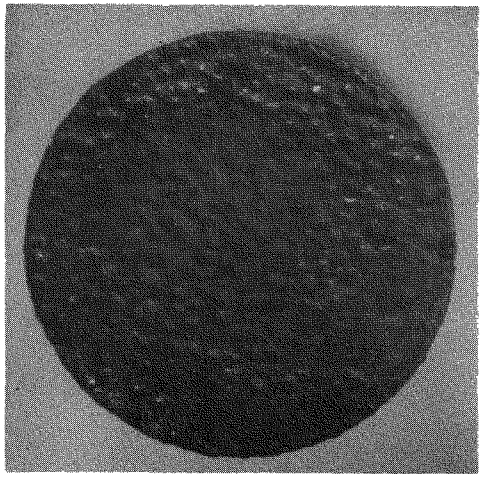

S7311-10 ∿4X

Fig. 8-8. Fuel rod 2-3-7 after irradiation in FTE-3 to 0.6 x 10^{21} n/cm^2 at 1150°C. Fuel rod 2-3-7 contained a blend of $(Th,U)C_2$ TRISO fissile and ThC_2 BISO fertile particles.

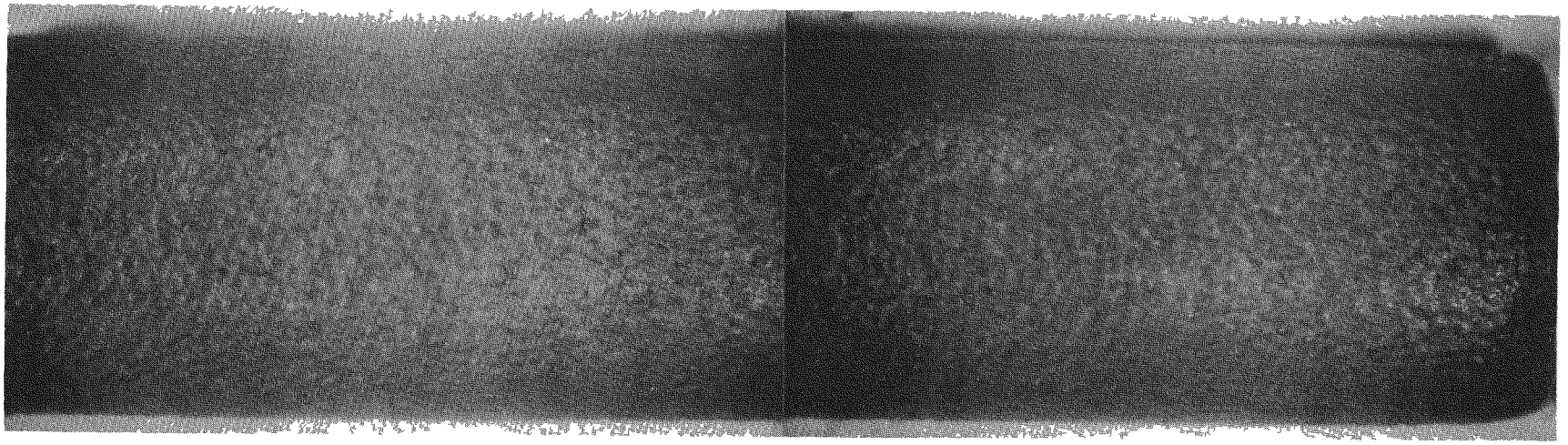

S7311-15,16 ∿4X

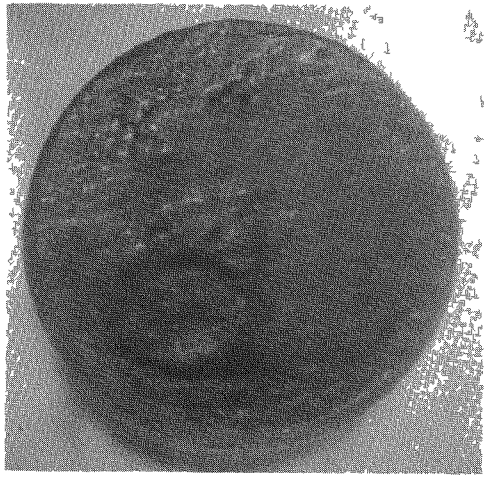

S7311-20 ∿4X

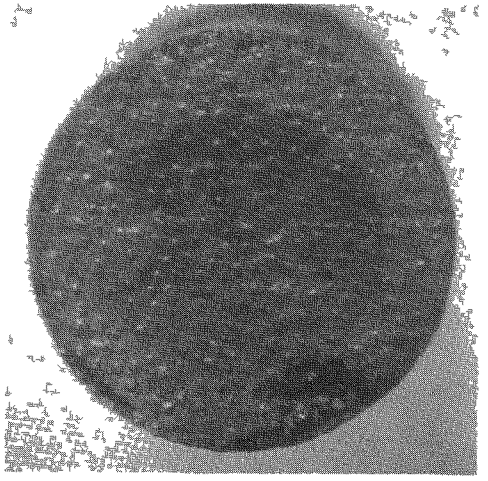

S7311-19 ∿4X

Fig. 8-9. Fuel rod 2-5-7 after irradiation in FTE-3 to 0.6 x 10^{21} n/cm^2 at 1175°C. Fuel rod 2-5-7 contained a blend of (Th,U)C_2 TRISO fissile and ThC_2 TRISO fertile particles.

Metallographic examination, postirradiation fission gas release measurements (TRIGA activation), and disintegration leach studies were conducted on selected fuel rod samples. Other analyses either planned or currently in progress include autoradiography on the fuel body graphite slices, graphite fuel body integrity and residual stress analysis, and additional graphite dimensional change data.

Metallographic examination was conducted on fuel rods 2-3-7, 2-2-7, 2-8-7, and 2-5-7, which contained each of the four representative particle blends. These fuel rods were from the center of body 2, which received the peak fast neutron exposure at the highest irradiation temperature. Photomicrographs of the fuel rod cross sections, matrix, and representative coated particles are shown in Figs. 8-10 through 8-17.

Coated particle fuel and matrix graphite in the four rods examined metallographically generally looked good. In fuel rods 2-5-7, 2-8-7, and 2-3-7, which contained carbide fuel, the onset of hydrolysis of the low-exposure carbide fuel early during the examination made it impossible to determine coating failure via metallography. However, no particle failure was observed in fuel rod 2-2-7, which contained oxide fuel particles.

No fuel kernel migration or other thermochemical effects were observed in either the carbide or oxide fuel particles. In both the TRISO coated oxide and carbide fuel particles, the buffer coatings densified slightly and debonded from the IPyC coating, leaving the IPyC coating bonded to the SiC coating. The small fraction of cracks noted in the OPyC coatings in the composite photomicrographs of the fuel rod cross sections (see Figs. 8-10, 8-12, 8-14, and 8-16) was attributed to metallographic polishing since no mounting resin was present in the cracks.

The graphite matrix in each rod examined was in good condition. No matrix cracking or signs of matrix-coating interaction were observed.

One of the primary objectives of the examination of the FTE-3 fuel rod samples was to develop a technique to disassociate irradiated fuel

L7311-57 (a) 650X

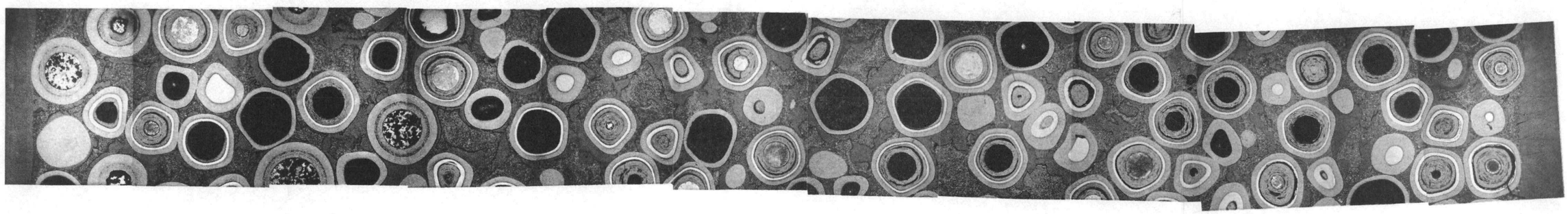

L7311 (61-72) (b) ~28X

Fig. 8-10. Photomicrographs of fuel rod 2-3-7 after irradiation in FTE-3 to 0.6 x 10^{21} n/cm^2 at 1150°C: (a) typical appearance of matrix graphite, and (b) composite showing radial cross section

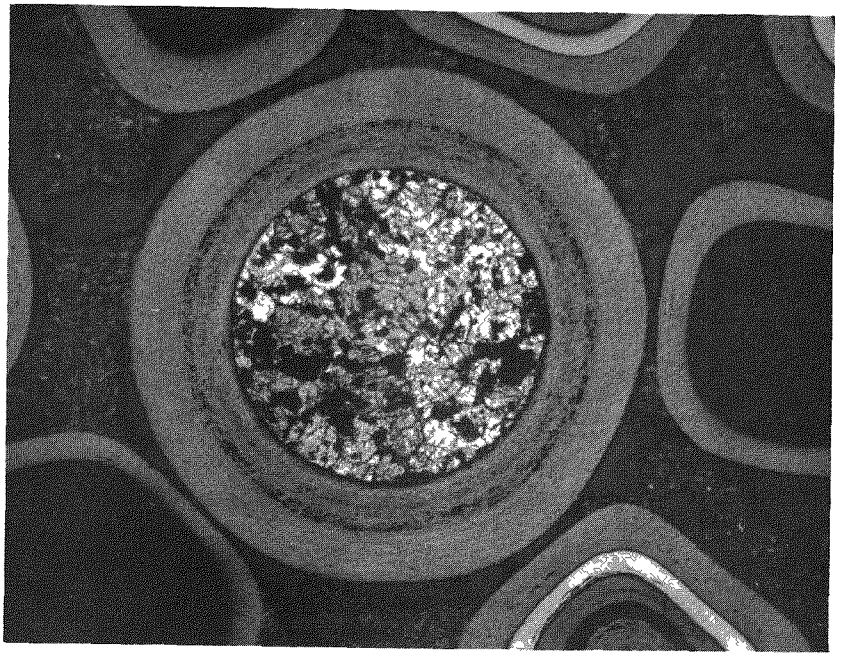

L7311-54 (a) 100X

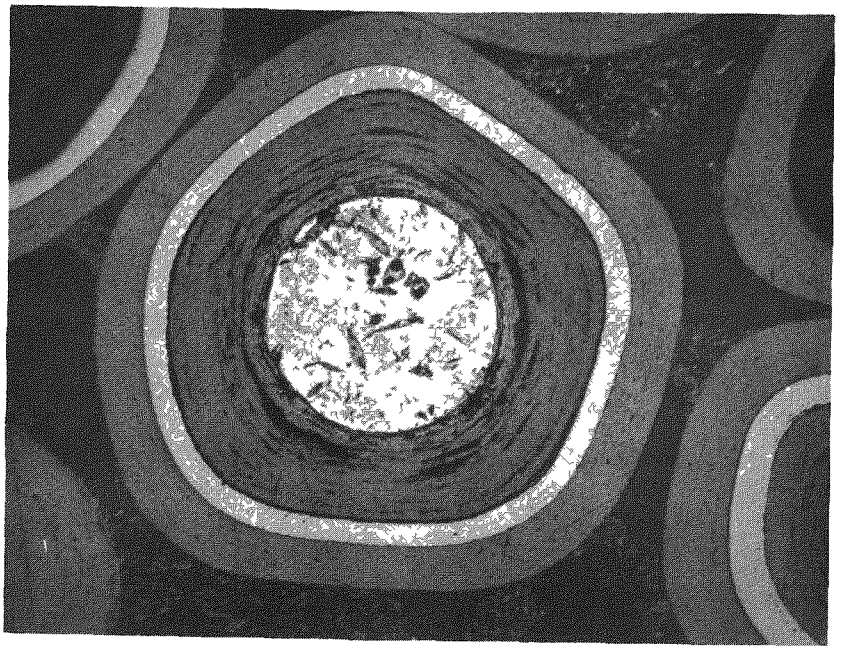

L7311-52 (b) 155X

Fig. 8-11. Photomicrographs of representative particles from fuel rod 2-3-7 after irradiation in FTE-3 to 0.6 x 10^{21} n/cm^2 at 1150°C: (a) ThC_2 BISO particle, and (b) $(Th,U)C_2$ TRISO particle

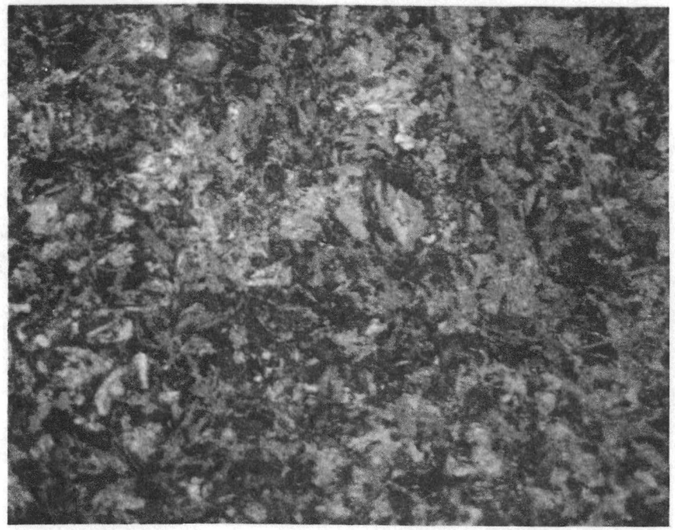

L7311-36 (a) 650X

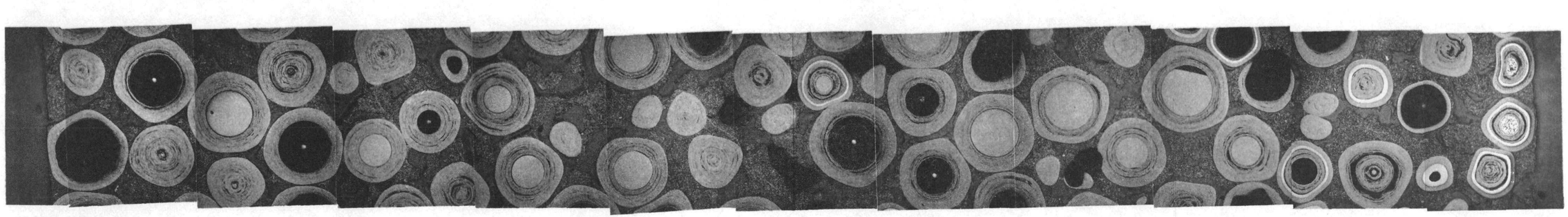

L7311 (37-48) (b) ∿28X

Fig. 8-12. Photomicrographs of fuel rod 2-2-7 after irradiation in FTE-3 to 0.6 x 10^{21} n/cm^2 at 1175°C: (a) typical appearance of matrix graphite, and (b) composite showing radial cross section

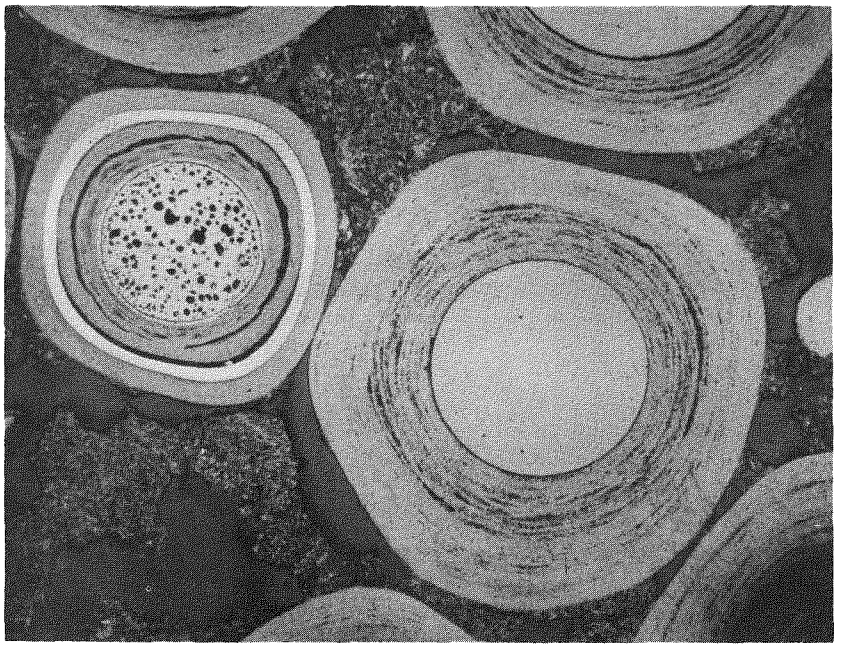

L7311-24 (a) 85X

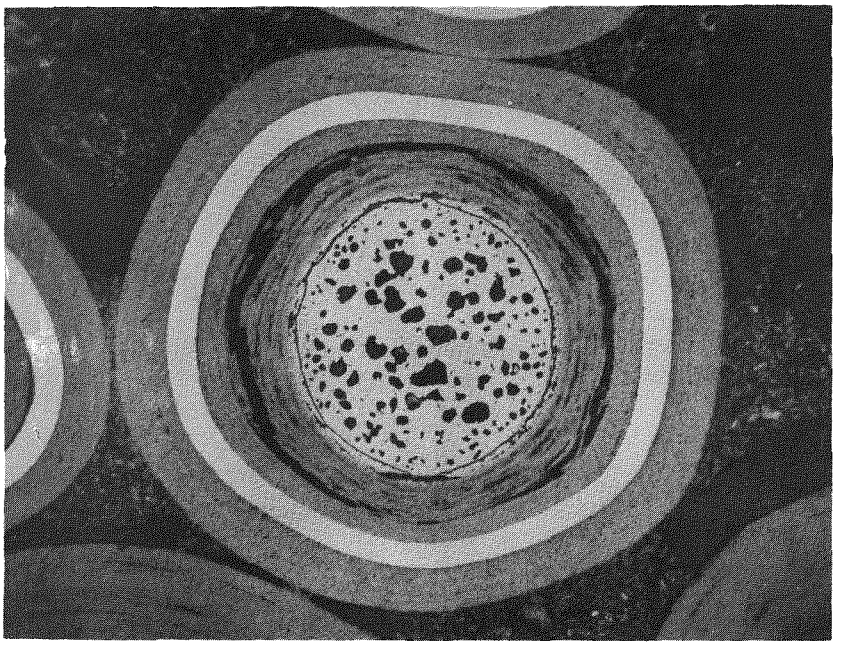

L7311-30 (b) 150X

Fig. 8-13. Photomicrographs of representative particles from fuel rod 2-2-7 after irradiation in FTE-3 to 0.6 x 10^{21} n/cm^2 at 1175°C: (a) UO_2 TRISO and ThO_2 BISO particles, and (b) UO_2 TRISO particle

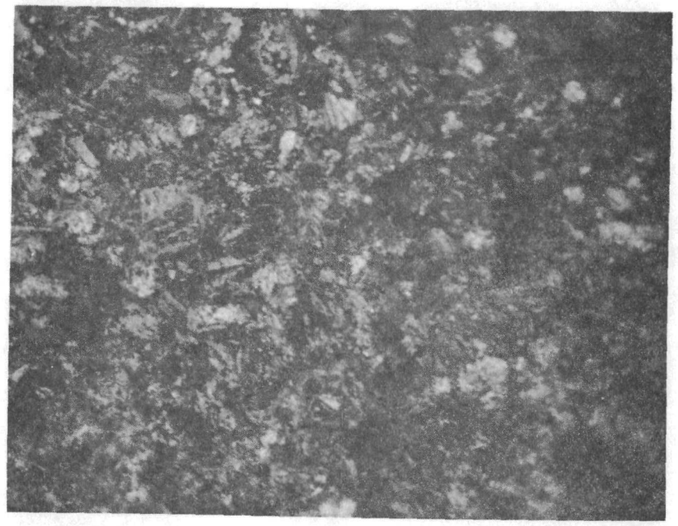

L7311-120 (a) 650X

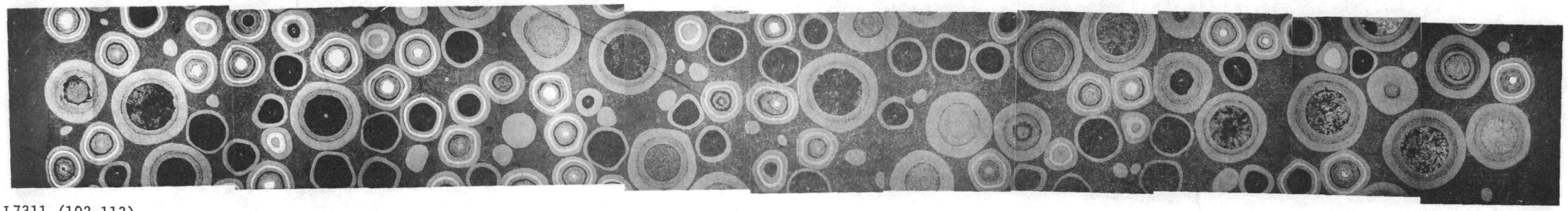

L7311 (102-113) (b) ~30X

Fig. 8-14. Photomicrographs of fuel rod 2-8-7 after irradiation in FTE-3 to 0.6 x 10^{21} n/cm^2 at 1175°C: (a) typical appearance of matrix graphite, and (b) composite showing radial cross section

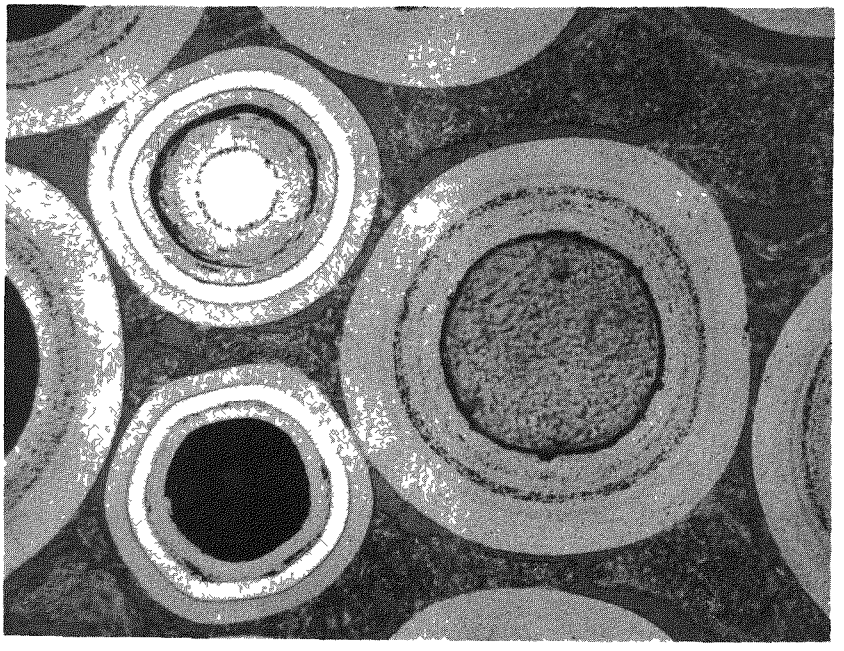

L7311-114 100X

Fig. 8-15. Photomicrograph of representative UC_2 TRISO and ThC_2 BISO particles from fuel rod 2-8-7 after irradiation in FTE-3 to 0.6×10^{21} n/cm^2 at 1175°C

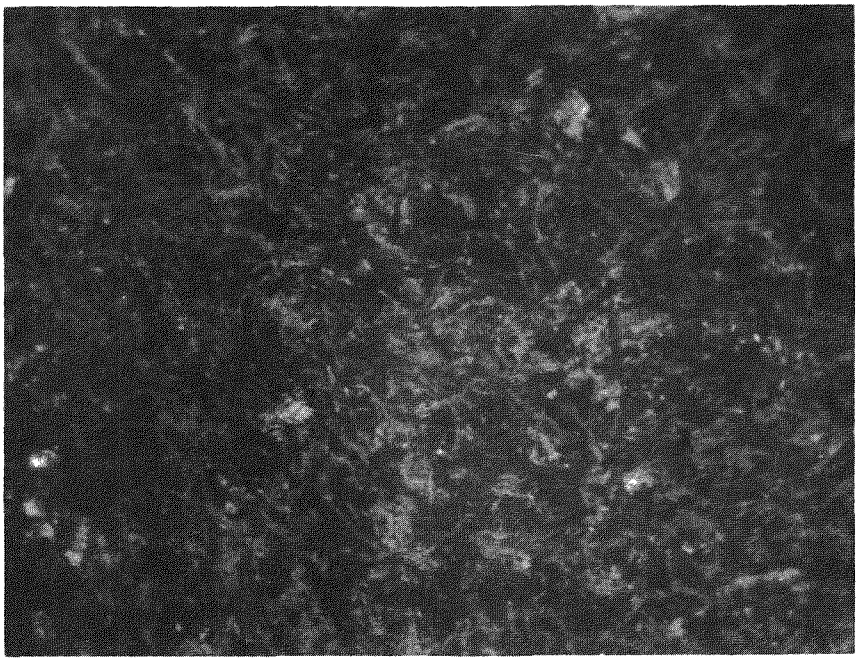

L7311-101 (a) 650X

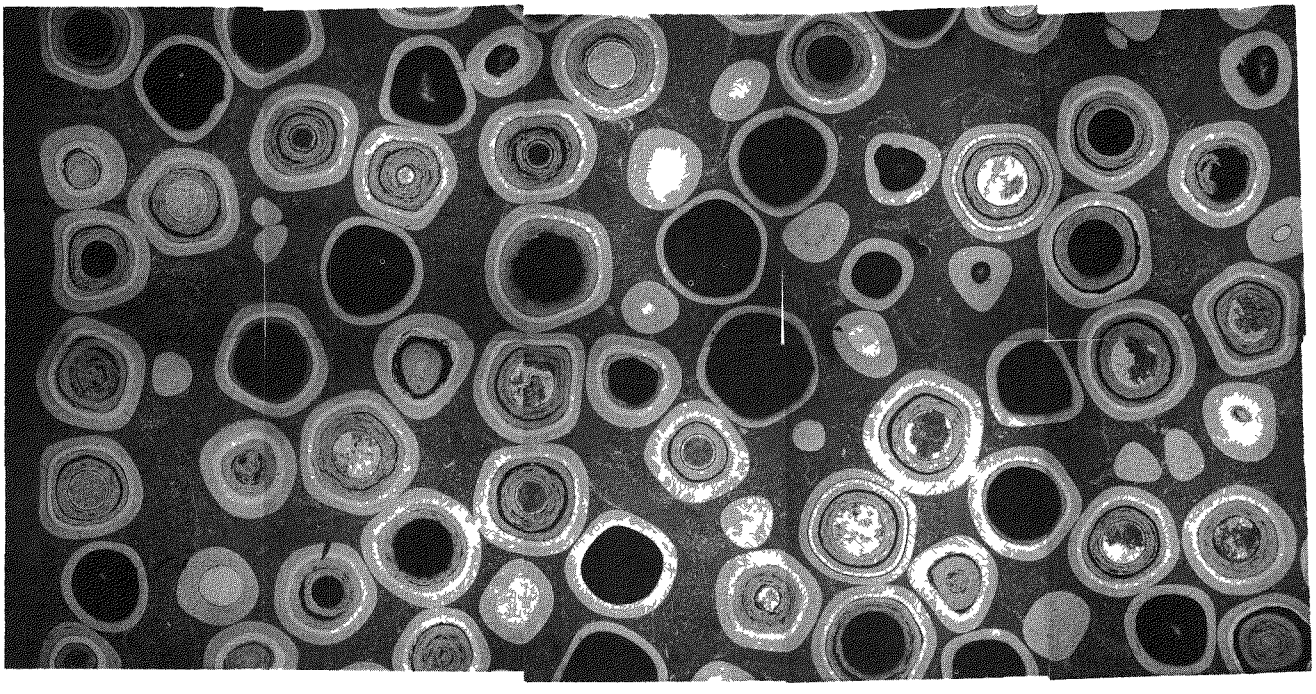

L7311 (87-96) (b) ∿29X

Fig. 8-16. Photomicrographs of fuel rod 2-5-7 after irradiation in FTE-3 to 0.6×10^{21} n/cm^2 at 1175°C: (a) typical appearance of matrix graphite, and (b) composite showing radial cross section

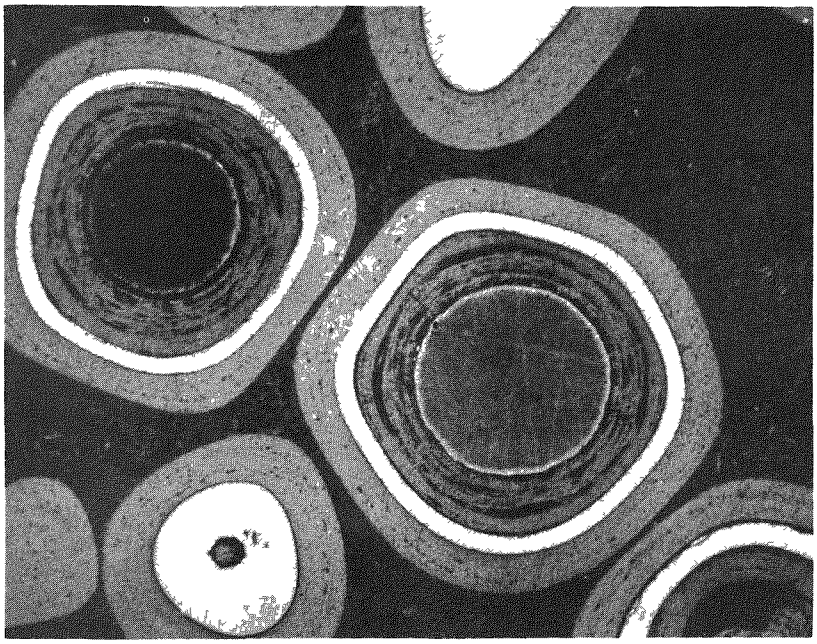

L7311-85 (a) 100X

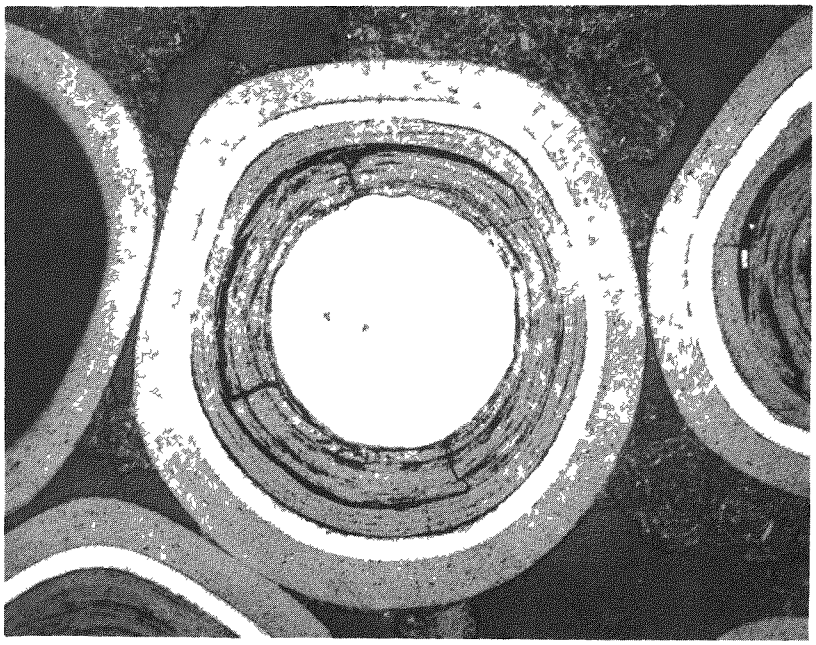

L7311-97 (b) 150X

Fig. 8-17. Photomicrographs of representative particles from fuel rod 2-5-7 after irradiation in FTE-3 to 0.6 x 10^{21} n/cm^2 at 1175°C: (a) (Th,U)C_2 TRISO particles, and (b) ThC_2 TRISO particle

rods, allowing separation of the coated fuel particles from the graphite matrix without damaging particle coatings. This operation allows a large number of particles irradiated in a bonded fuel rod to be examined using techniques applicable only to unbonded particle samples such as radiography and gamma spectroscopy. (A description of the disintegration-leach technique will be presented in a separate topical report.)

The results of electrolytic disintegration - acid leach studies conducted on five fuel rods irradiated in FTE-3 are reported in Table 8-16. Analysis of the fission product isotopes recovered in the leach solutions indicated coated particle failure fractions were <1.0% in all fuel rods examined. The low postirradiation fission gas release values (10^{-5} to 10^{-6} range) for these rods (see Table 8-16) also indicate negligible coated particle failure in these rods. Photomicrographs of coated fuel particles recovered from fuel rods 1-8-7 and 1-8-8 are shown in Figs. 8-18 and 8-19, respectively. Complete disassociation of the coated particles from the surrounding graphite matrix was achieved using the current densities and disintegration times noted in Table 8-16. Metallographic examination was conducted on samples of fuel particles recovered from fuel rods 1-8-7 and 1-8-8 to investigate the effects of the electrolyic disintegration on the integrity of the particle OPyC coatings. Representative photomicrographs of particles recovered from these rods are shown in Figs. 8-20 and 8-21. No signs of OPyC degradation were observed in either sample. These results indicate irradiated fuel rods can be effectively disassembled without damaging the constituent coated particle fuel.

Fuel rods irradiated in FTE-3 are being annealed at temperatures up to 2000°C to determine (1) time-temperature failure rate curves, and (2) the effects of hydrolysis on the R/B of exposed carbide fuel. Rods selected for this work contained UC_2 TRISO coated fissile and ThC_2 BISO coated fertile particles. The conditions and results of this experiment are given in Table 8-17. The fuel rod was annealed at 1600°C for 520 hr in dry helium. R/B measurements were frequently performed at 1100°C throughout the anneal. No increase in R/B was observed until a total of 520 hr

TABLE 8-16
RESULTS OF POSTIRRADIATION FISSION GAS RELEASE MEASUREMENTS AND ELECTROLYTIC DISINTEGRATION - ACID LEACH STUDIES ON SELECTED FUEL RODS IRRADIATED IN FTE-3

Rod I.D. Number[a]	Particle Blend	Postirradiation Fission Gas Release[b]	Current Density (amps/cm^2)	Disintegration Time (hr)	Acid Leach Time (hr)	Fission Product Isotopes Recovered (% of total inventory)
1-2-7	UO_2 TRISO/ThO_2 BISO	3.4×10^{-6}	--	--	--	--
2-5-8	$(Th,U)C_2$ TRISO/ThC_2 TRISO	2.1×10^{-5}	--	--	--	--
3-1-7	UO_2 TRISO/ThO_2 BISO	3.5×10^{-6}	--	--	--	--
3-7-8	UC_2 TRISO/ThC_2 BISO	1.2×10^{-5}	1.25	8	14	<<1.00[c]
2-2-8	UO_2 TRISO/ThO_2 BISO	4.2×10^{-5}	1.25	10	63	0.06
1-2-8	UO_2 TRISO/ThO_2 BISO	3.7×10^{-6}	0.20	52	2	0.20
1-8-7	UC_2 TRISO/ThC_2 BISO	3.6×10^{-6}	0.20	100	2	<<1.00[c]
1-8-8	UC_2 TRISO/ThC_2 BISO	3.4×10^{-6}	1.35	6	2	0.13

[a] First number: fuel body number
Second number: hole number in fuel body
Third number: rod number in rod stack (numbered from bottom).

[b] R/B for Kr-85m at 1100°C. Not corrected for steady-state conditions.

[c] Percentage of recovered isotopes may be considerably lower than 1%; however, counting errors associated with low concentrations of Pa-233 made analysis of fertile (U-233) particle contributions difficult.

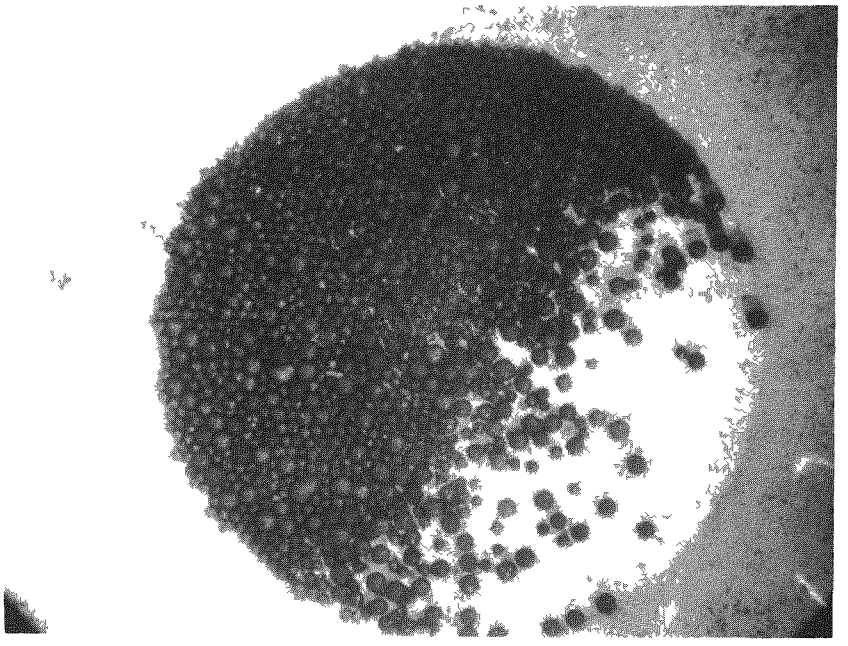

S7311-34 4X

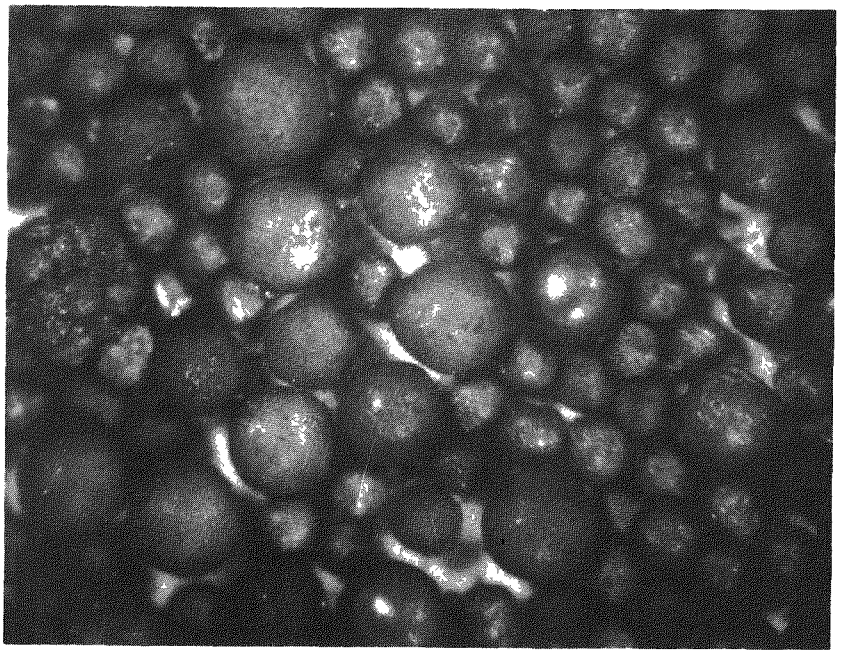

S7311-35 20X

Fig. 8-18. Photomicrographs of a portion of the fuel particles recovered from fuel rod 1-8-7 after it was electrolytically disintegrated and acid leached

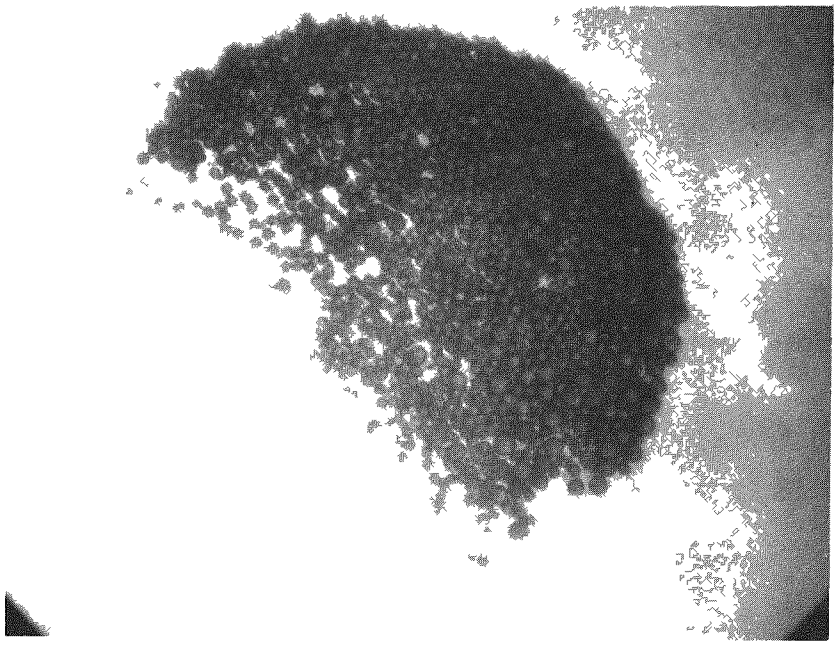

S7311-36 4X

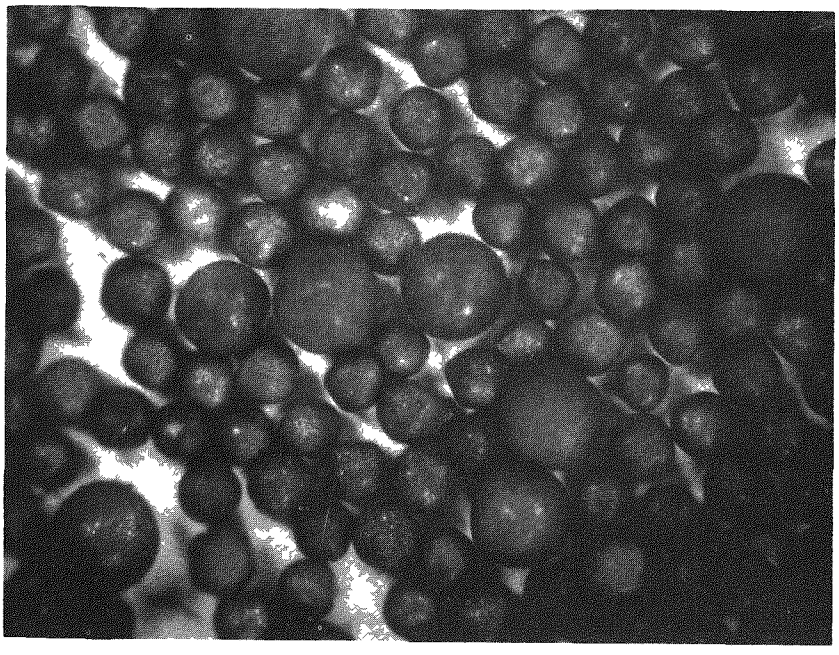

S7311-37 20X

Fig. 8-19. Photomicrographs of a portion of the fuel particles recovered from fuel rod 1-8-8 after it was electrolytically disintegrated and acid leached

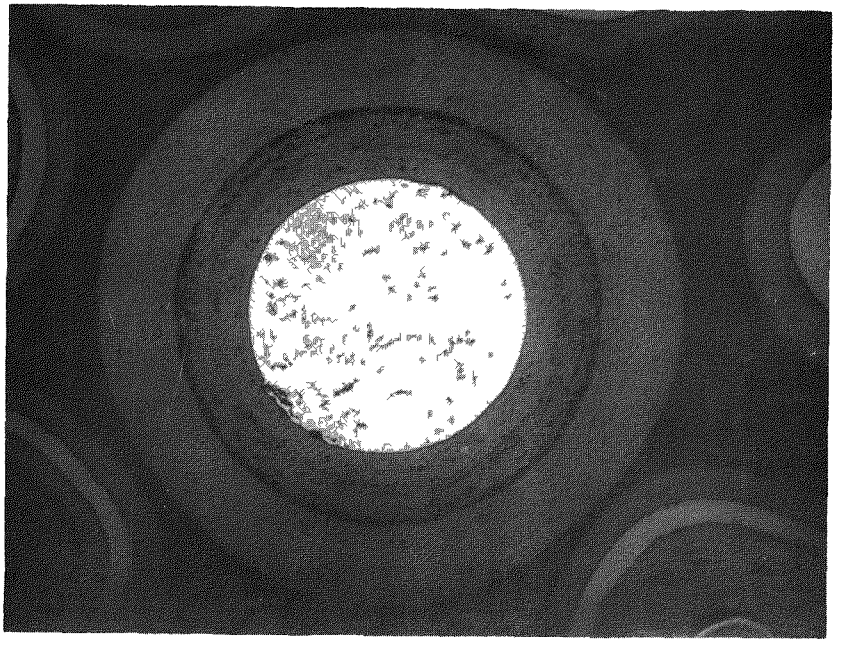

L7311-136 (a) 150X

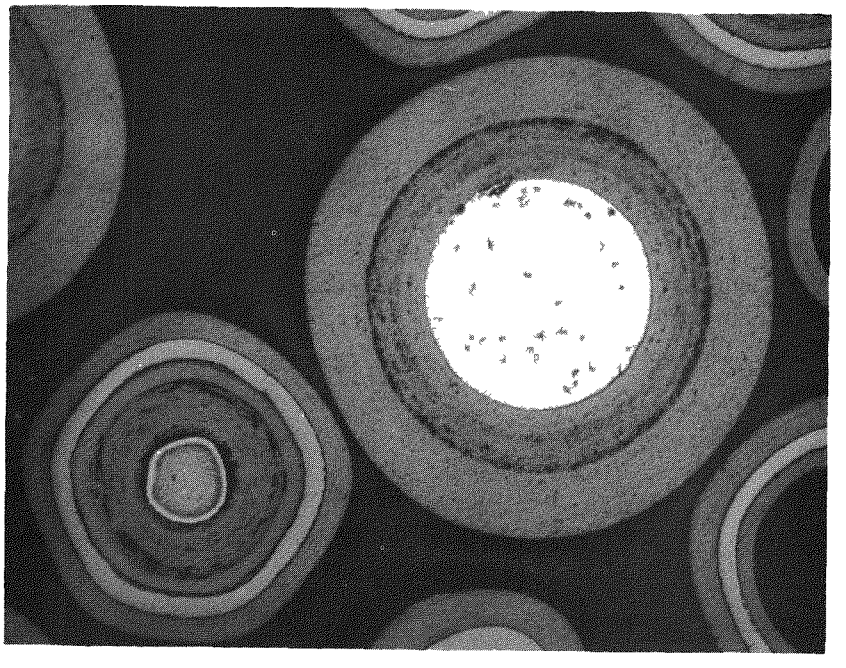

L7311-138 (b) 115X

Fig. 8-20. Photomicrographs of representative particles from fuel rod 1-8-8 after irradiation in FTE-3 to 0.5 x 10^{21} n/cm^2 at 1000°C: (a) ThC_2 BISO particle, and (b) UC_2 TRISO and ThC_2 BISO particles. Metallographic examination was conducted after the fuel rod was electrolytically disintegrated and acid leached.

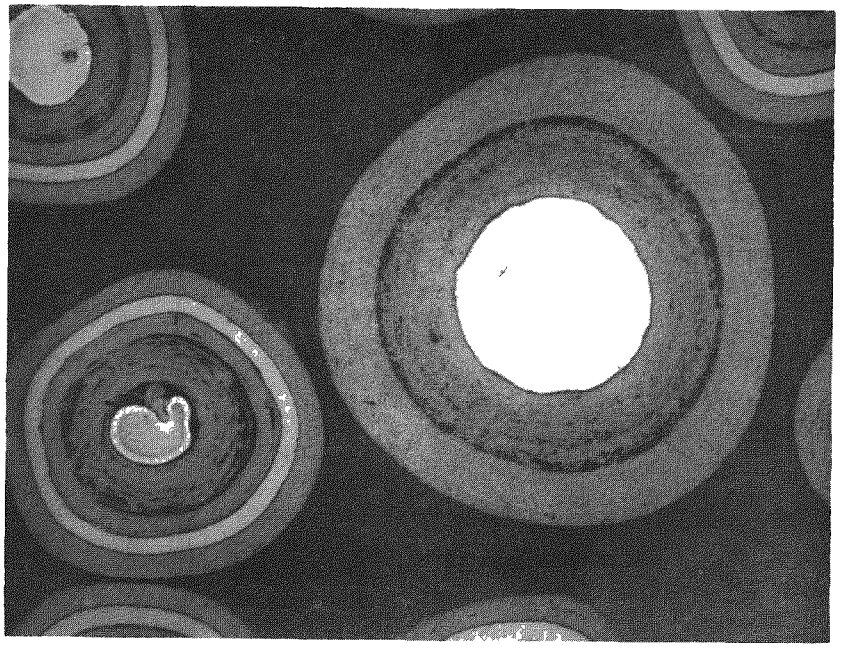

L7311-130 (a) 100X

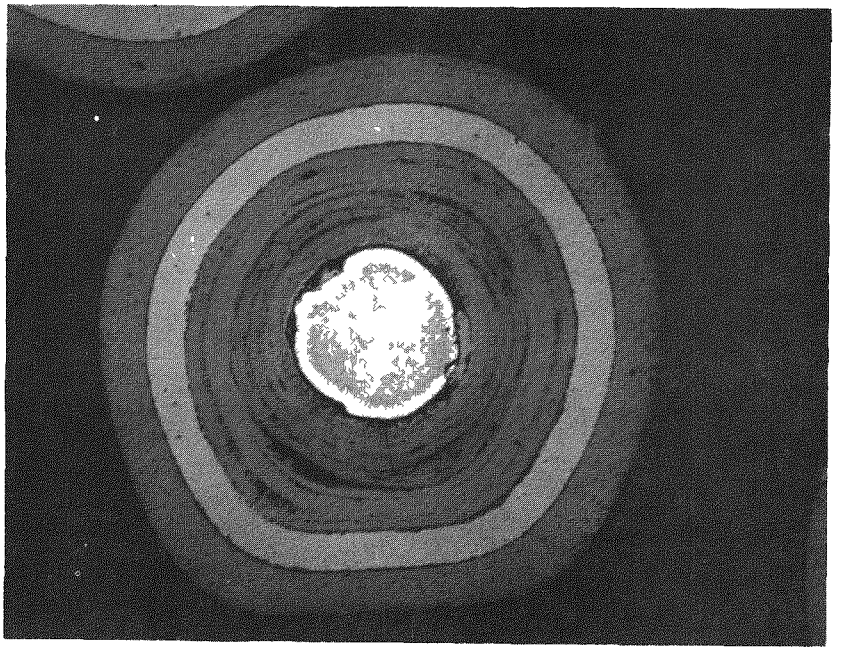

L7311-133 (b) 225X

Fig. 8-21. Photomicrographs of representative particles from fuel rod 1-8-7 after irradiation in FTE-3 to 0.5 x 10^{21} n/cm^2 at 1000°C: (a) UC_2 TRISO and ThC_2 BISO particles, and (b) UC_2 TRISO particle. Metallographic examination was conducted after the fuel rod was electrolytically disintegrated and acid leached.

TABLE 8-17
FISSION GAS RELEASE FROM FAILED, HYDROLYZED FTE-3 FUEL ROD 1-7-8

Run No.	Sample Condition	Total Anneal Time (hr)	Incremental Anneal Time (hr)	H_2O Content (ppmv)	Kr-85m R/B at 1100°C
1	As received	0	0	0	2.1×10^{-5}
2	Annealed at 1600°C	0-354	354	0	1.6×10^{-5} [a]
3	Annealed at 1600°C	354-520	166	0	2.1×10^{-4}
4	Annealed at 900°C	520-760	240	100	3.3×10^{-4} [b]
5	Annealed at 900°C	760-784	24	30,000	1.1×10^{-3}
6	Annealed at 1100°C	784-930	150	0	5.7×10^{-4}

[a] Average of 20 R/B determinations during the anneal.

[b] Average of 5 R/B determinations.

at 1600°C had accumulated, after which a Kr-85m R/B of 2.1×10^{-4} was determined. This value yields a failed fraction of about 0.04 assuming R/B (Kr-85m at 1100°C) for failed fuel $[(R/B)_f]$ in a rod is 5×10^{-3}. The value $(R/B)_f$ for Kr-85m at 1100°C of 5×10^{-3} has been determined in a prior series of tests.

This same rod was then exposed to 100 ppm water in the helium purge gas for approximately 240 hr at 900°C without a significant change in R/B. The moisture content of the purge gas was then increased to approximately 30,000 ppm H_2O for 24 hr, after which the Kr-85m R/B increased an order of magnitude indicating partial degradation of the kernel material. THe fuel rod was then annealed for 150 hr at 1100°C in dry helium resulting in a lowering of the Kr-85m R/B to a level approaching that found for failed fuel prior to hydrolysis. These results are encouraging. They indicate that the increase in R/B by hydrolysis of failed irradiated carbide fuel particles in a fuel rod will be much slower and lower then predicted. Additional failure rate annealing and hydrolysis experiments are being conducted at 1800° and 2000°C.

Center spine samples from FTE-3 are being analyzed for metallic fission product diffusion in fuel particle coatings and graphite fuel block material. Fission product release samples are composed of loose fuel particles contained in a small inner graphite crucible surrounded by matrix material inside an outer graphite crucible. These samples have been separated into component parts and gamma counted to determine a gross fission product concentration.

The inner and outer graphite crucibles are currently being sectioned on a lathe to determine fission product concentration profiles through the crucible wall. A knowledge of the fission product concentration between the inner wall-matrix and outer wall-matrix results in a partition coefficient (ϕ) that is a necessary input to the FIPER code for calculating fission product release in HTGR systems.

Additional diffusion coefficient data are being obtained from spine samples consisting of graphite matrix material tagged with Cs, Sr, Sm, and Ba contained in an H-327 graphite crucible. A gross gamma count was made on the matrix material and the crucibles sectioned to determine concentration profiles for the isotopes of interest. All the crucibles have been sectioned and gamma counted and the data are being analyzed to determine partitio. coefficients and diffusion coefficients.

Several fuel particle batches from the fission product release samples have been selected and annealing experiments on the loose particles are under way. During the anneal, fission products released from the particles are collected on a cold finger located near the particles. The fission products are removed from the cold finger by acid leaching and the solutions are gamma counted. The release curves obtained in this way are then used to determine diffusion coefficients in pyrocarbon coatings and kernels. Particle samples are being annealed at 1300°, 1500°, and 1650°C.

Plans for the postirradiation measurement of locked-in longitudinal graphite stresses in the fuel bodies of FTE-3, -4, -6, -14, and -15 have been completed and construction of necessary equipment is currently being performed in the hot cell. A method involving an axial strip cutting and bowing measurement technique will be used whereby axial strips are cut from full-length irradiated fuel bodies and the incremental bowing of these strips is measured by a simple dial guage jig in the hot cell. Information from TAC2D thermal analyses of the 6- and 8-hole telephone dial test elements will provide the basis for determining the positions of the strips to be cut. Upon completion of the bowing measurements, the related stresses will be calculated and compared to stresses predicted by SAFE-GRAFITE.

Summary of FTE Results

The results obtained to date from the examination of fuel rods irradiated in FTE-3 are briefly summarized as follows:

1. Hot-injected fuel rods containing oxide and carbide fissile and fertile particle blends were irradiated in FTE-3 to a peak fast neutron exposure of 0.6×10^{21} n/cm^2 (E > 0.18 MeV) at temperatures up to 1175°C for 132 EFPD.

2. Visually all rods appeared to be in excellent condition, with no major occurrences of particle-matrix debonding or matrix cracking observed.

3. No signs of fuel kernel migration or other thermochemical effects were noted in either the oxide or carbide fuel particles.

4. An electrolytic disintegration technique was developed to disassociate intact irradiated fuel rods, allowing separation of the coated fuel particles and matrix graphite.

5. Less than 1.0% particle failure was determined for all fuel rods examined based on metalographic examination, postirradiation fission gas release measurements, and electrolytic disintegration - acid leach studies.

6. The increase in R/B due to the hydrolysis of failed, irradiated carbide fuel particles in fuel rods has been shown through this test to be lower than previously predicted. The rate of increase in R/B has also been shown to occur at a lower rate than previously predicted.

FTE-4, -6, -14, and -15 and RTE-1, -2, -5, -6, and -8

During the reporting period fuel test elements FTE-4, -6, -14, and -15 and recycle test elements RTE-1, -2, -5, -6, and -8 continued to operate well within the Peach Bottom HTGR.

The Peach Bottom reactor is now scheduled for shutdown in mid-September 1973 for the planned 702 EFPD reactor inspection. Plans are being made for removal of FTE-4 and -14 and RTE-2 during this shutdown.

REFERENCES

8-1. Archibald, R. J., and D. R. Mathews, "The GAF/GAR/GAND Fast Reactor Cross Section Preparation System, Vol. II, GAND2 and GFE2, Computer Programs for Preparing Input Data for the GAFGAR, GGC, and MICROX Codes from an ENDF/B Format Data File, Gulf General Atomic Report GA-7542 (Vol. II), 1973.

8-2. Wälti, P., and P. Koch, "MICROX, A Two-Region Flux Spectrum Code for the Efficient Calculation of Group Cross Sections," Gulf General Atomic Report Gulf-GA-A10827, April 14, 1972.

8-3. Lenihan, S. R., "GAZE-2, One-Dimensional, Multigroup, Neutron Diffusion Theory Code for the IBM-7090," General Dynamics, General Atomic Division Report GA-3152, 1962.

8-4. Lippincott, E. P., "Measurement of the Temperature Dependence of k_∞ for a $^{233}UO_2$-ThO_2 HTGR Lattice," Battelle Pacific Northwest Laboratories Report BNWL-SA-3896.

8-5. Lippincott, E. P., "Measurement of the Temperature Dependence of k_∞ for a $^{233}UO_2$-ThO_2 HTGR Lattice," USAEC Report BNWL-1561, Battelle Pacific Northwest Laboratories, 1971.

8-6. Oakes, T. J., "Measurement of the Neutron Multiplication Factor as a Function of Temperature for a $^{235}UC_2$-ThO_2-C Lattice," Battelle Pacific Northwest Laboratories Report BNWL-SA-3621.

8-7. Oakes, T. J., "Measurement of k_∞ as a Function of Temperature for a $^{233}UO_2$-ThO_2-C Lattice," USAEC Report BNWL-1601, Battelle Pacific Northwest Laboratories, 1972.

8-8. Newman, D. F., "Temperature Dependence of k_∞ for a ThO_2-PuO_2 HTGR Lattice," Battelle Pacific Northwest Laboratories Report BNWL-SA-4409.

8-9. Lippincott, E. P., "Measurement of Physics Parameters of a MSBR Lattice in the HTLTR," USAEC Report BNWL-1633, Battelle Pacific Northwest Laboratories, 1972.

8-10. R. G. Bardes, et al., "Results of HTGR Critical Experiments Designed to Make Integral Checks on the Cross Sections in Use at Gulf General Atomic," Gulf General Atomic Report, GA-8468, February 12, 1968.

8-11. Borgonovi, G. M., "An Assessment of Noise Analysis Techniques for Large HTGRs," to be published.

TASK IX
FUEL MATERIALS DEVELOPMENT

FUEL IRRADIATIONS

Capsule P13N

Description of Experiment

Capsule P13N is the fourth in a series of irradiation tests of candidate HTGR recyclable-type fuels, and is the first P-capsule to be monitored for in-pile fission gas release during irradiation. The capsule contained five cells in which fuel rods and unbonded particle samples were tested. This capsule was a companion to the capsule P13P experiment; capsule P13P is currently in the hot cell awaiting post-irradiation examination. The two primary objectives of these experiments were: (1) to compare oxide, carbide, and resin kernel performance at very high temperatures (1350° to 1500°C) to moderate fast fluences ($\sim 5.5 \times 10^{21}$ n/cm^2) in capsule P13N and at high temperatures (1050° and 1350°C) to high fast fluences ($\sim 8 \times 10^{21}$ n/cm^2) in capsule P13P, and (2) to determine coated particle and fuel rod dimensional changes as a function of irradiation temperature, fluence, and particle design.

A total of 22 fuel rods, 24 loose particle samples, and 175 piggy-back samples was irradiated in capsule P13N. Particle samples from parent coated particle batches were tested in fuel rods. Particle samples separated from the parent batches according to size and density were tested as unbonded particle samples. Descriptions of the fuel particles and fuel rod samples were given in an earlier Quarterly Progress Report (Gulf-GA-A12150).

Capsule P13N was inserted in the ETR (I-135W core position) in cycle 114E on January 19, 1972, and completed its scheduled irradiation on January 5, 1973 after 3732 effective full-power hours of operation. It was then shipped to the GGA Hot Cell, where it is currently undergoing postirradiation examination.

Disassembly of the capsule was completed and all fuel samples have been removed from the five cells. A brief summary of the results, based mainly on metallography, visual examination, and postirradiation fission gas release measurements, is presented below:

1. Fuel rod samples were irradiated in capsule P13N to a peak fluence of 5.4×10^{21} n/cm^2 (E > 0.18 MeV) at integrated average temperatures up to 1490°C. Unbonded fissile and fertile particle samples were irradiated to 5.2×10^{21} n/cm^2 at temperatures up to 1575°C.

2. Irradiation stability of the fuel rods was good. Seventeen of the 22 rods tested were intact and in very good condition. Partial particle-matrix debonding was exhibited by four rods which contained failed carbide fuel particles. Debonding of the carbide-containing fuel rods was attributed to the high failure fraction of fertile (ThC_2) fuel particles and the onset of hydrolysis after the fuel was exposed to air.

3. A high fraction of coating failure in fertile oxide particles (15 to 100%) in bonded fuel rods caused crack formation in some rods but typically did not result in fuel rod debonding or swelling during irradiation or subsequent exposure to air.

4. Dimensions were obtained from the 17 intact fuel rods. All rods shrank both radially and axially, and the shrinkages were nearly isotropic.

5. Macroscopic and metallographic examination of unbonded particles in P13N was completed. Results of this work will be reported when the analysis of irradiation temperature data is completed.

Irradiation Effects in Fuel Rods and Particle Coatings

Twenty-two fuel rod samples were irradiated in capsule P13N. Eight of these fuel rods contained carbide particles, twelve fuel rods contained oxide particles, and two fuel rods contained resin fissile and BISO ThO_2 fertile particles. Twenty rods were fabricated at GGA by the hot-injection process using pitch binder and 6353 natural-flake graphite filler, followed by a heat treatment at 1800°C. Two fuel rods, 1D-1 and 3A-1, contained TRISO U(C,S) fissile and BISO ThO_2 fertile particles and were fabricated by a slurry blended, warm molded process at ORNL. A description of the fuel rods and irradiation conditions is given in Table 9-1.

After irradiation each fuel rod was examined visually. The majority of the rods were dimensioned and then submitted for fission gas release (TRIGA activation) measurements. Selected fuel rods were also examined metallographically or submitted for disintegration - acid leach procedures to determine the amount and distribution of fission products in the fuel rod. Fuel rods 1D-1 and 3A-1 where shipped to ORNL for further analysis.

Fuel rod dimensional change data are reported in Table 9-1. All dimensioned rods were found to have shrunk along both the diameter and the length. The measured shrinkages ranged from ∿1% for the TRISO/TRISO fuel rods to ∿2.5% for the TRISO/BISO fuel rods. Comparison of these data with predicted dimensional change calculations is in progress. These fuel rod dimensional changes appear to be consistent with expected performance based on the coated particle properties and irradiation exposures.

The results of the visual examination of the fuel rod samples were presented in the previous Quarterly Progress Report (Gulf-GA-A12599).

TABLE 9-1
DESCRIPTION OF FUEL RODS IRRADIATED IN CAPSULE P13N

Sample No.[a]	Coated Particles[b]						Matrix[c]			Particle Packing Fraction[d] (%)	Loading Uniformity[f] (± %)	Pre-irradiation Fission Gas Release[g]	Pre-irradiation Thorium Contamination[h]	Irradiation Conditions		Postirradiation Examination			
	Fissile		Fertile		Inert		Filler (wt %)	Apparent Density[d] (g/cm^3)	Macro-porosity[e] (%)					Temp.[i] (°C)	Fast Fluence x 10^{-21} (n/cm^2) (E > 0.18 MeV)	Fission Gas Release[j]	Dimensional Change (%)		Visual Appearance of Fuel Rod
	Type	Batch No.	Type	Batch No.	Type	Batch No.											Diam.	Length	
Cell 1																			
1A-5	UC_2 TRISO	4161-00-020	ThC_2 TRISO	4261-00-010	C-TRISO	3516-147	31.8	0.54	20.0	64.0	4.6	1.3×10^{-6}	3.5×10^{-5}	1415	4.2	8.4×10^{-4}	N.D.	N.D.	Cracked, slight particle debonding
1B-8	UC_2 TRISO	4161-00-020	ThC_2 BISO	4251-00-030	C-TRISO	3516-147	29.7	0.57	17.3	62.1	5.4	6.7×10^{-7}	$<6.7 \times 10^{-6}$	1490	4.3	N.D.[m]	N.D.	N.D.	Broken
1C-10	UC_2 TRISO	4161-00-020	ThC_2 BISO	4251-00-030	C-TRISO	3516-147	29.8	0.57	23.5	61.9	11.3	1.9×10^{-6}	$<4.2 \times 10^{-6}$	1475	4.4	N.D.	N.D.	N.D.	Broken
1D-1[k]	U(C,S) TRISO	OR1602[1]	ThO_2 BISO	OR1652[1]	--	--	N.A.	1.45	3.0	42.9	0.5	3.2×10^{-6}	7.0×10^{-6}	1415	4.6	1.4×10^{-4}[n]	-2.4	-1.8	Excellent condition
1E-3	$(Th,U)O_2$ TRISO	5466-37	ThO_2 BISO	4252-00-010	C-TRISO	3516-147	26.2	0.58	32.2	60.5	14.5	6.9×10^{-7}	$<6.0 \times 10^{-6}$	1445	4.7	1.2×10^{-3}	-1.8	N.D.	Good condition
Cell 2																			
2A-10	UO_2 TRISO	4162-01-020	ThO_2 TRISO	4262-00-050	C-TRISO	3516-149	30.6	0.64	30.4	58.6	13.0	9.7×10^{-6}	4.3×10^{-4}	1220	5.2	5.1×10^{-3}[n]	-0.8	-0.5	Excellent condition
2B-15	UO_2 TRISO	4162-01-020	ThO_2 BISO	4252-00-010	C-TRISO	3516-149	24.8	0.58	24.9	58.3	4.3	5.7×10^{-7}	$<9.1 \times 10^{-6}$	1230	5.3	7.8×10^{-4}	-2.1	-1.6	Excellent condition
2C-7	UO_2 TRISO	4162-01-020	ThO_2 TRISO	4262-00-050	C-TRISO	3516-149	30.3	0.62	31.0	59.4	13.9	4.9×10^{-6}	9.0×10^{-4}	1360	5.4	3.9×10^{-5}[n]	-1.2	-0.9	Excellent condition
2D-16	UO_2 TRISO	4162-01-020	ThO_2 BISO	4252-00-010	C-TRISO	3516-149	29.6	0.59	17.7	60.1	2.1	1.2×10^{-5}	9.8×10^{-6}	1350	5.4	9.1×10^{-4}[n]	-1.9	-1.3	Good condition
Cell 3																			
3A-1[k]	U(C,S) TRISO	OR1602[1]	ThO_2 BISO	OR1652[1]	--	--	N.A.	1.43	5.0	42.7	12.3	4.0×10^{-6}	6.6×10^{-6}	1450	5.1	2.6×10^{-5}[n]	-2.5	-1.8	Excellent condition
3B-9	UC_2 TRISO	4161-00-020	ThC_2 BISO	4251-00-030	C-TRISO	3516-147	33.6	0.66	4.3	60.5	3.7	2.0×10^{-6}	1.3×10^{-5}	1365	5.0	N.D.	N.D.	N.D.	Broken
3C-13	UC_2 TRISO	4161-00-020	ThC_2 BISO	4251-00-030	C-TRISO	3516-147	25.8	0.56	30.7	61.2	2.0	3.1×10^{-6}	$<8.2 \times 10^{-6}$	1350	4.9	2.9×10^{-3}	N.D.	N.D.	Broken
3D-7	UC_2 TRISO	4161-00-020	ThC_2 TRISO	4261-00-010	C-TRISO	3516-147	27.5	0.62	25.2	62.8	0.3	2.7×10^{-6}	6.6×10^{-5}	1375	4.7	9.1×10^{-4}	-0.9	N.D.	Slightly cracked
Cell 4																			
4A-13	UO_2 TRISO	4162-01-020	ThO_2 BISO	4252-00-010	--	--	28.0	0.57	28.7	62.8	5.2	2.7×10^{-7}	$<4.7 \times 10^{-6}$	1335	3.9	5.1×10^{-5}[n]	-3.0	N.D.	Broken
4B-9	UO_2 TRISO	4162-01-020	ThO_2 TRISO	4260-00-050	C-TRISO	3516-149	31.2	0.61	29.3	60.3	7.0	1.2×10^{-5}	1.4×10^{-4}	1300	3.7	3.0×10^{-4}	-0.8	-0.6	Excellent condition
4C-9	UO_2 TRISO	4162-01-020	ThO_2 BISO	4252-00-010	C-TRISO	3516-147	32.7	0.61	30.5	62.1	1.8	1.4×10^{-6}	N.A.	1260	3.6	2.8×10^{-4}	-2.4	-2.4	Excellent condition
4D-9	UO_2 TRISO	4162-01-020	ThO_2 TRISO	4252-00-050	C-TRISO	3516-147	30.5	0.59	28.7	58.7	8.3	1.5×10^{-5}	3.8×10^{-4}	1255	3.4	1.6×10^{-4}[n]	-0.8	-0.8	Excellent condition
Cell 5																			
5X-7	$(Th,U)O_2$ TRISO	5466-37[1]	ThO_2 BISO	4252-00-010	C-TRISO	3516-149	22.8	0.58	28.7	60.0	2.4	1.5×10^{-6}	$<6.0 \times 10^{-6}$	1290	2.4	1.5×10^{-5}[n]	-2.4	-2.2	Excellent condition
5A-19	UO_2 TRISO	4162-01-020	ThO_2 BISO	4252-00-010	--	--	27.2	0.58	31.0	59.9	3.1	5.8×10^{-7}	$<4.9 \times 10^{-6}$	1335	2.2	3.8×10^{-5}	-2.6	-2.8	Excellent condition
5B-7	UO_2 TRISO	4162-01-020	ThO_2 BISO	4252-00-010	--	--	29.5	0.62	25.6	59.4	1.1	8.8×10^{-7}	5.0×10^{-6}	1325	2.0	4.8×10^{-6}	-2.4	-2.3	Excellent condition
5C-9	UC_2 TRISO	4161-00-020	ThC_2 BISO	4251-00-030	C-TRISO	3516-149	29.2	0.56	25.9	61.7	3.5	2.4×10^{-6}	6.6×10^{-6}	1275	1.8	1.8×10^{-5}	-2.6	-2.5	Excellent condition
5D-25	UC_2 TRISO	4161-00-020	ThC_2 TRISO	4261-00-010	C-TRISO	3516-149	31.1	0.61	20.0	62.2	0.4	1.5×10^{-5}	5.8×10^{-6}	1120	1.6	1.6×10^{-5}[n]	-0.8	-0.8	Excellent condition

[a] All fuel rods were nominally 0.49 in. in diameter by 0.73 in. long.

[b] Particles coated in production-scale equipment, except where noted.

[c] Except where noted, fuel rod matrices have 15V pitch for the binder and 6353 natural-flake graphite for the filler. Rods were fabricated by the hot-injection process and were given an 1800°C preirradiation heat-treatment.

[d] Calculated from fired fuel rod dimensions and nominal particle parameters.

[e] Determined from metallographic cross section of a fuel rod from same batch.

[f] Percent variation from the mean uranium loading from end-to-end of the rod.

[g] R/B for Kr-85m at 1100°C.

[h] Determined by hydrolysis test (G Th/G Th). Value indicates amount of exposed thorium.

[i] Corrected to P13M thermocouple decalibration data.

[j] R/B for Kr-85m at 1100°C. Not corrected for steady state.

[k] Rods prepared by slurry-blended, warm-molded process at ORNL. Matrix composition is 31.5 wt % 240 pitch, 53.5 wt % 1074 graphite, and 15.0 wt % Thermax.

[l] Particles coated in laboratory equipment.

[m] N.D. - not determined.

[n] R/B measured at irradiation temperature and extrapolated to 1100°C based on temperature correlation.

All but one of the fuel rod samples in cells 2, 4, and 5 were intact and in relatively good condition. These cells contained 11 fuel rods comprised of oxide particles and 2 fuel rods containing carbide fuel particles. The single rod not intact was fuel rod 4A-13, which contained oxide particles. Failed ThO_2 BISO particles were observed at the fracture interfaces during the visual examination.

Previous irradiation experiments showed that the ThO_2 BISO particles used in these rods (4252-00-01X) had poor irradiation stability. These particles failed in fuel rod samples in capsule HRB-3 (see earlier Quarterly Progress Report Gulf-GA-A12422) and as unbonded particles in the HT-12 through HT-15 experiments (see previous Quarterly Progress Report Gulf-GA-A12599) conducted at ORNL. The OPyC coatings on the ThO_2 BISO particles used in these and the P13N experiments were of high density in order to determine the effect of density on coated particle dimensional change and hence fuel rod dimensional change. Preirradiation evaluation of these particles showed the coating attributes to be within the specified values; however, after irradiation a gradient in anisotropy became evident in the OPyC layer, especially in the initial 10 μm of the coating. During irradiation cracks were observed to initiate in the region of high density and high anisotropy where the PyC irradiation-induced dimensional change was maximized.

Outer PyC coatings on the ThC_2 BISO particles (4251-00-03X) were very similar to those on the ThO_2 BISO particles and would be expected to behave similarly under irradiation.

Four of the six rods in cells 1 and 3 containing carbide fuel particles exhibited cracks. Stereo examination of the fracture surfaces of these rods also revealed a large fraction of failed particles. Debonding of these rods occurred during the disassembly operation and was attributed to the onset of hydrolysis and associated kernel volume increase in the carbide fuel after the fuel cells were exposed to air.

Postirradiation fission gas release measurements were made on each fuel rod in the GGA TRIGA reactor with the exception of carbide-containing

fuel rods 1B-8, 1C-10, and 30-9, which were debonded. The fission gas release data are reported in terms of the release to birth fraction of Kr-85m and were obtained at 1100°C and/or at the fuel rod irradiation temperature and extrapolated to 1100°C based on a previously determined temperature dependence (Ref. 9-1). These data are reported in Table 9-1. Fuel rods irradiated to a relatively low fluence (i.e., cell 5) had low fission gas release values in the range of 1×10^{-5} to 5×10^{-6}. Fuel rods irradiated to higher fluences had somewhat higher fission gas release values, which is consistent with the observation that these rods also had high fertile particle failure fractions.

Two oxide rods (1E-3, 4A-13) and two carbide rods (1C-10, 3C-13) were disassociated electrolytically and acid leached to separate the exposed fuel and fission products. The gamma-ray spectrum of the acid-leach solutions was analyzed using a Ge(Li) detector coupled with a Sigma II analyzer to determine the amount of fission product isotopes in solution. Coated particle failure fractions will be determined by comparing the amount of fission product isotopes taken into the leach solutions with the theoretical amount present in the fuel rods after irradiation. Leach solutions from these four fuel rods have been submitted for isotopic analysis in order to separate the isotope contributions from the fissile and fertile particles. The results of the disintegration - acid leach studies will be reported in a future Quarterly Progress Report when the analyses have been completed.

Metallographic examination was performed on ten fuel rod samples. These samples included six oxide and four carbide fuel rods selected to represent the range of irradiation conditions and fuel rod performance of fuel types included in P13N. Representative photographs obtained from the metallographic examinations are shown in Figs. 9-1 through 9-16.

The irradiation stability of the TRISO coated fissile particles [UC_2, UO_2, and $(Th,U)O_2$] in all the rods examined metallographically was considered to be excellent under the very severe conditions of the

L7306-136 (a) 650X

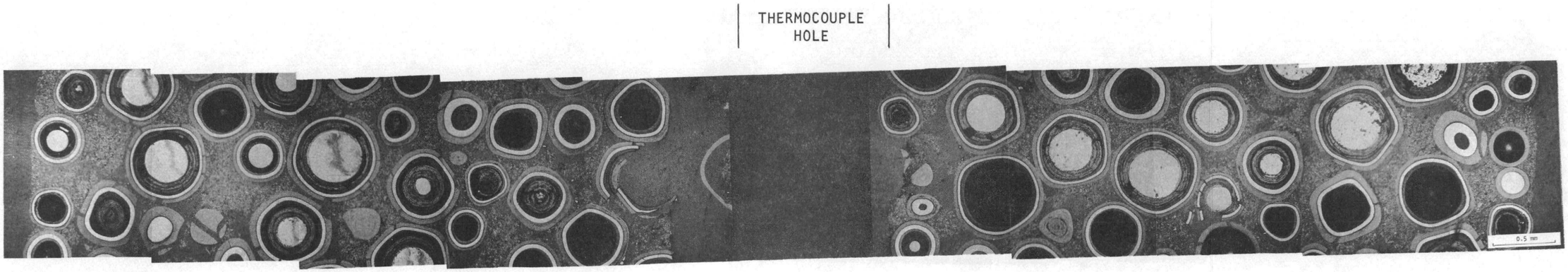

L7306 (137-146) (b)

Fig. 9-1. Representative photomicrographs of thermocouple fuel rod 1A-5 containing UC_2 TRISO and ThC_2 TRISO particles after irradiation in capsule P13N to 4.2×10^{21} n/cm^2 at 1415°C: (a) typical appearance of matrix graphite, and (b) composite showing radial cross section. (Note: Rod contained central thermocouple. Slight evidence of chemical interaction between the metal sheath and coated particles can be seen in the composite section.)

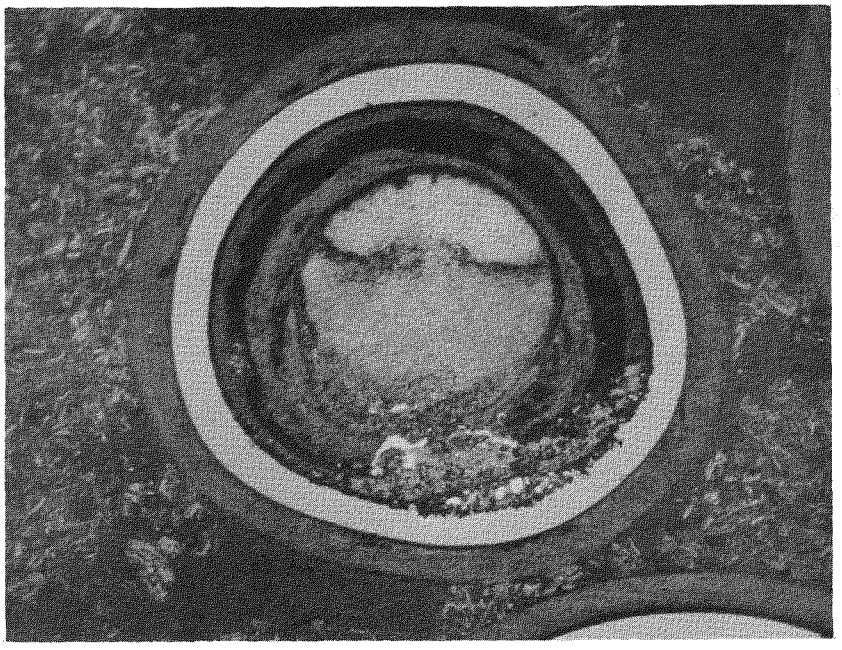

L7306-133 (a) 200X

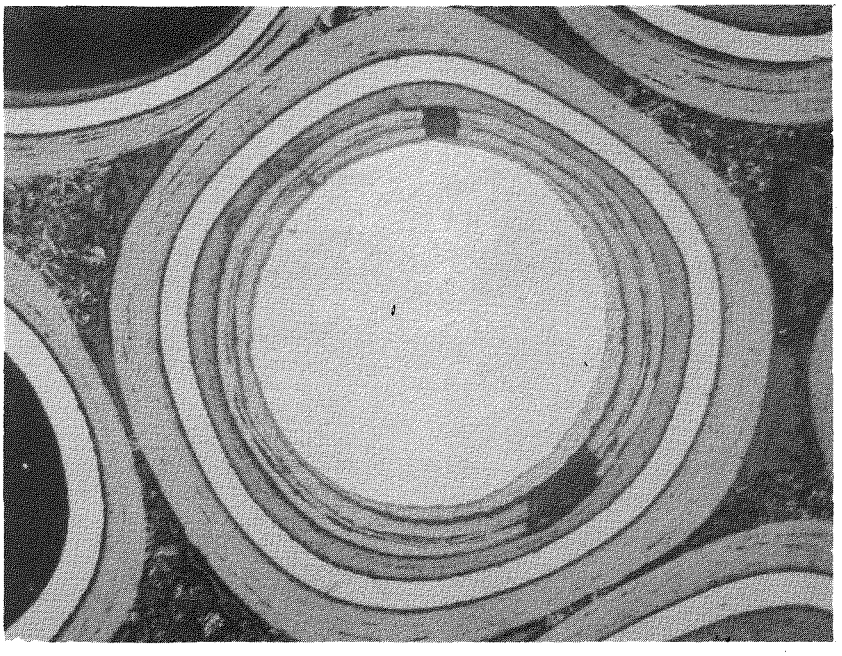

L7306-92 (b) 175X

Fig. 9-2. Representative particles from fuel rod 1A-5 irradiated in capsule P13N to 4.2 x 10^{21} n/cm^2 at 1415°C: (a) UC_2 TRISO particle, and (b) ThC_2 TRISO particle. Evidence of fission product attack of the SiC coating was observed in ∿60% of the fissile particles. Fuel kernel migration on the order of 10 to 30 μm toward the center of the fuel rod was observed in ∿45% of the ThC_2 fertile particles.

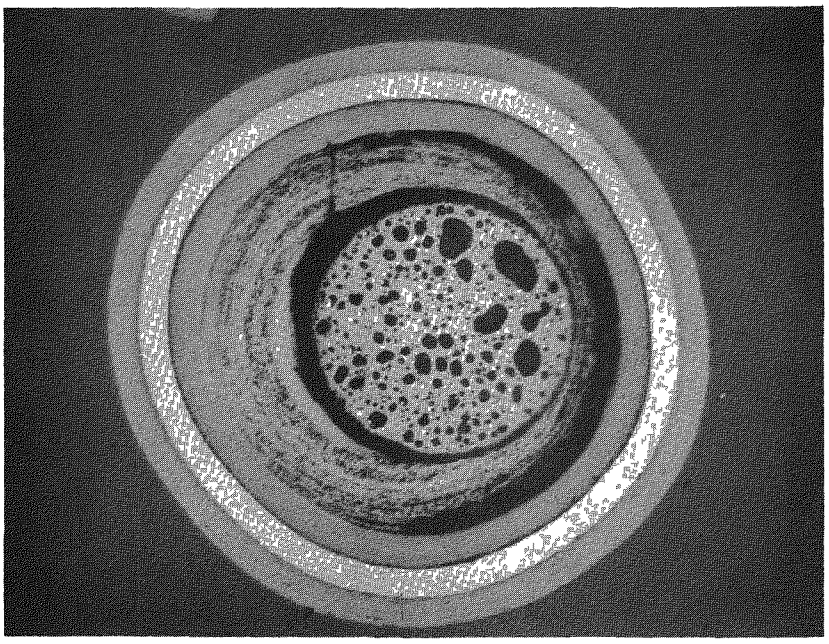

L7306-360 (a) 150X

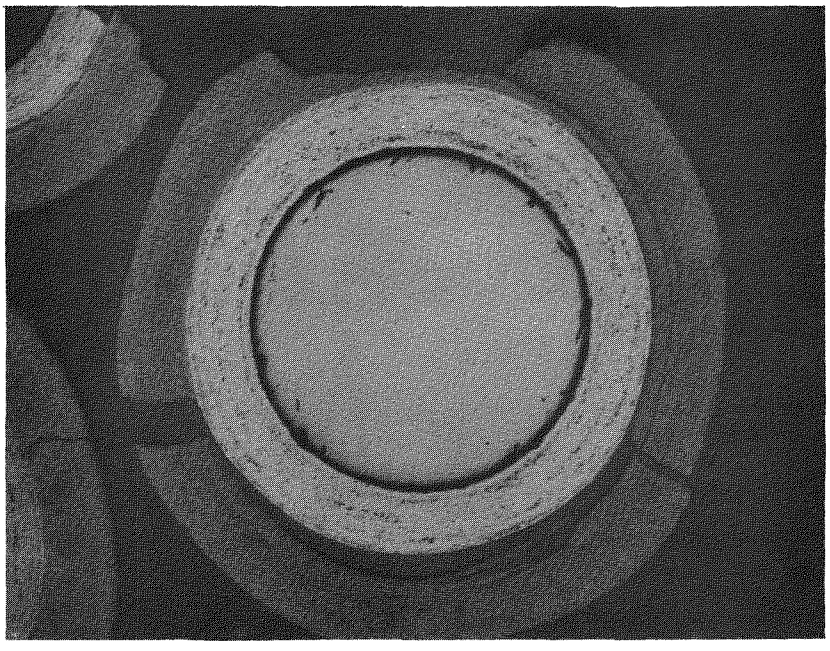

L7306-476 (b) 115X

Fig. 9 3. Representative particles from fuel rod IE-3 irradiated in capsule P13N at 1445°C to 4.7 x 10^{21} n/cm^2: (a) (Th,U)O_2 TRISO particle, and (b) ThO_2 BISO particle. After unloading, the rod debonded during additional handling and was subsequently disintegrated electrolytically and acid leached. Approxmimately 50 to 75% of the (Th,U)O_2 particles exhibited fuel kernel migration of distances up to 50 μm.

L7306-607 (a) 650X

THERMOCOUPLE HOLE

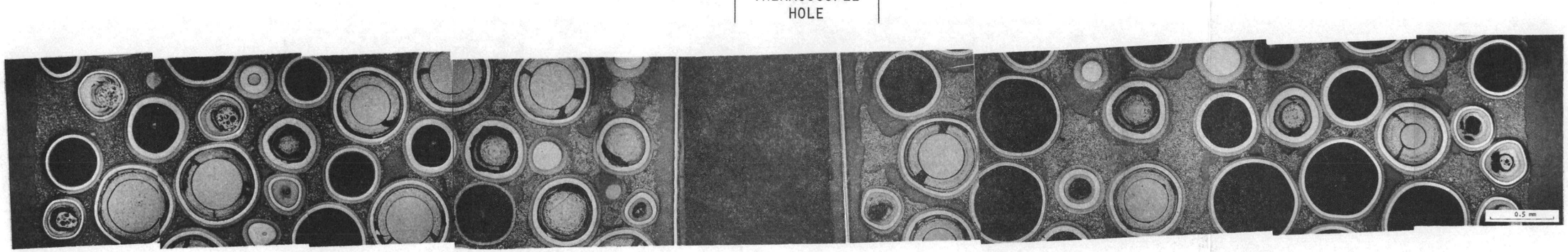

L7306 (596-605) (b)

Fig. 9-4. Representative photomicrographs of thermocouple fuel rod 2A-10 containing UO_2 TRISO and ThO_2 TRISO particles after irradiation in capsule P13N to 5.2 x 10^{21} n/cm^2 at 1220°C: (a) typical appearance of matrix graphite, and (b) composite showing radial cross section. Note UO_2 kernel migration toward the rod center, up the thermal gradient, near the rod surface. Also note very slight reaction between OPyC coatings and tungsten thermocouple sheath.

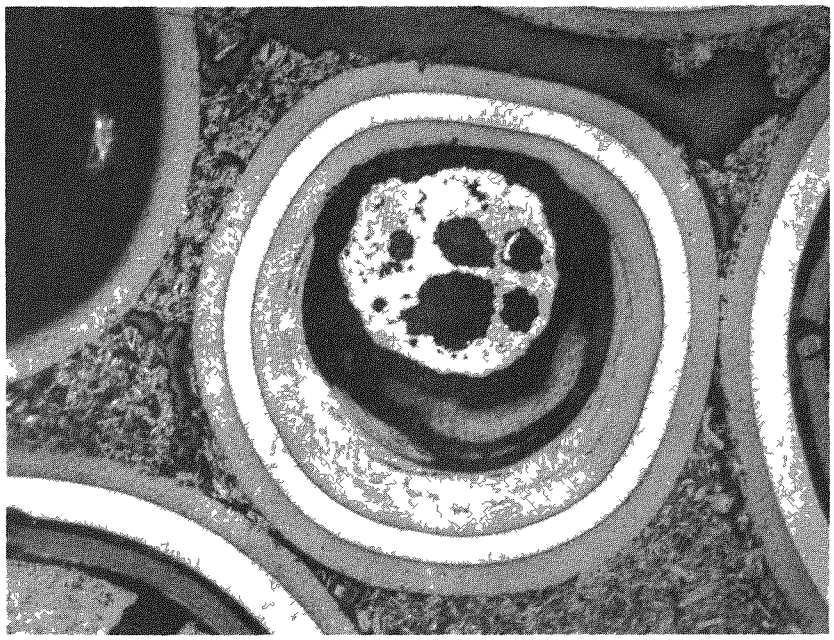

L7306-644 (a) 175X

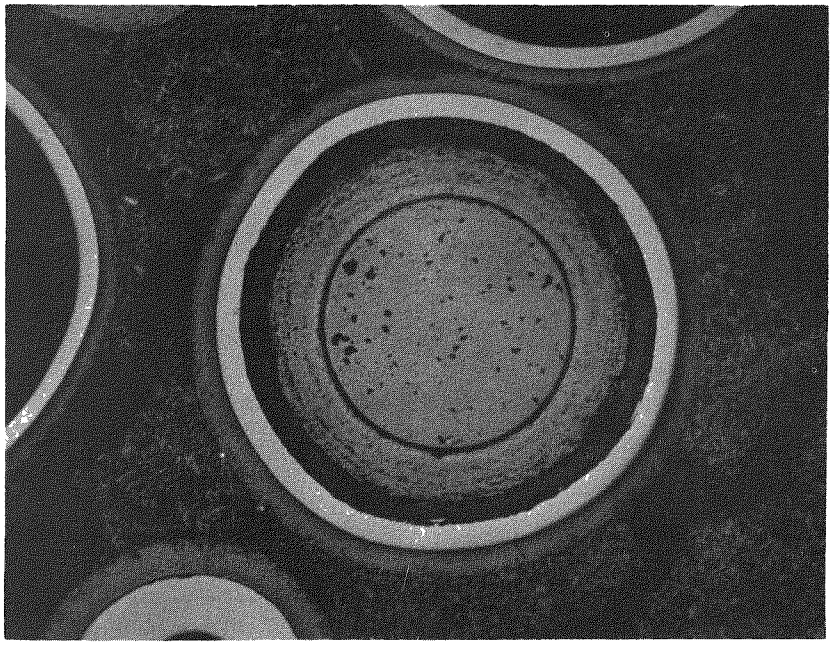

L7306-586 (b) 115X

Fig. 9-5. Representative particles from fuel rod 2A-10 irradiated in capsule P13N to 5.2 x 10^{21} n/cm^2 at 1220°C: (a) UO_2 TRISO particle, and (b) ThO_2 TRISO particle. The UO_2 particles exhibited extensive fuel kernel migration; however, no fuel kernel migration was observed in the ThO_2 particles.

L7306-702 (a) 650X

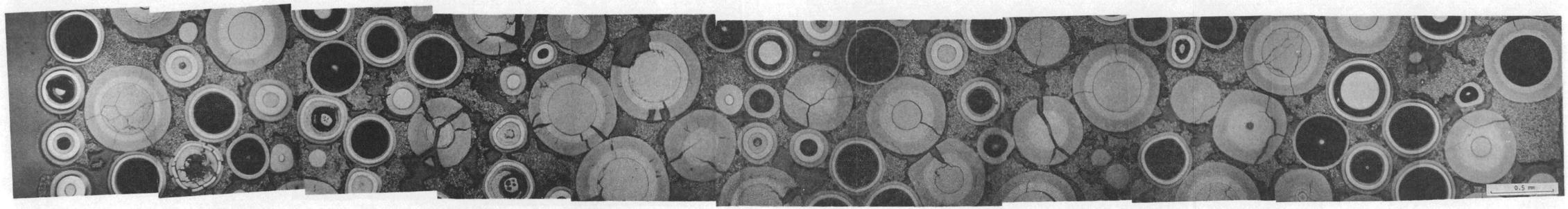

L7306 (688-698) (b)

Fig. 9-6. Representative photomicrographs of fuel rod 2D-16 containing UO_2 TRISO and ThO_2 BISO particles after irradiation in capsule P13N to 5.4 x 10^{21} n/cm^2 at 1350°C: (a) typical appearance of matrix graphite, and (b) composite showing radial cross section. The high failure fraction of ThO_2 BISO particles did not result in fuel rod debonding.

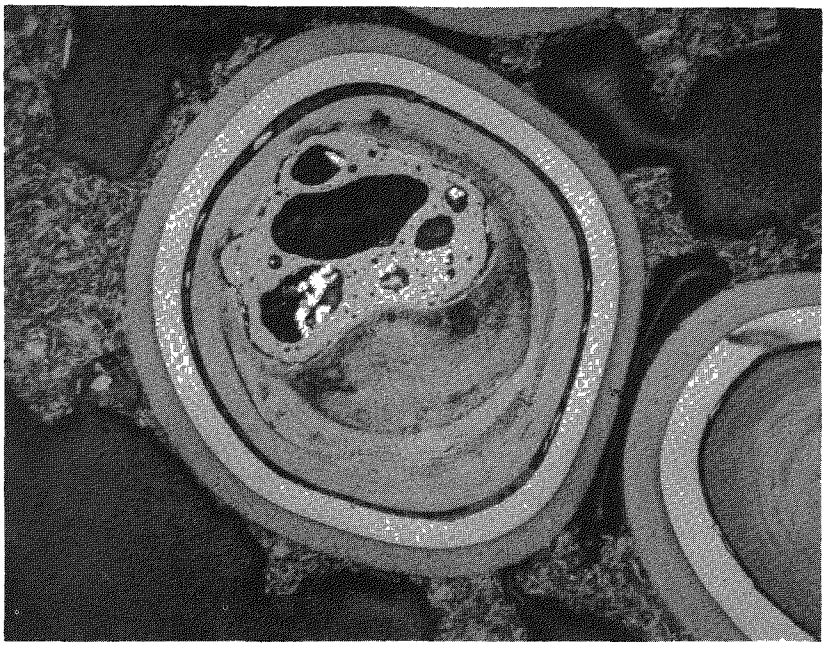

L7306-706 (a) 175X

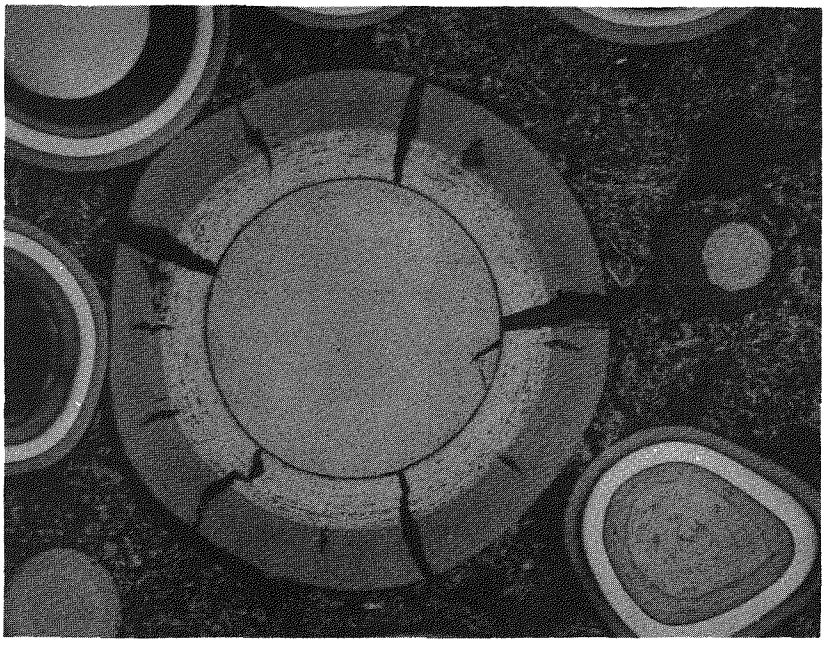

L7306-703 (b) 85X

Fig. 9-7. Representative particles from fuel rod 2D-16 irradiated in capsule P13N to 5.4 x 10^{21} n/cm^2 at 1350°C: (a) UO_2 TRISO particle, and (b) ThO_2 BISO particle. The BISO coated ThO_2 particles had close to 100% OPyC failure due to the poor stability of a highly anisotropic layer in the OPyC coating. Extensive fuel kernel migration accompanied by pressure vessel failure was observed in a high fraction of the UO_2 TRISO particles.

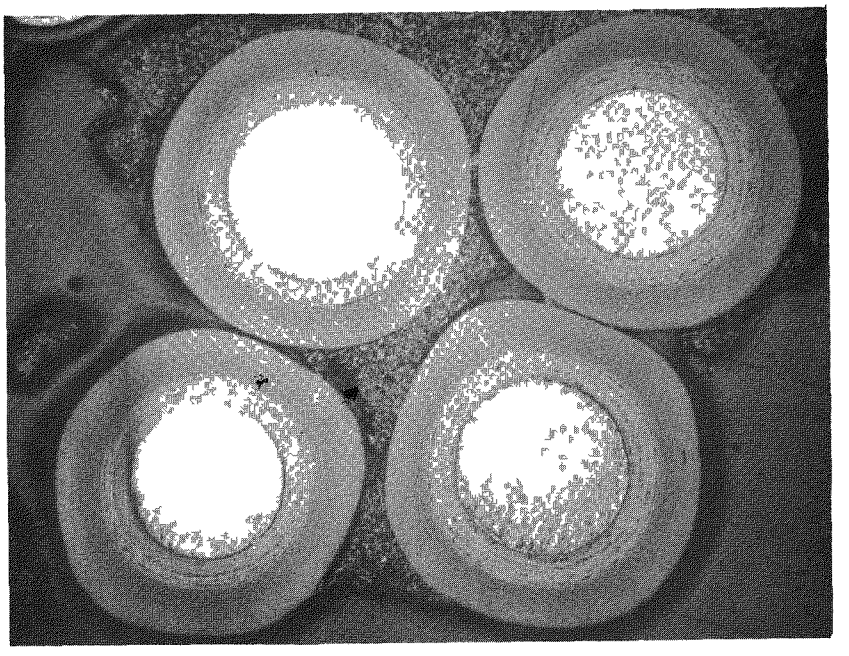

L7306-48 (a) 70X

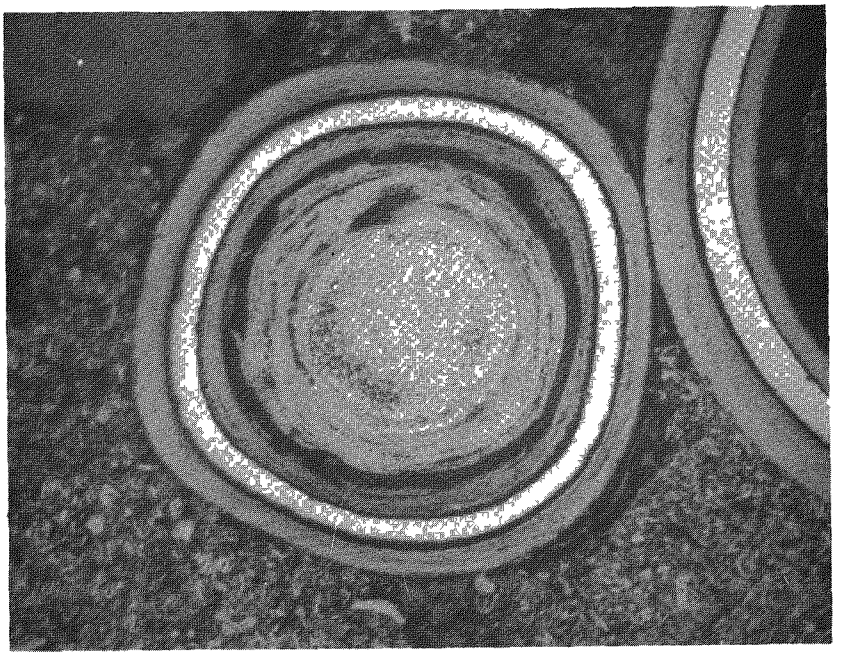

L7306-65 (b) 200X

Fig. 9-8. Representative particles from fuel rod 3C-13 irradiated in capsule P13N to 4.9 x 10^{21} n/cm^2 at 1350°C: (a) ThC_2 BISO particles, and (b) UC_2 TRISO particles. This rod experienced 30% failure of fertile particle coatings during irradiation and debonded during removal from the graphite sleeve.

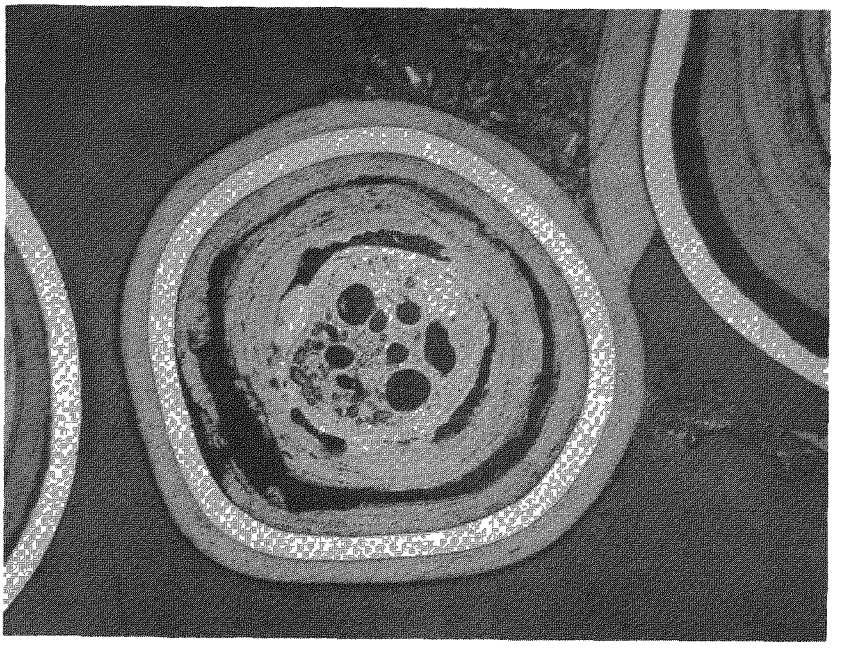

L7306-636 (a) 175X

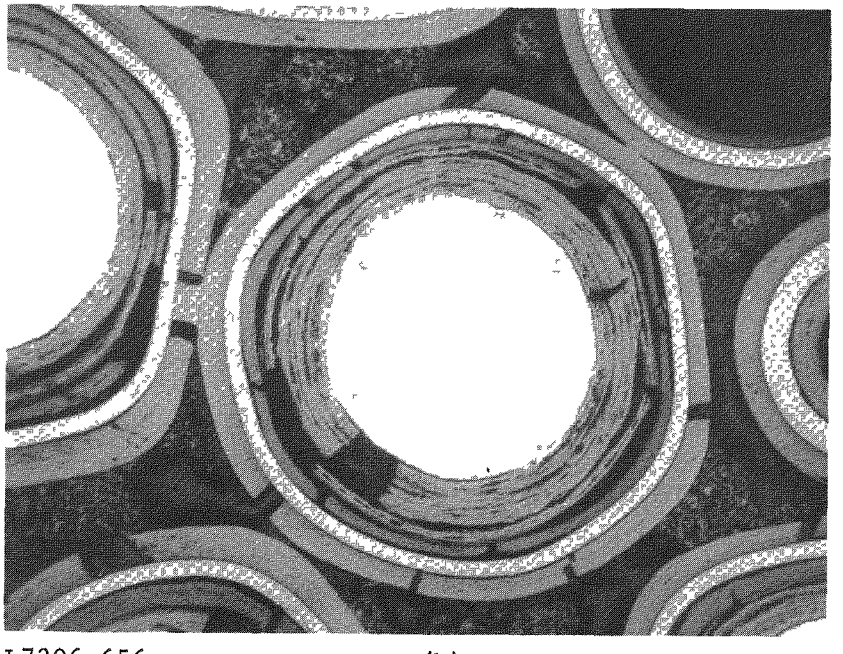

L7306-656 (b) 100X

Fig. 9-9. Representative particles from fuel rod 3D-7 irradiated in capsule P13N to 4.7 x 10^{21} n/cm^2 at 1375°C: (a) UC_2 TRISO particle, and (b) ThC_2 TRISO particle. High concentrations of fission products were present in localized regions in the IPyC coatings of the fissile particles; however, no SiC coating failures were observed as a result of fission product attack.

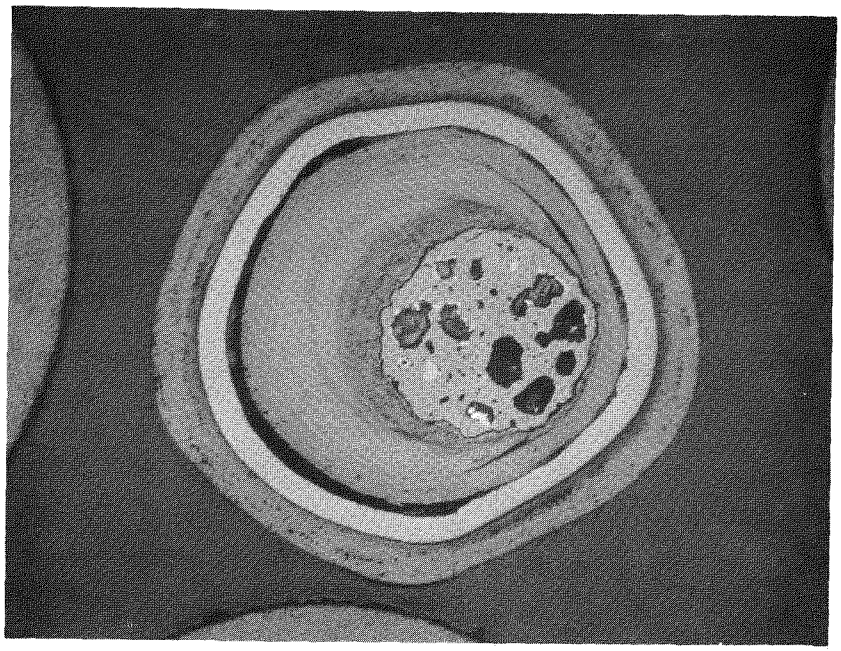

L7306-727 (a) 175X

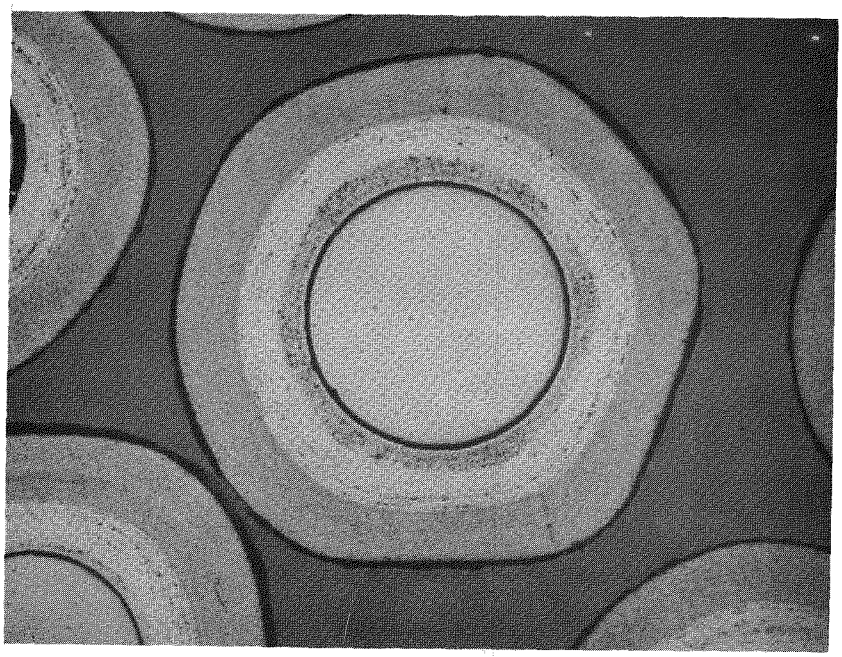

L7306-736 (b) 100X

Fig. 9-10. Representative particles from fuel rod 4A-13 irradiated in capsule P13N to 3.9 x 10^{21} n/cm^2 at 1335°C: (a) UO_2 TRISO particle, and (b) ThO_2 BISO particle. This rod debonded during removal from the graphite sleeve and was subsequently disintegrated electrolytically and acid leached.

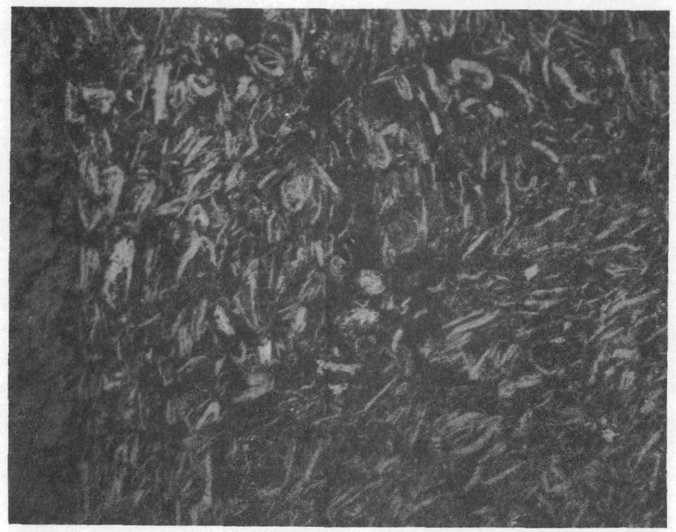

L7306-42 (a) 650X

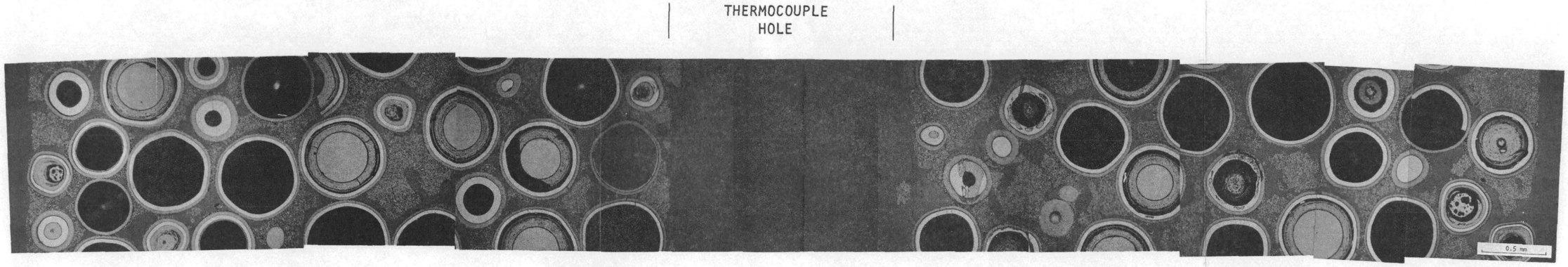

L7306 (31-40) (b)

Fig. 9-11. Representative photomicrographs of thermocouple fuel rod 4D-9 containing UO_2 TRISO and ThO_2 TRISO particles irradiated in capsule P13N to 3.4 x 10^{21} n/cm^2 at 1255°C: (a) typical appearance of matrix, and (b) composite showing radial cross section. Note the displacement of the UO_2 kernel in the TRISO particle on the fuel rod surface. Kernal migration up the thermal gradient has occurred. No interaction between coatings and the metal thermocouple sheath was observed in this rod.

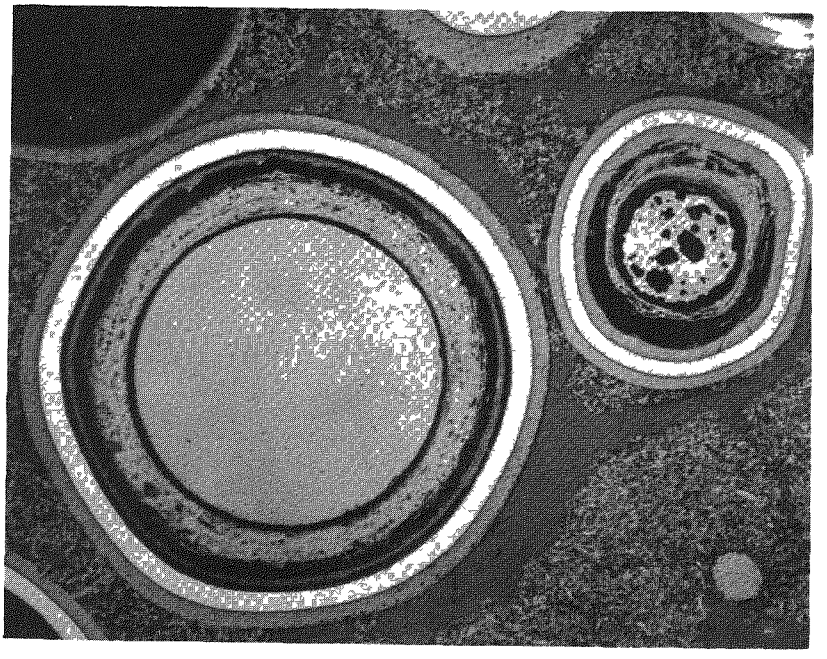

L7306-12 100X

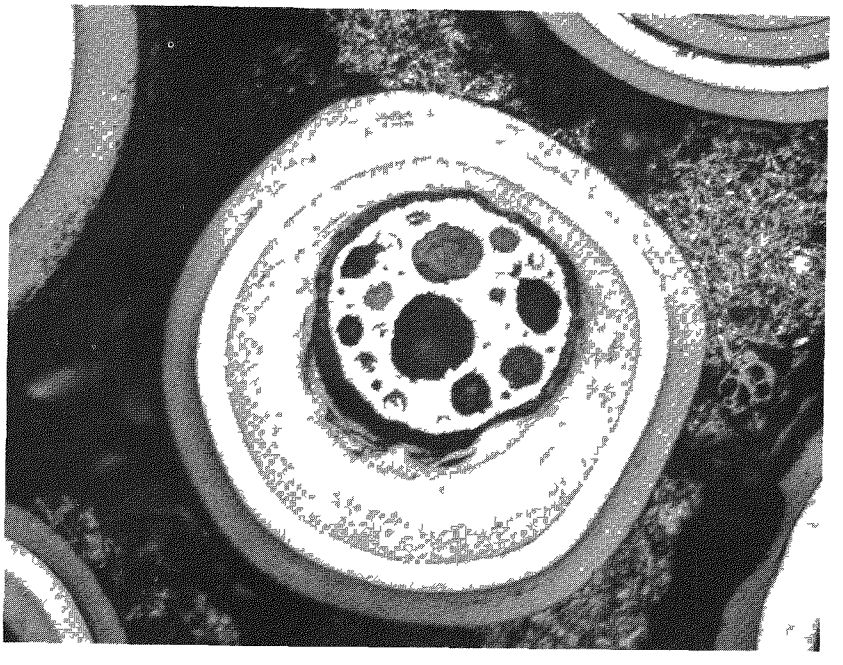

L7306-725 175X

Fig. 9-12. Representative particles from fuel rod 4D-9 irradiated in capsule P13N to 3.4 x 10^{21} n/cm^2 at 1255°C: (a) ThO_2 TRISO and UO_2 TRISO particles, and (b) UO_2 TRISO particles

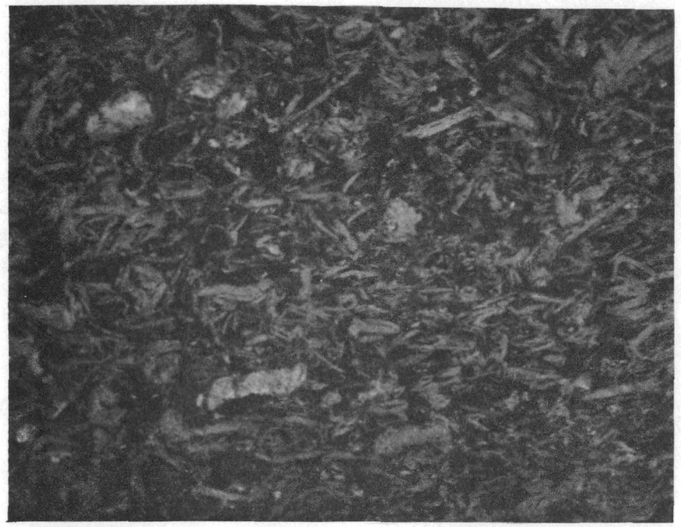

L7306-465 (a) 650X

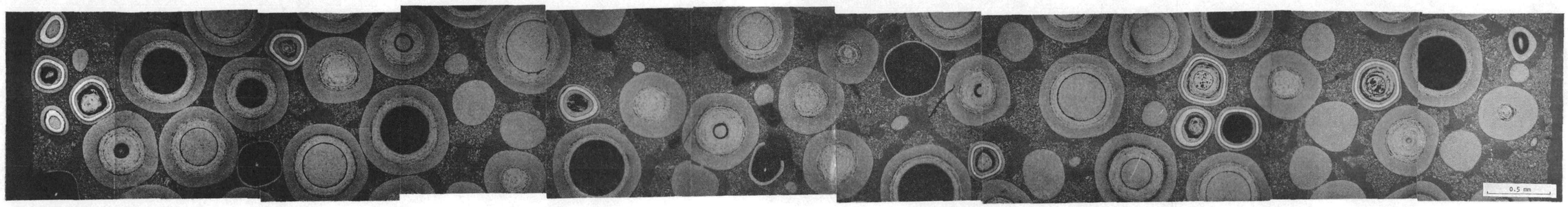

L7306 (533-543) (b)

Fig. 9-13. Representative photomicrographs of fuel rod 5A-19 containing UO_2 TRISO and ThO_2 BISO particles after irradiation in capsule P13N to 2.2×10^{21} n/cm^2 at 1335°C: (a) typical appearance of matrix graphite, and (b) composite showing radial cross section

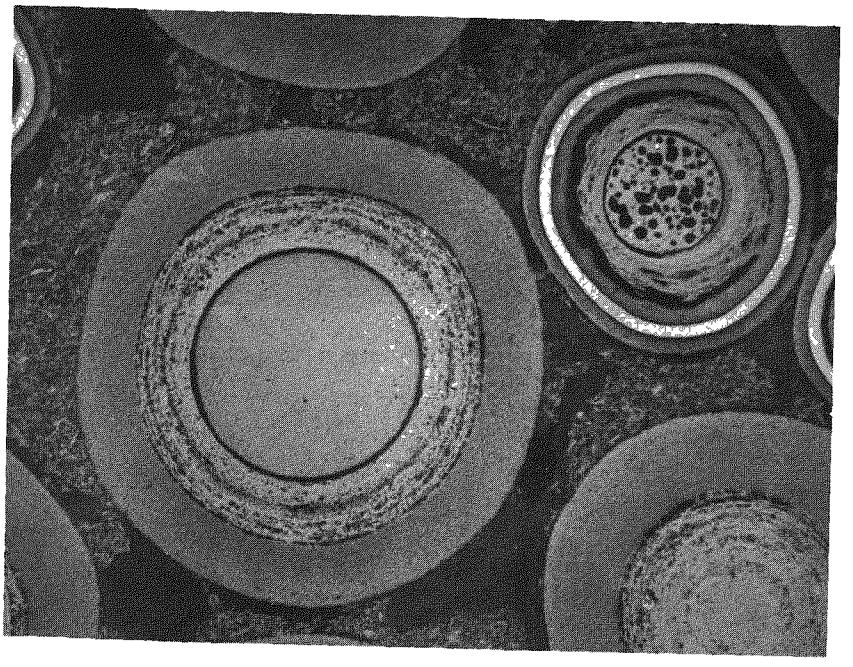

L7306-459 (a) 80X

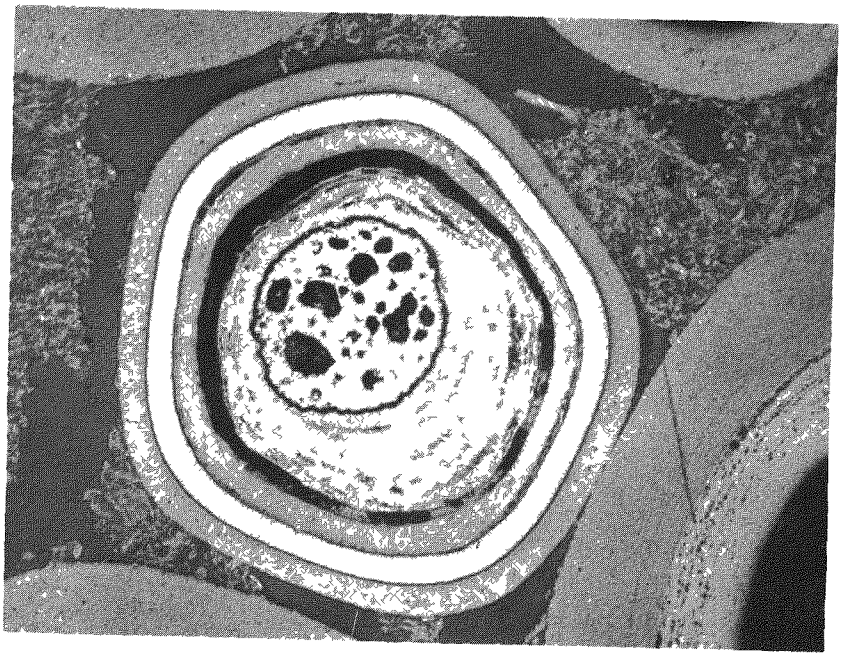

L7306-493 (b) 175X

Fig. 9-14. Representative particles from fuel rod 5A-19 irradiated in capsule P13N to 2.2 x 10^{21} n/cm^2 of 1335°C: (a) ThO_2 BISO and UO_2 TRISO particles, and (b) UO_2 TRISO particle

L7306-546 (a) 650X

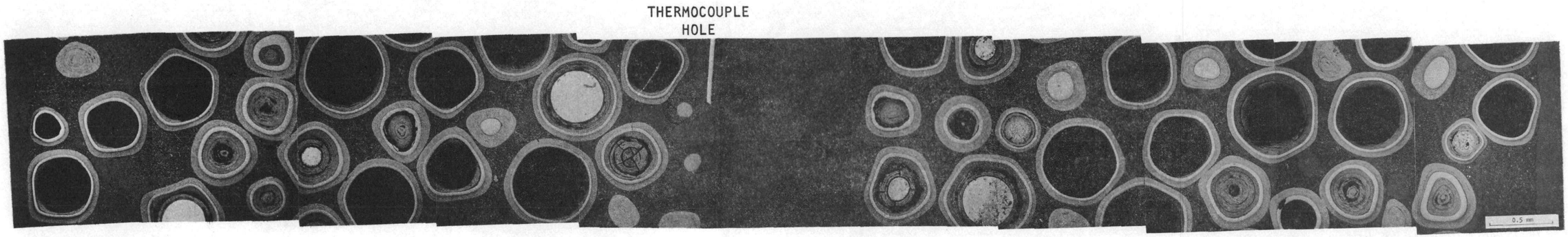

L7306 (548-557) (b)

Fig. 9-15. Representative photomicrographs of thermocouple fuel rod 5D-25 containing UC_2 TRISO and ThC_2 TRISO particles after irradiation in capsule P13N to 1.6×10^{21} n/cm^2 at 1120°C: (a) typical appearance of matrix graphite, and (b) composite showing radial cross section

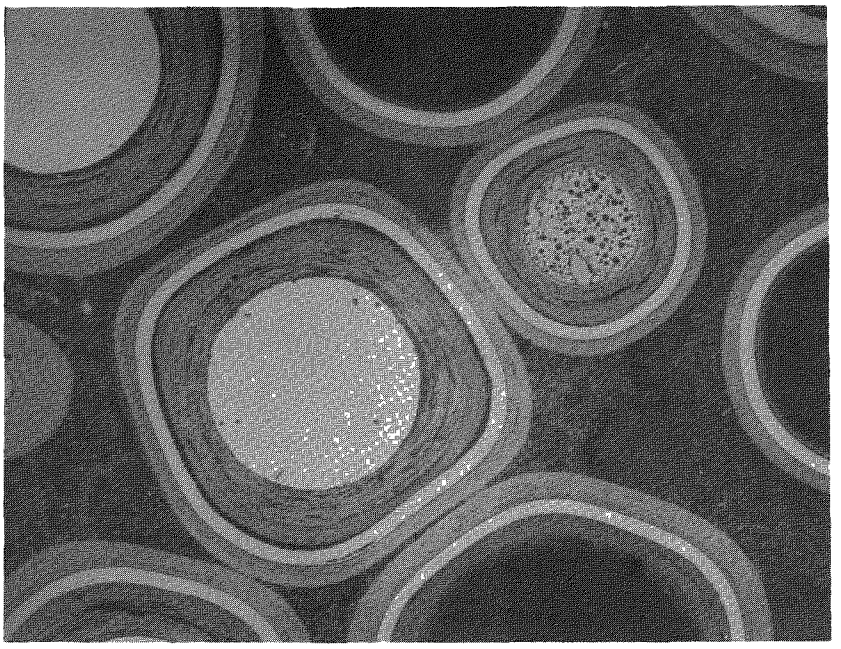

L7306-498 (a) 90X

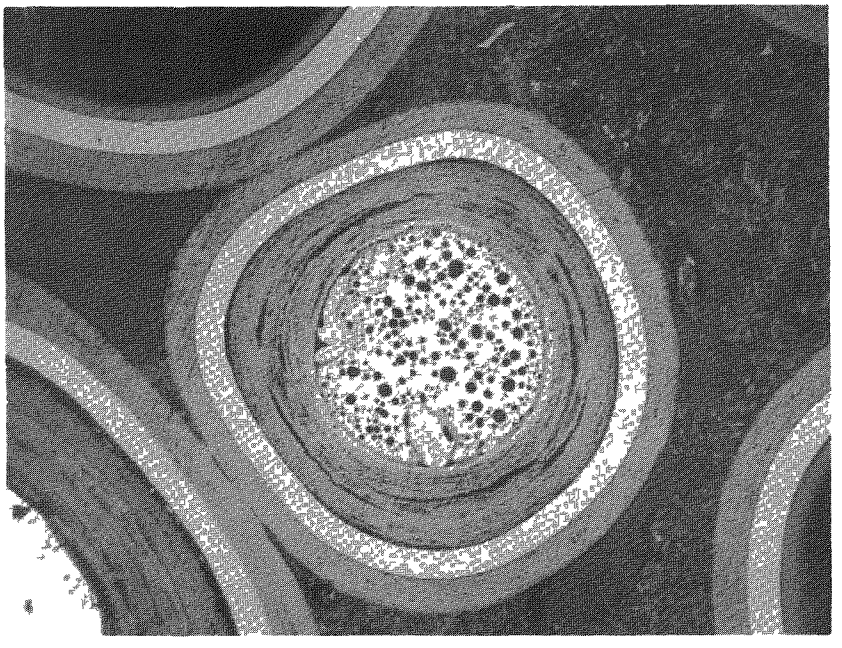

L7306-505 (b) 175X

Fig. 9-16. Representative particles from fuel rod 5D-25 irradiated in capsule P13N to 1.6 x 10^{21} n/cm^2 at 1120°C: (a) TRISO ThC_2 and TRISO UC_2 particles, and (b) TRISO UC_2 particle. No evidence of fission product interaction with the PyC or SiC coatings was observed in the TRISO coated UC_2 particles.

BRIGHT FIELD

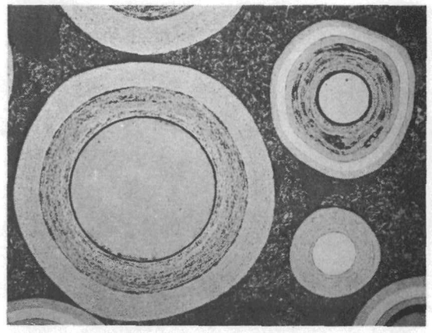

M36598-23 ∿56X

(a)

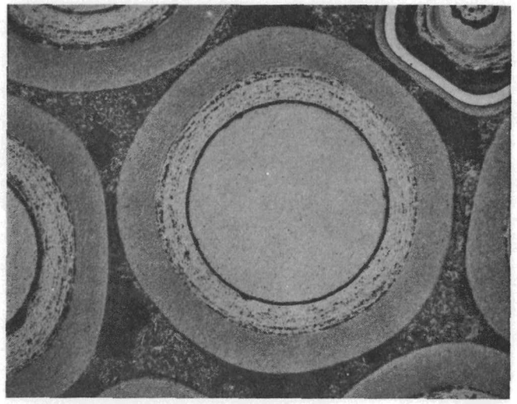

L7306-462 ∿86X

(b)

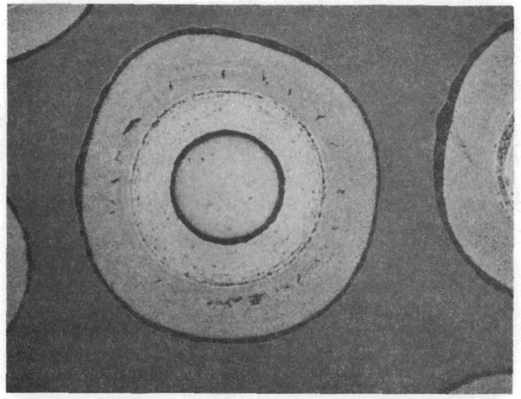

L7306-744 ∿86X

(c)

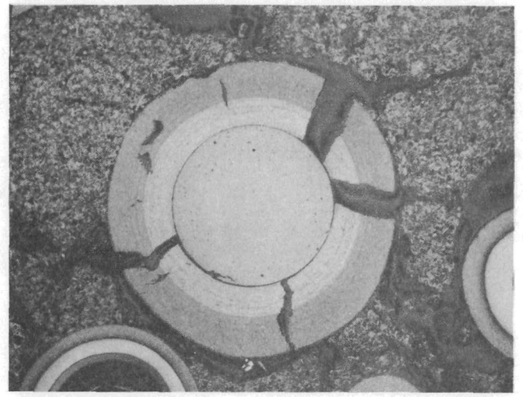

L7306-682 ∿86X

(d)

POLARIZED LIGHT

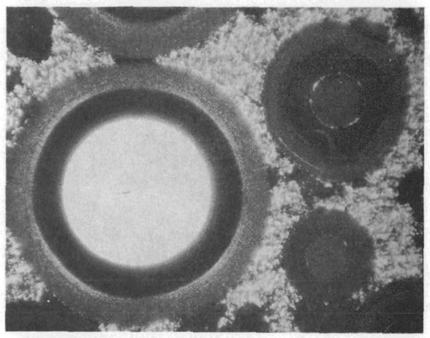

M36598-24 ∿56X

(a)

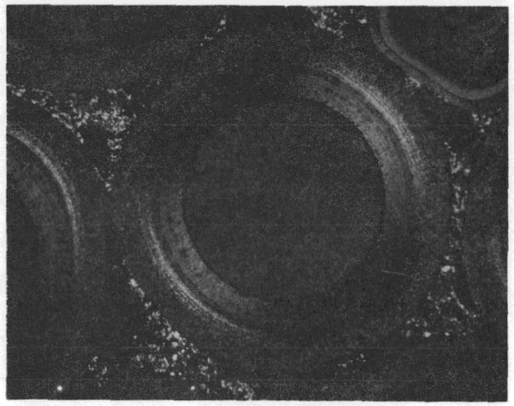

L7306-463 ∿86X

(b)

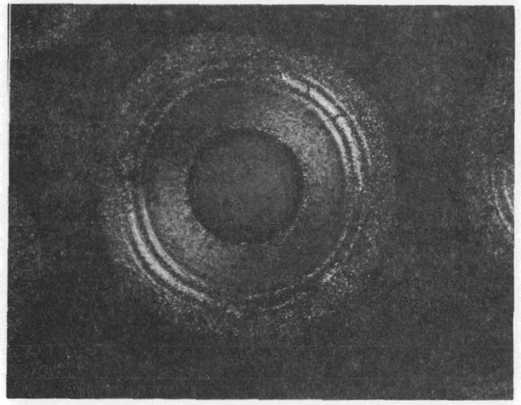

L7306-745 ∿86X

(c)

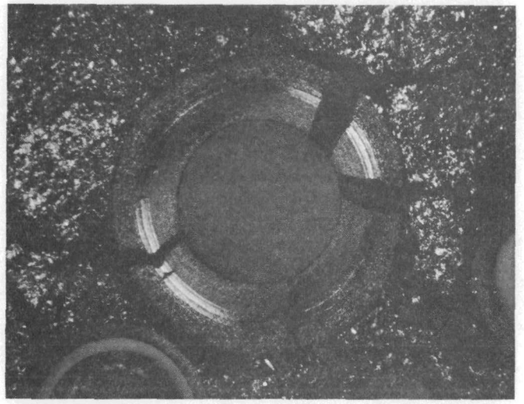

L7306-683 ∿86X

(d)

Fig. 9-17. Photomicrographs of ThO_2 BISO particles (Batch 4252-00-010): (a) before irradiation, (b) irradiated in fuel rod 5A-19 to 2.2 x 10^{21} n/cm^2 at 1335°C, (c) irradiated in fuel rod 4A-13 to 3.9 x 10^{21} n/cm^2 at 1335°C, and (d) irradiated in fuel rod 2D-16 to 5.4 x 10^{21} n/cm^2 at 1350°C. Note increase in intensity of anisotropic region in the inner 10 to 15 μm of outer pyrocarbon coating with increased fast fluence. Initiation of cracks in this anisotropic area of the coating can be seen in the particles irradiated to 3.9 x 10^{21} n/cm^2 . No cracking is visible at the lower fluence and total coating failure has occurred by 5.4 x 10^{21} n/cm^2.

P13N irradiation. Only isolated instances of coating failure, which could be attributed to irradiation damage of the TRISO coatings on fissile particles, were evident. On the other hand, significant coating failure resulting from irradiation damage of the high-density BISO coatings on both the ThO_2 and ThC_2 particles was observed in the higher exposure fuel rods.

All BISO ThO_2 particles tested in the oxide rods were from the same particle batch. Between 15 and 100% failure of the BISO coatings was noted in all high exposure samples. As has been shown from previous HRB and HT capsule results, coating failure in this particle batch initiated in the region of high density and high anisotropy where the irradiation-induced PyC dimensional change was maximum. Results from P13N samples clearly show that with increasing irradiation exposure, cracks generated in the high-density, high-anisotropy region propagate through the coating causing it to fail (Fig. 9-17). It should be mentioned here that irradiation results from the HT capsule series show that failure of BISO coatings attributed to these properties can be eliminated in optimized coating designs (see previous Quarterly Progress Report Gulf-GA-A12599).

Fuel rod 2D-16, irradiated at 1350°C to 5.4×10^{21} n/cm^2, exhibited almost complete failure of the ThO_2 BISO coating (Figs. 9-6 and 9-7). This rod remained intact following irradiation and was observed to have shrunk both radially and axially during irradiation. These results indicate that a high oxide particle failure fraction in bonded fuel rods does not lead to fuel rod debonding or swelling during irradiation.

The UC_2 TRISO/ThC_2 BISO particles from fuel rod 3C-13 were examined metallographically after electrolytic disintegration and acid leach of the rod. This operation was performed in order to determine the amount of exposed fuel (i.e., particle failure). This rod was broken and the coated particles partially debonded prior to the disintegration; the cracking and particle debonding were attributed to hydrolysis of the ThC_2 kernels which were exposed to the atmosphere during capsule disassembly. A fertile

particle failure fraction of ∿30% was estimated from the acid leach studies. The OPyC coatings on the ThC_2 BISO particles in this rod were also of high density and contained noticeable anisotropy gradients in the inner 10 to 15 μm before irradiation. Metallography revealed that failure of the OPyC coatings was initiated in the dense, highly oriented region of this coating, identical to the failure mode discussed for ThO_2 BISO particles above.

Fuel rods 2A-10 and 4D-9 irradiated at ∿1250°C to 5.2 and 3.4 x 10^{21} n/cm^2, respectively, and containing TRISO coated ThO_2 particles were examined metallographically. The OPyC failure fraction under these relatively severe HTGR thermal conditions was <5% in both cases. Some particle failure resulting from the hot-injection molding during production was evident from metallographic observation of matrix intrusion into failed particles.

TRISO coated ThC_2 particles from batch CT6A-2463, a Fort St. Vrain production batch, were tested in fuel rods 1A-5, 3D-7, and 5D-25. No coating failure was observed in these particles irradiated at 1120°C in the low-exposure fuel rod, 5D-25. In the two high-exposure fuel rods, 1A-5 and 3D-7, irradiated at extremely high temperatures of 1415° and 1375°C, respectively, an OPyC coating failure of ~50% was observed. The OPyC coatings had a marginal degree of oriented porosity which contributed to the observed coating failures. Failure fractions will be reduced with improved coatings but it should be borne in mind that the irradiation temperatures were higher than will be experienced by 99.5% of the HTGR core volume and failure fractions higher than core average are acceptable under these extreme conditions.

Thermal Effects in Particles and Fuel Rods

Metallographic examination was conducted on two intact fuel rods (1A-5 and 5D-25) containing UC_2 fissile and ThC_2 fertile particles. No thermochemical SiC failure in TRISO coated UC_2 particles was observed in the low-exposure 5D-25 fuel rod examined after irradiation for 3732 hours at 1120°C to ∿35% FIMA. Significant SiC failure (∿10%) was observed in a TRISO ThC_2, UC_2 fuel rod (1A-5) which was irradiated at 1415°C to a burnup

of ∿65% FIMA. Fission product attack of the SiC coatings on the cool side of the particles was noted in ∿30% of the fissile particles, as shown in Fig. 9-2. Another 30% of the fissile particle coatings was completely failed, possibly due to penetration of the SiC coating by fission products followed by pressure vessel failure of the entire coating. These results indicate that at irradiation temperatures above 1400°C, the thermal performance of TRISO coated UC_2 particles can be influenced by thermochemical attack of the SiC coating by fission products.

In five fuel rods (2A-10, 2D-16, 4A-13, 4D-9, and 5A-19) containing fissile UO_2 TRISO particles, significant fuel kernel migration was observed as shown in Figs. 9-5, 9-7, 9-10, 9-12, and 9-14. In all cases the fuel kernels migrated toward the center of the fuel rod and therefore up the temperature gradient imposed across the fuel particle. Fissile particle failure resulting from UO_2 kernel migration was only observed in fuel rods 2A-10 and 2D-16, which were irradiated at 1220° and 1350°C, respectively. In these instances the fuel kernels penetrated the particle coatings and the composite structure was weakened to the point where the particle failed from the high internal gas pressure, as shown in Fig. 9-18.

Attack of the OPyC coating by the fuel kernel of an adjacent particle which had failed (cascade attack) was noted in two cases in fuel rod 4D-9, an example of which is shown in Fig. 9-19. This type of attack is more frequently observed in unbonded fissile particle samples with point-to-point contact of particles exhibiting failure. In bonded fuel rods where the particles are isolated by the matrix, failure by a cascade effect has seldom been observed.

Twenty eight particles from fuel rods 2D-16, 2A-10, 4D-9, and 5A-19 were photographed and the extent of UO_2 fuel kernel migration subsequently measured. The location of these particles in the metallographic sections was verified, and temperatures and temperature gradients were calculated for each particle based on the RAT code thermal analysis. Kernel migration coefficients, calculated using the method discussed in Ref. 9-2, are plotted in Fig. 9-20 as a function of reciprocal temperature. Kernel migration

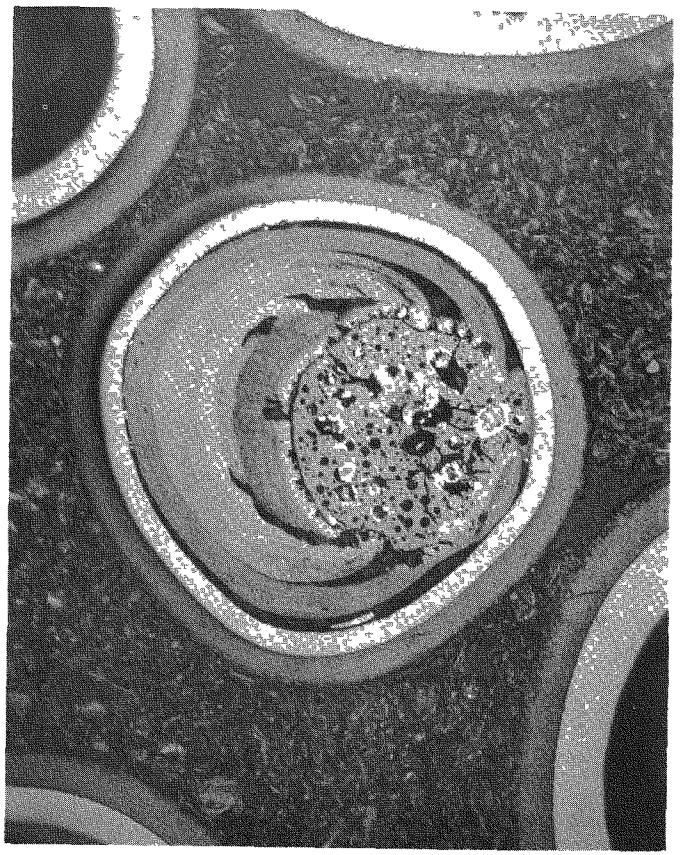

L7306-583 (a) 175X

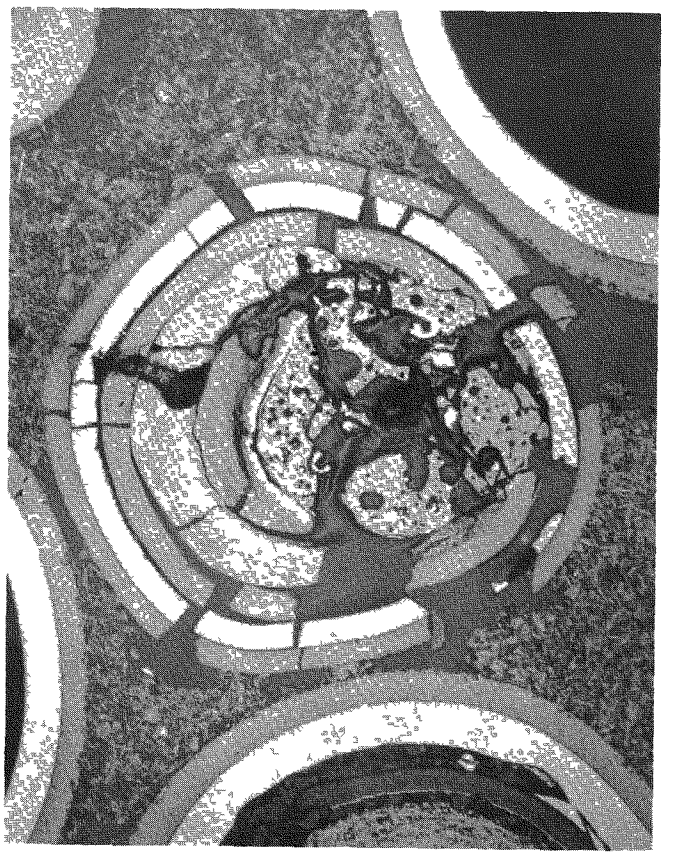

L7306-569 (b) 175X

Fig. 9-18. Photomicrographs showing fuel kernel migration in TRISO coated UO_2 particles from fuel rod 2A-10 irradiated in capsule P13N to 5.2 x 10^{21} n/cm^2 at 1220°C: (a) fuel kernel has migrated out to SiC coating leaving behind a region of deposited carbon, and (b) fuel particle has failed from internal gas pressure after coatings were weakened by migration of the fuel kernel out to the SiC coating

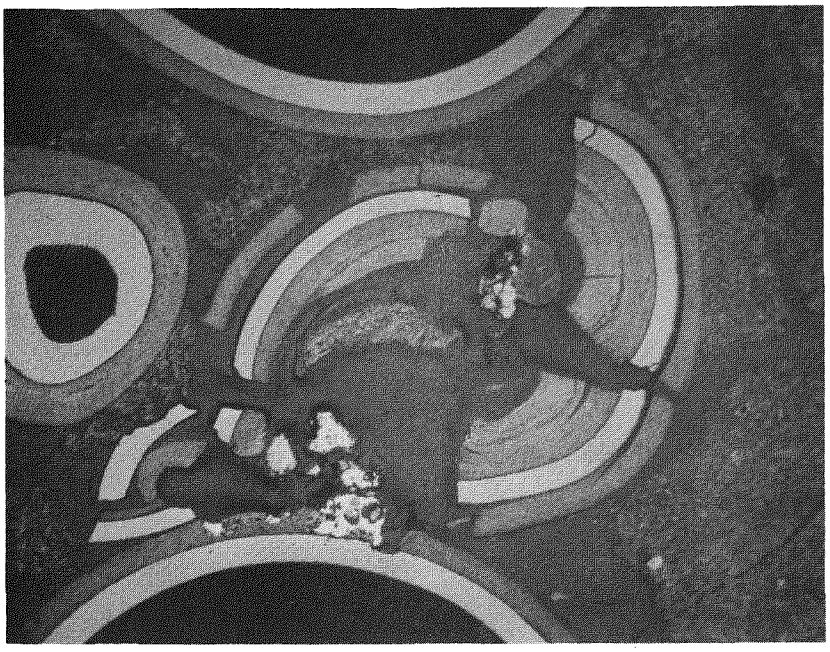

L7306-1 150X

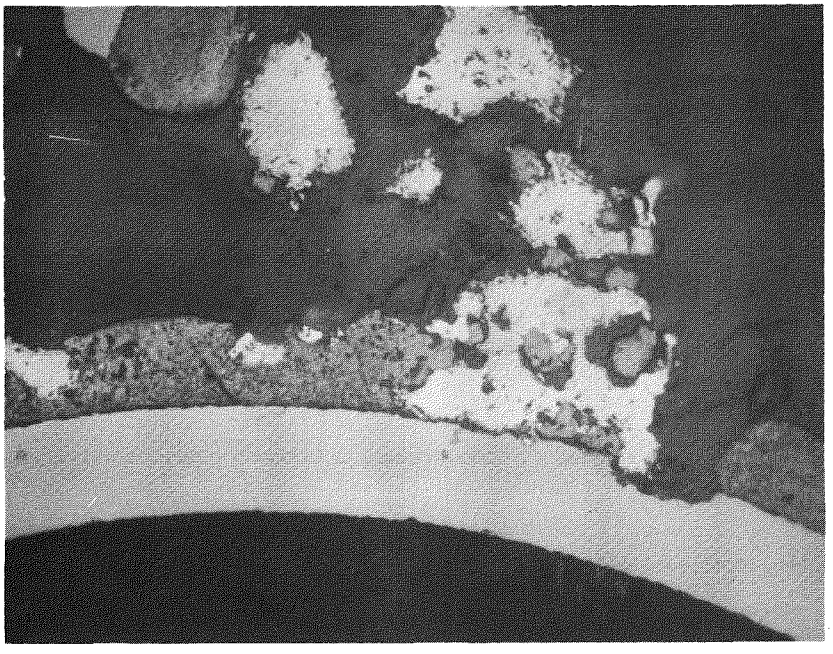

L7306-2 500X

Fig. 9-19. Photomicrograph showing attack of intact particle by fuel kernel from adjacent failed UO_2 particle in fuel rod 4D-9. Note oxide appears to have converted to a carbide phase. This type of interaction, termed the cascade effect, has seldom been observed in bonded fuel rods where the coated fuel particles are surrounded by graphite matrix.

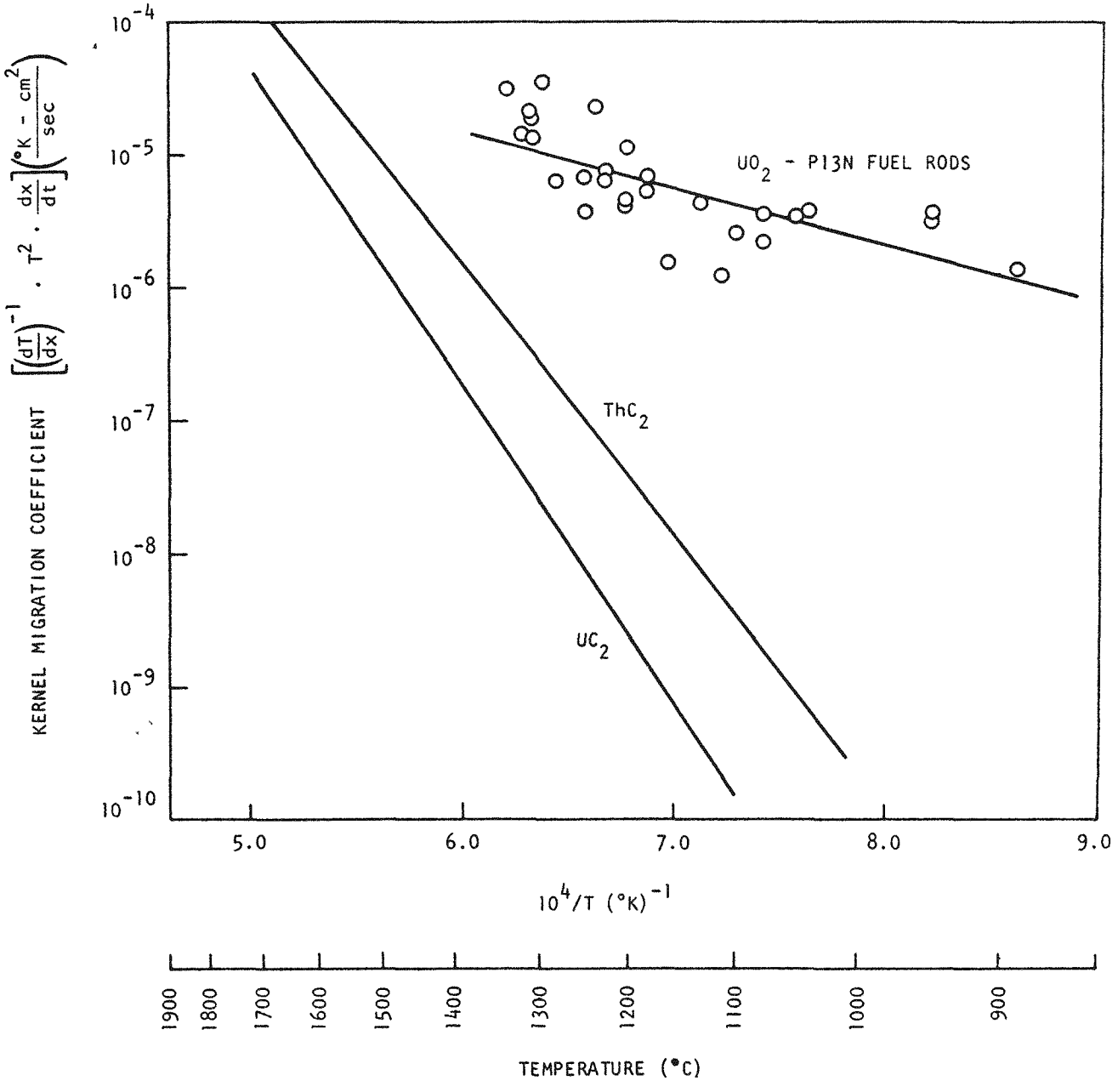

Fig. 9-20. Kernel migration coefficient versus 1/T for UO_2 TRISO particles from fuel rods 2D-16, 2A-10, 4D-9, and 5A-19 irradiated in capsule P13N. Kernel migration data for unirradiated ThC_2 (Ref. 9-2) and UC_2 (Ref. 9-3) are also shown.

coefficients determined previously for ThC_2 and UC_2 particles (Refs. 9-2, 9-3) are also plotted for comparison. It is apparent that UO_2 kernel migration has a much lower temperature dependence or activation energy than migration observed in carbide fuels. At temperatures below 1400°C the rate of UO_2 fuel kernel migration is significantly faster than either UC_2 or ThC_2 kernel migration.

Fuel rod 1E-3 containing a blend of $(Th,U)O_2$ TRISO/ThO_2 BISO particles was examined metallographically after the fuel rod had been electrolytically disintegrated. The $(Th,U)O_2$ kernels exhibited migration as shown in Fig. 9-3. Migration was not as extensive as in the fuel rods containing the UO_2 fissile particles. An analysis of kernel migration was not performed on this rod since it was disassociated prior to examination and, therefore, the location of the particles with respect to the fuel rod centerline could not be established. However, it is apparent that kernel migration in the thorium-diluted oxide kernels was much less than in the high burnup UO_2 under similar time-temperature conditions.

In carbide-containing fuel rods, the ThC_2 fuel kernels migrated toward the center of the fuel rod. A migration distance of approximately 10 to 30 μm was observed in fuel rod 1A-5 irradiated at 1415°C. No ThC_2 kernel migration was observed in the 5D rod irradiated at 1120°C.

Very little kernel swelling was noted in the ThO_2 kernels and in many cases the microstructural features were still visible, indicating the particles did not receive a very high heavy metal burnup. Thermal stability of the ThO_2 kernels appeared to be excellent in all the rods examined. No signs of kernel movement or other kernel-coating interactions were observed. These results further confirm the excellent thermal performance of ThO_2.

Fuel Compatability with Capsule Materials

In thermocouple rods 1A-5 and 2A-10, evidence of a reaction between the protective tungsten and tantalum thermocouple sheaths and the fuel

particles was observed, as shown in Fig. 9-21. Interaction appeared to occur only where the particle coatings were in contact with the tungsten and tantalum at temperatures above 1200°C. Similar interaction was not observed in thermocouple rods 4D-9 (1255°C) and 5D-25 (1120°C).

Summary

A general summary of the results obtained from examination of the fuel rods irradiated in capsule P13N is presented below:

1. Fuel rod integrity of TRISO/BISO and TRISO/TRISO particles is considered to be good even at extremely high irradiation temperatures of 1500°C. Both rod types shrink radially and axially. Rod shrinkages appears to correlate well with particle types and coating parameters.

2. No signs of matrix-coating interaction were observed in any fuel rods. All observed BISO OPyC coating failure was attributed to dimensional instability of high-density and optically anisotropic regions in the OPyC coatings.

3. A high oxide particle failure fraction in bonded fuel rods does not lead to fuel rod debonding or swelling during irradiation. If bonded fuel rods containing failed carbide fuel were exposed to the air following irradiation, hydrolysis of the exposed carbide fuel resulted in fuel rod debonding.

4. At irradiation temperatures above 1400°C the thermal performance of TRISO coated UC_2 particles irradiated to high burnups in bonded fuel rods is affected by thermochemical attack of the SiC coating by fission products.

5. ThC_2 kernel migration on the order of 10 to 30 μm was observed in a fuel rod irradiated at 1415°C. No ThO_2 kernel movement

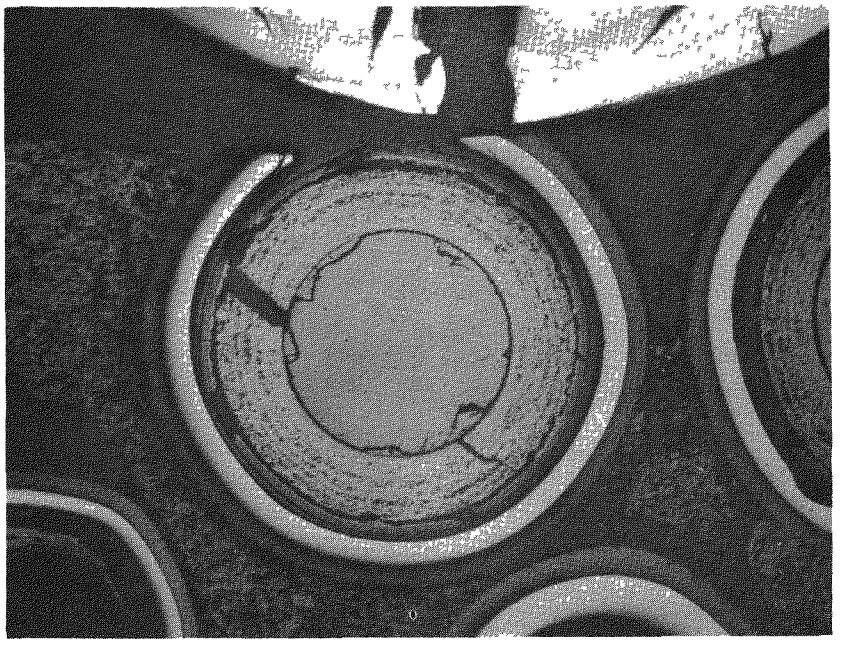

L7306-562 100X

Fig. 9-21. Photomicrograph showing interaction of tungsten and tantalum thermocouple sheath with fuel particle in fuel rod 2A-10

was observed in similarly irradiated fuel rods. These observations agree with previous data that indicate ThO_2 kernels exhibit better thermal stability during irradiation than ThC_2 kernels.

6. UO_2 fuel kernel migration was quantitatively analyzed in four fuel rods. It is apparent that unilateral movement of UO_2 fuel kernels occurs up the temperature gradient and has a much lower temperature dependence than migration observed in carbide fuel. At temperatures below 1600°C the rate of UO_2 fuel kernel migration is significantly faster than either UC_2 or ThC_2 kernel migration.

7. Dilution of UO_2 with Th reduces the burnup and significantly increases the thermochemical stability of the fissile oxide particle.

Capsules P13R and P13S

Capsules P13R and P13S will be the sixth and seventh in a series of irradiation tests of reactor fuels fabricated using candidate large HTGR materials and processes. Each capsule will consist of four fuel rod cells and two unbonded particle cells. A total of 20 fuel rods, 8 unbonded fissile particle samples, and 12 unbonded fertile particle samples will be included in each test. Each unbonded particle sample will include approximately 1000 particles.

The two capsules will be irradiated simultaneously under similar conditions allowing tests of duplicate specimens in a variety of neutron-temperature environments. The design concept for capsules P13R and P13S is given in Table 9-2. Thermal design of the experiments is nearly complete. An exact sample plan will be presented after final design analysis has been completed.

Capsules P13R and P13S will begin irradiation in the GETR in December 1973.

TABLE 9-2
DESIGN CONCEPT OF IRRADIATION CAPSULES P13R AND P13S

Cell Number	Sample Type	Expected Fast Neutron Exposure (10^{21} n/cm^2) (E ≥ 0.18 MeV)	Operating Temperature (°C)	
			P13R	P13S
1	Fuel rods	5.8	1050	1050 with intermittent temperature cycles to 1500
2	Fuel rods	8.7	1050	1050
3	Unbonded particles	9.0	1050	1050
4	Unbonded particles	9.0	1050	1050
5	Fuel rods	7.3	1250	1500
6	Fuel rods	3.9	1050	1050

GGA-ORNL Cooperative Irradiation Capsules

A series of cooperative irradiation tests is being carried out with ORNL in their irradiation facilities. These irradiations include tests in the HFIR target position (HT-capsules), the HFIR beryllium-reflector position (HRB-capsules), and the ORR facility.

Capsule P13Q

Capsule P13Q was designed to demonstrate the performance of fuel rods fabricated using candidate large HTGR processes and materials. Eighteen fuel rods, 0.63 in. in diameter by 2 in. long, will be irradiated in isotropic H-451 graphite bodies in a configuration similar to that planned for the large HTGR. The experiment was designed to operate isothermally in the ORR at a peak fuel rod temperature of 1150°C to a maximum fast neutron fluence of 9×10^{21} n/cm^2.

Experiment P13Q is the GGA portion of GGA-ORNL cooperative experiment OF-1. The GGA and ORNL halves of the test will be separated by a sealed bulkhead, and each half of the test will be controlled and monitored by seperate systems. The GGA fuel rods were loaded in the P13Q fuel bodies, sealed in the GGA portion of the capsule, and sent to ORNL for assembly of the ORNL portion of the test. Final fabrication of ORNL fuel samples and assembly of the ORNL capsule components is projected in time for a late August 1973 startup. This is a 1-1/2 month slippage over the schedule given in the previous Quarterly Progress Report (Gulf-GA-A12599).

Capsules HRB-4 and HRB-5

Capsules HRB-4 and HRB-5 represent a cooperative GGA-ORNL irradiation effort designed to evaluate the irradiation performance of fuel rods fabricated using candidate processes and materials for large HTGR startup and recycle fuel systems. Capsules HRB-4 and HRB-5 are companion capsules and were inserted in the beryllium-reflector position of the HFIR on

October 8, 1972. Both capsules were designed to operate isothermally with a 1250°C axial (centerline) temperature and were monitored for in-pile fission gas release during irradiation. Capsule HRB-5 was discharged from the HFIR in February 1973, after completing its scheduled irradiation (5 cycles) to a peak fast neutron fluence of 4.7×10^{21} n/cm^2 (E > 0.18 MeV). Capsule HRB-4 was discharged from the HFIR in July 1973, after completing its scheduled irradiation (11 cycles) to a peak fast neutron fluence of $\sim 10.5 \times 10^{21}$ n/cm^2.

The GGA samples in each capsule consisted of six fuel rods (two each of three different types) having nominal dimensions of 0.50 x 1.00 in. These samples included rods fabricated with three different graphite fillers, one binder, and two types of graphite shim material. All rods were fabricated by the admix compaction process and were carbonized and high-fired in H-327 graphite tubes to simulate in-block curing. The rather low fuel particle loadings specified by ORNL ($\sim$19% of fuel volume) required the use of coated inert particles to simulate higher particle loadings in the rods. The fissile particles (TRISO coated weak acid resins) and inert particles (BISO coated carbon) used in the fuel rods were supplied by ORNL, while the fertile particles (BISO coated ThO_2) were fabricated at GGA. A description of the fuel rods tested in capsules HRB-4 and HRB-5 was given in an earlier Quarterly Progress Report (Gulf-GA-A12422).

All fuel rods irradiated in capsule HRB-5 were intact and judged to be in good condition. Results of the visual examination, dimensional change measurements, and postirradiation fission gas release measurements (TRIGA activation) were reported in the previous Quarterly Progress Report (Gulf-GA-A12599). Additional analysis on the HRB-5 fuel rod samples will be conducted at the same time the companion HRB-4 fuel rod samples are examined.

Disassembly and preliminary examination of capsule HRB-4 was conducted at ORNL. The six GGA fuel rod samples were found to be in good

condition after irradiation to a peak fast neutron fluence of 10.2×10^{21} n/cm^2. All fuel rods were intact and very little matrix cracking was observed. The fuel rods are being shipped to GGA for further hot cell examinations.

Capsule HRB-6

Capsule HRB-6 is a cooperative GGA-ORNL irradiation experiment designed to evaluate fuel rods fabricated using candidate large HTGR type processes and materials. The experiment was designed by ORNL to operate at a constant peak fuel rod temperature of 1200°C to a peak fast neutron exposure of 9×10^{21} n/cm^2 ($E \geq 0.18$ MeV). The capsule is being monitored for fission gas release and, from the beginning, release values of 1×10^{-2} have been observed. ORNL has attributed the high release values to fuel rods fabricated by Oak Ridge in the ORNL U-233 facility. Current plans call for termination of the experiment on September 6, 1973 after eight HFIR operating cycles. A peak fast neutron exposure of 8×10^{21} n/cm^2 ($E \geq 0.18$ MeV) is expected.

Capsules HT-17, -18, and -19

Experiments HT-17 through HT-19 will be tests of unbonded, BISO or TRISO coated, ThO_2 particles. The tests are a cooperative venture with ORNL and will be conducted in the target position of the high-flux isotope reactor at ORNL. The schedule for the HT series and expected peak fast neutron exposures are listed in Table 9-3.

TABLE 9-3
SCHEDULE AND EXPECTED NEUTRON EXPOSURES FOR HT-17, -18, AND -19

Experiment	Insertion Date	Removal Date	Peak Fast Neutron Exposure (n/cm^2)
HT-17	Mid-July 1973	Early Sept. 1973	4×10^{21}
HT-18	Mid-July 1973	Mid-Oct. 1973	8×10^{21}
HT-19	Mid-July 1973	Early Dec. 1973	12×10^{21}

Each test will have a high-temperature and a low-temperature region. The experiments are designed so that the particles in the low-temperature regions operate at approximately 1100°C, while the particles in the high-temperature regions operate at approximately 1500°C.

GGA will supply samples from seven batches of coated particles for irradiation in each test. Forty-one particles from each batch will occupy low-temperature positions, while 58 will occupy high-temperature positions. Coating properties measured on the seven parent batches from which HT samples were selected are given in Table 9-4. To ensure that the small samples included from each batch are uniform, all particles tested from a given batch were separated to a constant density. Total particle densities are also given in Table 9-4. Duplicate samples from batch 6252-01-020 will be included. GGA samples will therefore occupy eight 1100°C and eight 1500°C positions in each test.

The objectives of the HT-17 through -19 experiments are as follows:

1. Compare postirradiation integrity of BISO coated ThO_2. Variables: (a) coating design, (b) OPyC density, (c) OPyC coating rate, (d) fast neutron exposure, and (e) irradiation temperature.

2. Compare neutron-induced BISO particle dimensional change as a function of the variables listed in (1).

3. Examine the effect of neutron exposure on kernel dimensions.

4. Irradiate TRISO coated ThO_2 for postirradiation fission gas pressure/composition studies.

TABLE 9-4
COATING ATTRIBUTES OF PARENT COATING BATCHES FROM WHICH PARTICLES FOR HT-17, -18, AND -19 WERE SELECTED

Parent Batch Number	Kernel		Buffer		IPyC		SiC			OPyC				Total Coated Particle		
	Diameter (μm)	Density (g/cm^3)	Thickness (μm)	Density (g/cm^3)	Thickness (μm)	Density (g/cm^3)	OPTAF	Thickness (μm)	Density (g/cm^3)	Thickness (μm)	Density (g/cm^3)	OPTAF	Coating Rate (μm/min)	Diameter (μm)	Th (%)	Density (g/cm^3)
6542-01-010	500	10.0	79	1.08	--	--	--	--	--	85	1.80	1.06	10.0	828	56.51	3.44
6542-01-020	504	9.8	81	1.17	--	--	--	--	--	74	1.82	1.10	2.7	813	57.46	3.54
6542-02-020	481	10.0	87	1.08	--	--	--	--	--	72	1.91	1.06	8.5	796	56.18	3.45
6542-02-030	481	9.8	79	1.18	--	--	--	--	--	74	1.89	1.12	2.2	786	55.97	3.54
6542-16-010	502	9.8	39	1.08	--	--	--	--	--	55	1.81[a]	1.07	3.7	687	70.36	4.78
6542-17-010	502	9.8	44	0.95	--	--	--	--	--	122	1.86	1.27	2.8	829	54.48	3.58
6252-01-020	486	9.8	95	1.26	28	1.91	1.13	30	3.21	36	1.80	1.08	3.0	858	48.50	3.28

(a) Value measured on grab sample taken following coating run. Buffer-OPyC separation was not achieved in subsequent attempts at density determinations.

REFERENCES

9-1. Burnette, R. D., W. E. Bell, and N. L. Baldwin, "Fission Product Retention Characteristics of HTGR Fuel," paper to be presented at International Conference on Nuclear Fuel Performance, October 15-19, 1973, London (Gulf-GA-A12679).

9-2. Scott, C. B., and O. M. Stansfield, "Stability of Irradiated Coated-Particle Fuels in a Temperature Gradient," USAEC Report Gulf-GA-A12081, Gulf General Atomic, September 18, 1972.

9-3. Preliminary Safety Analysis Report, Delmarva Power and Light, 1100 MW(e), Appendix F.

TASK XI

GRAPHITE RESEARCH

GRAPHITE DEVELOPMENT

Introduction

Work during the current quarter was divided among three major tasks: (1) final fabrication and shipment to ORNL of graphite irradiation capsule OG-1, (2) property measurements and irradiation of production-grade near-isotropic and needle-coke graphites, and (3) improvement of graphite stress-strain and tensile testing procedures.

Irradiation Capsule OG-1

Graphite irradiation capsule OG-1 was shipped from Gulf General Atomic on May 31, 1973, arrived at ORNL on June 4, 1973, and began its scheduled 6-month irradiation in the ORR on June 23, 1973. This capsule will provide an irradiation vehicle for advanced moderator graphites along with smaller quantities of pyrolytic carbons, silicon carbide, boronated control graphites, and fuel rod matrix materials. A description of capsule OG-1 was given in an earlier Quarterly Progress Report (Gulf-GA-A12422). The capsule is scheduled to operate at 600° to 1400°C to fluences of 0.5 to 3.5 x 10^{21} n/cm^2 (E > 0.18 MeV) and will be discharged from its position in the ORR in December 1973.

During the current quarter, OG-1 has been operating normally near design temperatures. Plans are being made to unload the capsule crucibles and samples at ORNL.

Plans are also under way to assemble materials for the construction of graphite capsule OG-2. OG-2 is scheduled to replace OG-1 in the ORR during the last half of FY-74. A portion of the samples from OG-1 will be reirradiated in OG-2.

Graphite Irradiation Studies

Several new graphites are currently under study along with Grade H-327, which is the current reference graphite for HTGR design. A description of these graphites (needle-coke and near-isotropic grades) was given in Table 11-1 of an earlier Quarterly Progress Report (Gulf-GA-A12515). In addition, a small sample of another Pechiney graphite, P_3JHA_2N, has been received and tested for tensile strength and elastic modulus. Additional values of these properties have also been obtained from specimens machined from a second sample (full log) of P_3JHAN. These new data are presented in Table 11-1.

The new tensile data were obtained on specimens 0.5-in. in diameter by 4.0 in. long. Both P_3JHAN and P_3JHA_2N failed to meet the guideline specifications for tensile strength. In addition, the new data for P_3JHAN do not agree with earlier published data (Ref. 11-1) which gave values of 1650 psi in the radial direction and 2120 psi longitudinally. Efforts are being made to resolve this disagreement.

Efforts are continuing in the development of a strain gage technique for the measurement of Poisson's ratio of moderator graphites. During the current quarter, experiments were completed which indicate that the epoxy joint between H-451 graphite and a strain gage does not alter the tensile or compressive strains produced in a specimen under load. These experiments thus indicate that reliable Poisson's ratio measurements can be made on graphite using conventional strain gage techniques.

Plans are now under way to measure Poisson's ratio of H-451 graphite as a function of orientation and position in a log.

TABLE 11-1
ULTIMATE TENSILE STRENGTH AND ELASTIC MODULUS OF NUCLEAR GRAPHITES
(0.5-IN.-DIAMETER BY 4.0-INCH-LONG SPECIMENS)

	End Center				Mid-Length Center				Mid-Length Edge			
	Tensile Strength (psi)	Range (psi)	E_c[a] (10^6 psi)	Range (10^6 psi)	Tensile Strength (psi)	Range (psi)	E_c[a] (10^6 psi)	Range (10^6 psi)	Tensile Strength (psi)	Range (psi)	E_c[a] (10^6 psi)	Range (10^6 psi)
AXIAL ORIENTATION (PARALLEL TO EXTRUSION AXIS)												
P_3JHAN	--	--	--	--	1032	839 to 1274	1.05	0.96 to 1.19	1982	1733 to 2223	1.30	1.14 to 1.47
P_3JHA_2N	--	--	--	--	1379[b]	1299 to 1573	1.27	1.09 to 1.39	--	--	--	--
RADIAL ORIENTATION (PERPENDICULAR TO EXTRUSION AXIS)												
P_3JHAN	--	--	--	--	1388	1148 to 1563	0.83	0.78 to 0.86	1499	1374 to 1649	0.87	0.81 to 1.0
P_3JHA_2N	--	--	--	--	1429[b]	1324 to 1583	0.84	0.78 to 0.93	--	--	--	--

[a] E_c = Chord modulus based on strains measured at 250 and 500 psi.

[b] Location of P_3JHA_2N sample in parent log not known.

Graphite Characterization

Efforts are under way to improve the present method of measuring the tensile and stress-strain properties of graphite. In this regard, preliminary tests have been conducted using a strain gage implemented (four gages located 90° apart) specimen to determine the axiality of the present stressing system (chain at each end of specimen) used to measure these properties. The results indicate that some bending moments are introduced in a specimen using the present system. Work is now under way to devise a new system for eliminating such bending moments. Tests using spherical bearings in place of the chains at the ends of a specimen have indicated a considerable decrease in the magnitude of the bending moments. Further tests with roller-bearing devices are planned.

FUEL MATRIX DEVELOPMENT

Introduction

The objective of this program is to evaluate fuel matrices for fuel rod development studies. The major portion of this work is currently aimed at developing measuring techniques and collecting data on thermal conductivity of fuel rods and fuel rod matrices.

Work in this area during the current quarter was divided between two major tasks: (1) calibration of a direct heating technique for measurement of the thermal conductivity of unirradiated fuel rods, and (2) repair and calibration of a device (Dynatech) for the measurement of the thermal conductivity of irradiated fuel rods.

Direct Heating Technique (Unirradiated Fuel Rod Thermal Conductivity)

The direct heating method (Refs. 11-2, 11-3), as used in the past to measure the thermal conductivity of unirradiated fuel rods, has been carefully analyzed to determine sources of measurement errors. This error analysis was prompted by past observations of large scatter in thermal conductivity for fuel rods of similar composition.

The analysis indicated that the large scatter and apparent anomalies observed in previous data were largely due to errors involved in fuel rod surface temperature and voltage gradient measurements. Errors in voltage gradient measurement have been considerably reduced. Errors in fuel rod surface temperature measurement have been minimized by periodic calibrations of the optical temperature measuring device.

Plans are now under way and specimens have been fabricated to conduct experimental measurements of fuel rod surface emissivity. A knowledge of this parameter is required for correcting the surface temperature (and hence thermal conductivities) of fuel rods measured by the direct heating method. Present estimates indicate that correcting the surface temperatures of fuel rods measured by this technique will increase the measured thermal conductivities by as much as 30%.

A theoretical correction for the apparent surface temperature of a fuel rod is being made for all thermal conductivity measurements. This will suffice until the surface emissivity is established by experimentation. A comparison of the direct heating technique for the measurement of thermal conductivity, based on this theoretical emissivity correction, has been made with two other techniques, thermal diffusivity (Ref. 11-4) and the Longmire slab technique (Ref. 11-5), using a specimen of H-451 graphite. The results of this comparison are shown in Fig. 11-1, where the thermal conductivities of the H-451 graphite as measured by the three techniques are indicated. The thermal diffusivity data and data obtained from the slab technique appear to complement each other. However, the data from the direct heating measurements complement the other data only at the highest temperature of measurement ($\sim$1250°C) and are significantly higher at lower temperatures ($\sim$20% high at 900°C). Part of the reason for the discrepancies is believed to be related to the thermal and electrical properties of the material used for the specimen end pieces and their ability to guard the specimen against the development of axial thermal gradients. Means to guard against such effects are presently being studied to aid in the measurement of fuel rod thermal conductivity. In addition, considerable error is involved in correcting the direct heating data at lower temperatures (around 900°C). At these temperatures the observed temperature gradients are small and are greatly affected by any inaccuracies in temperature measurement.

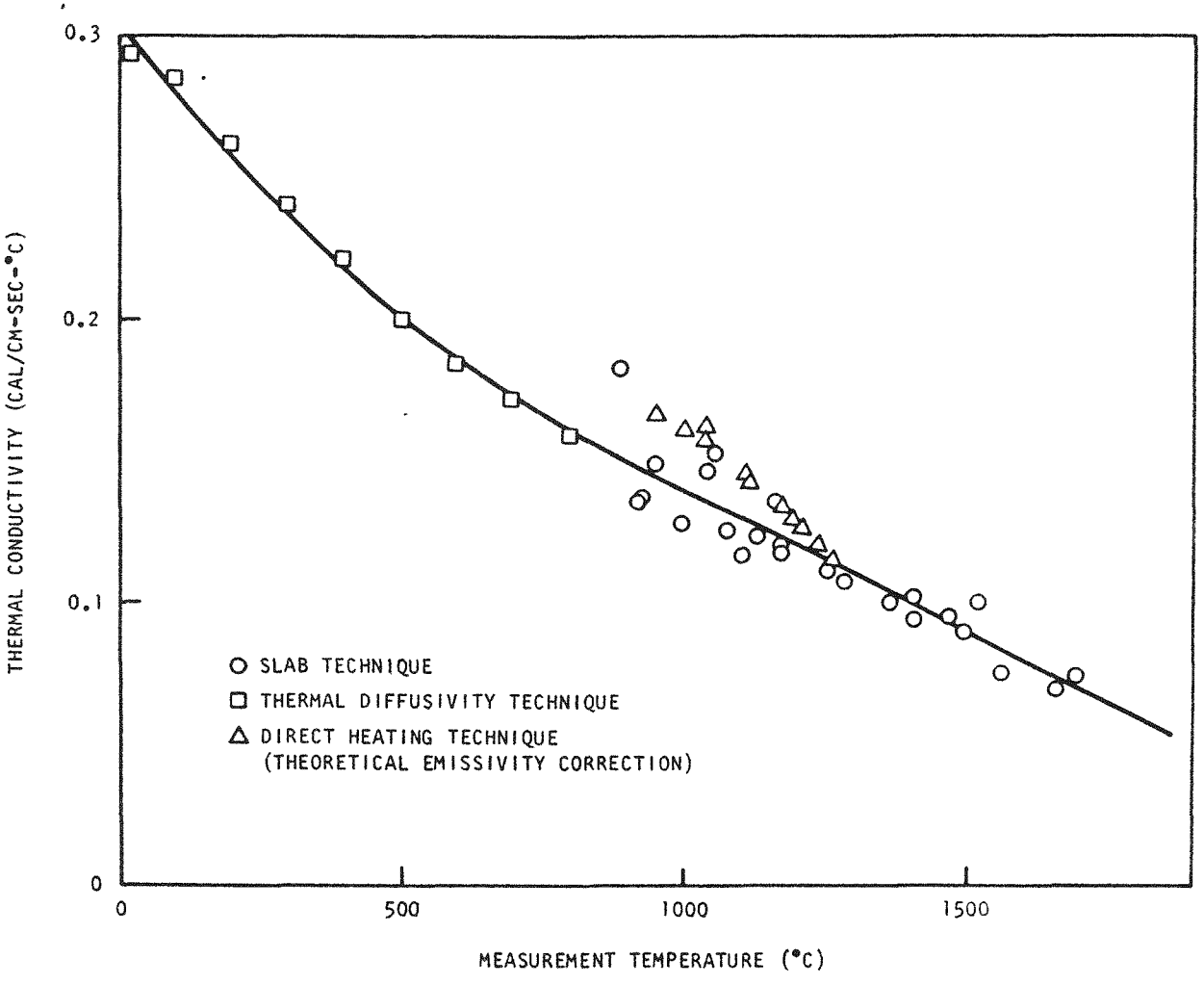

Fig. 11-1. Thermal conductivity of H-451 graphite (perpendicular to extrusion axis)

Preparations are now under way to make a similar comparative analysis for a material (ungraphitized carbon) with a thermal conductivity near that of typical fuel rods.

Dynatech Device (Irradiated Fuel Rod Thermal Conductivity)

A comparative cut-bar (Refs. 11-6, 11-7) thermal conductivity measuring device (Dynatech) has been modified for the purpose of measuring the thermal conductivity of irradiated fuel rods in the Hot Cell. Heaters in this apparatus were burned out, but were recently repaired by replacing 18 thermocouples and a guard heater.

An initial calibration run using a pyroceram standard has been made with this instrument, and the measured thermal conductivity values were within 10% of the published National Bureau of Standards curve for this material.

Preparations are now under way to measure the thermal conductivities of other materials with this device and the direct heating method in order to compare the two techniques.

REFERENCES

11-1. Mottet, P., J. Rappeneau, J. Love, and P. Cornuault, "Physical and Mechanical Properties of Nuclear Graphites. Their Applications in High-Temperature Reactors," in Carbon 72, International Carbon Conference, Baden-Baden, W. Germany, June 26-30, 1972, p. 183.

11-2. Angell, M. F., Phys. Rev. 33, 421 (1911).

11-3. Powell, R. W., and F. H. Schofield, Proc. Phys. Soc. Lond. 51, 153 (1939).

11-4. Parker, W. J., R. J. Jenkins, C. P. Butler, and G. L. Abbott, J. Appl. Phys. 32, 1679 (1961).

11-5. Longmire, C. L., Rev. Sci. Instruments 28, 904 (1957).

11-6. Francis, R. K., and J. R. Tinkelpaugh, J. Am. Ceram. Soc. 43, 560 (1960).

11-7. France, J., and W. D. Kingery, J. Am. Ceram. Soc. 37, 80 (1954).

APPENDIX

PROJECT REPORTS PUBLISHED DURING THE QUARTER

Gulden, T. D., D. P. Harmon, and O. M. Stansfield, "Design and Performance of Coated Particle Fuels for the Thorium Cycle HTGR," Gulf General Atomic Report Gulf-GA-A12628, August 15, 1973.

Haire, M. J., and L. R. Zumwalt, "Cesium Diffusion Coefficients and Other Results from the Analysis of Peach Bottom D13-05 Fuel Element Activity Profiles," USAEC Report Gulf-GA-A12492, Gulf General Atomic, July 26, 1973.